UNIVERSIDAD COMPLUTENSE DE MADRID
FACULTAD DE CIENCIAS FÍSICAS

TESIS DOCTORAL

Design and characterization of nanometric resonant structures and advanced concentration strategies applied to photonic devices

Diseño y caracterización de estructuras resonantes y estrategias de concentración avanzada aplicadasa dispositivos fotónicos

MEMORIA PARA OPTAR AL GRADO DE DOCTOR

PRESENTADA POR

Mahmoud Hamdy Elshorbagy

Directores

Javier Alda
Alexander Cuadrado

Madrid

Complutense University of Madrid

Faculty of Physical Sciences

Department of Optics

PhD Thesis

Design and characterization of nanometric resonant structures and advanced concentration strategies applied to photonic devices

This dissertation is submitted to
the PhD Program in Physics of the University Complutense of Madrid

Author:
Mahmoud Hamdy Elshorbagy

Supervisors:
Prof. Javier Alda
Dr. Alexander Cuadrado

June 29, 2020

Universidad Complutense de Madrid

Facultad de Ciencias Físicas

Departamento de Óptica

Tesis Doctoral

Diseño y caracterización de estructuras resonantes y estrategias de concentración avanzada aplicadas a dispositivos fotónicos.

Programa de Doctorado en Física de la Universidad Complutense de Madrid

Autor:
Mahmoud Hamdy Elshorbagy

Directores:
Prof. Javier Alda
Dr. Alexander Cuadrado

June 29, 2020

Abstract

Efficient low-cost optoelectronic devices are used for many applications, for example, energy production, and sensing. The development of these devices can be step-forward using nanophotonic and nanoplasmonic structures. In this dissertation we propose, design, and analyze several nanostructures to improve the performance of these devices.

For energy applications, we select amorphous silicon hydrogenated, and perovskite/crystalline silicon tandem solar cells. We choose amorphous silicon solar cells because this material is abundant, non-toxic, long-life compared to organic solar cells, and can be fabricated at a low cost. The tandem perovskite/crystalline silicon solar cells are devices with potential power conversion efficiency > 30 %. Our designs are based on dielectric nanostructures. We applied a 1D nanostructure array to the top and bottom of amorphous silicon hydrogenated solar cells, in two separate designs. The absorption enhancement within the auxiliary layers of these devices is dissipated as heat and partially mitigate the defects resulted from the Staebler Wronski effect. A metasurface in the form of multilayer gratings embedded in the active layer of the perovskite top cell of the tandem device, improves the absorption efficiency in the whole device. A sawtooth periodic back texture has been optimized and tested to work with the metasurface for further improvement of the device performance. These nanostructures are arranged to maximize the absorption efficiency of the selected solar cells, mainly by reducing their total reflectance. The analysis and calculations are completed by modeling the conditions of the sun illumination, i.e, unpolarized light, and oblique incidence. The performance of the devices is calculated under these conditions.

We used metallic gratings with different arrangements embedded in a dielectric buffer layer to excite surface plasmon resonances at metal/dielectric interfaces using normal incidence conditions. We optimize the designs using a merit function, which is carefully selected to maximize the sensing characteristics: sensitivity, figure of merit, and dynamic range. Two different optimized metallic gratings (nanoslits, and multilayer metal/dielectric grating structure) provide sensors with high sensitivity and figure of merit. However, the dynamic range of these devices is limited. High refractive index scatterers made of dielectric material embedded in low refractive index host, improve the dynamic range of the proposed devices. The improvement is attributed to the high refractive index contrast around the scatterers. We optimize several designs to work as refractometric sensors: ZnO nanoprisms embedded in MgF_2 substrate, a Si_3N_4 high aspect ratio grating in the analyte, and a GaP rectangular grating embedded in a MgF_2 buffer layer. We found that a GaP rectangular grating in a MgF_2 buffer layer produces a Fano resonance, and provides a sensor for which the three characteristics of the senor are enhanced together. In this case, the refractive index contrast of the scatterer is the largest one obtained with the studied materials. A high sensitivity, and figure of merit over a wide range of changes in the refractive index of the sensed medium were achieved.

We also proposed hybrid devices that can produce an electrical signal, and enhance their capabilities for sensing applications. We do that by exciting plasmonic resonances in these devices, and make them spectral selective. The direct readout of the electrical signal from these devices, and its relation to environmental changes, provides simple operation, low-cost, and compact sensors. A modified figure of merit is adapted for each one of these direct readout devices. We adapt it from the operational mechanism and the working principle of each device.

Resumen

Los dispositivos optoelectrónicos eficientes y de bajo coste se utilizan en muchas aplicaciones. Por ejemplo, en la producción de energía y en sensores. La incorporacion de estructuras nanofotónicas y nanoplasmónicas es un paso adelante en el desarrollo de estos dispositivos. En esta tesis doctoral proponemos, diseñamos y analizamos varias nano-estructuras que mejoran el rendimiento de estos dispositivos.

En aplicaciones para energía, hemos selecionado células de silicio amorfo hidrogenado, y células tándem de perovskitas y silicio cristalino. Hemos elegido las células solares de silicio cristalino porque es un material abundante, no tóxico, de larga vida comparada con las células orgánicas y fabricadas a bajo coste. Las células tándem perovskita/silicio cristalino son dispositivos con eficiencias de conversión superiores al 30 %. Nuestros diseños están basados en nano-estructuras dieléctricas. Hemos aplicado una nano-estructura periódica 1D a la superficie anterior y posterior de células solares de silicio amorfo hidrogenado en dos diseños separados. El aumento de la absorción en las capas auxiliares de estas células se disipa como calor y mitiga parcialmente los defectos producidos por el efecto Staebler-Wronski. Una metasuperficie hecha con redes apiladas en capas incluidas en las capa activa de la porción superior de una célula tándem mejora la eficiencia de absorción de todo el dispositivo. Una texturización con forma de diente de sierra en la capa posterior de la célula tándem ha sido optimizada y probada para su funcionamiento en conjunción con la metasuperficie para mejorar todavía más estas células. Las estructuras propuestas maximizan la absorción debido a una reducción de la reflectancia total. El análisis y los cálculos se completan incluyendo las condiciones reales de iluminación, es decir, considerando luz con polarización natural e incidencia oblícua.

Hemos utilizado redes metálicas incluidas en capas dieléctricas en distintas configuraciones para excitar resonancias de plasmones superficiales en las interfases entre metal y dieléctrico en condiciones de incidencia normal. Nuestra optimización utiliza una función de mérito que es cuidadosamente seleccionada para maximizar las características de sensado: sensibilidad, figura de mérito, y rango dinámico. Dos redes metálicas optimizadas (nano-aperturas, y estructuras de redes apiladas metálicas y dieléctricas) dan lugar a sensores con alta sensibilidad y figura de mérito. Sin embargo, el rango dinámico de estos dispositivos está limitado. El uso de dispersores dieléctricos de alto índice de refracción mejora el rango dinámico. Este aumento se atribuye al alto contraste en índice de refracción entre los dispersores y el medio de alrededor. Hemos optimizado varios diseños para que funcionen como sensores refractométricos: nanoprismas de ZnO en un substrato de MgF_2, redes de elevada razón de aspecto fabricadas en nitruro de silicio en contacto con el analito, y redes con perfil rectangular de GaP en un sustrato de MgF_2. Hemos encontrado que la red rectangular de GaP en MgF_2 produce resonancias de Fano, y genera un sensor en el que los tres parámetros característicos del sensor están mejorados. En este caso, el contraste entre índices de refracción es el mayor y una alta sensibilidad, una alta figura de mérito y una amplio rango dinámico para el índice de refracción es obtenido.

También hemos propuesto dispositivos híbridos qeu proporcional una señal eléctrica, y mejoran las capacidades de sensado. Esto se consigue mediante la excitación de resonancias plasmónicas, que hacen a estos dispositivos espectralmente selectivos. La lectura directa de una señal eléctrica, que además está relacionada con cambios en el ambiente, proporciona una operación sencilla, un bajo coste y un sensor compacto. En estos dispostivos, hemos adaptado la definición de la figura de mérito a esta lectura directa. Esta adaptación se realiza en función de los mecanismos de operación y los principios de funcionamiento de cada dispositivo.

Long abstract

The aim of this thesis is to develop efficient photonic devices using reliable modeling, design and optimization of practical nanophotonic, or nanoplasmonic structures, with potential application in energy harvesting and sensing. We apply numerical electromagnetic simulation based on the finite element method, using well established theories and physics to optimize the performance of such devices.

The work in this thesis contains three sets of devices with various structures of different scales: solar cells, plasmonic sensors, and solar cell based sensors. We always take into account the feasibility of the devices, in both the fabrication and the modeling aspects of the design, by being far from very complex designs and extremely tiny features. The computational package Comsol multiphysics, based on the finite element method, is a useful tool to explore the optical performance of the designs with the capability to optimize the devices in terms of materials, geometries, and structures. With this tool, we find out the distributions of the optical fields, the active and parasitic absorption at each layer of the proposed devices, and the total reflectance.

This thesis is divided into three parts as follow:

- Improving absorption efficiency of solar cells

Nano-photonic and nano-plasmonic structures enhance the optical performance of solar cells, sensors, and a combination of them. Flexible, lightweight, and low cost energy harvesting and testing devices for portable applications are based on thin films and nanostructures in what is called third generation optoelectronics. Among thin film semiconductors, amorphous silicon is an abundant material, non-toxic, and with moderate conversion efficiencies. The development of devices using this material relies on the enhancement of the optical absorption efficiency reducing the thickness of the active layer for a better collection of the photogenerated charge carriers. Another challenge is to mitigate the defects caused by the Staebler Wronski effect. These defects are thickness dependent, and can be recovered by annealing.

Planar antireflection coatings are not suitable for amorphous silicon hydrogenated (aSiH) solar cells. Instead, its active absorption can be enhanced by using dielectric nanostructures working as antireflection coatings. We focus our analysis on maximizing the short-circuit current (J_{SC}) delivered by the cell under solar irradiance. We analyze first the planar aSiH solar cell, taking into account every layer, including the buffer layers and contacts. A customized design of an antireflection coating in the form of nanostructured dielectric layers, produces a J_{SC} enhancement of 9% with respect to the reference flat solar cell, mainly due to the reduction in reflectivity of the cell. Three different geometries of 1D nanostructures have been analyzed and compared, obtaining quite similar results. An improvement in performance has been also obtained for realizable geometrical dimensions that could be fabricated while maintaining the electric conductivity of the front contact. Most of the enhancement from this nanostructure is lost in the front layers, and dissipated as heat. Fortunately, this will help to partially mitigate the defects caused by the Staebler-Wronsky effect.

Ultrathin aSiH solar cells grown on a one-dimensional dielectric subwavelength grating improve the short circuit current by a factor of more than 50% when compared with conventional, flat ultrathin aSiH devices. This improvement is possible due to several mechanisms. In addition to the increase in the exposed area caused by the nanostructured surface, a reliable computational electromagnetic evaluation of the interaction of the solar spectrum with the cell

structure demonstrates that absorption at the active layer is enhanced and also reflectivity is decreased. Besides, the absorbed power at the nonactive layers is larger, helping to increase the temperature and mitigate the defects. The detailed analysis of the power flux inside the structure has also shown that funneling and guiding mechanisms are at play, increasing the optical path within the active layer, and producing a better performance of the cell.

Solar energy is now dealing with the challenge of overcoming the Shockley–Queisser limit of single junction solar cells. Multilayer solar cells are a promising solution in the so-called third generation of solar cells. The combination of materials with different bandgap energies in multijunction cells enables power conversion efficiencies up to 30% at reasonable costs. However, interfaces between different layers are critical due to their optical losses. We propose a hybrid metasurface in a monolithic perovskite/crystalline silicon solar cell. The design takes advantage of the customized light management to optimize the absorption in the perovskite, as well as an efficient light guiding towards the silicon subcell. Furthermore, we have also included the effect of a textured back contact. The optimum proposal provides an enhancement of the matched short-circuit current density of a 20.5% with respect to the planar reference without nanostructure. We also study the effects of materials and geometry on the optical performance of layers forming the nanostructure. Our proposed design increases the performance of both subcells by managing light towards the active layer, as well as by minimizing reflections losses at the interfaces. We sweep both the refractive index and thickness of the transport layers and the dielectric spacer composing the metasurface, obtaining a range of these parameters for the proper operation of the device. Using these values, we obtain a reduction in the optical losses. In particular, they are more than a 33% lower than those of a planar cell. This approach leads to an enhancement in the optical response, widens the possibilities for the manufacturers to use different materials, and allows wide geometrical tolerances.

- Plasmonic sensors with high performance

The sensitivity of plasmonic sensors based on conventional Kretschmann configuration is limited to a theoretical maximum of 600 deg/RIU, for angular interrogation. Even, this limit can be reached at the cost of the device dynamic range, which is decreased at this high sensitivity. The angular and spectral interrogation methods require goniometers and high resolution spectrometers for optical signal illumination and detection. One way to simplify this sensing mechanism is to develop devices based on normal incidence conditions. These devices are compact and can be attached to the tip of an optical fiber. We propose several designs to improve the performance of plasmonic sensors that are based on normal incidence conditions. The most important quality parameters of the plasmonic sensors are: sensitivity, figure of merit (FOM), linearity, dynamic range, and limit of detection. In each design, we maximize sensitivity and FOM. Depending on the physical mechanism at play, and the materials forming the nanostructure, we find also, that the dynamic range extends very significantly.

A metallic nanostructured array that diffracts radiation toward a thin metallic layer generates surface plasmon resonances for normally incident light. The location of the minimum of the spectral reflectivity serves to detect changes in the index of refraction of the medium under analysis. The geometry of the arrangement and the material selection, are changed to optimize some performance parameters as sensitivity, the figure of merit, field enhancement, and spectral width. This optimization takes into account the feasibility of the fabrication. The optimized design has a maximum value of sensitivity as 1000 nm/RIU, and figure of merit 705 RIU^{-1}, which are competitive with those previously reported. The dynamic range of these

designs ranges from 1.33 to 1.35 RIU. This range is improved compared with Kretschmann configuration devices.

We have also analyzed a refractometric sensor realized as a stack of metallic gratings with subwavelength features and embedded within a low-index dielectric medium. Light is strongly confined through funneling and guiding mechanisms and excites resonances that sense the analyte medium. Two terminations of the structure are compared. One of them has a dielectric medium in contact with the analyte and exploits the selective spectral transmission of the structure. The other design has a metallic continuous layer that generates surface plasmon resonances at the metal/analyte interface. Both designs respond with narrow spectral features that are sensitive to the change in the refractive index of the analyte and can be used for sensing biomedical samples. In this design, having the same dynamic range as the metallic slits sensor, the sensitivity and the FOM are greatly improved, reaching values of 1130 nm/RIU and 2100 RIU^{-1}, respectively.

A periodic array of extruded nanoprisms is proposed to generate surface plasmon resonances for sensing applications. Nanoprisms guide and funnel light towards the metal/dielectric interface where the dielectric acts as the medium under test. The system works under normal incidence conditions and is spectrally interrogated. The performance is better than some designs based on classical Kretschmann configurations, and the values of sensitivity and figure of merit are competitive with other plasmonic sensor technologies. The geometry and the choice of materials have been made taking into account applicable fabrication constraints. Although the values of sensitivity and FOM are moderate and lower than the maximum theoretical limit of the Kretschmann devices, they are still competitive with some other reported designs. Furthermore, the dynamic range is extended up to 1.43 RIU, which is $\times 4$ larger than our two designs above (nanoslits, and the multi-layer gratings), and the Kretschmann counterpart. Here, the use of low loss dielectric grating to excite surface plasmon resonances improves the dynamic range of the device by better coupling the incoming light to the resonant mode. Furthermore, the refractive index contrast of the aluminum zinc oxide embedded in MgF_2 also helps to extend the dynamic range.

We use the findings of the nanoprism design to reconfigure the structure and propose a nanostructured device that hybridizes grating modes and surface plasmon resonances. The design uses an effective index of refraction that considers the volume fraction of the involved materials, and the propagation depth of the plasmon through the structure. Our geometry is an extruded low-order diffraction grating made of dielectric nano-triangles. Surface plasmon resonances are excited at a metal/dielectric interface, which is separated from the analyte by a high-index dielectric layer. The optical performance of the refractometric sensor is highly competitive in sensitivity and figure of merit because of the ultra-narrow spectral response (below 0.1 nm). Moreover, it is operative within a wide range of the index of refraction (from 1.3 till 1.56 RIU), and also works under normal incidence conditions.

High sensitivity, FOM, and wide dynamic range is a challenge to achieve large values for all of them together in one device. We designed a plasmonic refractometric sensor that works under normal incidence conditions, allowing its integration on a fiber tip. The sensor's material and geometry exploit the large scattering cross-section given by high-contrast of the index of refraction subwavelength dielectric gratings. Our design generates a hybrid plasmonic-Fano resonance due to the interference between the surface plasmon resonance and the grating response. We optimize the sensor with a merit function that combines the quality parameter of the resonance and the field enhancement at the interaction volume where the plasmon

propagates. Our device shows a high sensitivity of 1000 nm/RIU, and a high FOM equal to 775 RIU^{-1}. Also, the dynamic range extends to an extreme value of 2 RIU. This is possible thanks to the high refractive index contrast achieved by GaP (n=3.141 at λ =1350 nm), embedded in MgF_2 (n=1.37 at λ =1350 nm).

- Direct readout low-cost plasmonic sensors

In the last part of this dissertation, we designed sensing devices that combine both solar cells or bolometric effect with plasmonic effects. These devices are simpler and cheaper alternatives to conventional plasmonic sensors.

The bolometric effect allows us to electrically monitor the spectral characteristics of the plasmonic sensor. It provides a lower cost and simpler sample characterization compared with angular and spectral signal acquisition techniques. In this device, a monochromatic light source illuminates a spectrally selective plasmonic nanostructure. This arrangement is formed by a dielectric low-order diffraction grating that combines two materials with a high-contrast in the index of refraction. Light interacts with this structure and reaches a thin metallic layer, that is also exposed to the analyte. The narrow absorption generated by surface plasmon resonances, hybridized with low-order grating modes, heats the metal layer where plasmons are excited. The temperature change caused by this absorption modifies the resistance of a metallic layer through the bolometric effect. Therefore, a refractometric change in the analyte varies the electric resistivity under resonant excitation. We monitor the change in resistance by an external electric circuit. This optoelectronic feature must be included in the definition of the sensitivity and figure of merit parameters. Besides the competitive value of the FOM (around 400 RIU^{-1}), the proposed system is fully based on optoelectronic measurements. The proposed refractometer behaves linearly within a range centered around the index of refraction of aqueous media, n=1.33, and can be applied to the sensing of specimens in bio-physics, biology, and environmental sciences.

Perovskite solar cells are currently considered a promising technology for solar energy harvesting. Their capability to deliver an electrical signal when illuminated can sense changes in environmental parameters. A modified perovskite cell can also work as a refractometric sensor by generating surface plasmon resonances at its front surface. Metal-dielectric interfaces are necessary to excite plasmonic resonances. However, if the transparent front of a perovskite cell is replaced by a uniform metal layer, the optical absorption at the active layer decreases significantly. This absorption enhances again when the front metallic surface is nanostructured, adding a periodic extruded array of high aspect-ratio dielectric pyramids. This relief excites surface plasmon resonances through a grating coupling mechanism with the metal surface. Our design allows a selective absorption in the active layer of the cell with a spectral response narrower than 1 nm. The photo-current generated by the cells becomes the signal of the sensor. The device employs an optoelectronic interrogation method, instead of the well-known spectral acquisition scheme. The sensitivity and FOM parameters applicable to refractometric sensors were adapted to this new situation. The design has been customized to sense variations in the index of refraction of air between 1.0 and 1.1. The FOM reaches a maximum value of 1005 RIU^{-1}, which is competitive when considering some other advantages, as the easiness of the acquisition signal procedure and the total cost of the sensing system.

We proposed and analyzed another design that uses metallic nanoslits to generate surface plasmon resonances at the front surface of a perovskite cell. The device uses the variation

of the current delivered by a perovskite cell to detect changes in the index of refraction of air, that is in contact with the front surface of the cell. The calculation identifies which geometrical and material structures enhance this behavior. After replacing the top transparent electrode of a solar cell with an optimized subwavelength metallic grating, we find a large variation in the responsivity of the cell with respect to the change in the index of refraction of the surrounding medium. Such a refractometric sensor can be interrogated electronically, avoiding the cumbersome set-ups of spectral or angular interrogation methods. We present an adaptation of the performance parameters of refractometric sensors (sensitivity and FOM) to the case of optoelectronic interrogation methods. The values of sensitivity and FOM are promising for the development of refractometric perovskite-based sensors.

Descripción de la tesis en español

Título de la tesis

Diseño y caracterización de estructuras resonantes nanométricas y estrategias de concentración avanzada aplicadasd a dispositivos fotónicos.

Autor

Mahmoud Hamdy Elshorbagy

Directores

Prof. Javier Alda Serrano
Dr. Alexander Cuadrado Conde

Programa

Programa de Doctorado en Física de la Universidad Complutense de Madrid.

Departamento y Facultad

Departamento de Óptica
Facultad de Ciencias Físicas

Fecha

Mayo de 2020

Resumen largo

El objetivo de esta tesis es el desarrollo de dispositivos fotónicos eficientes que se realiza mediante un modelado, diseño y optimización fiables de estructuras nanofotónicas o nanoplasmónicas realizables, con aplicación potencial en la recolección de energía y en el sensado. Para ello, aplicamos simulaciones numéricas electromagnéticas basadas en el método de elementos finitos, usando modelos teóricos y físicos bien establecidos para la optimización del rendimiento de los dispositivos.

Este trabajo está distribuido en tres tipos de dispositivos con estructuras en escalas diferentes: células solares, sensores plasmónicos, y sensores basados en células solares. Siempre hemos tenido en cuenta la realización práctica de los dispositivos, tanto en los aspectos de fabricación como del propio modelado, tratando de evitar diseños muy complejos y rasgos extremadamente pequeños. El paquete computacional Comsol Multiphysics, basado en elementos finitos, ha sido una herramienta muy útil para explorar el rendimiento óptico de los diseños, y ha permitido optimizarlos en función de los materiales, la geometría y la estructura de los mismos. Con esta herramienta hemos obtenido los campos ópticos, las absorciones en las capas activas y las absorciones parásitas, y la reflectancia total del dispositivo.

Por ello, esta tesis está dividida en tres partes:

- Mejora de la eficiencia y absorción de células solares

  Las estrucuras nano-fotónicas y nano-plasmónicas mejoran el rendimiento de las celulas solares, los sensores y las combinaciones de los mismos. Los sensores y dispostivos recolectores de energía flexibles, ligeros, y de bajo coste están basados en láminas delgadas y nano-estructuras en lo que se viene en denominar como optoelectrónica de tercera generación. Entre los semiconductores de capa delgada, el silicio amorfo es un material abundantemente, no tóxico y con una eficiencia de conversión aceptable. El desarrollo de dispositivos que utilicen este material requiere una mejora de su eficiencia de abosrción, reduciendo el espesor de su capa activa para mejorar la recoleccion de los portadores de carga fotogenerados. Otro reto añadido es la mitigacion del efecto Staebler-Wronski, que es dependiente del espesor y puede ser reducido a través de efectos térmicos.

  Los recubrimentos antirreflejantes planos no son apropiados para celulas solares basadas en silicio amorfo hidrogenado (aSiH). En su lugar, la absorción en su capa activa puede aumentarse utilizando nano-estructuras dieléctricas que trabajan como recubrimientos antirreflejantes. Nuestro análisis se concentra en la maximización de la densidad de corriente en circuito cerrado (J_{sc}) que proporciona la célula solar irradiada. Primero, analizamos el comportamiento de una célula aSiH plana, teniendo en cuenta todas las capas, incluyendo las capas de transición y los contactos eléctricos. Un diseño particularizado a este caso de un antirreflejante formado por capas de dieléctrico nano-estructuradas, permite una mejora del 9% en J_{sc} con respecto a la referencia de una célula solar plana, sobre todo debido a la redución de la reflectancia de la célula. Tres diferentes tipos de geometrías 1D de las nano-estructuras han sido analizadas y comparadas, obteniendose resultados muy similares. Se ha obtenido una mejora del rendimiento mediante nano-estructuras con geometrías realizables que pueden ser fabricadas manteniéndose la conductividad eléctrica del contacto frontal. Buena parte de la mejora debida a la nano-estructura se pierde en las primeras capas, y se disipa como calor. Afortunadamente, esto ayuda a mitigar parcialmetne los defectos causados por el efeto Staebler-Wronski.

Las células solares de aSiH ultrafinas pueden ser depositadas y crecidas sobre una red 1D dieléctrica con periodo próximo a la longitud de onda. Este dispositivo genera una corriente de circuito cerrado un 50% mayor que el debido a una célula aSiH ultrafina y con geometría plana. Esta mejora es debida a varios mecanismos. Además del aumento del área expuesta debida al perfil de la nano-estructura, un cálculo fiable mediante electromagnetismo computacional indica que la absorción en la capa activa aumenta, y que la reflectividad disminuye. Además, la potencia absorbida en las capas no activas es mayor, lo que ayuda a incrementar la temperatura de la célula y disminuir sus defectos. El análisis detallado del flujo de energía en el interior de la estructura también muestra que los mecanismos de confinamiento y de guidado están jugando un papel importante, incrementando el camino óptico dentro de la capa activa, y produciendo un mejor rendimiento de la célula.

En el ámbito de la energía solar siempre es necesario tener en cuenta el límite de Schockley-Queisser aplicable a células mono-unión. Las células de multi-unión son una solución prometedora en la llamada tercera generación de células solares. La combinación de materiales con distintas bandas de absorción en células multi-unión permite eficiencias de conversión por encima del 30% a un coste razonable. Sin embargo, las fronteras entre caras y las capas de transicción son críticas, ya que aportan pérdidas. Hemos propuesto una metasuperfice híbrida en una célula tándem que combina una célula de perovskitas y una célula de silicio cristalino. El diseño aprovecha la capacidad de manejar la luz para optimizar la absorción en la perovskita y guiar de manera eficiente la luz hacia la subcélula de silicio. Además, hemos añadido el efecto de un superficie posterior texturizada. La configuración óptima proporciona un aumento de la corriente ajustada en cada una de las capas del 25% con respecto a la obtenida por una célula sin nano-estructuras. El diseño propuesto incrementa el rendimiento de ambas células ya que gestiona cómo se dirige la luz hacia la capa activa, y a la vez minimiza las reflexiones en las interfases. Hemos realizado un barrido en índice de refraccion y en espesor de las capas de transicción y de transporte, obteniendo un rango de esos parámetros para la mejor operación del dispositivo. Usando esos valores, obtenemos una reducción de las pérdidas. En particular, conseguimos pérdidas un 33% menores que las obtenidas para una célula plana. Estas propuestas proporcionan un aumento de su respuesta óptica y amplia las posibilidades de los fabricantes para utilizar diversos materiales y relajar las tolerancias geométricas.

- Sensores plasmónicos de alto rendimiento.

  La sensibilidad de sensores plasmónicos basados en las configuraciones convencionales de Krestchmann está limitada a un máximo teórico de 600 deg/RIU cuando se utilizan métodos de interrogación angulares. Además, este límite se alcanza sacrificando el rango dinámico que disminuye para esta alta sensibilidad. Los métodos de interrogación angulares y espectrales requieren el uso de goniómetros y espectrómetros de alta resolución para la iluminación y para la detección. Una manera de simplificar estos mecanismos de sensado es el desarrollo de dispositivos que trabajen en incidencia normal. Así se podrían generar dispositivos compactos y acoplables al extremo de una fibra óptica. Hemos propuesto varios diseños que mejoran el rendimiento de sensores plasmónicos y que trabajan en incidencia normal. En este tipo de sensores plasmónicos, los parámetros de interes son: sensibilidad, figura de mérito (FOM), linealidad, rango dinámico, y límite de detección. En cada uno de los diseños, hemos maximizado la sensibilidad y la FOM. Dependiendo del mecanismo físico involucrado en cada diseño, hemos encontrado que el rango dinámico también se extiende considerablemente.

Una distribución de nano-estructuras que difractan la luz hacia un capa delgada de metal genera resonancias de plasmones superficiales en condiciones de incidencia normal. La localización del mínimo de la reflectividad espectral se utiliza para detectar cambios en el índice de refracción del medio bajo análisis. La geometría de esta distribución y la selección de los materiales se ajustan para optimizar algunos parámetros de rendimiento, como la sensibilidad, la figura de mérito, el incremento local de campo, o la anchura espectral. Esta optimización tiene en cuenta la posibilidad de fabricar el dispositivo en la práctica. El diseño óptimo tiene un valor máximo de sensibilidad de 1000 nm/RIU y una figura de mérito de 705 RIU^{-1}, que son competitivos con resultados de la literatura. El rango dinámico de estos dispositivos va de 1.33 a 1.35 RIU. Este rango es mejor que el obtenido mediante dispositivos basados en la configuración de Kretschmann.

Hemos analizado un sensor refractométrico que consiste en un apilamiento ordenado de redes metálicas con rasgos por debajo de la longitud de onda y embebido en un medio dieléctrico de bajo índice. La luz se confina fuertemente a través de mecanismos de confinamiento y guidado que excitan resonancias que a la vez son sensibles a cambios en el analito. Se han considerado y comparado dos posibles acabados de esta estructura. Uno de ellos termina con un material dieléctrico en contacto con el analito y explota la selectividad espectral de la transmitancia de la estructura. El otro diseño termina con un recubrimiento continuo y metálico que genera plasmones superficiales en la interfase entre el metal y el analito. Ambos diseños responden con respuestas especyrales muy estrechas que son sensibles al cambio en el índice de refracción del analito y pueden utilizarse para el sensado de muestras biomédicas. En este diseño, que tiene el mismo rango dinámico que el sensor con nano-aperturas, la sensibilidad y la FOM han aumentado notablemente, alcanzando valores de 1130 nm/RIU y 2100 RIU^{-1}, respectivamente.

Hemos desarrollado una distribución de nanoprismas extruidos que generan resonancias de plasmones superficiales para sensado. Los nanoprismas guían y confinan la luz hacia la interfase metal/dieléctrico donde el dieléctrio es el medio que se desea medir. Este sistema trabaja en condiciones de incidencia normal y es interrogado espectralmente. Su rendimiento es mejor que algunos diseños basados en configuraciones de Kretschmann, y los valores de sensibilidad y figura de méritos son competitivos con otros sensores plasmónicos. La geometría y la elección de materiales ha sido realizada teniendo en cuenta los límites impuestos por la fabricación. Aunque los valores de sensibilidad y FOM son moderados y menores que la máxima sensibilidad teórica, estos diseños son mejores que muchos otros de la literatura científica. Además, el rango dinámico se extiende hasta 1.43 RIU, lo que es 4 veces más grande que los diseños desarrollados por nosotros previamente (nano-aperturas, y redes multicapa), y que el de la configuración de Kretschmman. En este diseño utilizamos una red dieléctrica de baja pérdida para excitar resonancias de plasmones superficiales que aumentan el rango dinámico al acoplar mejor la radiación hacia el modo resonante. Además, el contraste en índices de refracción del óxido de zinc rodeado de fluoruro de magnesio también ayuda a extender el rango dinámico.

Los resultados obtenidos con los diseños de nanoprismas han sido usados para reconfigurar la estructura y proponer un dispositivo nano-estructurado que hibridiza los modos de la red de difracción con las resonancias plasmónicas. En este caso, utilizamos el concepto de índice de refracción efectivo que considera la fracción del volumen de los materiales y la profundidad de penetración del plasmón en el interior de la estructura. Nuestra geometría es una red de difracción de bajo orden con perfil extruido nano-triangular. Las resonancias de plasmones superficiales se excitan en la interfase entre el metal y el dieléctrico que está separada del analito por una capa dieléctrica de alto índice de refracción. El rendimiento

óptico de este sensor refractométrico es fuertemente competitivo en sensitividad y figura de mérito debido a su respuesta espectral ultra estrecha (por debajo de 0.1 nm). Además, puede operar dentro de un amplio rango de índices de refracción (desde 1.3 hasta 1.56 RIU), y trabaja en condiciones de incidencia normal.

La obtención de una alta sensibilidad, gran valor de la función de mérito, y un amplio rango dinámico es un reto para conseguirlo en un solo dispositivo. Para ello, hemos diseñado un sensor refractométrico que funciona en incidencia normal y permite su integración con una fibra óptica. El material del sensor y la geometría explota la gran sección transversal de scattering dada por el algo contraste en el índice de refracción de la red de difracción dieléctrica. Este diseño genera resonancias de Fano, debidas a la interferencia entre las resonancias plasmónicas y la respuesta de la red. Hemos optimizado este sensor mediante una función de mérito que combina el factor de calidad de las resonancias y el aumento local de campo eléctrico en el volumen de interacción donde se propaga el plasmón. Nuestro dispositivo consigue una alta sensibilidad de 1000 nm/RIU y una alta figura de mértio de 775 RIU^{-1}. También el rango dinámico se extiende hasta un valor extremo de 2 RIU. Esto es posible gracias al alto contraste en el índice de refracción conseguido al utilizar GaP ($n = 3.142$ a $\lambda = 1350$ nm) rodeado por MgF_2 ($n = 1.37$ a $\lambda = 1350$ nm).

- Sensores plasmónicos de lectura directa y bajo coste.

  En la última parte de esta tesis doctoral hemo diseñado dispositivos que combinan células solares o el efecto bolométrico con efectos plasmónicos. Estos dispositivos son más sencillos y más baratos que los sensores plasmónicos convencionales.

  El efecto bolométrico nos permite monitorizar eléctricametne las características espectrales de un sensor plasmónico. Proporciona una caracterizción más simple y de menor coste comparado con técnicas espectrales o goniométricas para la adquisición de la señal. En este dispositivo, una fuente monocromática ilumina una nano-estructura espectralmente selectiva. El dispositivo está formado por una red de difracción dieléctrica de bajo orden que combina dos materiales con un alto contraste de sus índices de refracción. La luz interacciona con esta estructura y llega hasta una capa metálica delgada que está expuesta al analito. La estrecha absorbancia espectral generada por las resonancias plasmónicas, hibridizadas a su vez con los modos de difracción, calienta el metal en el que se excitan los plasmones. El cambio en temperatura causado por esta absorción modifica la resistencia de esta capa metálica a través del efecto bolométrico. Por lo tanto, un cambio refractométrico del analito varía la resistencia eléctrica en condiciones de resonancia. Nuestro diseño monitoriza este cambio mediant un circuito externo. Esta propiedad optoelectrónica debe incluirse en la definición de los parámetros de sensibilidad y figura de mérito. Además de su competitividad en FOM (alrededor de 400 RIU^{-1}), el sistemas propuesto está basado integramente en medidas optoelectrónicas. Este refractómetro se comporta linealmente dentro de un rango centrado alrededor del índice de refracciónd el agua, $n = 1.33$, y puede ser aplicado en el sensado de especímenes en biofísica, biología y ciencias medioambientales.

  Las células solares de perovskitas se consideran actualmente como una prometedora tecnología para la recolección de energía solar. Su capacidad para proporcionar una señal eléctrica cuando se iluminan puede utilizarse para medir cambios en parámetros medioambientales. Una célula de perovsitas puede modificarse para trabajar como un sensor refractométrico mediante la generación de plasmones superficiales en su superficie frontal. Para excitar resonancias plasmónicas es necesario utilizar interfases entre dieléctricos y

metales. Sin embargo, si el electrodo frontal transparente de una célula de perovskitas se reemplaza por una capa metálica uniforme, la absorción en la capa activa disminuye considerablemente. Esta absorción crece de nuevo si la superficie frontal metálica se nano-estructura, añadiendo una distribución extruida de pirámides con alta razón de aspecto. Este perfil excita resonancias de plasmones superficiales a través de un mecanismo de acoplamiento entre la red y la superficie metálica. Nuestro diseño permite una absorción espectral selectiva con respuestas más estrechas de un 1 nm. La fotocorriente generada por la célula se convierte en la señal del sensor. El dispositivo emplea un método de interrogación optoelectrónico en vez de los los procedimiento clásicos más conocidos. Las definiciones de sensibilidad y FOM han de ser adaptadas a esta nueva situación. El diseño ha sido preparado para ser sensible a variaciones del índice de refracción del aire entre 1.0 y 1.1. La FOM alcanza un valor máximo de 1005 RIU^{-1}, que es competitivo cuando consideramos otras ventajas, como la facilidad del procedimiento de adquisición de la señal y el coste total del sistema sensor.

Hemos propuesto un nuevo diseño que utiliza nano-aperturas para generar resonancias de plasmones superficiales en la superficie frontal de una célula solar de perovskitas. El dispositivo emplea el cambio de la corriente entregada por la célula para detectar cambios en el índice de refracción del aire que está en contacto con su superficie frontal. Nuestro cálculo identifica qué parámetros geométricos y qué estructuras materiales mejoran este comportamiento. Después de reemplazar el electrodo frontal transparente con una red sub-λ metálica, hemos encontrado una gran variación de la responsividad de la célula con respecto al cambio de índice de refracción del medio a su alrededor. Este sensor refractométrico puede ser interrogado electrónicamente, evitando el uso de complicados montajes espectrales y goniométricos. Hemos presentado también una adaptación de los parámetros característicos de sensores refractométricos (sensibilidad y FOM) al caso de este método de interrogación optoelectrónico. Los valores de sensibilidad y FOM son alentadores para el desarrollo de senores basados en perovskitas.

Acknowledgements

Always, it is not sufficient to use some words for thanking people who help, support, and are a part of our progress. However, it is a good way to recognize them in our big events. I have spent eight years in my research career in physics, four of them were in Egypt, my home country, and the other four were in Spain, where I lived a new life experiment scientifically and socially which in general is great to me.

Four years is a long time to meet and interact with many people and fortunately, this interaction was always positive. The student character is formed and shaped taking part of the teacher. I hope that one day I become a picture of my teachers who were always generous with me. To start, I have to begin with the person who has the highest positive effect on me during my Ph.D. years. I would like first to deeply express my appreciation and thanks to Prof. Javier Alda, the first person I have met in Spain, and he continuously supports me until the end of this work. His support was not only in the thesis work but also in every situation and event I face throughout this period, which were a lot. Very simply, a good teacher, boss, and person is Javier. Back to the other four years in Egypt, I want to express my thanks and appreciation to Prof. Kamal Abdel-Hady, whom I start my first steps in the research with him, learn a lot, and built the base that helps me too much here in my thesis. The first two years of my Ph.D. Prof. Kamal was a co-supervisor. Unfortunately, he passed away before I complete this work, I ask Allah to forgive and bless him. In the second year of my thesis, Dr. Alexander Cuadrado, joined the supervision, and he was a great addition to the committee, I am not surprised because he is one the most talented students of Prof. Javier, and he is a scientist with a bright future. Dr. Alex is not only my supervisor who teach me a lot and I gained a lot of experiences from him, but he is also a friend who helped me to fix many situations through the years he joined us. Prof. Javier and Dr. Alex help me to start a collaboration with the Group of Displays and Photonic Applications of the University Carlos III of Madrid. I would like to thank, Prof. José Manuel Sánchez-Pena, Prof. Ricardo Vergaz for allowing me to collaborate with their group. Prof. Ricardo, help me to fix my stay, I learnt a lot from him. I want also to thank the members of his team Prof. Braulio García-Cámara, and my friend Eduardo López-Fraguas. I also want to express my thanks to Dr. Hala Kamal, and Dr. Adel Fathey, both help me a lot to be adapted in the Spanish environment and host me in their house in the first days here. I would like to thank Dr. Irene Alda for her help in editing and improving the quality of some published articles, although she was busy too in her thesis, she always was helpful.

I would like to thank also the whole members and friends in the Department of Optics, Faculty of Optics and Optometry for being always kind and helpful with me.

My thanks to the Ministry of Higher Education, Egypt, Missions Section, for the financial support through the first two years. Along this, Prof. Mostafa Farghal, and Prof. Amer Mohamed help me a lot from the Egyptian side, Many appreciations and thanks to them.

My last and great thanks to my family who were so patience and great supporter through the whole journey. Together we face a lot and I can't find the special words to thanks them. My especial last and all thanks to my parents, the best people I know. Tireless workers always with a smile, you have taught me everything and I hope someday to be at your level. This thesis goes for you, for what you have done for me, I am here because of your efforts.

M.Hamdy Elshorbagy

Contents

1

Introduction

The prefix "nano" is introduced when dealing with objects at the nanometer scale [1]. Light can't be focused or squeezed at the nano-scale (subwavelength sizes) using conventional optical components, like lenses or mirrors, because of the diffraction limit (Rayleigh criterion) [2]. Modern nanodevices in optics and optoelectronics take advantage of light manipulation by nanostructures to have functionalities and responses superior to conventional devices [3, 4]. In nanophotonics, researchers study the behavior of light at the nanometer scale or the interaction of nanometer-scale objects with the electromagnetic field [5]. Nanophotonics is a multidisciplinary field connecting several fields: nanotechnology, optics, optical and electronic engineering, and material engineering, among others. Another emerging field applied to photonic devices is plasmonics, which deals with surface plasmon resonances and its applications. Surface plasmons are coherent oscillating electrons at metal surfaces adjacent to a dielectric medium. This oscillation produces a longitudinal electromagnetic wave that travels along the metal surface. Both the surface plasmon and the accompanying electromagnetic field forms the surface plasmon polariton. Surface plasmon can resonate under the effect of an incident photon, and produce strong optical confinement near the metal surface. This resonance of surface plasmons is called surface plasmon resonance, which is extensively applied in many photonic devices with extraordinary responses and performances [6, 7].

A nanophotonic structure is a solution that reduces the device's size while maintaining the same, or even better, optical response of the conventional device [8, 9]. Furthermore, nanophotonics also, reveals light-matter interaction mechanisms that do not occur at the macroscale. Light focusing and concentration using nanophotonic structures have to be optimized to direct, guide, and confine light into the desired location in the device efficiently. In the following section, we will see how nanophotonic and plasmonic nanostructures enhance the performance of optical devices by controlling the light propagation in optical media and produce various physical effects, such as focusing, confinement, and efficient coupling.

1.1 Nanophotonic designs for solar cells and optical sensors

Nanophotonics includes a very wide variety of advanced technologies in many fields, such as optics, biochemistry, electrical engineering, optoelectronics, and many others [4]. We will summarize some attempts to apply nanophotonic structures to photonic devices. However, it will be difficult to cover all the contributions on this topic during the last two decades. So, we will give different examples of recent designs with a focus on the two main subjects covered by

our study. These are the solar cell devices and optical sensors based on plasmonic resonances.

1.1.1 Solar cells

There are many global issues that researchers around the world work to overcome: energy, health, food, and water supplies come on the top of these issues. Likely, the most important of them is energy, as the production for others depends on it. So far, energy extracted from fossil fuels is still dominant in the market. The attempts to find an alternative source are still in progress and we are close to succeeding. However, sticking to just one of the alternatives may not be the best option [10]. The variety of renewable energy sources increases the chances to overcome the energy issue, where biomass, hydropower, geothermal, wind, and solar energy sources could work together to supply countries with their needs of energy. Solar irradiation, wind, and water availability are different from place to place and could change dramatically due to global warming. In that case, setting different energy plants with a suitable variety of renewable energy sources for each country assures better the energy needs for it. Particularly speaking about solar energy, there are two major generation methods: solar thermal and photovoltaics, being the cost for large scale plants still the main challenge for this technology. In photovoltaics, we can generate power from sunlight using semiconductor materials of suitable bandgap, where a photon in the visible (VIS) or near-infrared (NIR), could directly excite electron-hole pairs in a semiconductor. Alternatively, in thermo-solar conversion, sunlight drives a mechanical heat engine. The cost of a solar cell in 1972 was about $50.28US\$/W$, in today's dollars that value is reduced to $0.37US\$/W$ for monocrystalline-silicon (c-Si) passivated emitter and rear cell (PERC) modules manufactured in China [11, 12, 13]. Cost, lifetime, recycling, the weight of the module, and efficiency are the major parameters for commercial photovoltaic systems. Focusing more on the cost, weight, and efficiency, we arrive at an option of thin-film solar cells that incorporates nanophotonic and plasmonic structures.

If the surface is textured perfectly, it will lead to an ideal diffuse reflectance (a Lambertian diffuser [14]). The textured surfaces in the back of a solar cell could diffusely reflect the light that reaches the back surface of the cell and hence it moves in a longer path in the active layer increasing the probability to be absorbed. This is the so-called Lambertian light trapping. The first application to this mechanism in solar cells was proposed by Goetzberger [15] and Yablonovitch [16]. Yablonovitch and Cody show that a textured optical sheets enhancement is limited to a $\times 4n^2$ (where n is the refractive index of the texture layer) increase in the effective absorption of solar cells based on c-Si [16]. Lambertian light trapping reduces the thickness of the active layer required to achieve a specific short circuit current J_{SC} compared to plane devices. As an example, in Si solar cells, light trapping decreases the thickness of the active layer that is required to achieve a specific output photocurrent. Let us define the maximum photocurrent output of a cell as the J_{SC}, so to achieve J_{SC} of 35 mA/cm^2 we need a plane device of 40 μm active layer thickness that is reduced to only about 2 μm when using light trapping. A thin-film GaAs solar cell device with an active layer thickness of 1 μm and output of J_{SC} of 28 mA/cm^2, can be converted to an ultra-thin device with an active layer thickness of 50 nm while keeping the same J_{SC} value using the Lambertian light trapping mechanism [17]. Semiconductors with very low diffusion lengths, like CuO and FeS_2, could be used as alternatives in photovoltaic devices because of the thickness reduction offered by the Lambertian light trapping mechanisms.

Another strategy to improve the performance of solar cells is the reduction of the optical losses in the structure of the cell by light confinement using textured surfaces. These textured surfaces contain nanofeatures added to the surface of one or more layers in the device, and

could be random or periodic. However, using this mechanism the absorption will not be enhanced only in the active layer, but also in the transparent contacts (TC) which is considered as losses [18]. An optimization of the cell layers and texture type is necessary to improve the final performance of the device. One approach, close to the texture mechanism, is to control the surface roughness of the front transparent conducting oxide (TCO) layers in amorphous silicon solar cells, which leads to an enhancement in the cell performance even before defined considering it as a random nanophotonic structure [19]. In reference [19], the surface roughness is investigated and shows a light trapping mechanism and an enhancement in the cell performance. The TCO surface doesn't only affect the topology of the amorphous solar cell layers deposited on it, but it also traps light at the active layer of the cell. Later on, a detailed optical modeling study is reported for amorphous silicon hydrogenated (aSiH) solar cells deposited on textured glass/TCO substrates, including different thickness for the active layer and oblique incident light conditions [20].

With the development of nanostructure fabrication methods in the last decade, a huge number of designs applying nanophotonic and plasmonic structures to optoelectronic devices were reported. These technologies allow the emerging of nano and micro-devices with improved responses. Small devices of thin-film semiconductors deposited on nanowire structures can generate a reasonable photocurrent sufficient to illuminate portable devices [21]. Optical energy is highly confined in a small regime when surface plasmons (SPs) are excited. This important phenomenon is also applied to enhance optical absorption in the active layer of solar cells [22]. A customized nanophotonic structure improves the optical performance of solar cells when working as anti-reflection coatings. One of the most efficient approaches is the use of bio-inspired periodic shapes like moth-eye [23]. These structures function as anti-reflection coatings over a wide range of wavelengths, so the optical absorption is enhanced over a broadband region. Broadband absorption enhancement is a requirement that makes a nanophotonic or plasmonic design useful for solar cell applications. Talking about plasmonic effects, SPs generated locally around nanoparticles increase the optical absorption in solar cells [24]. A periodic grating array in the back contact of a solar cell works as a scaffold for the conformal deposition of nanostructured solar cells with improved performance [25]. When the silver (Ag) back contact is nanopatterned, the J_{SC} enhances around 26% compared with the flat device. An experimental demonstration of the theoretical studies of the moth-eye or nanodome structure cells, that is formed by the conformal deposition of the cell layer over periodic grating arrays, shows a large enhancement of the optical absorption and 25% better efficiency than the flat solar cells [26]. Not only periodic grating or nanoparticles arrays in the back contact are proposed, but a nanoparticle array on the top of solar cells is also considered [27]. In this case, the forward diffraction of the incoming light is key for this design to work. Anti-reflection, diffraction, or plasmonic resonances are the mechanisms involved in these designs to improve the optical absorption in the active layer of the device.

Zongfu Yu, *et al.* [28] reported the fundamental limitations of nanophotonic structures to improve the optical performance of solar cells. This evaluation could direct the efforts in the right way, and save time when proposing designs. Along with this theoretical study, there are some important features for the design that has to take into account like fabrication feasibility, and the selection of adequate materials, etc.

Lithographic techniques allow the fabrication of high-resolution nanostructures. However, its application to a large area scale is a challenge. An approach called self-powered parallel electron lithography that has high-throughput and sub 35 nm high resolution was applied to fabricate large-area ordered nano-conical-frustum array structure [29]. With this technique,

a high absorption in the active layer, reveals a high- conversion efficiency (this parameter measure how much electricity can be produced by the solar cell when illuminated by light, so, its the maximum output electrical power divide by the input optical power) solar cell of 10.8%. Also, a solar cell in the form of a periodic nanowire array structure achieved better enhancement in the optical absorption and the overall performance of the cell [30]. In this design, the periodic arrays of silicon nanowires trap the incident solar radiation by a factor up to $\times 73$. Experimental studies succeeded to apply large-area, nanoscale patterning of TCO front contact, to aSiH solar cells. This addition reveals a high absolute conversion efficiency of 10.1% [31]. In this study, the absorption of the cells increases when a nano-imprint technique is applied to obtain large-area nanopatterned top contact for thin-film solar cells. In another proposal, a closed packed array of dielectric nano-spheres is added to the top of a thin-film solar cell. This array supports guided whispering gallery modes that concentrate optical power in the active layer of thin-film aSiH solar cells [32].

Random nanophotonic structures, like textured surfaces, are easy to manufacture in large scale using, for example, chemical etching, but these structures have some disadvantages. For example, reproducing patterns is difficult, and uncontrolled losses appear due to scattering of charge carriers by the random texture surfaces before extraction. A periodic array reduces this kind of loss and can be reproduced using the different lithographic high-resolution techniques. The question of which is better, random or periodic nanophotonic arrays, was answered in a complete study that compares a cell deposited with a random pyramidal morphology of state-of-the-art zinc oxide (ZnO) electrodes, and a cell deposited onto nanostructured glass/TCO using nanoimprint lithography [33]. The development of high-resolution large scale lithographic technologies enables the production of periodic nanophotonic arrays that perform better than its random counterparts. Self-assembly techniques have been used to fabricate plasmonic metal nanoparticle arrays that work as a back reflector of thin-film solar cells and diffusely reflect light back to the active layer which increases its possibility to be absorbed so acts as another mechanism of light trapping [34]. The addition of sophisticated nanostructures generates a large enhancement of the performance, and a relevant reduction to the thickness of the active layer. A couple of nanophotonic structures, one of them on the top and working as an anti-reflection coating, and the other trapping the light within the active layer, could achieve a high photo-current for an ultra-thin c-Si solar cell of only 2-micron thick [35]. Previous studies comparing ordered and disordered nanophotonic structures, show that periodic arrays are much better for the performance of solar cells [33]. Another study shows that increasing the disorder in the nanostructure of the nanophotonic light trapping geometry produces a better performance than when using an ordered periodic array [36]. This experimental work proves that, at specific conditions, the random texture improves the performance of solar cells better than the periodic light trapping profile, but it doesn't prove the possibility of reproducing the same random profile that leads to high optical absorption enhancement. Furthermore, high order random means higher scattering losses of the charge carriers which is not also examined in this study.

At this point, it is important to check how the light trapping nanostructures affect the charge carrier collection efficiency, *i. e.*, the electrical performance of the cell. Although some scattering losses of the charge carriers could exist due to textured layers at the interfacial surfaces between the buffer layers and electrodes, or the active layers and electrodes, this nanopatterning increases the carrier collection for most of the cases. A coupled optical-electrical study reveals that light trapping nanostructures do not only improve the optical absorption in the active layer of the cell, but they also enhance the electrical performance [37, 38, 39].

A photovoltaic cell only uses efficiently a portion of the solar spectrum in the VIS, and NIR range. However, heat engines generate electricity available from radiation in the infrared (IR) spectral band. The hybrid technology for solar power generation could be another promising option by converting sunlight into thermal emitters, radiating light directly above the photovoltaic bandgap where a heat absorber or an IR non-dissipative device can be used. Such a system, called solar thermophotovoltaics is able to harvest energy from the entire solar spectrum, so that higher efficiency power plants are possible. Nanophotonic structures could also improve the design of this hybrid system and make it more efficient [40].

High-efficiency perovskite solar cells are promising low-cost solar harvesters that are expected to compete with c-Si based technology. However, despite the increased interest in this technology, it has not still solved a key issue about its fast degradation and short lifetime. An active layer of thickness around 300-500 nm made of perovskite materials (the most commonly used is methylammonium lead halides, $MAPbI_3$) could efficiently absorb more incoming light in its absorption band when compared with other thin-film materials because of the high absorption coefficient of perovskites. Also, the diffusion length of the generated charge carriers is large enough to be efficiently extracted through the electrodes by applying the proper selective charge transport layers. The high absorption coefficient and large diffusion length of perovskite materials make the optical losses for state of art plane perovskite solar cells relatively smaller than many other thin-film technologies, like aSiH and organics, etc. As a result, nanophotonic designs account for a small optical enhancement when applied to devices with active layer thickness more than 300 nm. As an example, only 5% improvement is achieved by nanopatterning the front contact of a perovskite cell, that now works as a light trapping structure [41]. On the other hand, perovskite materials are toxic and expensive, so, a much thinner layer is safer and cheaper. Moreover, the charge extraction will be more efficient as the charge carriers travel shorter distances before being collected by the electrodes. These reasons show that it is preferred to manufacture perovskite devices with small thickness to overcome these issues. With thickness reduction, absorption in the active layer becomes lower. In this case, nanophotonic designs could be used to increase the absorption efficiency in the active layer and reduce the losses.

Nanophotonic structure designs are efficiently applied to multi-junction solar cells with semiconductors of different bandgaps, to achieve improved spectral responses over a wideband spectrum. This structure could be seen as a piled arrangement of solar cells tuned to complementary bandgaps. The aim of these devices is to overcome the Shockley-Queisser limit for a single p-n junction solar cell, which is stated as 30% [42]. Metamaterials with appealing different optical effects such as resonance, controlled diffraction, and scattering, are preferred for this purpose [43]. Using these structures, we can take advantage of the resonance effects in one junction that is close to the structure, and use diffraction to redirect light towards the other junctions. Overall, both effects will reduce the total reflectance of the device.

The thermodynamic limit for plane single-junction solar cells was introduced by Shockley-Queisser. When including nanostructures, it seems necessary to revise this analysis for these advanced designs. As an example, a nanowire single-junction solar cell was used for this study. In this case, the power conversion efficiency and cell parameters for a planar solar cell are no longer applied because a nanowire absorbs light from an area much larger than its own size [44]. Moreover, an array of nanophotonic structures can take many shapes. Therefore, the effect of the geometrical shape, and the surface/volume ratio of these structures on the thin-film solar cell performance, requires further analysis in terms of optical absorption efficiency and total reflectance of the device [45]. The increase in efficiency of perovskite solar cells is the fastest and

highest among other thin-film technology. Its efficiency reached 23% [46], and it is considered as one of the most promising technology for photovoltaic devices, even though its poor stability is under extensive investigation [47]. Multijunction solar cells and its simplest monolithic form are reported to outperform the single-junction devices and achieve a higher power conversion efficiency. By incorporating perovskite technology in a monolithic perovskite/c-Si tandem solar cells, we could overcome the theoretical limit for the power conversion efficiency of silicon single junction cells [48]. This type of devices contains many essential buffer layers for charge carrier extraction that introduces several interfaces generating unwanted reflectances. In this case, nanophotonic strategies are at play to overcome this problem [49, 50]. The extraction of charge-carriers is more efficient in ultra-thin layers below 200 nm in thickness than in devices with larger values of the thickness. This happens because the photogenerated charge carriers will travel a shorter distance. However, the optical absorption decreases significantly for these ultra-thin devices. Nanophotonic structures with broadband responses are used to boost the optical absorption efficiency or even make it larger than the efficiency of thick active layer devices [51]. As stated above, the optical absorption of thick perovskite solar cells with an active layer in the range of 300-500 nm is relatively large compared with other thin-film materials. For this reason, the enhancement of the absorption for this device using nanophotonic structures, in general, will be small compared with the state-of-the-art plane devices [52].

Thin and ultra-thin solar cells energize many applications. For example, portable devices and small machines may benefit from well-designed nanometric and plasmonic structures to obtain high-efficiency cells, with the ultimate goal of the self-powering operation. At a larger scale, the incorporation of thin-film technology in tandem, and multi-junction solar cells could be applied to power plants and remote areas energy as low-cost high-efficiency power technology. For this reason, we will focus our study on these types of solar cells.

1.1.2 Plasmonic sensors

Optical sensors are widely used in laboratories, medicine, and industry to check the quality of different materials, or detect changes in a physical parameter like temperature, pressure, refractive index, etc. Important advances in the capabilities of optical sensors have been achieved thanks to the incorporation of nanophotonic and plasmonic structures in such devices.

The first practical setup utilizing surface plasmon resonances (SPRs) in a device that could be useful for sensing application was achieved by E. Kretschmann and H. Raether [53]. The device setup for this method consists of a transparent dielectric prism coated with metal that is used to excite surface plasmon resonance at the metal/air interface. The air can be replaced by any material to be sensed by the setup. Separately from this study, A. Otto [54] proposed another setup where a thin dielectric layer (or sensed medium) is introduced between a transparent dielectric prism and a semi-infinite metal layer. The excitation method in both configurations is called prism coupling SPR, while Kretschmann-Raether is the most used as its more practical for sensing applications. The principle of operation and excitation condition used in these methods described in detail in chapter 2. Since these pioneering reports, several designs were developed to apply these setups for different measurements and detection methods.

The excited surface plasmon waves (SPW) are bounded to the metal surface and attenuated in the dielectric medium in contact with the metal, so that any changes in that medium disturbs the SPW. This phenomenon is applied to detect the thickness of the coating on the metal surface [55]. In another application, if an SPW is excited at the interface of a metal/aqueous solution,

the SPR setup can detect changes and processes at metal interfaces. For example, it can detect changes in the density of electrons bounded or close to the metal surface, ion attachment to the metal surface by adsorption processes, and modifications in the optical properties of the ionic bi-layer [56]. In other areas, it is known that the optical properties of some organic materials are changed upon exposure to gases. This functionalization concept is used to detect these gases by coating the metal layer in the SPR device with an organic layer that changes its optical properties when exposed to the gas. This design is applied to the anesthetic gas halothane detection [57]. The application of SP based setup in biosensing has been also demonstrated using prism coupling methods (Kretschmann - Otto configurations) to detect bio species in a water-based solution in contact with the metal layer [58, 59].

Another method to excite SPR is the grating coupling method [60]. This happens when a diffracted wave incident on the metal surface with a wavevector matches the SP propagation constant. Practical devices that use this mechanism are applied to biological detection [60]. At this point, it is interesting to compare the sensitivities of sensors based on prism coupling, with those of diffraction-grating couplers [61]. Both methods were studied in terms of angular and wavelength interrogations, showing that in wavelength interrogation, the prism coupling is more sensitive than the grating coupling method, meanwhile, their sensitivities are similar in the case of angular interrogation.

After the presentation of Kretschmann and Otto configurations, many researchers developed a variety of designs adapting the setup for different applications in many areas. This blossoming of ideas can be considered as a true revolution in optical sensing. Devices with ultrahigh sensitivity and a very low detection limit were designed. The development of self-assembly nanoparticle arrays and nanophotonic structures leads to improved sensing devices with better responses [62, 63, 64]. This enhanced performance devices applied in chemistry, and biology allows precise detection and monitoring of changes of binding states in different species and samples.

A localized SPR (LSPR) can be excited using colloidal metallic nanoparticles, or designed finite nanostructures. This resonance is characterized by a high near field intensity around the metallic nanoparticles. Biomolecules could be attached to the surface of these colloids where any interaction between these biomolecules will affect the optical absorption of the colloids. This idea is applied as a label-free optical method to study biomolecular interactions in real-time [65]. The light confinement through nanoparticles and its characteristic near field enhancement, where light is squeezed in the nanosize scale, make the optical properties of these nanoparticles sensitive to environmental changes, for example, attaching a biomolecule to it. This allows scientists to design commercial nanoscale biosensors [66].

The development of lithographic, self-assembly techniques and wet chemistry methods allow the fabrication of noble metal nanoparticles with a wide range of controlled sizes, shapes, and within different arrangements. This significant progress has been successfully applied to plasmonic sensors with improved responses [67]. The prism coupling method uses reflectivity as a parameter to sense changes near the metal surface. Metallic nanoparticles change absorption or reflectivity, while a nanohole array in a metallic surface uses SP enhanced transmission as the sensing parameter [68]. Plasmonic based sensors also determine the orientation of polarization-dependent nanostructures by measuring the state of polarization of the light scattered from a single nanoparticle, for example, a nanorod [69].

The interrogation of SP based sensors can be made measuring the angle of incidence, the

wavelength shift, the reflected or transmitted intensities, employing a wide range of geometries and materials [70]. Depending on the interrogation method, it could be possible to integrate the sensor with compact optical fiber devices [71]. Moreover, the combination of different physical effects in one device may lead to improved performance. For example, a magneto-optic SP based biosensor could enhance the sensor sensitivity threefold with a feasible structure from the fabrication point of view [72]. The excitation of long-range surface plasmon resonance (LRSPR) excited at near IR wavelengths using metallic nanorings, where the optical response of the structure is much sensitive to changes of the surrounding medium, achieves a high-bulk sensitivity [73]. After more than one decade of plasmonic sensor development, a large number of designs were reported for the detection of different chemical and biological species, making optical sensors based on plasmonic resonance a very powerful tool for sensing and diagnosis applications [74]. Currently, the excitation methods of SPRs are well established, both theoretical and experimentally, including the different realizations of SPs, for example: the long- and short-range SPRs and the localized SPs for nanoparticles case. Multi-function sensors that are able to detect interactions of two different species by generating two plasmonic modes using a single geometry are also reported [75]. Some sensors were designed for a single specimen or material. In this case, the sensor detects a very small change in the refractive index of this material with high efficiency, for example, a sensor for hydrogen detection [76].

In any case, it seems important to investigate the limits in performance of different types of plasmonic sensors to drive the research for the next generation of optical sensors [77, 78, 79]. The kretchmann based sensors need movable parts like goniometer, which limits its integrability with other systems like optical fibers. The excitation of SPR at normal incidence eases the integration of the sensor with optical fibers and waveguides, so that, some designs report efficient and feasible sensors [80, 81, 82]. Most gases and chemicals are subjected to environmental changes that lead to a significant variation in their properties. In this case, it is necessary to design sensors with a wide dynamic range to be able to detect these changes [83]. To overcome any given limitation, it is necessary to focus on the parameters of the sensor that make it suitable for a specific application, and allows selective and sensitive detection [84]. 2D materials, such as graphene has been also applied to plasmonic sensors to improve its sensitivity and optical response [85]. The addition of nanosheets, or very thin layers onto the exposed surface of a plasmonic sensor enhances its sensitivity and optical response [86, 87, 88]. Also, photonic crystal fiber-based plasmonic sensors are designed for ultra-high sensitivity sensors. In this case, the shape and material configuration allow the design of a large number of new sensors [89, 90, 91].

In this section, we have reported many SPR based optical sensors with improved designs and performance. Through this literature survey, we have made a selection, and give some examples for different approaches and functionalities. We conclude that nanophotonic and plasmonic nanostructures boost the performance of optical sensors based on plasmonic resonances. The excitation of SPR with normal incident light eases the operation of the device and the integration in optical systems such as fiber tip. Some challenges are also extracted related to sensitivity values, spectral resolution, and feasibility of geometrical parameters in fabrication. In our study, we have to take all of them into account to develop reliable and competitive optical sensors.

1.2 Motivation and aims

In this dissertation, we will focus on two types of photonic devices: i) thin-film solar cells incorporating nanophotonic structures for single junction or multi-junction devices, ii) plasmonic sensors, and iii) hybrid devices that combines both of them.

Efficient, lightweight, and low-cost solar cells for a potential application in energizing portable devices like laptops, cell phones, small machines, cars, drones, etc. Solar cells are able to power these devices in remote areas and locations with no other electricity sources. Besides, they help to reduce electricity consumption in populated zones by powering lighting, small engines, and water pumps. On the other hand, fast, efficient, compact, and feasible plasmonic sensors are key in disease diagnosis, material quality tests, detection of environmental changes, etc. Optical sensors are at work when large complicated devices are not an effective solution, for example, in airports, mines, factories [92]. In the following subsections, we will analyze the characteristics of these devices and some of the possible issues that could be solved by applying nanophotonic and plasmonic structures.

1.2.1 Fundamental characteristics and origin of losses

The main goal of nanophotonic and plasmonic designs is light focusing, for specific wavelengths (spectral), within the desired layer (spatial), or both. These designs can produce optical effects such as near field enhancements, scattering, and resonant effects. If we place a nanophotonic, or plasmonic design on top of a solar cell, their optical effects may not reach the active layer because of the front layers of the cell. For example, thin-film solar cells have a transparent top contact with a thickness of a few tens of nanometers, and may also involve one, or more buffer layers. Unfortunately, these top layers obstacle or dissipate the electromagnetic field enhancements generated by a plasmonic or photonic nanostructures arrays, that could be placed on top of it, and prevent them from reaching the active layer. Relocating the nanostructure inside the active layer could be a solution to get a benefit from the high near field enhancement produced by the nanostructure. Even, it could enhance IR absorption of the device where the effective absorption of the semiconductor is too low or negligible [93]. A careful analysis of this situation shows that the best possible location to deposit the nanoparticles array happens to be inside the active layer. However, this strategy has some disadvantages: it is difficult to experimentally control the location of the nanostructure array, and it will work as trapping sites for recombination of charge carrier within the active layer; and finally, if the nanostructure is metallic, atoms from the nanostructure could diffuse in the semiconductor and change the doping level [94]. A core-shell structure partially solves these issues by isolating the metal particle within a dielectric shell. This configuration is still affected by scattering losses at the defect sites, disturbing the dynamics of charge carriers. Placing the nanostructure on top or bottom of the device is a solution, but we still have to optimize the structure to enlarge the penetration depth of the electromagnetic field to expose the active layer efficiently to near-field enhancements. High index lossless nanostructures provide high directional scattering effects that could be useful to improve the optical response of photonic devices [95]. These materials can be tuned to have a narrow or broadband responses for different applications in sensing or solar energy harvesting.

Flexible, low cost, and lightweight solar cells are preferred for portable devices [96]. There are many types of semiconductor materials used for these types of solar cells, for example, aSiH, organic and polymer semiconductors, perovskites, and chalcogenide semiconductors, etc, [97, 98, 99]. Some of these materials are already in use in commercial solar cells, like aSiH.

However, one of the drawbacks for aSiH is that it suffers degradation due to light exposure, which is called the Staebler-Wronski effect (SWE) that is proportional to the thickness of the active layer [100]. Fortunately, it can be reduced via thermal annealing. Therefore, it is possible to produce self-annealing by increasing the parasitic absorption in buffer layers [101]. Organic semiconductors typically have a small charge carrier diffusion lengths. Then, solar cells fabricated with these materials also require an ultra-thin active layer [102]. For perovskite solar cells, although they have a large charge carrier diffusion (about 1 micron), it's desirable to use thin layers to reduce the cost and amount of the raw material that, besides, are toxic [103]. We can conclude that, for these technologies, the electrical extraction of the generated charge carriers is more efficient when an ultra-thin active layer is used, because they will travel shorter distances before reaching the electrodes, and will not likely suffer recombination [104]. However, ultra-thin active layers present diminished absorption. Here is where nanophotonic strategies concentrate light to improve absorption (spectrally and spatially) in the active layer or any other location within the cell.

Optical sensors, spectrally or angularly interrogated, require narrow responses to lower the limit of detection and become highly sensitive to variations in the sensed physical parameter. Coupling focused light on the device leads to ultra-narrow responses and highly sensitive optical sensors for many applications, as we see in the previous examples in section 1.1.2. Nanophotonic structures based on lossless dielectrics can control how light flows through a device within a broad or narrow spectral band without significant reflection losses and negligible absorption losses. Actually, by coupling customized nanostructures to specific material arrangements, it is possible to generate perfect absorbers [105], that can be applied to sensing applications [106], or perfect transmission structures for solar cell applications [107].

1.2.2 Reliable nano-photonic structures

There are several aspects and considerations extracted from previous sections, that need to be taken into account when designing photonic nanostructures. One of the most important constrains is related to the practical realization of the design. Although the literature is plenty of designs with many functionalists and appealing responses, some of them may be difficult to be practically fabricated or operated. Here, we introduce the most important parameters that have to be taken into account in a design that is fabricable and able to be applied in real devices:

Compatibility of fabrication methods and process. Each device and material has a well-known fabrication method. For example, in aSiH solar cells, the p-i-n semiconductor layer is usually deposited by plasma-enhanced chemical vapor deposition, while most organic and polymer solar cells are fabricated by ink-jet or spin coating processes. Based on this, it's not adequate to assume that aSiH layers will fill nano-grooves or holes. Instead, if we have a nanostructure substrate, the layers will be conformally stacked on it. The reverse happens for organic or perovskite layers over a nanostructured substrate where we can't propose a conformal stack. Instead, the spin-coated material will fill the nanostructured surface. The fabrication process of nanostructures has to be compatible with the fabrication environment of the original device. For example, organic and perovskite solar cells are usually fabricated within a glove box or controlled atmosphere, so the use of large fabrication tools are compromised after depositing the active layer of these devices. Then, it is preferred to grow the nanostructure before the active layer deposition, for example, by spin coating the active layer on top of a nanostructured substrate.

Device area limitations. Optical sensors are small area devices. In fact, it is desirable to have micro or nanochips that are portable and easy to mount onto different systems. On the contrary, solar cells will be large area devices to harvest as much as possible energy. In that case, the design has to take into account if the required size can be realized using the available production technologies.

Nanostructure feature resolution. Very tiny features below 10 nm generally are not recommended because they are difficult to be realized for large scale fabrication. Even more, dimensional steps smaller than 25 nm in lateral dimensions are not advisable because of the reliability of the fabrication techniques. Therefore, the geometrical dimension of the design has to take into account the different scales, tolerances, spatial resolution, accuracy, and reproducibility available for each fabrication method and its applicability to the proposed designs.

Auxiliary layers of opetoelectronic devices. We have seen that every layer of the device has to be taken into account when determining the effect of nanophotonic structures. Otherwise, the fabricated structure will have a response different from the optimized design. For example, the transport layers in organic and perovskite solar cells, as well as the p and n layers in aSiH solar cells, can't be neglected when designing a nanostructure for the device. The performance value caused by the plasmonic or photonic structure will not be reliable if these layers are not properly taken into account. However, the situation is different when working with tandem solar cells that involve a wafer cell and a thin-film cell at the top. In that case, the ultra-thin transport layers of the bottom cell could be optically neglected as they have no impact on the optical behavior of the system, although they can't be dismissed in the electrical domain.

1.2.3 Nanophotonic structures for next generation photonic devices

The two previous sections described some of the losses sources in thin-film solar cells, and the most relevant requirements to design efficient plasmonic sensors. Also, as we have seen from the selected examples in sections 1.1.1 and 1.1.2, nanophotonic and plasmonic structures allow the development of photonic and optoelectronic devices with extraordinary responses and features. Particles, structures, and features with nanoscale dimensions alter light propagation and produce several important effects like scattering, resonances, guiding, focusing, etc., that in turn give useful characteristics as low reflectivity and perfect absorption or transmission. The first step before applying a nanostructure to a device, is to understand the operation and fabrication requirements of this device to define the objective from the nanophotonic design. The next generation of photonic devices that include nanostructured elements, will show high absorption efficiency, they will be low cost, flexible, compact, ultra-sensitive, and of course, feasible to be fabricated and operated. Although we outlined above some guidelines to design and fabricate reliable structures, the progress of nanophotonic science and technology will depend on two major research lines: first the continuous investigations of new ideas and the evaluation of its response, even if its difficult to be fabricated now. The second research line is the development of nanoscale fabrication techniques that eases the high-resolution production of such designs. In this quest, we also need to know that materials at the nanoscale exhibit different physical properties from their bulk form. Therefore, we expect to witness new devices with extraordinary responses and qualities are expected that incorporate nanophotonic designs.

1.3 Structure of this dissertation

The thesis consists of six chapters, five main chapters, and a final conclusion one. The first chapter is an introduction that reviews some recent contributions on the topics of the thesis. Chapter 2 contains the theoretical background, equations, methods used in our calculations, the optical model description, and its flow chart, and the model validations. In chapter 3 we present some designs to improve the optical absorption of aSiH thin-film solar cells, and tandem perovskite/c-Si cells. We select these designs, taking the advantage of light diffraction by gratings to increase the path length of light into the cells, and hence the probability to be absorbed. Concentrating and guiding effects are at play when a high aspect ratio grating is placed at the backside of a thin-film aSiH solar cell. In chapter 4 we proposed some designs that use dielectric or metallic gratings to excite SPRs at normal incidence illumination. We find out the parameters of each design, that affect the sensitivity, FOM, and the dynamic range of the sensor. Chapter 5 deals with devices that combine both plasmonic effects and electrical signal generation. For example, we used a bolometer, and solar cells as sensors, where the sensing mechanism is based on direct readout of their electrical output signal. The coupling of SPRs in these devices make them more sensitive to environmental variation and improve their capabilities for sensing applications. Finally, in chapter 6 we summarize the original contributions and results of the thesis.

2

Theoretical background and methods

2.1 Propagation of Electromagnetic waves

Electromagnetic (EM) waves propagate in different media with oscillating electric and magnetic fields that are always perpendicular to each other and to the direction of propagation, as is shown in figure 2.1,a. The wave nature of light is recognized by its polarization, interference, and diffraction behavior [108]. Maxwell equations describe the propagation of EM waves in optical media and the relationship between the associated electric and magnetic fields and their time derivatives. In a non-conducting material (conductivity, $\sigma = 0$), the electric field associated with the EM wave interacts with the electrons in molecules or ions in the material revealing polarizability in the medium due to the displacement of electrons and ions from their position of equilibrium. Usually, this polarization happens at the frequency of the propagating wave. Therefore, the propagation of EM waves in that medium is analogous to the propagation of the polarizability through the medium, meanwhile, the electric field interacts with the induced dipoles. The capability of different medium molecules to be polarized is different, so the relative electric permittivity, ϵ, is used to express how a medium becomes polarized. Relative electric permittivity also measures the strength of the interaction between the optical field and the induced dipoles in the medium. For that reason, the velocity of EM waves in any medium rather than free space will propagate with a lower velocity, v, than the speed of light in vacuum, c. The ratio between the EM wave velocity in free space, c, to that velocity in any other medium defines the refractive index of that medium, $n = \frac{c}{v}$.

If an EM wave propagates through a conducting material, it will be attenuated at specific frequencies in the direction of propagation, as illustrated in figure 2.1,b. This attenuation comes from the absorption of the light energy by the material, that is usually converted to other forms of energy. For example, light is converted to heat energy if absorbed by lattice vibrations during the polarization of the molecules of the medium or by local vibrations of impurity ions. Absorption and light attenuation also comes from the excitation of electrons from the valence band to the conduction band, and it mostly happens in semiconductors. If the material absorbs light energy, then its relative permittivity and refractive index become complex and defined as $\tilde{n} = n + ik$, where n is the real part of the refractive index and measures the phase velocity of the EM waves in the medium, and k is the imaginary part (also called extinction or attenuation coefficient), which indicates the amount of attenuation of the EM wave amplitude when propagating through the material.

If the absorption of light is converted to a useful form of energy (for example, light into

electricity), we call it active absorption. However, if it is dissipated as heat losses, it is called passive absorption. In most optoelectronic devices, the goal is to reduce the passive absorption losses and increase the active ones, unless the device operation improves when both of them increase, as it happens with aSiH solar cells for example [109]. Light scattering and diffraction are other phenomena that happen when light is routed towards some other directions of propagation. In this case, the propagating EM waves are distributed into several secondary EM waves, propagating in other directions different from the original direction of propagation.

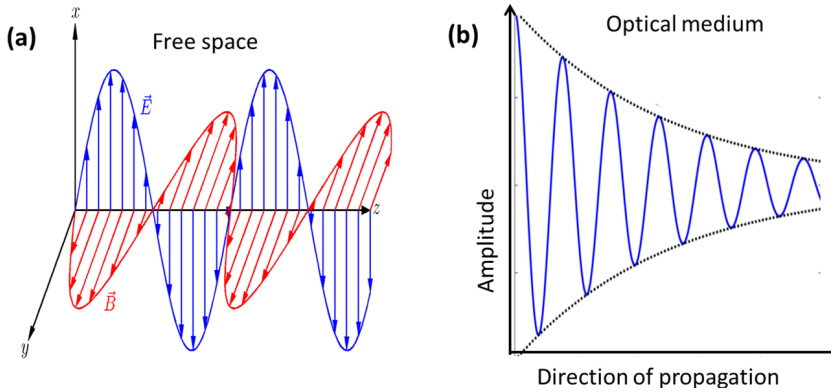

Figure 2.1: (a) Wave propagation in space with oscillating electric and magnetic fields. These fields are always perpendicular to each other, and also perpendicular to the direction of propagation. (b) Attenuation of an EM wave in lossy media due to absorption.

To describe well the different interaction process that EM may encounter when propagating through a multi-layer system or device, we need to use the optical constants of each material along with its spatial geometry to solve Maxwell equations, and determine the optical field distributions inside the different layers and mediums, and account for possible optical losses and excitation.

2.1.1 EM waves propagation in a homogeneous medium

The propagation of EM waves through a medium, or in vacuum, is described by an EM wave equation that is a second-order partial differential equation derived from Maxwell equations [110].

In a vacuum and charge-free space, Maxwell equations for the case where charge and current are zero read as [110]:

$$\nabla \cdot \overrightarrow{E}(r,t) = 0, \tag{2.1}$$

$$\nabla \times \overrightarrow{E}(r,t) = -\frac{\partial \overrightarrow{B}(r,t)}{\partial t}, \tag{2.2}$$

$$\nabla \cdot \overrightarrow{B}(r,t) = 0, \tag{2.3}$$

$$\nabla \times \overrightarrow{B}(r,t) = \mu_0 \varepsilon_0 \frac{\partial \overrightarrow{E}(r,t)}{\partial t}. \tag{2.4}$$

With simple math, we can derive the wave equations that can be solved using numerical models for the evaluation of EM waves propagating in optical devices, which reads:

$$\frac{1}{c^2}\left(\frac{\partial^2 \overrightarrow{E}(r,t)}{\partial t^2}\right) - \nabla^2 \overrightarrow{E}(r,t) = 0, \tag{2.5}$$

$$\frac{1}{c^2}\left(\frac{\partial^2 \overrightarrow{B}(r,t)}{\partial t^2}\right) - \nabla^2 \overrightarrow{B}(r,t) = 0, \tag{2.6}$$

where c is the speed of light in free space, which is $c = \frac{1}{\sqrt{\mu_0 \varepsilon_0}}$, and equations (2.5, 2.6) are the wave equations that describe the propagation of EM waves in free space.

2.1.2 EM waves at the interface between two dielectric media

The simplest form of an EM is a plane polarized wave, which can be defined by a direction of propagation given by the wave vector. For an interface between two dielectric media, the incident electric field can be decomposed into two components, that correspond to two polarization states. The first is S-polarization (also known as transverse electric, TE, or perpendicular polarization), for which the electric field is perpendicular to the plane of incidence, and consequently, the magnetic field is parallel to the plane of incidence. The second is the P-polarization (also known as transverse magnetic, TM, or parallel polarization), which occurs when the electric field is parallel to the plane of incidence and the magnetic field is perpendicular to it. These components define two orthogonal states of polarization. When a polarized plane wave propagating through a medium with a refractive index ($n = n_1$) as shown in figure2.2, is incident upon a semi-infinite dielectric medium ($n = n_2$), it is partially reflected and partially transmitted. The incident and reflected EM waves are in one medium and the refracted EM waves are in the other one. The angle of incidence, the reflection angle, and the refraction angle are all given with respect to the normal of the interface between the two media, and they obey the Snell law: $n_1 \sin\theta_i = n_2 \sin\theta_t$, and the reflection law: $\theta_r = -\theta_i$. The amount of reflected and refracted light is determined by the reflection and transmission coefficients, which are calculated analytically from the Fresnel equations [108]. Fresnel equations evaluate the transmission and reflection coefficients in terms of the refractive indices of the media on both sides of the interface along with the incidence and refractive angles.

The reflection (r_i) and transmission (t_i) coefficients for i can be s-polarization or p-polarization are defined respectively as [108]:

$$r_S = \frac{n_1 \cos\theta_i - n_2 \cos\theta_t}{n_1 \cos\theta_i + n_2 \cos\theta_t}, \tag{2.7}$$

$$t_S = \frac{2n_1 \cos\theta_i}{n_1 \cos\theta_i + n_2 \cos\theta_t}, \tag{2.8}$$

$$r_P = \frac{n_2 \cos\theta_i - n_1 \cos\theta_t}{n_1 \cos\theta_t + n_2 \cos\theta_i}, \tag{2.9}$$

$$t_P = \frac{2n_1 \cos\theta_i}{n_1 \cos\theta_t + n_2 \cos\theta_i}. \tag{2.10}$$

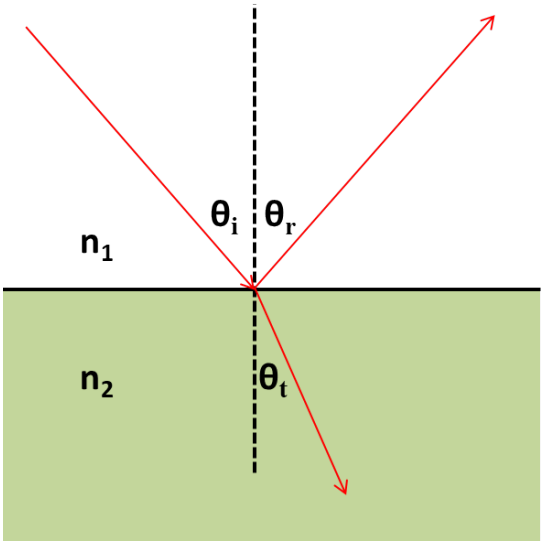

Figure 2.2: Light incident on a plane interface between two optical media at angle of incidence θ_i

,

Then, the reflectance and transmittance are defined from the Fresnel coefficients as

$$R = |r_i|^2, \tag{2.11}$$

$$T = \frac{n_2 cos\theta_t}{n_1 cos\theta_i}|t_i|^2, \tag{2.12}$$

where i can be S- or P- polarization state.

2.1.3 Optical absorption in solar cells

For thin-film solar cell technology, materials exhibit poor optical absorption, which poses a challenge that needs to be investigated for obtaining efficient competitive devices. The research efforts in this direction are reported in hundreds of articles. For this purpose, we revise some of them in the introduction chapter. In chapter 1 we present, the state-of-the-art of some thin-film solar cells, and focus our attention on improving the optical absorption of these devices by proposing advanced light concentration strategies based on nanophotonic structures. The optical study solves Maxwell equations to obtain the optical fields (electric $E(r, \lambda)$ and magnetic $H(r, \lambda)$) distributions in terms of space and wavelength, or frequency, for each layer of the device, when an EM wave propagates through it. Once we have the optical fields distributions, the absorbed power density, $p(\lambda)$, is calculated from the divergence of the Poynting vector as [111]:

$$p(\lambda) = \frac{\pi c}{\lambda}\varepsilon''(\lambda)|(E(\lambda))|^2, \tag{2.13}$$

where λ is the wavelength of the incoming radiation in free space, ε'' is the imaginary part of the dielectric permittivity of the material. It can be calculated from the refractive index real and imaginary parts using $\varepsilon'' = 2nk$. And $|E(\lambda)|^2$ is the local intensity of the electric field. In

that case, to increase the absorbed power density in a specific layer, we need to maximize or concentrate the optical fields within this layer.

The total absorbed spectral power density inside a volume space is the integration of equation (2.13) over that volume [111]:

$$P(\lambda) = \iiint_V \frac{\pi c}{\lambda} \varepsilon''(\lambda) |(E(\lambda))|^2 dV. \tag{2.14}$$

The spectral absorbance is evaluated by dividing the spectral absorbed power by the incident power [112, 113]:

$$A(\lambda) = \frac{P(\lambda)}{P_{\text{input}}}, \tag{2.15}$$

where P_{input} is the incident optical power. In the analysis of solar cells, light is modeled as a plane wave source with a defined polarization, which differs from the spatially–incoherent thermal light source feature of the sun. So an average calculation of two orthogonal polarization states is required to account for the nonpolarized nature of sunlight.

In a solar cell, an important parameter is the short-circuit current, J_{SC}, delivered from the cell for a given solar irradiance. The ideal short current density is calculated from the active absorption in the cell which occurs in the active layer only if we assume that every absorbed photon generates an electron-hole pair [112]:

$$J_{SC} = \int \frac{q}{hc} A(\lambda) \lambda \Phi_{\text{AM1.5g}}(\lambda) d\lambda, \tag{2.16}$$

where $\Phi_{\text{AM1.5g}}(\lambda)$ is the solar spectral irradiance as a function of wavelength [114], which is the global standard spectrum used to characterize solar cells for terrestrial applications. The term AM refers to the air mass coefficient, which defines the direct optical path length through the Earth's atmosphere, expressed as a ratio relative to the path length vertically upwards, *i. e.*, at the zenith. The subindex AM1.5g refers to the spectrum measured under representative geometric and atmospheric conditions, for example, light absorption and scattering. And q is the electron charge, c is the speed of light in vacuum, and h is the Planck's constant. The value of J_{SC} obtained from equation 2.16 is the maximum achievable photo-current from the device. This happens because some losses, such as electrical transport, recombination, and extraction losses, are not included in our optical model. However, there are many contributions that show how the results of the optical modeling agree well with the experimental measurements [115, 116, 117, 118]. Our model will always determine the device performance with a nanophotonic design and compare it to the performance of the planar form, so, it is a quantitative analysis that explores how we can use these structures and designs to provide efficient devices, that are competitive with the current devices.

2.1.4 Surface plasmon polaritons

A surface plasmon is an oscillation of the electrons, which exist at interfaces between two materials of an opposite sign real part of the dielectric function, for example, metal/air [110]. The electron oscillations create an electromagnetic field that decays in the metal and the adjacent dielectric medium. Together, the electron oscillations and the accompanying electromagnetic field are called surface plasmon polariton (SPP) [61]. The accompanying electromagnetic

field propagates adjacent to the interface between the metal and the dielectric and called surface plasmon waves (SPW). When a plane EM wave incident on the interface between metal and dielectric layers, as in figure 2.3, it decomposes into two components, one perpendicular to the interface, and the other parallel to it. If the frequency, and wavevector of the incident light match those of surface plasmons an SPR is excited [61].

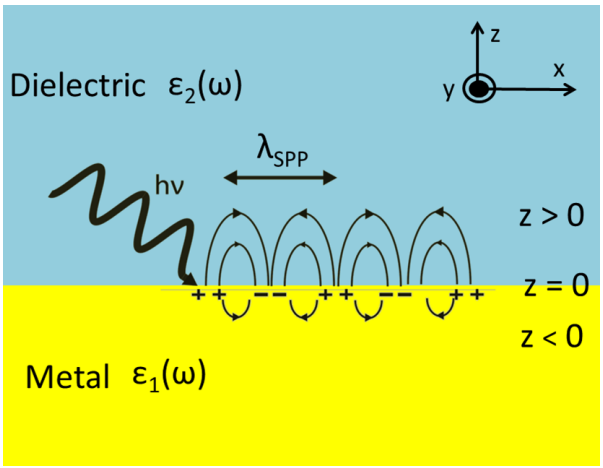

Figure 2.3: Metal - dielectric interface where SPPs are generated. A surface wave propagates longitudinally and couples to the surface plasmons of the metal. A surface plasmon resonance is excited when the frequency, and wavevector for the incident light and the surface plasmons are matched.

The fundamental dispersion relation for SPPs can be obtained by analytically solving the wave equations (2.5, 2.6), for those solutions propagating adjacent to the interface and decaying exponentially in the direction perpendicular to the interface. The derivation of this dispersion relation is reported elsewhere, for example in [119]. Such solutions exist for TM modes only [119]. The propagation constant β of the surface plasmons is given by:

$$\beta = k_0 \sqrt{\frac{\varepsilon_1 \varepsilon_2}{\varepsilon_1 + \varepsilon_2}}. \tag{2.17}$$

As for most metals, ε_1 is a complex value, and has the form of $\varepsilon_1' + i\varepsilon_1''$, with a negative real part, $\mathrm{Re}(\varepsilon_1) < 0$, applying to the β value the same consideration. The imaginary part of the propagation constant indicates the attenuation while propagating. By assuming $|\varepsilon_1'| \gg \varepsilon_1''$ which holds for most metals, we obtain the attenuation term of the propagation constant as follow:

$$\beta = \beta' + i\beta'' = k_0 \sqrt{\frac{\varepsilon_1' \varepsilon_2}{\varepsilon_1' + \varepsilon_2}} + i k_0 \frac{\varepsilon_1''}{2(\varepsilon_1')^2} \left(\frac{\varepsilon_1' \varepsilon_2}{\varepsilon_1' + \varepsilon_2} \right)^{3/2}. \tag{2.18}$$

The attenuation term, β'' shows the surface nature of these plasmonic waves as it decays to zero far from the surface with a typical decay length in the order of 1–10 wavelengths. In the following section, we will describe some common excitation methods of an SPR.

2.1.5 Surface plasmon resonance excitation methods

Figure 2.4,a shows the case of a dielectric medium with dielectric constant ε_a adjacent to a metal layer with dielectric constant ε_m. To excite an SPR mode at this interface, we can

use photons, where the wavevector of this photon must match the propagation constant of the surface plasmon given by equation (2.17). This matching is called the wavevector matching condition. There are a lot of methods to excite the SPR, however, the most used ones are presented in figure 2.4: prism coupling (Kretschmann figure 2.4,b left and Otto figure 2.4,b right) , waveguide coupling figure 2.4,c, grating coupling figure 2.4,d, and optical fiber coupling figure 2.4,e.

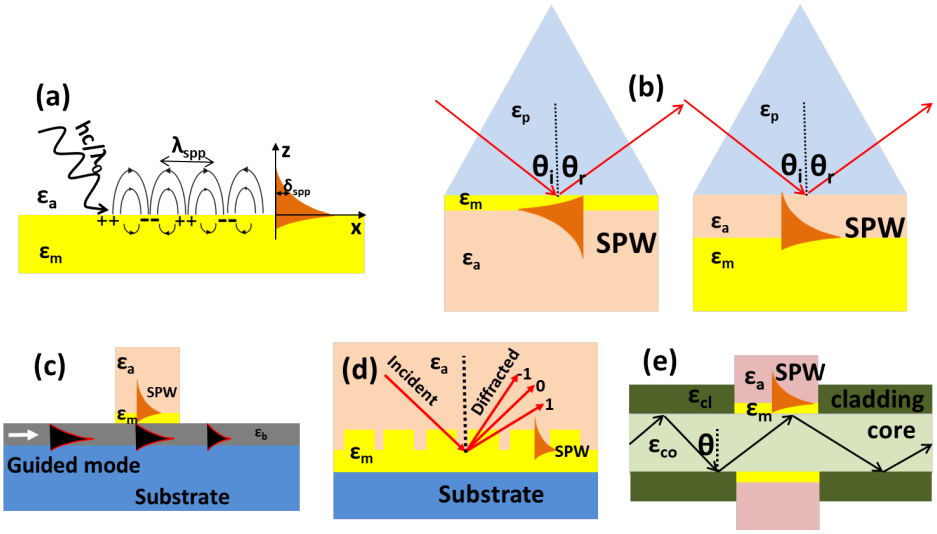

Figure 2.4: (a) The general condition for SPR to be exist the a structure has a metal layer in contact with a dielectric layer, then, SPR is excited using the following methods: (b) Prism coupling methods, Kretschmann (left) and Otto (right)). (c) Waveguide coupling. (d) Grating coupling. (e)fiber optic coupling

We will focus on the prism coupling and the grating coupling methods as we used both of them in our designs. In the prism coupling method, light is launched from a light source at one side of the transparent prism with dielectric constant ε_p as in figure 2.4,b, then totally reflected at the prism–metal interface before collected by a detector. Through this process, an evanescent field is generated and penetrate into the metal layer. When the propagation constant of the evanescent field matches that of the SPW as described in equation (2.17), light is coupled to a SPW that decays on the analyte medium of dielectric constant ε_a. If the incoming field is perfectly coupled to the SPR mode, the reflection is zero or very small, and the angle of incidence is called the resonance angle. The coupling condition read as [53, 54]:

$$\frac{2\pi}{\lambda} n_p \sin(\theta) = \beta_{\text{spp}}, \tag{2.19}$$

where λ is the incident wavelength, n_p is the prism refractive index, θ is the incident angle, and β_{spp} is the propagation constant of the SPW. Two important parameters of the SPWs, are the maximum field intensity of the SPW in the dielectric medium, and the penetration depth (δ_{spp} in the schematic of figure 2.4,a), which is the spatial length of the SPW decay in the dielectric medium. These parameters determine the interaction volume and strength of the SPW within the dielectric medium.

In the grating coupling method, the SPW is generated by one of the diffraction lobes that fulfills the wavevector matching condition instead of directly excited through the incoming

light, for this, the wavevector matching condition reads [61]:

$$\vec{k}_{0x} + \vec{k}_{\text{grating}} = \vec{k}_{\text{spp}}, \tag{2.20}$$

where $\vec{k}_{0x}$ is the x-component of the wavevector of the incoming wavefront; $\vec{k}_{\text{grating}} = 2\pi m/P$ is the grating wavevector, being P the grating period, and m the diffraction order; and $\vec{k}_{\text{spp}}$ is the SP wavevector generated at the interface. If we include the angle of incidence in the wavevector matching conditions, it becomes [80]:

$$n_1 k_0 \sin\theta \pm \frac{2\pi m}{P} = k_0 \sqrt{\frac{\varepsilon_m \varepsilon_{\text{eff}}}{\varepsilon_m + \varepsilon_{\text{eff}}}}, \tag{2.21}$$

where k_0 is the wavevector in vacuum, θ is the angle of incidence of the incoming wave,n_1 is the refractive index of the incidence medium, ε_m is the real part of the complex electric permittivity of the metal, and $\varepsilon_{\text{eff}} = n_{\text{eff}}^2$ is the dielectric permittivity of an effective medium in contact with the metal. We use the effective index to account for the medium near the metal surface that combines the grating and surrounding materials.

2.2 Numerical methods

Numerical methods are mathematical algorithms typically used to find the solution of differential equations that describe phenomena of which exact solutions may not be determined analytically, or when a numerical solution is required. Usually, in these methods, initial values and boundary conditions serve to start the solution by weighting it with an error function of the solution guess, that has to be reduced. Depending on the problem domain size and the complexity of the differential equations we can decide the applicability of each method. Sometimes, various methods can be applied to the same problem. In this case, the computational cost and accuracy help us to decide which one should be used, or how to link the available methods. In the following subsections, we will give a brief definition of some of the numerical methods used in optical modeling.

2.2.1 Finite difference time domain

Finite-difference time-domain (FDTD) is a numerical method introduced by Yee in 1968 [120, 121] where the Maxwell equations are solved by discretizing time and space. In this method, we use a Yee lattice to spatially discretize domains in terms of time where the E and H field are stored at intermediate positions to reduce the memory consumption. Maxwell equations in the partial differential form are then solved at discrete time intervals within the Yee lattice to obtain the E and H field at these intervals. The time resolution is related to the spatial resolution, so we can account for several frequencies for non-dispersive mediums within the time interval in one run. The FDTD method solves Maxwell equations for periodic and non-periodic structures If we have a periodic structure, the Bloch boundary conditions may be applied for simulations of waves in periodic media. A software-based on the FDTD method computes the E and H field at every time step until we obtain the full solution of the fields for the domain under analysis.

2.2.2 Ray tracing

Ray tracing in geometrical optics is an approximation that is used to calculate the optical response like absorption, reflection, and transmission, by assuming that the light moves along a trajectory. The transmission of light between interfaces is obtained after applying Fresnel equations, to determine the optical response of the structure [122]. Although some physical effects such as interference and scattering are ignored in this method, some software allows thin-film interference effects by applying this as surface properties to interfaces. This method is suitable when simulating very large domains compared to the operating wavelength which can't be achieved using discretization based methods because of the computational cost. There are some other propagation methods as: beam propagation method, rigorous coupled wave analysis, Rayleigh-Sommerfeld diffraction, etc. These methods are the diffractive "versions" of the ray-tracing methods and they are very well fitted to large volumes (tens, hundreds, or thousands of wavelengths)

2.2.3 Finite element method

The finite element method (FEM) is a numerical method for mathematical physics that finds approximate solutions for partial differential equations complying with boundary constrains and initial conditions. Finite element theory in general, and for Maxwell equations in particular, is covered in many textbooks, for example, [123, 124]. The finite element method allows us to discretize and solve differential equations using a mesh. A set of polynomial functions express the field displacement of each mesh element. Then, the total solution is determined for the whole domain by the summation of these individual solutions. In the FEM, the computational domain should be discretized into non-overlapping subdomains called finite elements. The typical discretization geometric elements for a computational domain are triangles or quadrilaterals etc., in 2D, and cuboids, tetrahedrons, pyramids, etc., in 3D. The FEM converts the boundary value problem into a system of algebraic equations. The method uses initial values and boundary conditions to approximate the unknown function over the domain. Each mesh element is represented by a simple set of equations, while a collection of theses equation in a complex system of equation is used to represent the whole problem system. The goal of FEM is to use the variational methods, which are mathematical methods from the calculus of variations, to obtain an approximated solution through the weighted of an error function that has to be minimized for more accurate solutions. Each numerical method has some advantages. In our laboratory a commercial software based on the FEM is available, so we will use it to construct and solve our optical models for various geometries and devices. Having a small volume domains, through the discretization to tiny volume subdomains, the methodology works satisfactorily. For this reason, FEM is widely applied to many fields [125].

2.2.4 Simulation package: Comsol Multiphysics

Comsol Multiphysics (Comsol) simulation package (COMSOL, Inc) is a commercial software based on the finite element numerical method [126]. RF and wave-optics modules solve Maxwell equations in the frequency domain (or wavelength domain) for obtaining optical fields in terms of spatial and frequency parameters. The main advantage of Comsol is the friendly user interface that allows to set up complex optical problems and geometries, and let the built-in solvers do the complex math. It also contains various visualizations and results processing capabilities along with easy data export features. Its built-in boundary conditions and operators allow the shrink of infinite device size into a 2D or 3D nanometer-scale unit cell and account accurately the result for the large scale device.

Although the package can work for almost all practical system because of being based on FEM, the modelization of large volumes requires an extremely high number of mesh points. For this, Comsol uses a variety of solvers that adapt to each system to economize memory usage and reach a solution faster and with a better accuracy. In many cases, the paradiso (parallel sparse direct solver) [127] is used to compute the solutions to the models as it much suitable for this purpose.

2.3 The optical model structure

In our study, we use the optical model to obtain optical designs with improved properties using photonic and plasmonic effects. Figure 2.5 describes the flow-chart process that we have applied in this dissertation. We study several optical and optoelectronic devices which are solar cells, optical sensors based on plasmonic resonances, and a hybrid technology that combines both. So, we begin by selecting the device and determining its operating principles as the first important step to build the model. We do that to know which elements and parameters have to be taken into account in our model, which will have an impact on the performance of the device, and those that can be neglected without any significant effect on the final result.

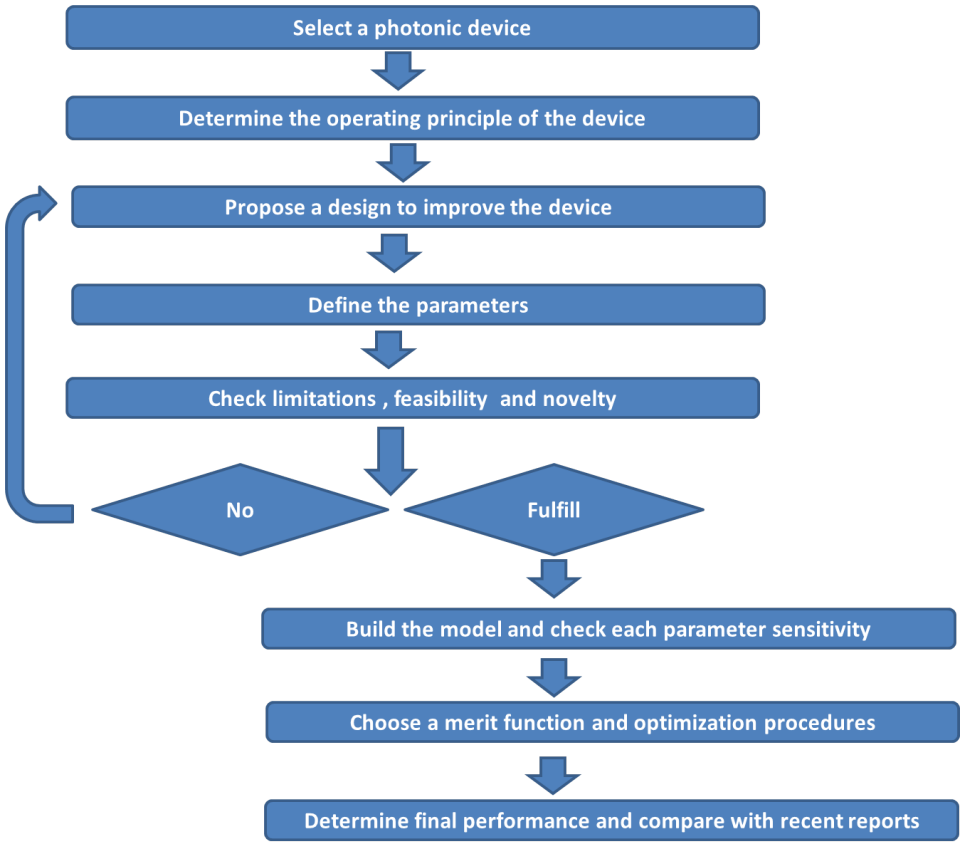

Figure 2.5: Flow-chart summarizing the steps of our work: from the start point of selecting the photonic device of interest, until we reach an optimum optical design for it

To understand how the model works, we illustrate it with an example where we analyze the importance of a 17 nm paSiH layer in an aSiH thin-film solar cell, which accounts for 21.45% (mainly at short wavelengths from 300 to 450 nm) of the total absorption of a planar cell with an active layer of 350 nm, and another example where we study the importance of 10 nm

paSiH layer in a perovskite- c-Si multijunction (tandem) cell, which accounts for only 0.01% of the total absorption in the planar device. In the case of the thin-film device, the paSiH layer is located at the front surface of the device, below the top contact, and account for a high absorption. In fact, we cannot ignore this layer in an optical model of thin-film aSiH cells, because the increase in the optical field gained by any nanophotonic or plasmonic structure in the front surface can be lost in this layer, and the same applies for other layers. However, for the case of the tandem device, the layer is located at the front surface of the bottom junction, so most of the incoming optical energy that can be lost at this layer is already absorbed or reflected by the layers on the top cell. Furthermore, it has a negligible optical absorption, so withdrawing this layer from the model has no impact on the final performance of the device. However, doing that will simplify the model and reduce the computational cost as very thin layers with a large domain typically require a high-density mesh.

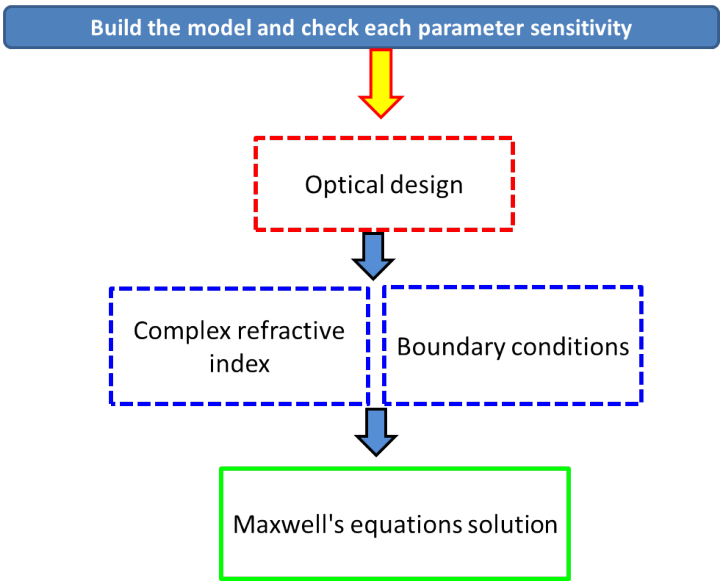

Figure 2.6: Detailed steps in the optical model.

After this first important step, we already built some knowledge about our device and we are aware of the losses, so we can move to the design step that reduces these losses. When proposing a design, we have to take into account the fabrication compatibility and feasibility of such design. In general, avoiding ultra-thin features and unreasonable structures will be better. The next step is to define which parameters affect the performance of this design to optimize it. As we mentioned, many researchers and groups are working actively in this area, so we have to always check the novelty and the impact of our design as a first step and through the study. At this point, we can decide if the proposed design has merit to be subjected to our analysis or move on to another proposal. Once all the issues discussed above are fulfilled, we start building the Comsol model for the selected design. First, we check the sensitivity of the device's performance on each geometrical and material parameter in the design. After this, we define a merit function that aims to improve the device's performance, then we change the design parameters to minimize or maximize this merit function. As a final step, the performance of the device with and without the optimized design should be compared. The part that takes most of the study time is the model building and parameter sensitivity check step. More detail steps inside this item are shown in figure 2.6.

Comsol allows the implementation of the characteristics of the optical source. For example, we can illuminate the structure with the standard solar spectral irradiance obtained from the National Renewable Energy Laboratory (NREL), AM1.5g for the solar irradiance by inserting the data in Comsol, and assign the power to the source for this data while sweeping in wavelength. Operators, functions, or physical effects can be easily integrated into the model. Complex experimental refractive index data can be plugged into the model to complete the large library of optical and physical constants that already exist in the package. The periodic boundary conditions can be applied to the sides of the unit cell geometry. This allows shrinking the full device into a manageable unit cell. Figure 2.7 shows an example of a periodic nanostructure array placed on a thin-film solar cell, that only requires the computation of a small unit cell for optical modeling. When necessary, the perfect matching layer condition removes reflections from the unit cell domain boundaries and makes such small domain work as a full large domain. The model tree starts with the parameterization of the constants and variables for which we define each and reserve a name for it in the model. Then we built the geometry using the Comsol environment, or import the design from another CAD software.

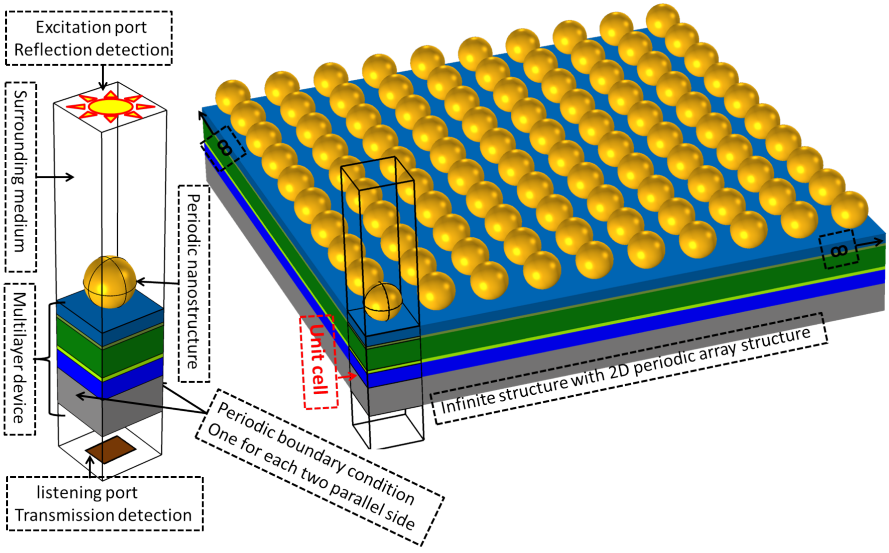

Figure 2.7: A schematic plot of a 3D optical design (right) with a spherical periodic array on top this design is infinite in space, however in the model the boundary conditions can be used to convert it to a small unit cell on the left, the details of each part in the unit cell is included in the plot

The model tree also contains the material section to assign a specific material to each layer. The required properties and material constants depend on the physics and the set of equations that will be solved in Comsol. So, the important section in the model is the physics section as we can define the excitation, initial conditions, boundary constraints, and physical equations. As a final step before performing the study, we should mesh the geometry. This, require experience and patient until we obtain the best mesh that achieves a stable accurate solution for the problem. During this study Comsol, uses a built-in statistical calculation to parameterize the mesh quality that helps us to detect the property that needs refinement. In any case, the most important parameters are the maximum and minimum element sizes which have to be correctly defined according to the physics in the model. Finally, we need to perform the study which can be in the frequency domain (RF module) or wavelength domain (wave optic module). Loops in the study section and study steps are used to make a parameter sweep within the model and perform multiphysics simulation.

2.3.1 Analysis and postprocessing

Comsol is a powerful computational package that has many ways to evaluate and visualize the results of a given model. The example presented in figure 2.7 is created using Comsol. The post-processing and visualization tools are used to better understand the results. Once the model has been evaluated, it is possible to explore the importance of variables using graphical representations. These graphs present the result in terms of spatial maps, and plots in terms of some other quantities, like frequency or angle of incidence, etc. We can create 1D, 2D, and 3D plots for different quantities like the optical field maps for the full structures, or for a specific location within the device. The full list is shown in figure 2.8,a. Some of the post-processing tools are derivations, integrals, or differentiation of data sets that extract the results in the form of tables see figure 2.8,b. For further processing of the results and data in other software

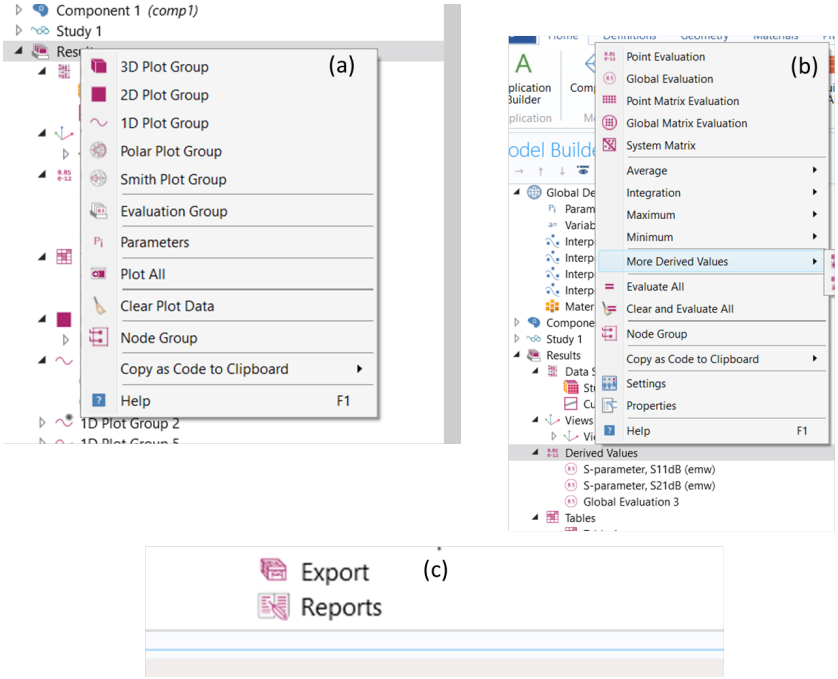

Figure 2.8: Several screenshots from Comsol interface show some of the possible post processing features that can be conducted inside Comsol environment

like Originlab or Matlab, we can export the results out of Comsol (see figure 2.8,c). The maps and plots in Comsol can be directly saved as an image file or to the clipboard.

2.3.2 Model validations

One important step is to make a sanity check of the model and see how close the calculated responses are to those obtained from experimental and analytical models. A good numerical model has to agree with the analytical solutions, as both are built on theoretical assumptions. Although the numerical solution is done through some approximations and the analytical one gives the exact solution of the problem, the numerical model can be improved by reducing the difference with the test function that determines the error as much as possible.

Here in this section, we will show the excellent agreement between our optical model and the analytical solution of some simple optical structures. First, we will calculate the transmission and reflection response of a linear polarized plane wave incident on the flat interface between

air and glass substrate. A schematic of this structure is presented in figure 2.2. The refractive index n_1 of the incident medium is replaced with a semi-infinite air medium with a refractive index $n_1 = 1$ and the other medium is a semi-infinite glass substrate with refractive index $n_2 = 1.45$. The structure can be modeled using a small unit cell and periodic boundary conditions to account for the real dimensions in 2D. The analytical solutions, along with the

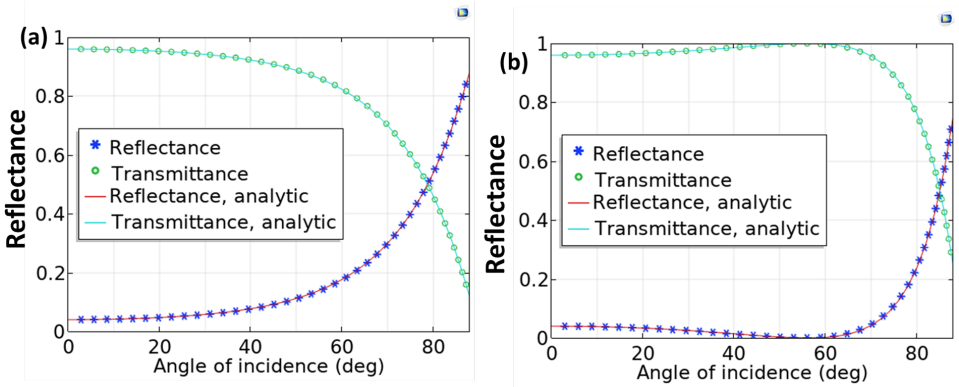

Figure 2.9: Analytical and Comsol computed reflection and transmission spectra of a plan wave incident from air side on a glass substrate with (a) TE polarization (b) TM polarization

Comsol computed results are presented in figure 2.9. The results for TE polarized wave are shown in figure 2.9,a and those for TM are in figure 2.9,b. As we can see, there is an excellent agreement between the computed and the analytical solutions.

Another example with more complexity as a multi-layer structure that contains metallic thin-film is the Kretschmann setup for the optical sensors. A map of the magnetic field H_z component at resonance is represented by the inset in figure 2.11. The transmission and

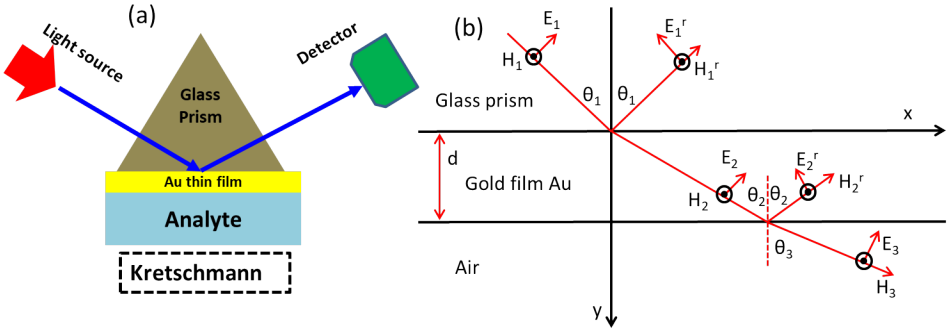

Figure 2.10: (a) schematic of the Kretschmann setup where light is obliquely incident on the metallic thin-film using a glass prism. The signal is retrieved using an optical detector. (b) The incident , reflected and transmitted fields at each interface are represented The transmission and reflection are governed by Fresnel equations and the SPR mode is excited when the wavevector matching condition is fulfilled.

reflection at each interface are given by the Fresnel equations as in the previous example. However, here we have several interfaces and a spectral dependence of the absorption at the metal surface determined by the excitation of SPR mode. By applying Fresnel equations at each interface we have an analytical expression for the total reflection from the structure in the form:

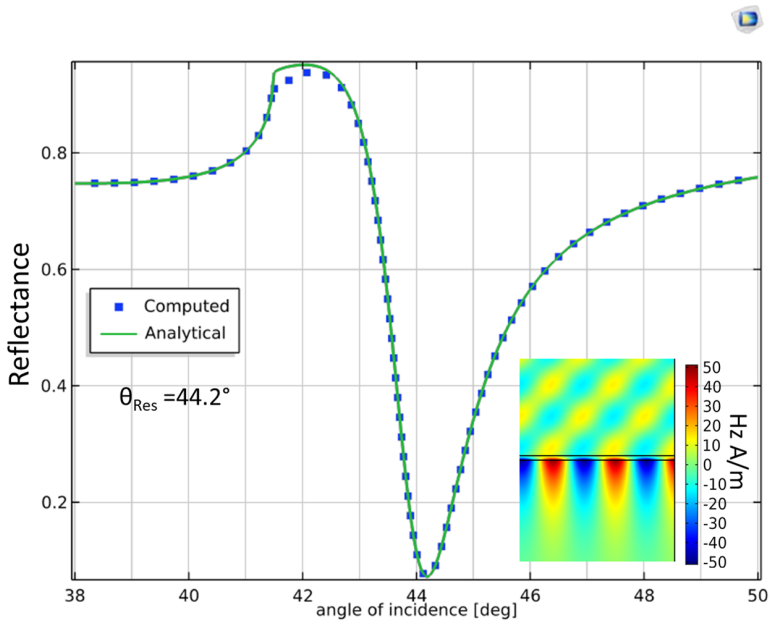

Figure 2.11: The analytical and computed solution for a Kretschmann setup optical sensor, the inset schematic is tthe magnetic field map for an angle of incidence where the plasmonic resonance is excited.

$$R = \left| \frac{r_{12} + r_{23} e^{-2kd}}{1 + r_{12} r_{23} e^{-2kd}} \right|^2 , \tag{2.22}$$

where r_{12}, r_{23} are the Fresnel reflection coefficients at the glass/metal and metal/air interfaces respectively, k is the wavevector in the direction of propagation, and d is the metal thickness. The SPR mode is excited when the wavevector matching condition in equation (2.17), is fulfilled. We apply these calculations to a glass prism of refractive index $n = 1.5217$ coated with a gold (Au) thin-film with thickness 40 nm. The wavelength-dependent complex refractive index extracted from [128]. Both the analytical solution and Comsol evaluation are presented in figure 2.11. An excellent agreement between the analytical and computed solutions is observed, and also, the results agree well with the experimental study by having a resonance angle $\theta = 44.2^o$ [129].

2.3.3 Significance and importance of optical modeling

In general, simulations are used to verify or optimize a design before prototyping and fabrication. We can explore how the geometry, materials, or other parameters will affect the quality of the device. However, that is not the only advantage of the numerical simulation. Understanding which parameters affect the most to the performance adds value to the design process. Using simulation we can characterize how sensitive the response is with respect to uncertainties; for example, manufacturing tolerances or material properties. Then, we can deduce which changes are the most relevant, to improve the performance of a design. Although the numerical calculation implies approximations, some ideal assumptions, and ignores some layers of the design for model simplicity, modeling can save a lot of effort and cost that could be wasted through uneducated experimental trials. As a special case of our study, the optical modeling of photonic devices provides the manufacturers and experimental laboratory with numerically tested structures that perform as perfect absorbers [130], wide-angle optical acceptors [131], and high efficient optoelectronic devices [132]. Many contributions show the good agreement

of optical modeling results with experimental and analytical solutions [115, 116, 117, 118]. However, the main purpose of our optical models is to qualitatively and quantitatively study the effect of an optical design on the performance of a photonic device. To make our models more reliable, we should pay close attention to the following issues:

- The validity of the device arrangement to function under the operation principle of the device.
- To take into account all the structures that have an optical impact on the device performance, including contacts, buffer layers, and selective transport layers.
- To consider the fabrication feasibility of the design into account by assuming reliable geometries and shapes.

Finally, the results should always be compared to the state-of-the-art design of the device under study, or to the device without the proposed structure.

3

Nanophotonic designs for solar cells applications

Single junction based on c-Si is the dominant photovoltaic technology to produce commercial, stable, and long-life devices. This is because of its high efficiency, raw material abundance, and being nontoxic [133]. However, it has some disadvantages such as its high cost, complex fabrication methods, and heavy-weight panels which also, increases the final waste of the expired devices [134, 135]. Therefore, it was necessary to develop new technologies to keep pushing the progress of this important renewable energy source for different future applications [136]. Low cost devices are based on thin-film solar cells, some of them are already commercialized in the photovoltaic market [137, 138]. Their efficiency is compromised by the low absorption gained by the small thickness of the thin-film semiconductor material, that forms their active layer [139]. The variety of high precision thin-film coating technologies allows their fabrication on large areas [140]. For thick wafer based solar cells, a high purity material is required to obtain efficient solar cell devices, and in some cases, even a single crystal structure is required [134, 135]. However, for thin-film based solar cells, less purity and various crystal structures could be used depending on the cell material type [141]. Therefore, thin-film based solar cells reduce the cost of device fabrication and the raw material itself. Various inorganic and organic materials are candidates for thin-film solar cells. However, in terms of stability and long lifetime, inorganic semiconductors are much better for high efficiency solar cells [142]. Perovskites and organic semiconductors are also promising because most of them can be deposited using solution processing techniques. So, they can be applied to flexible solar cells, but their stability and lifetime still need to be improved [143, 144]. Among the inorganic materials, aSiH is a good choice for large scale fabrication because of its abundance and non-toxic properties. However, they still have some challenges to overcome caused by the low mobility and short lifetime of their charge carriers that reduce the probability of being extracted at the device electrodes. Due to this, the optimum thickness of the state-of-the-art devices is limited to $\approx$ 350 nm. Although higher thickness leads to a higher absorption, low probability carrier collection results in a reduction of the photocurrent and the fill factor [145, 146, 147]. The second limitation for this material is a performance degradation induced by light exposure arising from SWE [100], where the dark conductivity of aSiH can drop by orders of magnitude after prolonged exposure to VIS. The origin of this degradation mechanism is the shift of the Fermi level close to midgap, which leads to the photo-induced creation of 10^{16} – 10^{17} new states near the middle of the energy gap. The SWE is a bulk phenomenon, *i. e.*, it is thickness dependent and can be compensated by annealing [148]. The efficiency of an aSiH solar cell can be returned to its initial state if the cell is annealed at 150° C for four hours [100], or at lower temperatures (e.g. at 80° C) over extended times [149]. Even more, light induced annealing could partially

compensate SWE defects [150], as solar cell temperature under operation, reaches values of 50° C to 60° C [151]. So, increasing the parasitic absorption losses increases the cell operating temperature, and produces self-annealing in the device, which partially mitigates the SWE defects.

As we have seen before, silicon is an abundant and non-toxic material that allows both large scale fabrication and portable devices. This is because it's lightweight and can be deposited on different substrates as a thin-film. However, some limitations about active layer thickness limit, and the SWE defects, have to be overcome, mainly by promoting the absorption of ultra-thin active layer [152]. Reducing the thickness while keeping the absorption high, would improve the probability of extraction of the charge-carrier, and hence the overall performance of the device. Moreover, as an special case for this material type, a reduction or mitigation of SWE could be achieved by increasing the cell temperature under operation, that produces *in situ* annealing of the device. This could be done if we simultaneously improve the absorption at every layer in the cell, along with the active layer. In this case, the absorption enhancement in the active layer will be translated to an increase in the photo-generated current, while absorption enhancements in other layers will mainly be converted to heat [101]. This happens because of the dissipative losses and charge carrier recombination, which arises form the short diffusion length and low mobility of minority carrier in this layers, and to the high density of defect states [101, 153, 154, 155, 156]. We aim to improve the performance of aSiH thin-film solar cells by integrating it with a nanophotonic structure with broadband anti-reflection characteristics, useful focusing, and scattering capabilities.

Both wafer and thin-film based single junction cells have an efficiency limit calculated by Shockley–Queisser that is 30% for a semiconductor with a bandgap of 1.1 eV [42]. Shockley and Queisser assume the spectrum of a black body at temperature 6000 K for the solar spectrum to simplify their calculation, while more recent calculations use the air mass solar spectrum AM 1.5g, provides a maximum efficiency of 33.7% at an optimized bandgap of 1.34 eV [157]. However, the most common material employed in the market for solar cells applications is Si, which has a bandgap of 1.1 eV. Therefore, the maximum theoretical efficiency is reduced to about 32%. In practice, the commercial mono-crystalline solar cells reach an efficiency close to 24% for large scale modules, and they can achieve up to 26% for small size devices in laboratory conditions [133]. As we have seen, the theoretical limit is difficult to reach in practice, because of the reflective, parasitic, and resistive losses from different interfaces in the device. To make photovoltaic technology more competitive it is necessary to overcome this limit, for example, by using multi-junction solar cells. In multi-junction solar cells a stack of two or more junctions between materials with different bandgaps is arranged in one device. This element can absorb a wider band spectrum, and can overcome the Shockley–Queisser limit of the single p-n junction devices. Even the multi-junction solar cells have a maximum limit for their conversion efficiency, which reaches 86.8% depending on the used materials, the number of layers, and the structural design [158].

Another option is a tandem solar cell that consist of two junctions solar cells sitting one on top of the other [159]. They can offer a higher efficiency than single junction devices at a moderate cost. In a monolithic tandem solar cell, the photons with short wavelengths are absorbed in the top cell, having a larger bandgap, and the photons of long wavelengths are transmitted to the bottom cell. A combination of thin-film solar cells on top of a c-Si wafer solar cell has been widely investigated in the last decade [160]. Perovskite thin-film solar cells are a promising candidate for the top portion of the solar cell or as a valuable option by themselves [161]. They are low cost, easy to be fabricated through solution processing

techniques, and highly efficient [143]. Perovskite materials have a good optical response, and a tunable bandgap near the silicon one (1.5–1.8 eV), making them easy to combine with current silicon technology. In the last five years, researchers report several designs for monolithic devices composed of perovskite/c-Si, and most of them use texture surfaces as a light trapping mechanism [162]. There are two ways to arrange the cells together: 4-terminal setups, and 2-terminal [163]. In the 4-terminal configuration the two cells are mechanically stacked on the top of each other with a transparent separation layer, typically made of glass, in between. Each subcell is fabricated independently, and also is electrically isolated, to avoid the constraints arising from having them directly in contact, such as output current matching, multi-layer deposition, and tunnel junctions compatibility [164]. However, in this configuration, each subcell has a separated top and bottom electrical contacts, which involves more reflection and absorption losses than two contacts only for the whole device. Also, the insulator transparent layer that separates the two cells, adds additional reflection losses. In contrast, the two cells in a 2-terminal device are directly stacked over each other and separated by a thin single tunnel junction in an unique device. For the 2-terminal, the electronic circuit is simplified and the number of contacts is reduced. Besides, the removal of the intermediate insulator makes the optical management simpler. However, the 2-terminal configuration requires current matching between the top and the bottom cell for proper operation, and fabrication compatibility of each layer should be considered [164]. In this work, we will focus our study on these two types: namely aSiH thin-film solar cells, and 2-terminal monolithic perovskite/c-Si solar cells. We aim to use nanophotonic structures to reduce reflection losses and concentrate the light in the active layer of the device over a wide band spectrum, where the selected device operates. Manufacture feasibility, effective operation of each device will be considered in our optimization.

3.1 Nanostructured broadband anti-reflection coating for aSiH thin-film solar cells

Anti-reflection coatings (ARC) are used to trap light in optoelectronic devices and increase its probability of being absorbed. The simplest form of this coating is a planar dielectric thin-film, which can realized as a single or multilayer arrangement. If the thickness of the front buffer layers and/or electrode of the a solar cell is comparable to the active layer thickness, their optical losses are not negligible and a planar ARC may not offer an efficient solution to reduce the total reflectance of the solar cell. For this reason, a nanostructured ARC can be a suitable option for a better performance. First, we will study the optical response of the planar device and optimize a single and double layer ARC. Then, we will explore the effect of a one dimensional dielectric grating printed on top finished device. That means that the fabrication of the devices does not change, and only we need to add an additional step of fabrication. Finally, we will compare the results in terms of the absorption at the active layer, and absorption/reflection losses for each design.

3.1.1 Planar aSiH solar cell

We begin our study by modeling the optical response of the planar thin-film aSiH solar cell. The refractive index for each layer extracted from previous studies as follow: aSiH layers, [101], indium tin oxide (ITO) [165], Ag [128], silicon nitride (Si_3N_4) [166], n-type, p-type, and intrinsic aSiH (n, p, i aSiH) [101], and aluminum zinc oxide (AZO) [167].

Semiconductor materials absorb light in the ultra-violet (UV), VIS and NIR spectra depending on the material's band-gap. Each semiconductor material is characterized by its

wavelength dependent absorption coefficient, which determines the required thickness to absorb light at each wavelength. Intrinsic amorphous silicon hydrogenated (iaSiH) has a low absorption coefficient at the edge of the VIS near to the material bandgap edge [168], so, it has a low absorption at these wavelengths. We can improve the absorption of iaSiH layers by increasing their thickness, where the light travels longer distances in the material and its probability to be absorbed will increase. The optical response of a thin-film of iaSiH with different thicknesses is shown in figure 3.1,a.

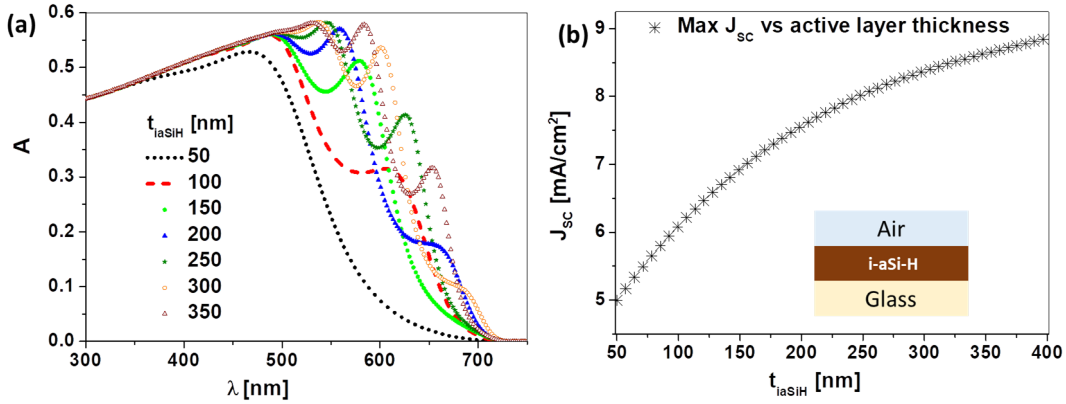

Figure 3.1: (a) Spectral absorption of a thin iaSiH thin-film with different thicknesses deposited on a glass substrate. (b) Maximum photo-current generated from the absorption in (a), as a function of the iaSiH film thickness.

As we can see in figure 3.1,a, the absorption increases with thickness at long wavelengths. We limit our calculations until 400 nm due to the limitation of the active layer thickness discussed in section 3. The thickness of the iaSiH active layer is relevant to the overall performance of the cell. Larger thickness means larger absorption within the absorption band of the material, particularly at longer wavelengths. The J_{SC} , is calculated from an integral function of the absorption (see equation (2.16)). As J_{SC} reaches an asymptotic value, it means that a thicker active layer does not produce a significantly larger absorption [169, 170, 171].

Solar cells made of aSiH semiconductors, are used in many applications in the photovoltaic market as commercial solar cells. A conventional layer structure of aSiH thin-film solar cells is as follow (see figure 3.2,a) (bottom-to-top): Ag (200 nm) / AZO (100 nm) / naSiH (22.4 nm) / iaSiH (350.5 nm) / paSiH (17.5 nm) / (ITO 70 nm) [172, 173, 174]. Each layer in this device is necessary for the device to operate properly. For example, n, and paSiH are buffer layers that build the junction potential barrier to separate the photo-generated charge carrier, and route them toward the contacts. AZO is placed between the metallic back contact and the semiconductor layer to prevent the metal atoms from diffusing in the semiconductor. This is important because the diffusion of the metal atoms would change the doping level in the semiconductor layers and create trapping sites for the photo-generated charge carriers, reducing the collected J_{SC}. ITO serves as an electrical contact for charge carrier collection and transparent for allowing light transmission to the active layer of the cell. The active layer is iaSiH layer at which the absorbed photons will contribute to the electrical current. The complete optical response of all layers in the device and the total reflectance are presented in figure 3.2,b.

After describing the function of each layer in the cell operation, we evaluate the impact of every layer on the optical response of the cell (see figure 3.3). The back contact is responsible

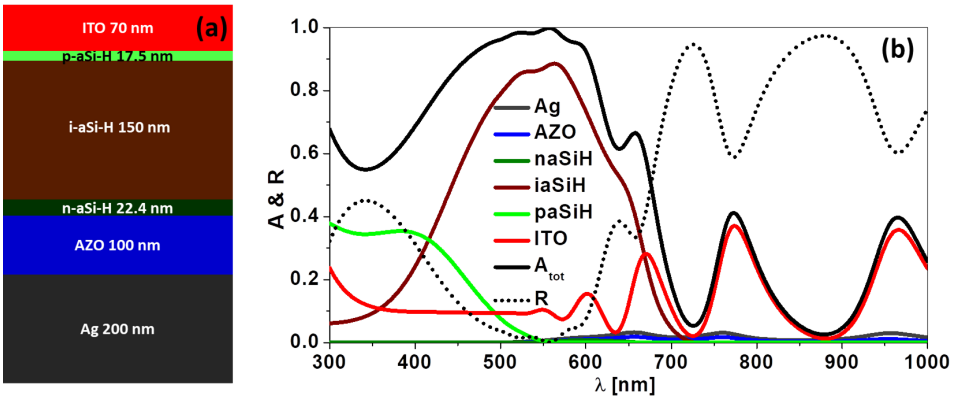

Figure 3.2: (a) Geometrical arrangement of the layers of a reference solar cell (the numbers mean the thickness of each layer). (b) Spectral absorptance of each layer for the reference cell described in (a).

for reflecting back the long wavelengths (they have a low probability to be absorbed in the front layers and can reach the back contact) and increases its absorption probability. Besides the function of ITO as an electrical top contact for the device, it works as a transparent window for the device illumination, and also as an ARC. In fact, once we add the ITO layer, the absorption of the iaSiH layer enhances, due to the functionality of ITO as ARC. The paSiH layer accounts for high absorption losses at short-wavelengths, as it is placed on top of the active layer and exposed to the incoming light first (see the bright green line in figure 3.2,b). Finally, the naSiH layer and the AZO layer have a negligible effect on the optical response of the cell, because they are placed below the active layer, and a small amount of light reaches them.

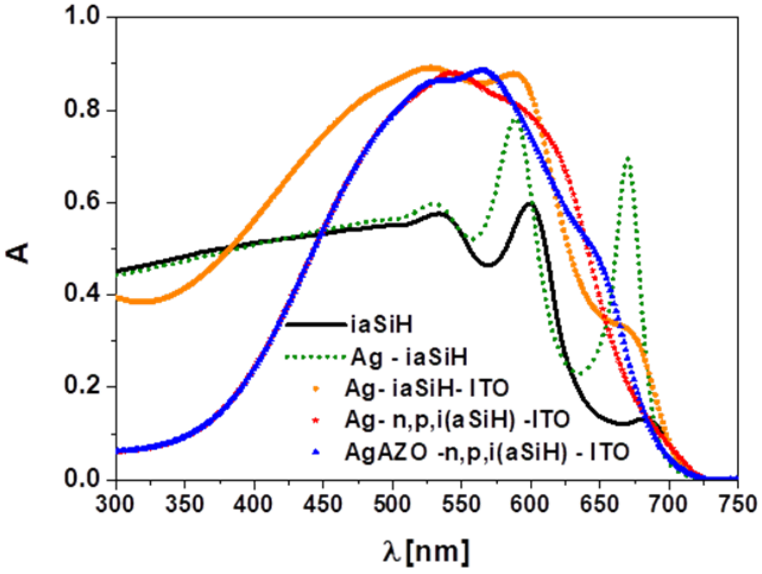

Figure 3.3: Optical response of the device after the successive addition of each layer.

In table 3.1 we present the values of J_{SC}, after the addition of each layer, as in figure 3.3, and how it is affected by each layer. The layer-by-layer calculation of the planar device is made only as a demonstration of the impact of each layer on the optical response of the device. However, a real practical device can't work properly without all of these layers. As we have

Table 3.1: Effect of each layer in the planar device on the J_{SC} of the device.

Structure	J_{SC} [mA/cm^2]
iaSiH/glassg	8.59
iaSiH/Ag/glass	10
ITO/iaSiH/Ag/glass	13.3
ITO/paSiH/iaSiH/naSiH/Ag/glass	11.7
ITO/paSiH/iaSiH/naSiH/AZO/Ag/glass	11.67

already seen, increasing the absorption in the active layer enhances J_{SC}, and the enhancement in the absorption of the buffer layers, partially mitigates the SWE defects, so we always will consider every layer in the solar cell structure, instead of taking the active layer only into account. Actually, we can't ignore the buffer layers as they have a non-negligible optical effect and a significant part of the enhancement of any proposed design will be lost in these layers.

3.1.2 Optimization of a planar ARC

Our goal is to maximize the absorption of the active layer, and reduce the reflectance. As the absorption of the iaSiH active layer extends from 300 nm to 800 nm (we will call this range λ_A, which refers to the wavelength interval of active absorption), the optimization will be limited to this range. Finally, after optimization, we will calculate the whole response of the device in the range from 300 to 1000 nm (we will call this range λ_T , which refers to the wavelength interval that includes active and parasitic absorptions) to account for the total heat losses too.

We see in subsection 3.1.1, how ITO layer works as an ARC. To further explore this functionality of the ITO layer, we calculate the J_{SC} and the weighted reflection (weighted to the standard solar irradiance, AM1.5g) losses of the device for different ITO thicknesses. The simplified weighted reflection losses R_{w,λ_A} can be calculated from the following equation [175]:

$$R_{w,\lambda_A} = \frac{\int_\lambda \Phi_{\mathrm{AM1.5g}}(\lambda) R(\lambda) d\lambda}{\int_\lambda \Phi_{\mathrm{AM1.5g}}(\lambda) d\lambda}, \tag{3.1}$$

where R_λ is the spectral reflectance and $\Phi_{\mathrm{AM1.5g}}(\lambda)$ is the solar spectral irradiance.

An efficient ITO layer (in terms of electrical conductivity and transparency) has a thickness around 70 nm [176]. The J_{SC} and the $R_{w,\lambda 1_A}$ of the device using this thickness is 11.7 mA/cm^2 and 3.39% respectively. However, this thickness is not the optimum for the ITO as an ARC. In figure 3.4,a an ITO layer of 50 nm thickness gives a J_{SC} and R_{w,λ_A} of 12.1 mA/cm^2 and 3.17% respectively. The direct deposition of very thin ITO leads to poor conductive thin-films. Another approach is to deposit a thick ITO layer and use chemical etching to reduce its thickness [176]. In this approach, an ITO layer with a reliable optical and electrical properties can have a small thickness down to 35-40 nm. Although it is possible to fabricate a functional ITO layer with the optimized ARC thickness, the enhancement is not enough to compensate the extra fabrication steps in the device.

Another proposal is to use an additional planar dielectric layer on top of the cell to form with ITO a two layers ARC. We first assume a dielectric material with negligible losses (*i. e.* the refractive index is real). This assumption is applicable for many dielectric materials such

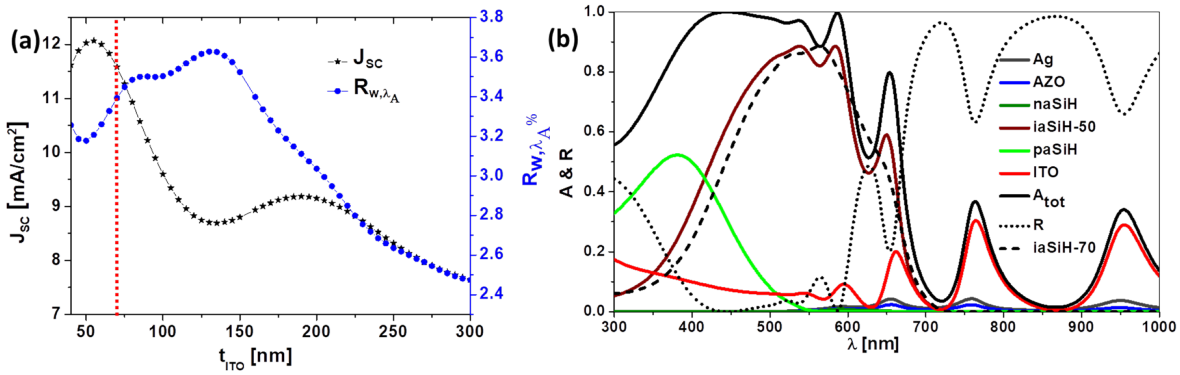

Figure 3.4: (a) Effect of the ITO thickness on the J_{SC}, and the reflectance (over the wavelength range λ= 300-800 nm) of the cell. The red vertical line define the values for the cell with ITO layer of 70 nm. (b) The optical response of all cell layers for the optimum ITO thickness selected from (a) as 50 nm which combines the highest J_{SC} and a low reflectance

as SiO_2 , magnesium fluoride (MgF_2), Si_3N_4 ,etc). A two variable optimization of the short circuit current of the cell in terms of the parameters of this layer, that includes the refractive index and thickness is presented in figure 3.5,a and the corresponding R_{w,λ_A} is in figure 3.5,b. In these two figures we can see that a planar dielectric ARC on the top of ITO, can provide minimum reflectivity and a J_{SC} comparable to that of the planar device ($J_{SC} = 11.67$ mA/cm^2) for materials with refractive index below 1.3. So, this design doesn't provide any enhancement compared to the optimized planar device with single ARC from ITO.

However, if we reduce the thickness of the ITO layer to only 40 nm, which is the minimum fabricable reliable layer [176], some materials with refractive index between 1.3- 2.0, and thickness below 50 nm can give a J_{SC} and R_{w,λ_A} of 12.66 mA/cm^2 and 2.9%, respectively. The results of this design are presented in figure 3.5,c,d. The optimum refractive index and thickness of the ARC that give the highest J_{SC} enhancement (see the area highlighted with dotted black ellipse in figure 3.5,c) does not exactly coincide with those which give the minimum reflectance (see the area highlighted with dotted black ellipse in figure 3.5,d). This is because the enhancement in J_{SC} comes mainly from a reduction in the absorption in the ITO layer itself and slightly from the reduction of reflectance. The main difference between the single ITO 50 nm thick ARC and the double ITO/dielectric ARC is that the double ARC can redirect the light energy gained from the ITO thickness reduction to the active layer of the cell, and therefore it produces a larger J_{SC} value.

If we take two materials in the optimized range of figure 3.5,c,d ($t_{\mathrm{ARC}} < 50$ nm , n_{ARC} 1.3- 2.0) namely MgF_2 ($t_{\mathrm{ARC}} = 40$ nm, $n_{\mathrm{ARC}} \approx 1.37$ at $\lambda = 500$ nm), and Si_3N_4 ($t_{\mathrm{ARC}} = 20$ nm, $n_{\mathrm{ARC}} \approx 2.063$ at $\lambda = 500$ nm), we obtain an enhanced optical response of the device in terms of both J_{SC} increase and reflectance decrease. The results for these two optimum cases are presented in figure 3.6,a,b. The J_{SC} and R_{w,λ_A} are 12.549 mA/cm^2 and 3.0% for MgF_2 , and 12.62 mA/cm^2 and 3.27% for Si_3N_4. Although R_{w,λ_A} for the optimized ITO 40 nm/Si_3N_4 double ARC is larger than that of ITO 40 nm/MgF_2, the first produces a better J_{SC} value. This is because more light is absorbed in the p layer for the MgF_2 case instead of being directed to the active layer. As a conclusion from figure 3.5,c,d, a planar double layer ARC made of ITO/dielectric material could achieve an average enhancement in the J_{SC} of about 7.7% and an average reduction in the reflectance of 11.5% in the range of λ= 300-800 nm.

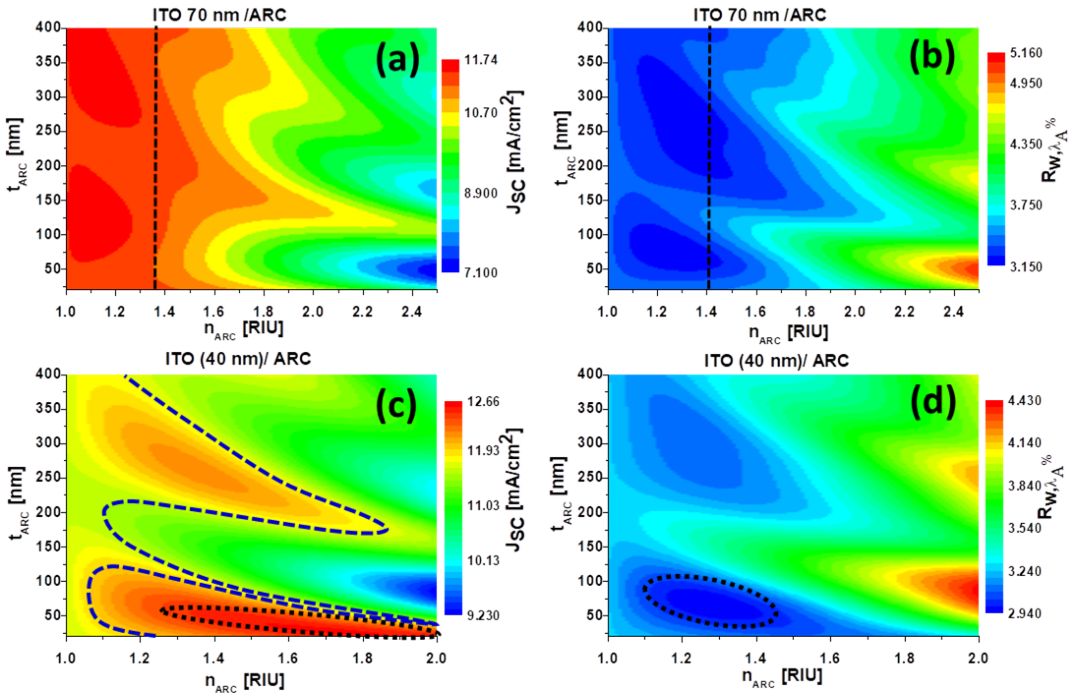

Figure 3.5: (a), (b) Optimization of a dielectric ARC layer on top of the 70 nm ITO layer as a function of the refractive index and the thickness of this layer. The values on the left of the vertical black dashed lines in (a), and (b) are those that give a performance comparable with the planar device with single ARC made of ITO, where the values on the right provides a lower performance. (c), (d) Optimization of a dielectric ARC layer on the top of a 40 nm ITO layer. The areas marked with dotted black ellipses in (c), (d), show the locations where the device of 40 nm ITO layer performs better than the planar device of ITO 70 nm layer. The dotted blue curve in (c) defines the refractive indices and thicknesses of the planar dielectric ARC layer, that gives the same values of the planar device with an ITO 70 nm layer.

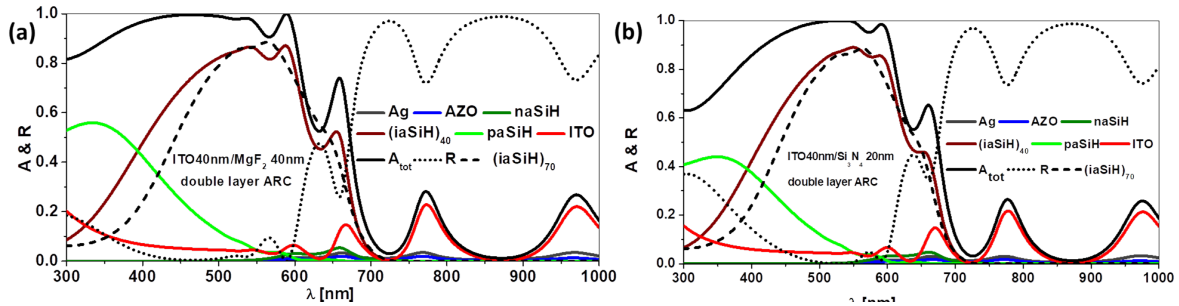

Figure 3.6: The optical response of the optimized: (a) ITO 40 nm/MgF_2 40 nm double ARC. (b) ITO 40 nm/Si_3N_4 20 nm double ARC

3.1.3 Dielectric nanostructures for iaSiH cells

The next proposal is a nanostructured 1D grating with different profile shape (rectangular, trapezoidal, and triangular) placed on top of the planar device [177]. A schematic diagram of the proposed design is shown in figure 3.7,a. The proposed nanostructures, when properly arranged and deposited on top of the ITO layer, increase the J_{SC}. The unit cell of the model has a fixed arbitrary period of 1000 nm (for simple optimization and fabrication feasibility).

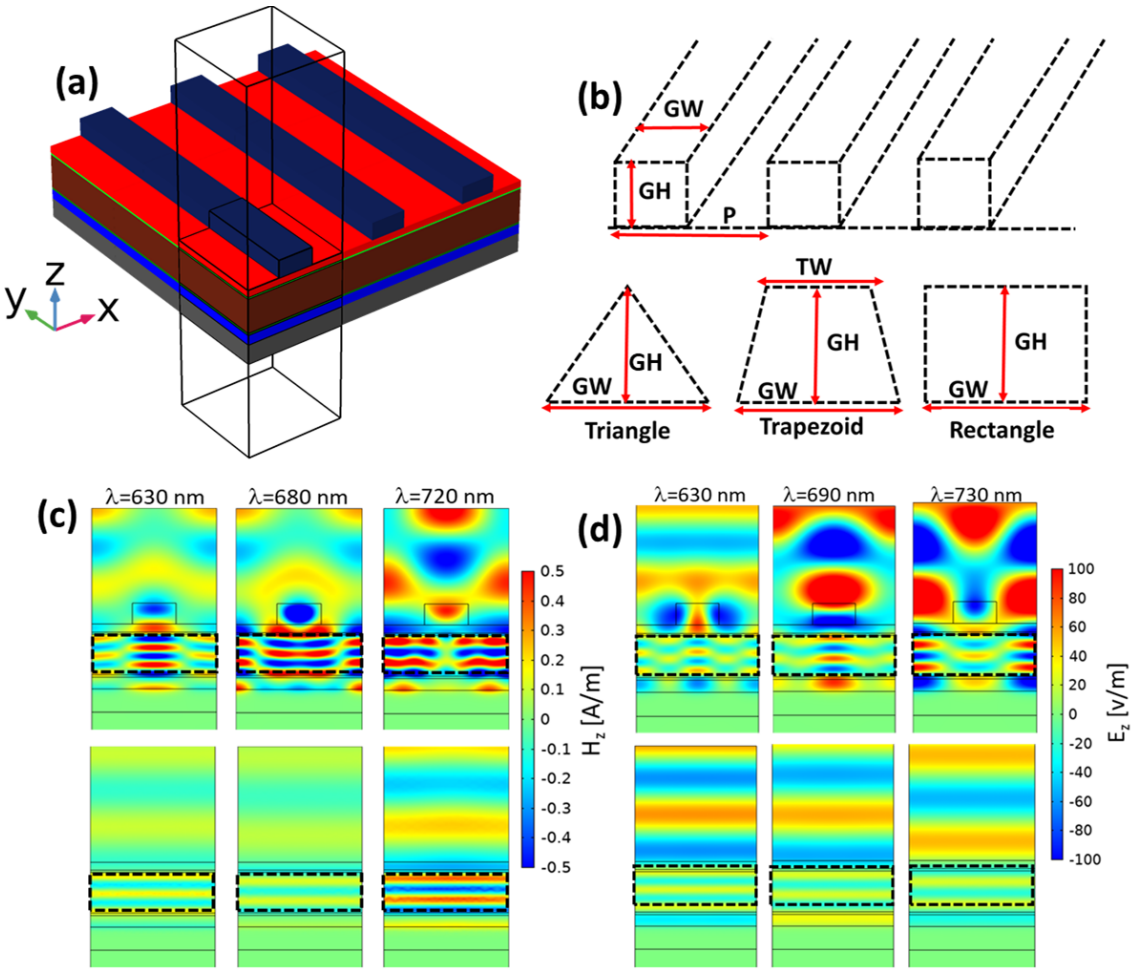

Figure 3.7: (a) 3D diagram for the patterned cell showing the modeled unit cell selection. (b) The geometrical parameterization with different 2D profiles of the nanostructure. (c),(d) Maps of the electric (TE polarization) and magnetic (TM polarization) field distributions for a selected wavelengths of the nanostructure (top maps) and the corresponding planar device (bottom maps).

The grating parameters are its height (GH) and width (GW), with an additional parameter for the trapezoidal case, that have a fixed top width (TW) of $GW/2$. This TW, is zero for triangular geometry. We aim to maximize J_{SC} by selecting GH and GW for the three profiles. When evaluating the electromagnetic behavior of the device with the rectangular grating structure, we find that, at some wavelengths, the electric and magnetic fields are highly concentrated inside the active layer(see figure 3.7,c,d). Similar effects occur for other shapes too. The light confinement at specific wavelengths is a result of diffraction and resonances of the subwavelength grating structures [178].

3.1.4 Optimization of the nano-grating ARC

The optimization of the proposed nanostructured ARC layer is made by maximizing the short-circuit current, J_{SC}, when varying the geometrical parameters of the grating GW and GH. The dielectric grating and the surrounding medium (air in our case) forms an effective medium, that behaves like a planar slab with effective refractive index [179]. The effective refractive index index of the grating is polarization dependent, and is calculated according to

the homogenization method [180]. For a dielectric grating with refractive index n_g, surrounded by a medium of refractive index n_s, and the grating has a geometrical parameters, height (GH), width (GW), and period (P), the grating material has a fraction f of the total volume containing the grating and the surrounding medium. Then, the zero order approximation to effective refractive index is given for TE and TM polarizations as:

$$n_{\mathrm{TE},0} = \sqrt{n_s^2(1-f) + n_g^2 f}, \tag{3.2}$$

$$n_{\mathrm{TM},0} = \frac{n_s n_g}{\sqrt{n_s^2 f + n_g^2(1-f)}}. \tag{3.3}$$

In our design, the dielectric grating forms a medium with effective refractive index on the top of ITO that produces better coupling of the incoming light waves in the cell [181, 182, 183]. Figure 3.8,a,c,e shows the value of J_{SC} in terms of GW and GH, for the nanostructured ARC design with rectangular, trapezoidal, and triangular profiles respectively. We may check that a maximum value of J_{SC}=12.77 mA/cm^2 is obtained when $GW = 850$ nm and $GH = 260$ nm. This value is about 9.15% larger than the reported value of 11.7 mA/cm^2 corresponding to the planar reference aSiH cell. The J_{SC} enhancement of all profiles is almost the same, being the triangular shape a little better than the other shapes. We have to notice that the main reason for the J_{SC} enhancement is the reduction in the reflectance, as we didn't reduce the thickness of any absorbing layer in the cell for the nanostructured case.

The R_{w,λ_A} deceases to 1.95%, 1.9%, and 1.7% for the rectangular, trapezoidal, and triangular gratings, respectively, which is more than 40% for all grating shapes. This improvement translates to an average enhancement of 9% in the J_{SC}, besides the enhancement in other layers of the cell. The single and double planar ARC optimization requires a reduction in the ITO layer thickness which may compromise its capability to work as a front contact. Moreover, the small thickness ITO needs complex ultra-thin fabrication techniques [176, 184] or a chemical etching process in hard solvents which may affect the other cell layers. In contrast, the simple nanostructured ARC can be fabricated on a large area using nano-imprint technology, or a soft etching of a predefined pattern on an operational thin-film device. Another important advantage is the wide range of geometrical parameters available for the fabrication, instead of being limited to a very thin layer of the planar optimized ARC. J_{SC} reaches a maximum value for several combinations of the geometric parameters. The optimization was made using the average of TE and TM polarization to represent the unpolarized nature of sunlight. In the optimization maps in figure 3.8,a,c,e we can also notice that the location of optimum geometrical parameters for each profiles, moves to larger height and width when changing from the rectangular to trapezoidal, then to triangular. The reason for that is the effective index required for a good coupling of the incoming light to the cell depends on the volume fraction of the grating. The effective refractive index for gratings with the same height and width decreases when moving from rectangular profile to trapezoidal and triangular profiles. This is because the rectangular profile covers a larger area than other shapes. If the volume fraction of the rectangular grating that achieves the required effective index has values GW and GH, then other profiles will need larger values of GW and GH to achieve the same optimum effective refractive index.

In the optimization of the geometrical parameters of the grating, we choose Si_3N_4 as a material for the grating itself. However, for more fabrication feasibility and compatibility, we checked if other materials can replace Si_3N_4 without compromising the ARC performance.

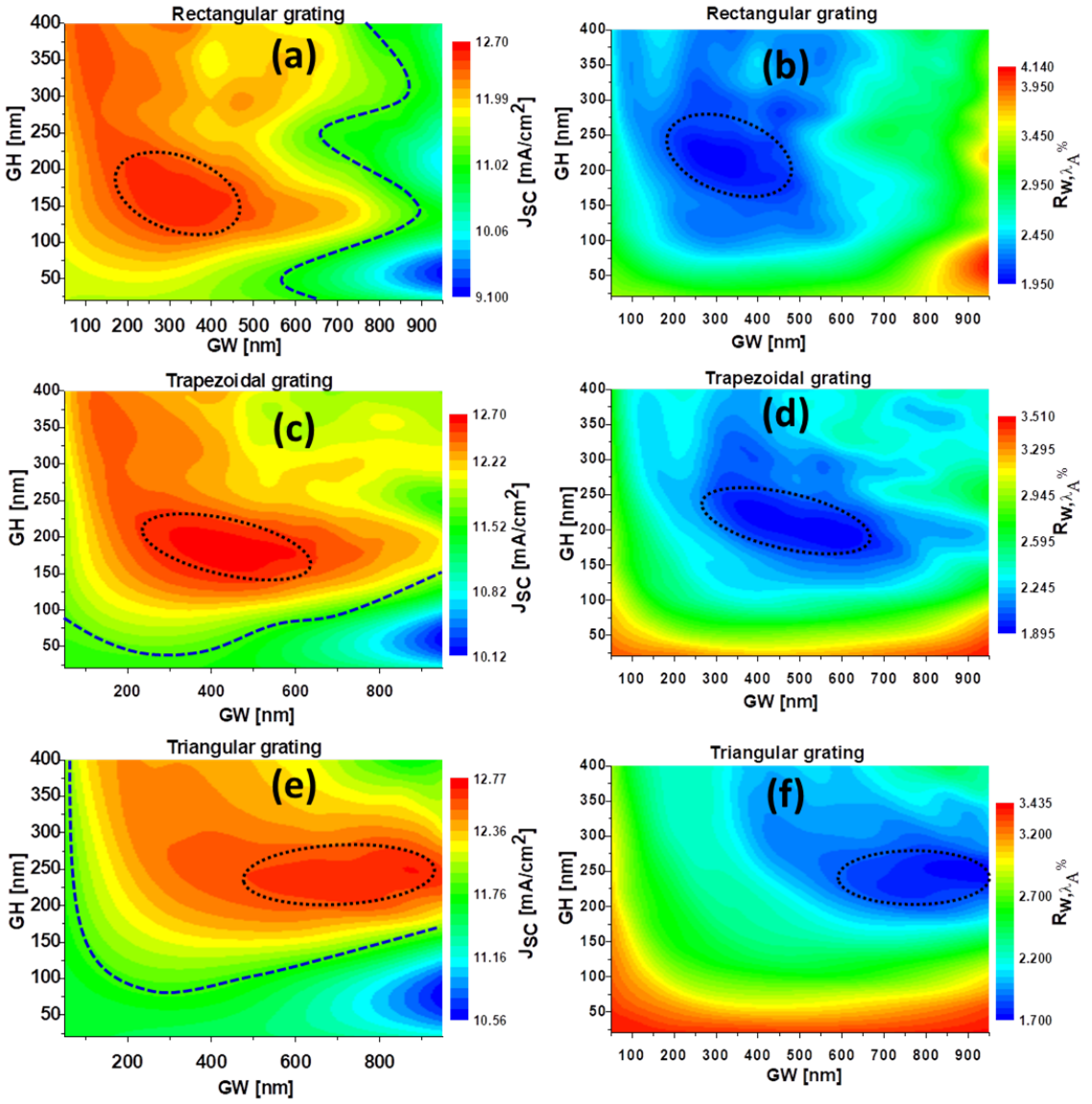

Figure 3.8: Maps of the value of J_{SC} as a function of the geometric parameters GW and GH, of the grating with (a) rectangular profile, (c) trapezoidal profile, and (e) triangular profile. The corresponding maps of the weighted reflectance for each case are presented in (b),(d), and (f) respectively. The blue dashed line in the J_{SC} maps define the GW and GH that gives the same values of the planar device without the nano-grating ARC. While the black dotted circles defines the GW and GH values that give the highest J_{SC} and the minimum reflectance.

This step provides the manufacturer with the possible materials set that could be used for the nanostructured ARC.

To do that, we assume first a lossless dielectric material with real refractive index, and scan for the changes in the J_{SC} when changing the refractive index, and GH, of the grating. Through this second optimization, we will use the findings of the first step optimization, we choose the triangular profile because of its better response than the two others. The GW and GH determine the amount of material necessary to achieve an effective refractive index for the best coupling of the incoming light into the cell layers. Then, for simplicity of the optimization,

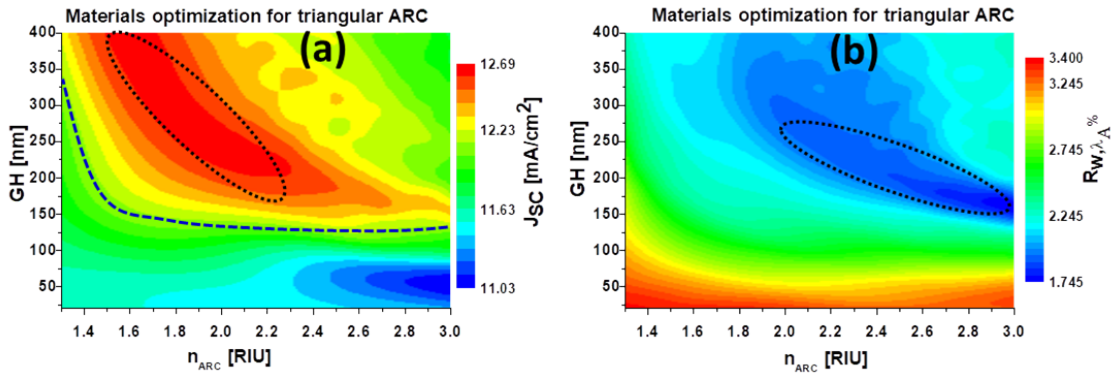

Figure 3.9: (a) Map of the value of J_{SC} as a function of the geometric parameters n_{ARC}, and GH, of the triangular grating. (b) Map of the weighted reflectance. The blue dashed line in the J_{SC} maps define the n_{ARC} and GH that gives the same values of the planar device without the nano-grating ARC. While the black dotted circles defines the n_{ARC}, and GH values that give the highest J_{SC} and the minimum reflectance.

we choose only one of them, so, we fix the width and the period at $GW = 500$ nm and 1000 nm, respectively, and change only GH, and the refractive index of the nanostructured ARC. The optimization map in figure 3.9, shows that a wide range of dielectric materials can be used for the nanostructured ARC, with refractive index in the range ($n_{\mathrm{ARC}} = 1.3$ to 2.4), while maintaining a J_{SC} enhancement. As example we can use MgF_2 ($n_{\mathrm{ARC}} = 1.3798$ at $\lambda = 500$nm) [185], silicon dioxide (SiO_2, $n_{\mathrm{ARC}} = 1.4623$ at $\lambda = 500$nm) [186] , Poly-methyl methacrylate (PMMA, $n_{\mathrm{ARC}} = 1.4973$ at $\lambda = 500$nm) [187], or Si_3N_4 ($n_{\mathrm{ARC}} = 2.0634$ at $\lambda = 500$nm) [188].

3.1.5 Response of the optimized nanostructure

The resonances in figure 3.7,c,d also appear as peaks in the spectral absorption (see figure 3.10). In this figure, we keep using Si_3N_4 as the grating material and calculate the response for each design. The selected optimized geometrical parameters GW and GH are 350 nm, and 150 nm for the rectangular profile, 450 nm, and 180 nm for the trapezoidal profile, and 700 nm, and 240 nm for the triangular profile. Although we did this selection to plot the response of the optimized nanostructured ARC, several combinations of geometrical parameters can be made within the highlighted zones in figure 3.8,a,c,e. Therefore, more light is arriving at the active iaSiH layer when using a nanostructured ARC. This is proved by evaluating only the absorption at the iaSiH layer spectrally. In figure 3.10,a, we can see how the improvement appears at every wavelength for the iaSiH layer, while figure 3.10,b,c shows a large reduction in the reflectance of the device that translates to absorption in all layers of the cell. The device works as a perfect broadband absorber through the whole absorption band of the cell when using the triangular grating ARC for example. Figure 3.10,b indicates that the origin of the enhancement of the absorption is due to the reduction of the reflectance. The total spectral reflectance and absorption of the reference cell, and the optimum nanostructured ARC cell, are shown in figure 3.10,b,c. From these figures, we can see how a nanostructured ARC increases the absorbed power in the active layer and the auxiliary layers together by reducing reflectivity. At this point, we should remember that increasing absorption in the auxiliary layers helps to heat the cell, and this thermal dissipation improves the repairing effect of those damages caused by SWE [100].

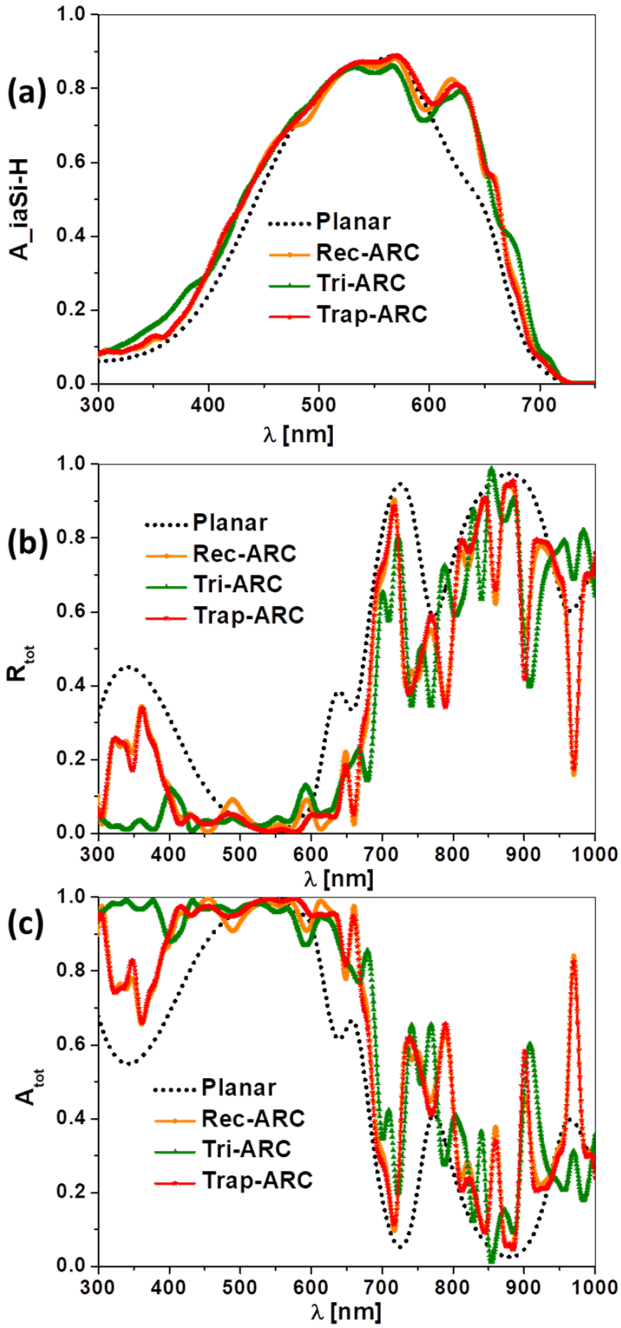

Figure 3.10: (a) Spectral absorptance at the iaSiH layer for the planar and nanostructured devices with different grating profiles. (b) and (c) are the corresponding total reflectance and total absorption, respectively.

3.1.6 Power budget analysis

To better understand where the active and losses happen, we calculate the absorption of each layer as a percentage of the incident solar irradiance along with R_{w,λ_T} for each case. The range between 300 nm and 800 nm (λ_A) describes the spectral region where the photovoltaic conversion occurs. The extended range between 300 nm and 1000 nm (λ_T) includes the NIR, where absorbed light is converted mainly to heat. Also in the λ_T region, reflectivity is lower

for the nanostructured case, meaning larger absorption that repairs SWE damage. This could help us to improve future designs by properly direct the confined light to the active layer of the cell. From figure 3.11,a we can see that the total absorption losses in buffer layers and contacts increases from below 25% for the planar device, to more than 35% for the devices with nanostructured ARC. This is more than a 42% increase in the absorption losses, which means that we need to refine the design to properly direct this energy to the active layer of the cell. From the same figure, we can also see that the total absorption losses for the device with an optimized single (ITO50) and double layer (ITO40/dielectric) is lower than for the planar device (ITO50 means an ITO layer having a thickness of 50 nm). This confirms that the origin of the J_{SC} enhancement for this planar ARC designs comes from the reduction of both absorption losses in buffer layers, and a slight contribution due to the reduction in the reflectance for the planar ARC designs. Figure 3.11,b shows how more absorption in the active layer is obtained when using optimized planar and nanostructured ARC. The triangular grating can provide about 12% enhancement in the absorption of the active layer. Finally, figure 3.11,c summarizes the total reflectance and absorption of each design. The total reflectance of the planar device in the range (λ_T) is about 49% and 51% for the total absorption. Most of this reflection happens beyond the absorption band of the active layer and only 3.39% are in the range (λ_A). However, the largest intensity of the solar irradiance lies in the VIS band, so, any variation in reflectance is very important if the light is properly collected in the active layer. A slight decrease in the total reflectance happens for the optimized ITO layer with 50 nm thickness and ITO40/ MgF_2 double layer planar ARC, being the values 48.7% and 47.2% for both cases, respectively. The ITO40/ Si_3N_4 double planar ARC shows a small decrease in the reflectance in the range (λ_A), but the total reflectance of this design for the whole range (λ_T) is even higher than the reflectance of the planar device. Finally, the total reflectance of the devices with the nanostructured ARC decreases significantly for all profiles reaching 35.24%, 35.32%, and 33.7% for the rectangular, trapezoidal, and triangular profiles, respectively. This

Table 3.2: Total Reflectivity for the proposed designs in two spectral ranges. The number in parenthesis corresponds to the relative change (as a percentage) with respect to the reference cell.

Structure	R_{w,λ_A} %	R_{w,λ_T} %
planar ITO 70 nm	3.39	49
lanar ITO 50 nm	3.17 (- 6.5)	48.7 (-0.6)
MgF2-ITO	2.9 (- 14.5)	47.2 (-3.7)
Si3N4-ITO	3.3 (- 2.6)	49.8 (+1.6)
Nano-rectangular	1.95 (-42.51)	35.2 (-28.16)
Nano-trapezoidal	1.89 (-44.2)	35.32 (-27.9)
Nano-triangular	1.7 (-49.9)	33.7 (-31.22)

means that we have a total reduction in the reflectivity of the device of about 31.2% for the triangular structure in the range (λ_T). As an additional remark to emphasize the goodness of the proposed nanostructured designs, we show in table 3.2 the reflectivity values for the optimum designs obtained previously.

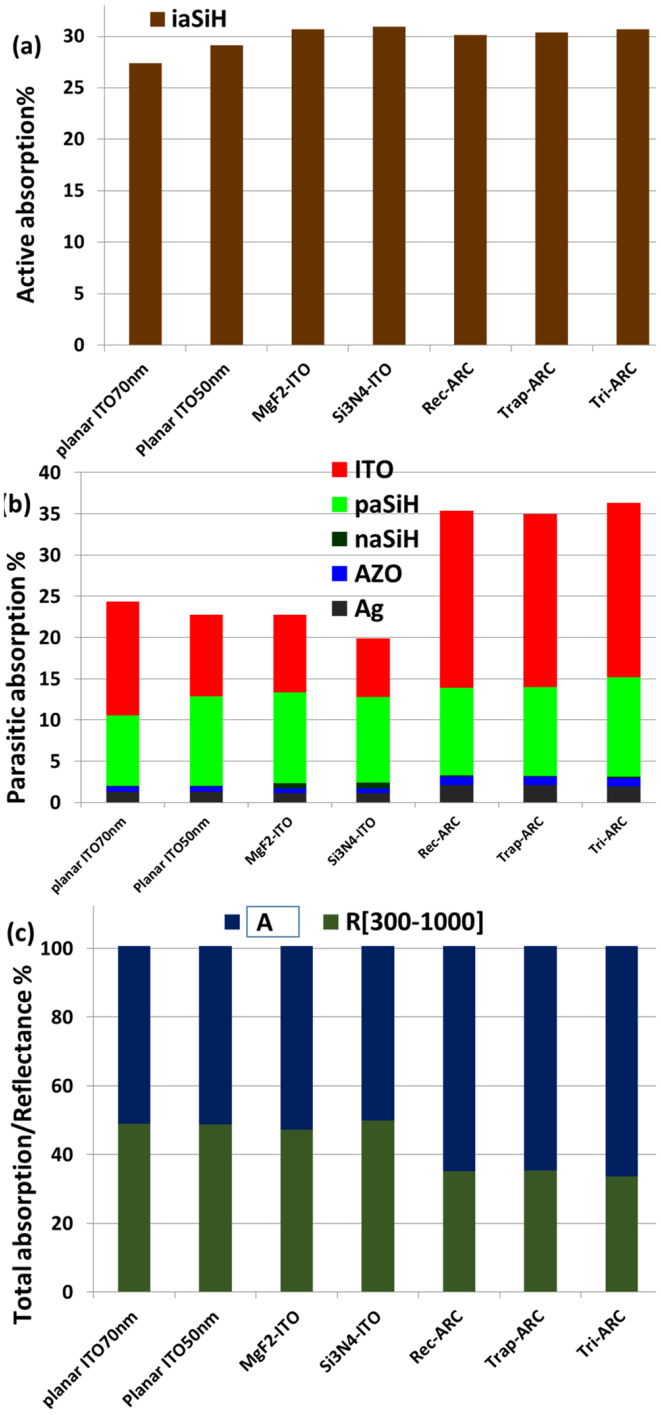

Figure 3.11: (a) Active absorption in the iaSiH layer. (b) Parasitic absorption in buffer layers and contacts. (c) Total reflectance and absorption in the range of λ_T.

3.2 Funneling and guiding effects in aSiH thin-film solar cell

As we discussed in section 3, the thickness of the active layer of the solar cell is very important from the optical and electrical points of view. Each cell type has an optimum thickness that gives the best absorption and an efficient photogenerated carrier extraction.

Larger thickness means better absorption until all the photons with different energy in the entire absorption band of the active layer have a chance to be absorbed. However, large thickness means a long distance for the charge carriers to travel before being collected at the corresponding electrodes. So, a trade-off between both mechanisms gives the optimum thickness that makes the cell perform efficiently. One of the strategies to optimize solar cell design is to reduce the thickness as much as possible and use nanophotonic structures to concentrate the light in the active layer. This advanced concentration strategy is based on a nanostructure design with a broadband response, suitable for solar cells with its broadband absorption spectrum. Here, we use the same planar aSiH as in the previous model, reducing the thickness of the active layer by more than 57% until 150 nm. The next step is to apply a nanophotonic design that is able to enhance the absorption in this active layer over broadband, and make this ultra-thin layer absorbs better than a planar cell with conventional thickness.

3.2.1 Design of advanced light concentration strategies for ultra-thin solar cell application

We start our model by simulating the optical response of the planar device with an active layer of 350 nm thickness and compare it with the same cell when the thickness is reduced to only 150 nm. From an electrical point of view, reducing the thickness of the active layer means a shorter distance for the photo-generated charge carriers to move until collected through the corresponding electrodes. As a particular case for aSiH thin-film solar cells, small thickness means a lower number of SWE defect states [189]. The experimental optical constants of the n,i and p aSiH layers were from [101], the optical constants for each layer in the cell presented in figure3.12,a is the same like in Vora. et *al.*, [101]. The reference planar is arranged from bottom to top as follow : Ag 200 nm / AZO 100nm / naSi- 22.5 nm / iaSi- (150 or 350) nm / paSi- 17.5 nm / ITO 70 nm, where the numbers represent the thickness of each layer. The results are presented in figure 3.12,b, and the obtained short-circuit current is $J_{SC} = 11.7$ mA/cm^2, which is the same result given by Vora *et al.* [101].

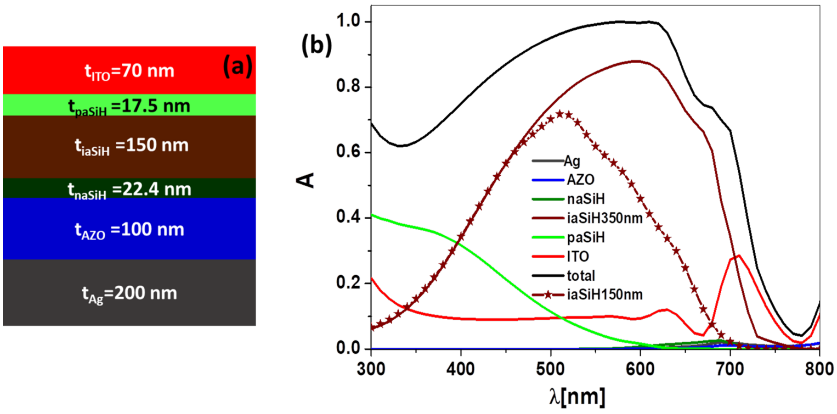

Figure 3.12: (a) Schematic diagram of the reference planar cell arrangement and thicknesses. (b) Spectral absorptance of each individual layer in the cell when the active layer thickness is 350 nm, the absorption of 150 nm iaSiH active layer is added as a line with stars.

The absorbed power at each layer depends on its optical constants and thicknesses. The absorption band for each layer is also limited by its bandgap [169, 190, 191, 192]. Besides, the absolute amount of absorbed light at a given layer depends on the amount of light that is actually reaching it. So, front layers usually account for more absorption than deep bottom

layers. These reasons explain the different contributions to the absorbed power within the cell structure. In the case of 150 nm iaSiH layer shown in figure 3.12,b as a starred symbol line, the cell accounts for only $J_{SC} = 8.98$ mA/cm^2. This expected low value is due to the reduction of the thickness of the active layer and hence, its absorption. The optical losses due to the reduction in the thickness of the active layer is distributed as more parasitic absorption in all other layers and also leads to more total reflection of the device.

3.2.2 1D nanostructured profile for aSiH cells

Texturing the geometry of the front or back contacts at the nanoscale has been proposed to enhance the trapping of light inside the active layer of the cell [14, 15, 16, 17, 18, 19, 20]. This approach requires the combination of an optimum geometry, and an appropriate material choice compatible with the cell structure, maintaining a good optical and electric behavior. Our design is a 1D high aspect ratio grating with different profiles [193]. This is used as a template for the cell deposition. The goal for this design is to reroute the light by the grating structure and increase its path length within the active layer, allowing a higher probability to be absorbed. Also, this design increases the total area of the active layer exposed to light without increasing its thickness. Our first choice of material to generate such scaffolding for the structure has been Si_3N_4. Although this dielectric material is widely used as an ARC material, here we use it to create a textured surface on the back contact of the structure. Once this nanostructure is built, it can act as a pattern to grow on it the multilayer cell arrangement conformally. Several shapes may results from the conformal deposition over a high aspect ratio grating [194, 195]. Perfect trapezoidal layers [196], and cylindrical shaped [197] were fabricated using an atomic layer deposition method. The profile that results from the conformal deposition of thin-films over a stepped grating structure is a layer with a shape close to the textured template with different coverage thicknesses on top, side, and bottom of the grating [198], that can be controlled using the fabrication parameters. We can take advantage of this natural behavior to check if it works better for multi-layer devices, like solar cells. In this case, we modeled different profiles and final shapes of the conformally deposited layers: the triangular grating with small side coverage for cell layers, round top grating with perfect cylindrical layers of the cell, and finally a trapezoidal profile with conformal layers with the same shape. The drawing in figure 3.13,a shows different locations of the grating which will be differently or homogeneously coated through the conformal deposition process, depending on the deposition technique [194, 195]. A schematic 2D of the nanostructured cell for each case is represented in figure 3.13,b,c,d. The grating profile in figure 3.13,b,c has a triangular shape with width GW, and height GH, after the deposition of all layers over the grating profile, the whole shape will be separated from each other by the geometrical parameter S, as shown in figure 3.13,b. The grating profile in figure 3.13,d is with a trapezoidal shape, which has a base width of BW, and a top width TW, which is fixed at 100 nm for simplicity. The S has the same definition for the trapezoidal shape in figure 3.13,d. Each grating period P of the three unit cells includes the grating and all the layers deposited from both sides and the separation distance S, so $P = GW + 2 * (t_{ITO} + t_{paSiH} + t_{iaSiH} + t_{naSiH} + t_{AZO}) + S$. The whole device final shape in 3D is represented in figure 3.13,e where we highlighted the unit cell in blue. This design enhances the absorption efficiency of the device by better coupling the incoming light into the cell through funneling and guiding mechanisms. As a result, the total reflectance of the cell will be reduced. To show better this guiding effects, we evaluate the electromagnetic quantities of interest. Figure 3.13,f,g shows the transverse Z component of the electric field for two cases of interest at $\lambda = 630$ nm, having two angles of incidence $\theta = 0°$, and $\theta = 50°$. Actually, when evaluating the radiation at the bottom of the structure, we may see that energy

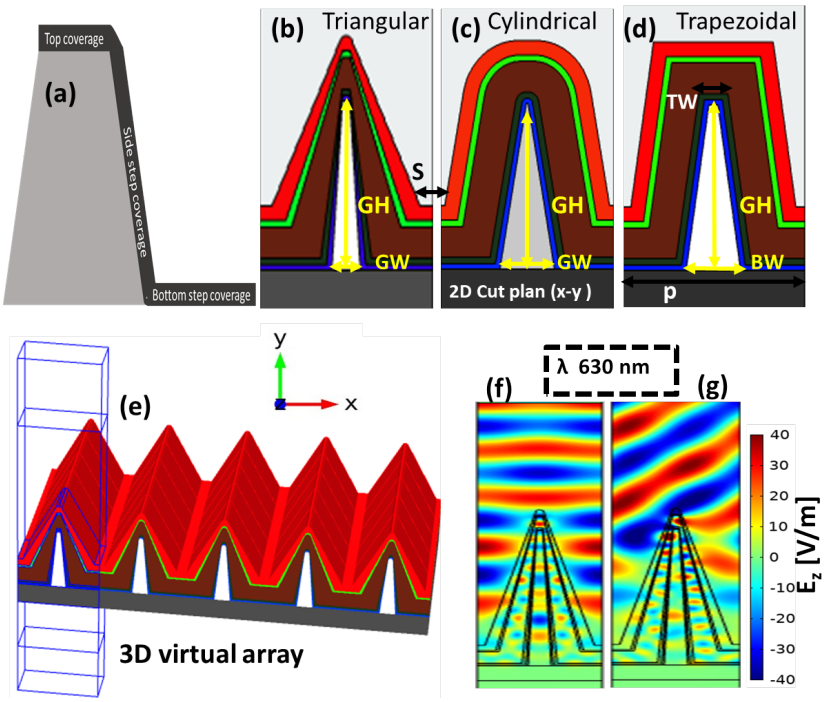

Figure 3.13: (a) A schematic diagram shows the different locations that will be filled through the conformal deposition process. (b), and (c) A 2D unit cells cross section over the $X-Y$ plane for the nanostructured cell deposited on a triangular profile non-homogeneously and homogeneously, respectively. (d) A 2D unit cell cross section over the $X-Y$ plane for the nanostructured cell deposited on a trapezoidal profile. (e) 3D representation of the proposed structure showing the unit cell used in the numerical calculation. (f) Map of the transverse electric field for normal incidence conditions at $\lambda = 630$ nm. (g) Map for the electric field distribution for a plane wave inciding at a angle of 50° for $\lambda = 630$ nm. Reproduced from our article [193] with permission of SPIE.

is trapped within it, increasing the optical power density at the intrinsic layer. Figure 3.13,g shows the electric field distribution for oblique incidence, $\theta = 50°$ at $\lambda = 630$ nm. In this case, we can check how the wave propagates through the structure for a non-normal incident case, particularly at the iaSiH layer.

When considering the spectral absorption of the structure, the unit cell will be illuminated with an irradiance distribution of the solar spectrum given by the spectral irradiance function, $\Phi_{\mathrm{AM1.5g}}(\lambda)$ [114]. From figure 3.12,b we can see that the absorption is happening at every layer of the cell, especially at the front layers where the irradiance is higher. The absorption enhancement in the iaSiH layer will mainly contribute to the photo-generated current. However, the parasitic absorption enhancement in other layers will be dissipated as heat, which should reinforce a self-annealing mechanism of the device leading to a reduction of the SWE defects.

3.2.3 Optimization of the pattern geometry

Until here, we have discussed the potential of using the 1D vertically elongated dielectric structure to improve the light trapping and SWE defects repair. Now, we will find out the optimum geometry for each profile through the selection of the geometric parameters and the material choice. The parameter that should be maximized through the optimization process is the absorption efficiency in the active layer, that in turn will improve the J_{SC}. So, simply the

merit function for the optimization is J_{SC}. To ease the first optimization step, we arbitrary fix the grating height at $GH = 600$ nm as a starting value which is selected to be large enough to create a high aspect ratio of the grating. Then the optimization process changes the grating width (GW) and grating separation, S. We select these two parameters for the optimization because the grating is placed at the back of the solar cell, and the separation of the elements of whole structure S (see figure 3.13,a) affects the air gap between these elements.

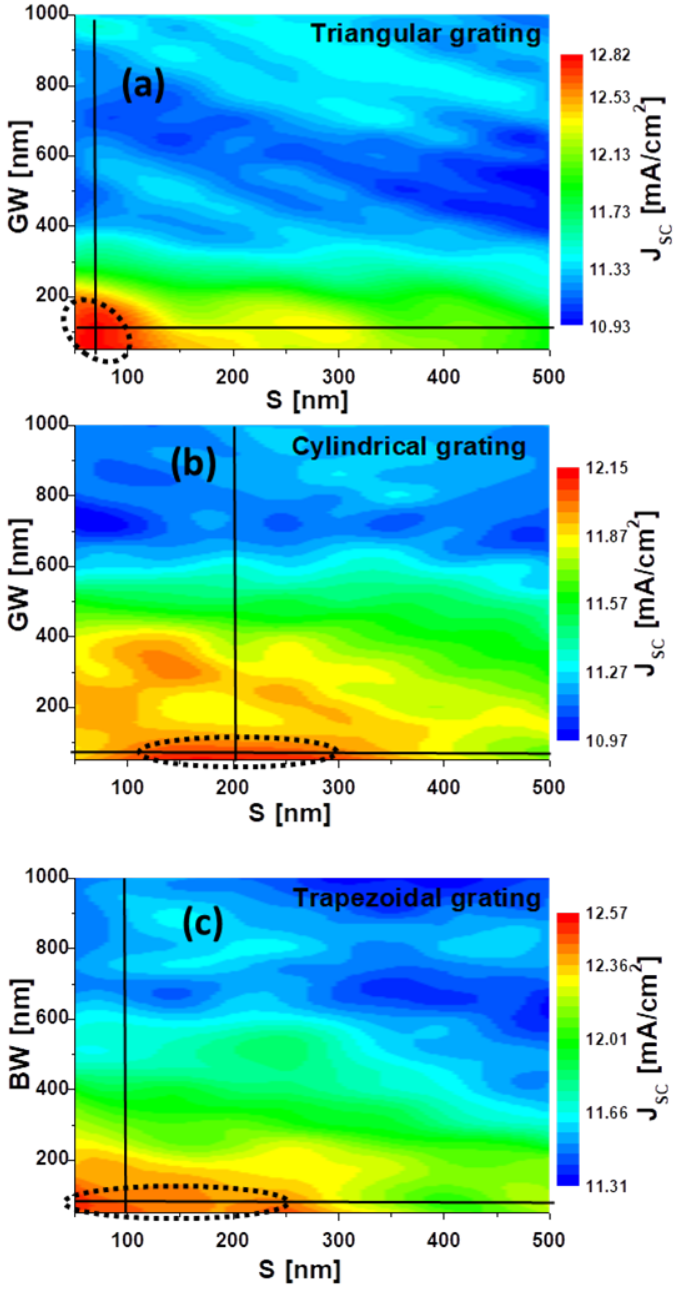

Figure 3.14: J_{SC}, as a function of GW and S for the nanostructured cell with different grating profile shapes (a) triangular, (b) trapezoidal and (c) cylindrical. The crossed black lines defines the selected optimum which lies at the center of the area with the highest J_{SC}, highlighted by the dashed ellipses. Reproduced from our article [193] with permission of SPIE.

In figure 3.14 we have located optimum values of the J_{SC} for the geometrical parameters of each profile with two black lines crossed at the center of the area that produces a high J_{SC}, this area is also highlighted by dashed black ellipses. So, the selected geometry for each profile are, $GW = 100$ nm, $S = 50$ nm for the triangular shape (see figure 3.14,a), $BW = 50$ nm, $S = 100$ nm for the trapezoidal shape (see figure 3.14,b), and $GW = 75$ nm, $S = 200$ nm for the cylindrical shape (see figure 3.14,c). At the same time, there are other combinations of S and GW providing values close to the maximum one, as it has been denoted with the dashed circles in figure 3.14. Then, it should be possible to choose geometric parameters complying better with fabrication constraints. This optimization shows that not only an increase in the exposed surface area is important. Changing the grating geometrical parameters and repetition period can also maximize the J_{SC} of the cell by increasing the absorption efficiency at the active layer. The explanation of this is that the multi-layer structure of the cell supported by the grating generates, along with the surrounding air, an effective index combining all of them. By changing the grating width and separation, we change this effective index and hence, the matching efficiency of the incoming light into the cell. The results for different profile shapes agree well with that obtained for the nanostructured ARC in the previous example in section 3.1.4. In the above optimization step, the height, GH, was fixed at 600 nm to optimize other parameters (GW, and S). Now, the optimization of the height is made by considering the optimized values of GW and S previously obtained for each profile. It is important to check this parameter GH, as it will increase the absorption efficiency by increasing the total exposed area of the active layer to light. To illustrate this fact, we analyze the increase in the exposed area when having a triangular shape. The iaSH layer will have a new length over each period, a horizontal length FL, and vertical length (the two side of the dashed triangular, see figure 3.15,a). Then the total length of iaSiH layer will be:

$$L_{\text{tri}} = FL + 2 \times \sqrt{GH^2 + PW^2}, \tag{3.4}$$

where $PW = GW + 2 * (t_{iaSiH} + t_{naSiH} + t_{AZO})$, and $FL = S + 2 \times (t_{paSiH} + t_{ITO})$, this length should be compared to P (the length for planar devices with the same unit cell), to obtain the increasing in the exposed area, which is proportional to L_{tri}/P. With a simple calculation using equation 3.5 and value of 1500 nm for GH, 100 nm for GW, and 50 nm for S (these values are the optimized values for the triangular grating, see figure 3.14,a, and figure 3.16,a), we can see that the exposed area increases by more than $\times 4.6$. It is clear that, the new length of the active layer L_{tri} is longer than the period P due to the elongation in the vertical direction. The increase in the exposed area for the other two designs can be calculated in the same way, using the geometrical parameters of the shapes shown in figure 3.15b,c. By approximating the cylindrical profile as a trapezoidal shape as shown in figure 3.15,b, the new length of the iaSiH layer for the cylindrical and trapezoidal profiles will be:

$$L_{\text{trap, cylin}} = FL + 2 \times GH + PW, \tag{3.5}$$

where $PW = GT + 2 * (t_{iaSiH} + t_{naSiH} + t_{AZO})$, with $GT = 0$ for the cylindrical profile. The exposed area increases by more than $\times 5.28$ for the trapezoidal profile, and more than $\times 4.63$ for the cylindrical profile.

Increasing the GH parameter without limit produces high aspect-ratio geometries that may become difficult to fabricate. Therefore, an optimization in terms of GH is required to be combined with a detailed calculation of the interaction between light and active realizable structures. Using the previously presented model, we can evaluate numerically the dependence of J_{SC} with respect to GH. The results are shown in figure 3.16,a where J_{SC} increases rapidly

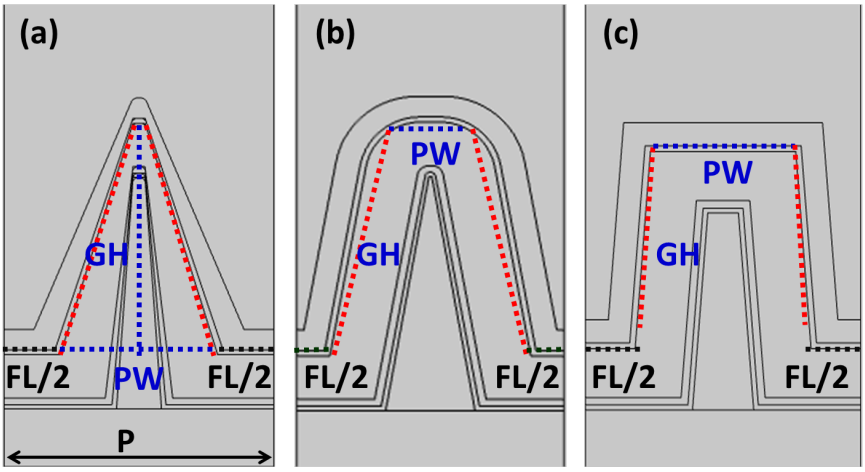

Figure 3.15: (a), (b) and (c) Geometrical parameterization to understand how we calculate the increase in the active area exposed to light when using the nanostructure design. Reproduced from our article [193] with permission of SPIE.

with GH until reaching a saturation level. This happens because most of the optical power is absorbed in the top portion of the nanostructure, and by increasing the height of the triangle there is not a substantial improvement of J_{SC} when reaching the bottom of the structure. Actually, the saturation level occurs for values around 1800 nm for all shapes. However, the improvement in the J_{SC} when moving from GH=1500 nm to GH =1800 nm is very small, so, we selected 1500 nm as an optimum value for the height. We choose this height for the grating because it is easier to be fabricated than 1800 nm height grating. As can be seen in figure 3.16,a, the weighted reflection losses R_{w,λ_A} calculated from equation (3.1) have the same trend as J_{SC} in terms of the GH parameter. Implying that, the J_{SC} enhancement mainly comes from reducing the reflectance losses.

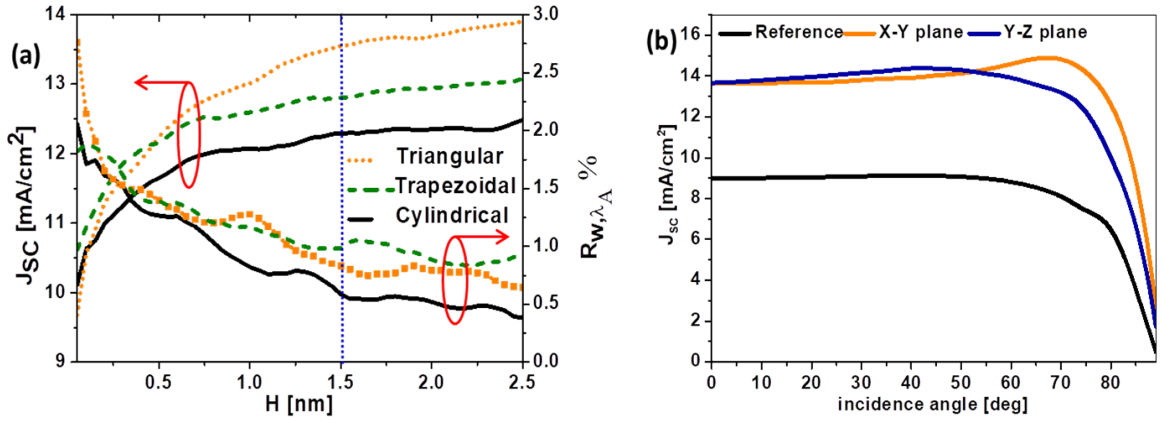

Figure 3.16: (a) Effect of increasing GH on the J_{SC} (left scale) and weighted reflectance (weighted to the solar irradiance function) in the wavelength range λ from 300 nm to 800 nm, (right scale) (b) Angular dependence of the J_{SC} (the two color lines) for the nanostructured cell for two orthogonal planes of incidence, parallel and perpendicular to the grating profile. Each line is the average of the TE and TM sates of polarization. The angular dependence of the J_{SC} for the reference planar cell is plotted as a black line. Reproduced from our article [193] with permission of SPIE.

The nanostructured cell has an enhancement of 51% in absorption compared with the planar reference cell (the active layer thickness for both the nanostructured and the planar cell is 150 nm). In figure 3.16,a, the three grating profiles have a similar dependence on GH, being the triangular shape with the non-homogeneous side coverage (which commonly resulted from conformal deposition process, [194, 195]) better than the other two designs. Table 3.3 summarizes the J_{SC} for the flat reference cell and the optimized nanostructured cells using a naturally polarized light illumination condition (average of the TE and TM results).

Table 3.3: J_{SC} for the planar reference cell and three geometries of the optimized nanostructured cell. All the values are for the average of the two polarization states TE and TM. The enhancement value calculated with respect to the planar device

Structure	J_{SC} [mA/cm^2]	Enhancement
planar reference	8.98	-
Triangular	13.53	50.7%
Trapezoidal	12.8	42.5%
Cylindrical	12.3	37%

When dealing with low-cost solar cells, we should also pay attention to the dependence of its performance with respect to the angle of incidence changes. This is even more important when no active tracking is deployed. Typically, J_{SC} decreases strongly when the angle of incidence is large increases. Besides, for the extruded structure proposed here, the dependence varies with the polarization state and the orientation of the plane of incidence with respect to the profile. After considering all these previous conditions and situations, in figure 3.16,b we have plotted the values of J_{SC} for the case of a nanostructured cell for two possible orientations of the plane of incidence. In this same plot, we have also included the angle dependence obtained for a planar reference solar cell [101]. From these results, besides the wide angle of acceptance, we can see an increase in the J_{SC} that reaches a maximum value of $J_{SC} = 14.4$ mA/cm^2 and $J_{SC} = 14.8$ mA/cm^2 for incidence within the YZ plane, and for the XZ plane of incidence cases, respectively. These values are higher than those listed in table 3.3, which is for the normal incident case. This means that, the high aspect ratio grating trap and guide the light better for oblique incidence illumination with small angles. These results are the average of the TE and TM polarizations.

3.2.4 Optimization of the materials

Not only the geometrical design and shape are important parameters to optimize the performance of solar cells, but also an appropriate choice of materials makes possible further improvements. To show this, we have evaluated the performance of the structure when different materials are used for the fabrication of the grating template where the cell structure is deposited (see figure 3.17,a). We have seen in figure 3.17,b that, materials with high n value and low k value performs better in this structure (being n and k the real and imaginary parts of the index of refraction, respectively). A smaller k is responsible for lower absorption losses at the scaffolding structure. The performance of the structure using different materials for the grating profile can be explored by calculating the short-circuit current in terms of the refractive index of the grating. We used for this calculation the optimized geometrical parameters for the triangular profile and the optimized grating height (GW= 100 nm, S= 50 nm, and GH=1500 nm). The triangular profile is selected because it gives a better response than the other two.

First, we consider the dielectric material as lossless, and ignore the imaginary part of the refractive index. This assumption is valid for many dielectric materials such as MgF_2, SiO_2, PMMA, SiN_x, etc. The results in figure 3.17,a show that a value of $n_g = 2.2$ is a threshold between high and low enhancements. SiN_x is a possible option where its refractive index can be tuned around this value [199]. As a second step, we select materials with different losses (Ag, ZnO, Si_3N_4), to compare the performance of the device for each of them. In this step, we use the complex refractive indices of these selected materials. We calculated the J_{SC} values corresponding to the three grating materials in figure 3.17,b. The cell with the grating made of Ag gives a $J_{SC} = 12.66$ mA/cm^2, ZnO gives $J_{SC} = 13.3$ mA/cm^2, and for Si_3N_4 we obtain $J_{SC} = 13.64$ mA/cm^2. These previous results already average the TE and TM polarization. The obtained values of J_{SC} can be explained as follow: materials with significant optical losses (Ag and ZnO) reveals lower J_{SC}, while low loss material (Si_3N_4) provides a higher J_{SC}.

Using Si_3N_4 as the grating material, we observe a broadband absorption improvement in the cell active layer (see figure 3.17,c) where the absorption at the iaSiH layer is higher than that of the reference planar cell at all wavelengths within the range 200-720 nm. Also, as we mentioned above, the enhancement is not only in the iaSiH active layer but in all layers. We have also calculated the weighted reflection using equation (3.1) and weighted absorption using a similar equation given as:

$$A_{w,\lambda} = \frac{\int_\lambda \Phi_{\mathrm{AM1.5g}}(\lambda) A(\lambda) d\lambda}{\int_\lambda \Phi_{\mathrm{AM1.5g}}(\lambda) d\lambda}, \tag{3.6}$$

where $A_{w,\lambda}$ is the spectral absorption and $\Phi_{\mathrm{AM1.5g}}(\lambda)$ is the solar spectral irradiance. In figure 3.18 we show the power budget at each layer for different structures. The nanostructured cell shows a better absorption in the active layer for all profiles, as shown in figure 3.18,a. The significant absorption enhancement caused in the nanostructured cell is shared by the ITO, p- and naSiH layers, producing heat by dissipation and recombination as shown in figure 3.18,b. This heat will partially mitigate the SWE [101, 200]. The total weighted absorption for the nanostructured cell is significantly improved compared to the planar reference (see figure 3.18,c). This is caused by a decrease in the total reflectance of the device. As we described in section 3.2.3, several strategies are responsible for this enhancement which can be summarized as follow:

- Increasing the active layer area exposed to light without increasing its thickness, by elongating the whole cell in the vertical direction.
- Generating funneling and guiding effects by the high aspect ratio grating that couple better the incoming light into the cell.
- Determining the materials better suited for the grating structure.

We have studied two designs to improve the absorption efficiency of aSiH solar cells, the first is a nanostructured ARC (see section 3.1.3), and the second is a back grating relief (see section 3.2.2). If we compare the back grating relief design with the nanostructure ARC, we can see that, the location of the nanostructure (close to the active layer) is important, which enhances its ability to redirect the electromagnetic energy to the active layer of the cell. Although the total absorption of the device is greatly enhanced for both designs, the portion that is routed to the active layer is better for the back grating relief.

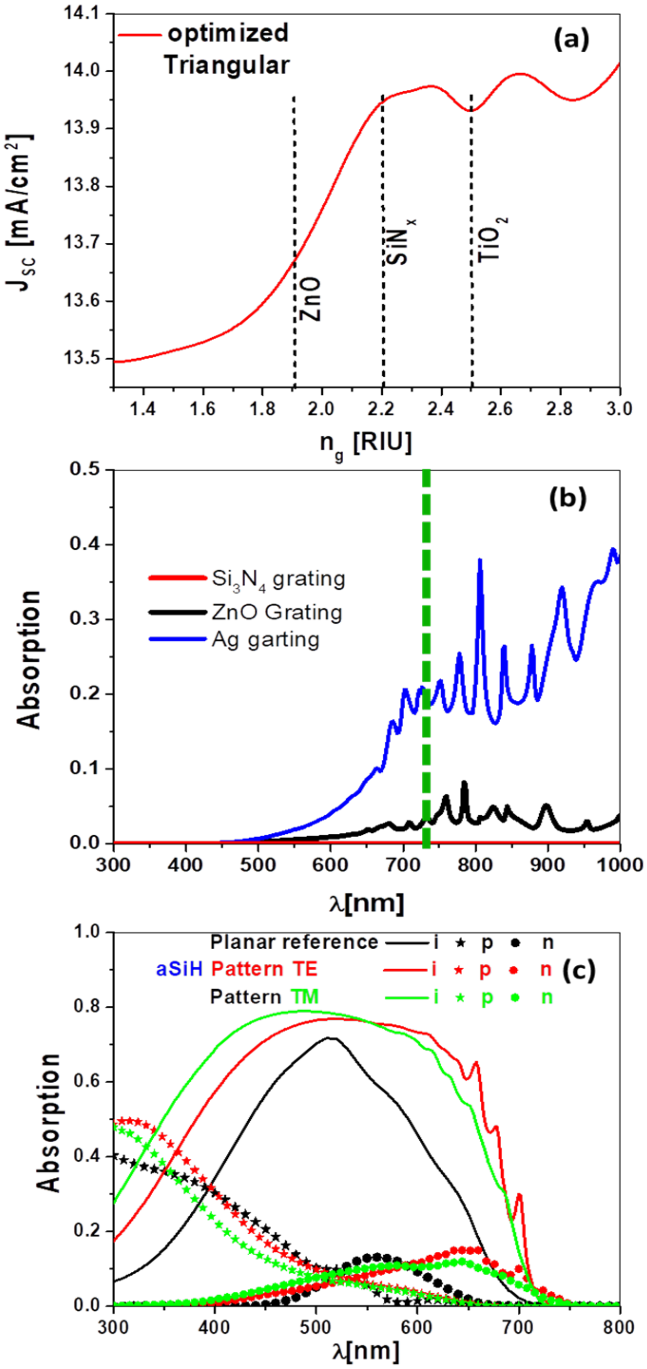

Figure 3.17: (a) J_{SC} of the optimized solar cell with gratings of different refractive indices. (b) Absorption inside the grating for different grating materials, the vertical dotted green line located at the absorption edge of iaSiH layer. (c) Spectral absorptance in the iasiH layer for the reference planar cell, and textured cell (TE and TM polarizations). Reproduced from our article [193] with permission of SPIE.

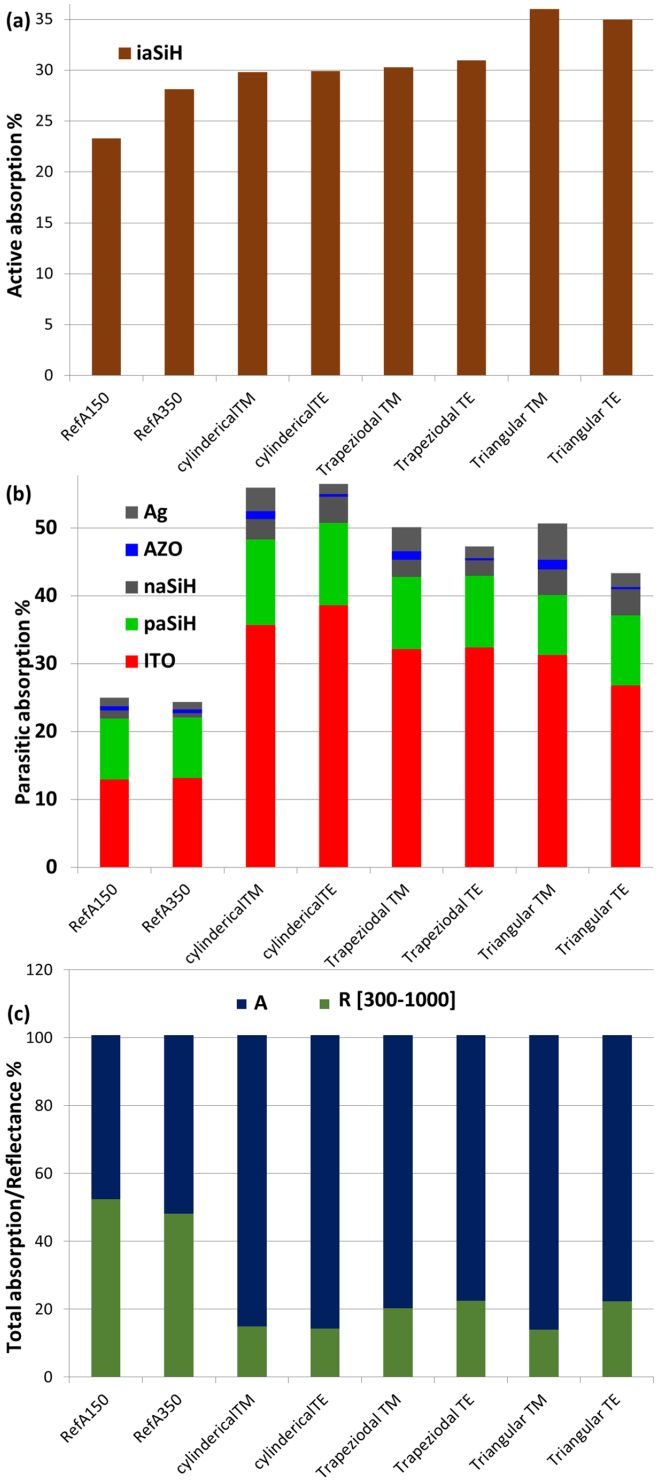

Figure 3.18: Weighted absorption and reflection for different grating profiles (triangular, cylindrical, and trapezoidal), and the planar reference cells. (a) Weighted absorption in the cell active layer. (b) Weighted parasitic absorption in the buffer layers and contacts. (c) Total weighted absorption and reflection. Reproduced from our article [193] with permission of SPIE.

3.2.5 Funneling and guiding effects

Light funneling is one of the light trapping mechanisms which can be applied to solar cells to improve their performance. Previous contributions show that this mechanism is at work

in high aspect ratio metallic grooves, or in multi-layer metal-dielectric structures [201] [202]. However, metallic layers combined with dielectric layers that can produce light funneling effects account for both high reflections from the metal surface and high absorption inside the metal itself.

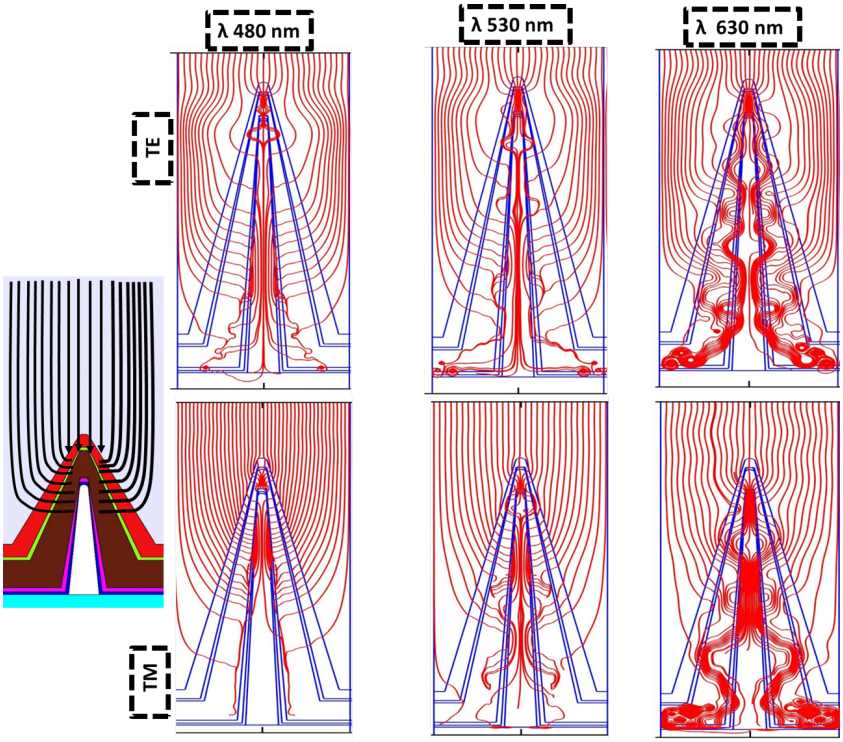

Figure 3.19: The left graph shows a schematic picture of the structure that represents how incoming light is diverted towards the inner layers. The rest of the plots show the Poynting vector flux for three wavelengths $\lambda = 480, 530$, and 630 nm, and two orientations of the electric field. Funneling appears within every plot and guiding in the active layer is stronger at $\lambda = 630$ nm. Reproduced from our article [193] with permission of SPIE.

In our case, we could produce a similar effect with high aspect ratio dielectric structures. Figure 3.19 shows the case of the optimized structure in sections 3.2.3 and 3.2.4, for three wavelengths and two orthogonal orientations of the electric field. These plots represent the Poynting vector flux. From these plots, we can check how the incoming flux propagates within the structure. At some specific wavelengths, light is guided within the active layer (see for example the case of $\lambda = 630$ nm in figure 3.19).

3.3 Improvement of perovskite/c-Si tandem cell using metasurfaces

Tandem monolithic solar cells that combine a thin-film top cell with a wafer based bottom device are devices with a potential efficiency larger than 30%. As we discussed in section 3, one of the promising candidates to this type are perovskite/crystalline Si (c-Si) devices. Here in this section, we describe a nanophotonic design that improves the performance of a two-terminal structure of this type (see figure 3.20) [203]. As a common feature in multi-junction solar cells, they involve many interfaces for each junction, and the tunnel layer between them. These

interfaces account for significant reflection and absorption losses. So, an important key in the design of tandem solar cells is to achieve an efficient absorption in both active layers in their corresponding bandgap ranges by reducing these losses. This requires an efficient absorption of shorter wavelengths in the top cell, and an efficient transmission of the longer wavelengths to the bottom cell.

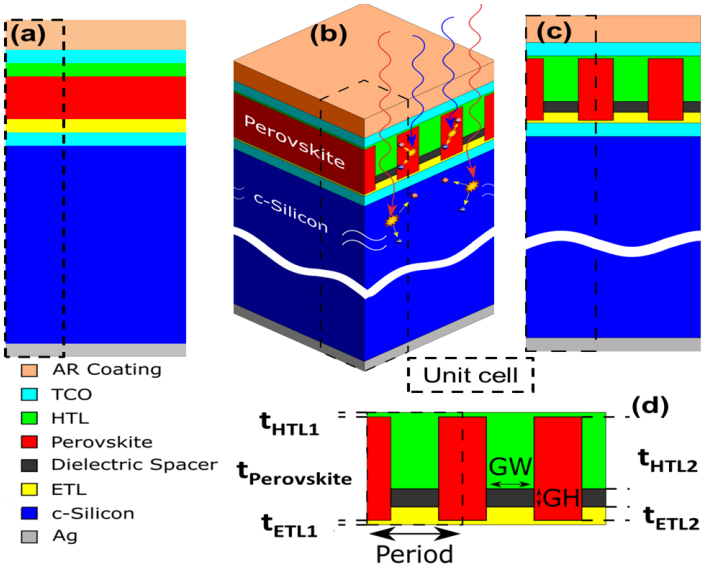

Figure 3.20: (a) 2d diagram of the planar monolithic perovskite/c-Si tandem device, 3D (b) and 2D (c) Diagram of the proposed nanostructured configuration. The proposed structure allows a guiding effect of photons of long wavelengths (red lines in (b)) towards the silicon layers, while short wavelengths (blue lines) generate electron-hole pairs in the perovskite layer. The detail of every layer, and the considered unit cell of our simulations (dashed lines) are also included. (d) Detail of the nanostructure with the corresponding geometrical parameters.

We start by modeling the planar structure of the monolithic perovskite/c-Si tandem shown in figure 3.20,a to validate our model. Then, we propose structuring the perovskite cell layers as a one-dimensional multilayer grating, acting as a metasurface. Figure 3.20,b shows a 3D schematic of the complete stack of the different layers. This figure only shows those layers relevant to the optical behavior. One of the possible configurations of tandem Perovskite-c-Si solar cells is arranged from bottom to top as follow: back contact - ITO - naSiH - iaSiH - n-type c-Si - iaSiH - paSiH -ITO - ETL - Perovskite ($MAPbI_3$)- HTL - top contact [204]. The pin aSiH layers are necessary to generate a suitable electric field to separate the solar photo-generated charge carriers in the c-Si active layer. ETL and HTL are the electron and hole transport layers, respectively. They are required to extract the charge carriers from the perovskite active layer. The ITO layer on top of the rear contact prevents the diffusion of the metal atoms in the semiconductor adjacent layer. The ITO layer that intermediates the two junctions is the tunneling layer that connects both cells electrically, and finally, the top indium zinc oxide (IZO) layer is the transparent top contact. The thickness of the pin aSiH is very small [204] and has a negligible optical loss. Moreover, we simulated the complete stack to check this assumption and we found very small optical losses for the pin aSiH layers. So hereinafter, we exclude pin aSiH layers from our calculations to simplify the optical model. Figure 3.20,c,d depict the details of the materials for the considered layers and a scheme of the perovskite subcell with a description of the different geometrical parameters. We define the dimensions of the dielectric grating (GW and GH in figure 3.20,d) instead of the perovskite

geometry, because they control the dimensions of the whole metasurface, including perovskite. The layer structure of the modeled device are listed in table 3.4, from top to bottom. The hole transport layer is, 2,2',7,7'-tetrakis[N,N-di(4-methoxyphenyl)amino]-9,9'-spirobifluorene, which abbreviated as Spiro-OMeTAD. These values and materials were initially considered like those of the planar structure in reference [204] to properly validate our model by taking this planar cell as a reference. The complex refractive indices of the materials were obtained from [128, 188, 205, 206, 207, 208, 209, 210, 211]. Perovskite materials have a diffusion length of the photo-generated carriers that range from 100 nm to 1 μm, [212, 213, 214], so the thickness of the active layer is limited to a few hundreds of nanometers for efficient electrical carrier extraction [215]. In a monolithic two terminal tandem device, there is another limitation for

Table 3.4: Materials and layer structure of the metasurface design for the tandem device

Layer	Material	thicknesses
Antireflection coating	MgF_2	105 nm
Transparent top contact	IZO	44 nm
Hole transport layer	Spiro-OMeTAD	t_{HTL1} = 10 nm, t_{HTL2} = 160 nm)
Top cell active layer	perovskite	$t_{HTL2} + GH + t_{ETL2}$
Dielectric spacer	Si_3N_4	GH
Electron transport layer	TiO_2	t_{ETL2} = 30 nm, t_{ETL1} = 10 nm
Tunnel layer	ITO	44 nm
Bottom cell active layer	c-Si	200 μm
Back contact	Ag	300 nm

the perovskite thickness that is related to the value that produces the same current of the c-Si cell current. This condition is called current matching. In a single junction perovskite solar cell, the optimum active layer thickness ranges from 300 nm to 500 nm [215]. However, the value that produces current matching in our planar tandem is only 260 nm, as shown in figure 3.21,a. The optical absorption in the active layer of each cell, the total absorption in both active layers, and the total reflection of the whole device are shown in figure 3.21,b. These results agree well with those obtained by Grant *et al.* [204]. From figure 3.21,b, we can see that the planar tandem device accounts for a significant reflectance in the whole band of both junctions. Our goal is to reduce these reflection losses and redirect the gained optical energy to the active layers of both cells.

By introducing the 1D perovskite grating, we try to optimize the tandem solar cell performance by:

- Efficiently guiding long-wavelength photons to the silicon layer to increase light absorption in this subcell.
- Producing strong diffuse scattering at short wavelengths to increase the absorption in the perovskite.
- Tuning the J_{SC} in both cells through the geometrical parameters of the grating to achieve the best current matching.

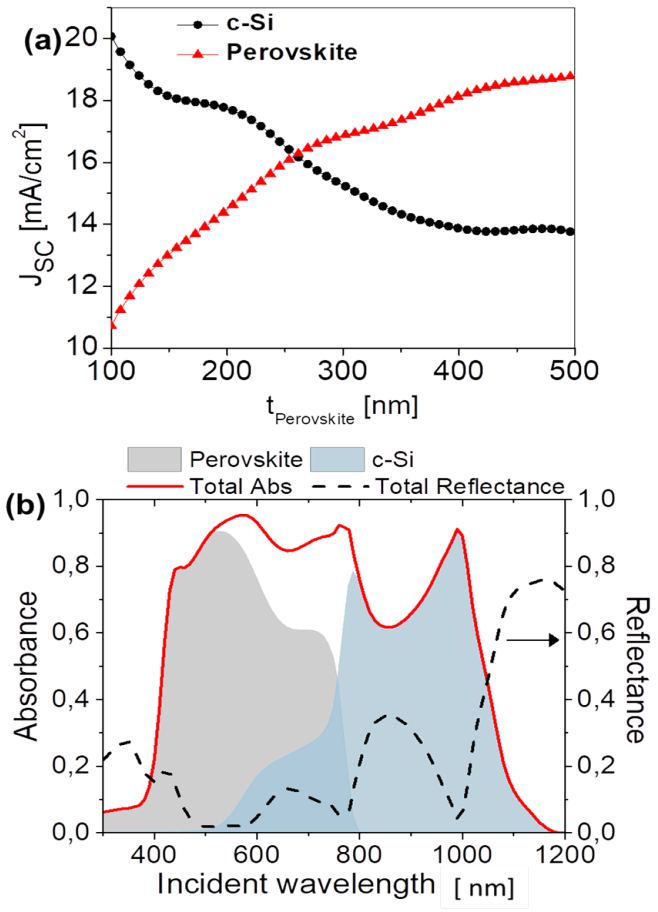

Figure 3.21: (a) Short-circuit current density generated in c-Si (black circles) and perovskite (red triangles) subcells as a function of the thickness of the top active layer (perovskite layer). (b) Spectral evolution of the absorbance in each subcell of a typical monolithic tandem solar cell composed by a perovskite (gray area) and a c-Si (blue area) layers. The total reflectance (black dashed line, right axis) and absorbance (red solid line) of the device are also included.

- Increasing the interface surface between the perovskite and the charge transport materials (HTL and ETL), to enhance the charge collection of the photogenerated carriers. Additionally, it reduces the perovskite/transport layers interfacial problems that appear with large scale planar surfaces [216].
- Reducing the reflection and parasitic absorption losses.

3.3.1 Optimization of the meatsurface

The optimization of the proposed device was carried out by changing the geometrical parameters of the grating while evaluating the short-circuit current in both active layers. As we change the height and width of the grating (GH and GW in figure 3.20,d, respectively), the thickness of the perovskite layer was also varied because it is the sum of GW, t_{HTL2} and t_{ETL2} ($t_{perovskite} = GW + t_{HTL2} + t_{ETL2}$). The period of the unit cell (dashed line in figure 3.20,a,b,c) was arbitrarily fixed to 1μm. So, if the grating width increases, the width of the perovskite slab (see the red slabs in figure 3.20,d) decreases (GW + perovskite slab width = 1 μm).

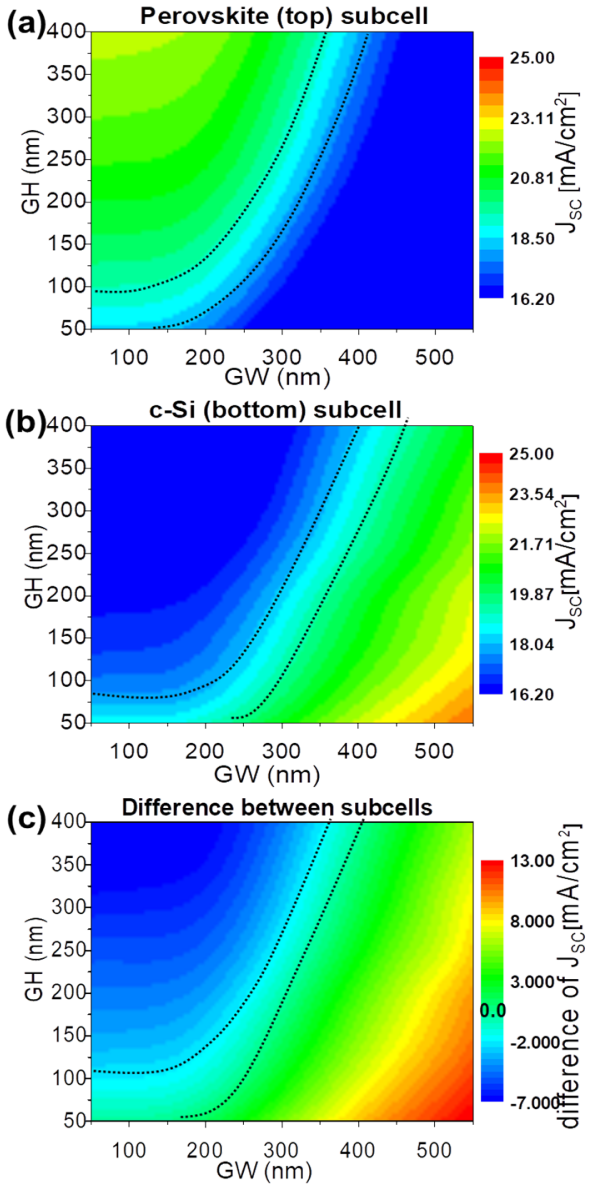

Figure 3.22: Simulated values of the short-circuit current density (J_{SC}) in: (a) the perovskite and, (b) the c-Si subcells as a function of the geometrical parameters (GW and GH) of the proposed grating. (c) Difference of the generated currents in each subcell as a function of the geometrical parameters of the grating. The values producing the perfect current matching (null difference) are located between the two black dotted curves.

The optimization of the proposed metasurface improves the optical performance of both cells of the tandem device through scattering and guiding effects enabled by the metasurface. However, as in the planar device (see figure 3.21,a), maximizing the J_{SC} in one subcell reduces the current of the other cell (see figure 3.22,a,b). Although the same behavior is maintained when using the metasurface design, differently from the planar device, the optimum geometries of the device layers are not unique. Several combinations of the grating parameters produce a matching current between both subcells. These combinations involve a range of 150 nm to around 400 nm for the GW parameter, which corresponds to an interval of 50 nm to 400 nm for GH. The pale turquoise region in figure 3.22 (located between the two black dotted curves)

matches the current in both cells. Although there is a collection of GW- GH pairs producing current matching, we select one of them, which gives the maximum current value as (J_{SC} = 18.8 mA/cm^2) at GW = 300 nm, and GH = 225 nm. This is a 16% improvement compared with the planar cell 3.21,a [204], where the enhancement factor (EF) in % defined as:

$$EF = \frac{J_{SC}(\text{proposed}) - J_{SC}(\text{planar })}{J_{SC}(\text{planar})} \times 100\%. \tag{3.7}$$

a width of more than 50 nm in terms of the grating width for all heights, which means better fabrication tolerance. In the planar device, the thicknesses and materials choice for all perovskite cell layers is limited by the optical and current matching conditions between the two junctions. We will show later that the metasurface design doesn't only offers an optical enhancement, but also adds a new degree of freedom to choose materials and fabrication processes. Increasing GH during the optimization means an increase in the perovskite thickness. The optimized GH value involves 12% increment in perovskite thickness in the metasurface device compared with the optimized thickness of the planar device. We may think that the achieved enhancement when using the metasurface is due to this increment in the amount of perovskite. To check that we calculate J_{SC} for the planar device when the thickness of the perovskite increases by 12%, the calculation gives a J_{SC} = 16.7 mA/cm^2. This value is still lower than that of the optimized metasurface value. So, the increment of the perovskite thickness in the metasurface design is not the main reason for the obtained enhancement. Consequently, there must be other physical effects producing the obtained improvement, which we will investigate in the next section. Furthermore, increasing the thickness of perovskite in the planar device is not realistic, because it compromises the current matching with the c-Si subcell(see figure 3.21,a).

3.3.2 Results and Discussion

To figure out the physical mechanisms involved in the structure, figure 3.23 depicts the z-component of the electric and magnetic fields inside the planar (figure 3.23,a,c,e,g) and the proposed structured solar cell (figure 3.23,b,d,f,h) at λ = 680 nm, and 860 nm, for two angles of incidence: 0° and 50° using a TE (transverse electric) polarized plane wave. This selection is made to explore the ability of the proposed design to scatter and confine light in the perovskites at short wavelengths ($\lambda \in [300, 800]$ nm), and guide the light towards the c-Si at long wavelengths ($\lambda \in [800, 1200]$ nm). The angle of incidence varies to evaluate the angle of acceptance of the device. Similar maps for both planar and nanostructured device using the TM (transverse Magnetic) incident plane wave are presented in figure 3.23,i,k,m,o and j,l,n,p respectively. The orientation of the incident electric field for TE polarization, or the magnetic field for TM polarization, is always parallel to the grating (along the z direction).

The short wavelength, λ = 610 nm, is within the absorption band of the perovskite, and λ = 860 nm is within the absorption band of the c-Si cell. The maps in figure 3.23,a,c,i,k show the propagation through the structure of an uniform distribution, due to absorptions into each one of the layers. In the nanostructured cell (figure 3.23,b,d,j,l) a remarkably different field distribution appears (note that the color scale is the same in both planar and nanostructured graphs): the electric field is locally enhanced within the perovskite volume, increasing the absorption rate. This spatial field profile is produced by the scattering effects of the nanostructured geometry of the metasurface. On the other hand, 860 nm is a wavelength in the c-Si absorption range. In this case, a diffraction effect, due to the grating metasurface, occurs in

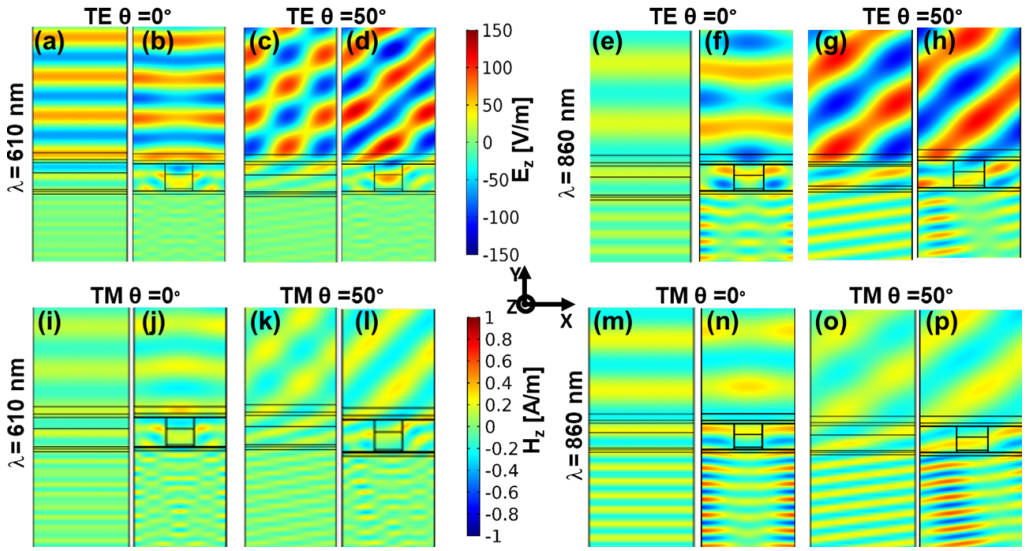

Figure 3.23: Z-component of the electric field for TE polarization at $\lambda = 680$ nm: considering a planar device (a) under normal incidence, and (c) with 50° angle of incidence, and for the proposed nanostructured design, (b) under normal incidence, and (d) with 50° angle of incidence. Z-component of the electric field in for TE polarization at $\lambda = 860$ nm: considering a planar device (e) under normal incidence, and (g) with 50° angle of incidence, and for the proposed nanostructured design, (f) under normal incidence, and (h) with 50° angle of incidence. Z-component of the magnetic field for TM polarization at $\lambda = 680$ nm: considering a planar device (i) under normal incidence, and (k) with 50° angle of incidence, and for the proposed nanostructured design, (j) under normal incidence, and (l) with 50° angle of incidence. Z-component of the magnetic field for TM polarization at $\lambda = 860$ nm: considering a planar device (m) under normal incidence, and (o) with 50° angle of incidence, and for the proposed nanostructured design, (n) under normal incidence, and (p) with 50° angle of incidence.

the c-Si subcell (figure 3.23,f,h,n,p), showing an efficient guiding of light inside it with respect to the planar one (figure 3.23,e,g,m,o).

Figure 3.24,a shows the simulated total effective absorption for TE polarization (adding the c-Si and perovskite contributions) and the results for TM appear in figure 3.24,b. A significant enhancement in both subcells is observed.The increment in the c-Si band (800–1000 nm, region III in figure 3.24,a,b) was due to the increment of light reaching this layer as a result of the guiding ability of the new top subcell, as figure 3.23,f,h,n,p revealed. At shorter wavelengths, in the perovskite absorption band, (region II in figure3.24,a,b), the spatial concentration of light inside the grating (Figure 3.23,b,d,j,l) allowed a higher absorption, which is proportional to the square of the electric field (see equation (2.13)). At even shorter wavelengths (region I in figure 3.24,a,b) the increment in absorption is a consequence of the decrease in reflectance due to the proposed structure. An efficient and realistic design of a solar cell should maintain this enhancement for a given range in the angle of incidence, according to the angular location of the Sun. Figure 3.24,c shows the angular dependence of J_{SC} in the active regions for both the planar and the nanostructured geometries. The geometrical parameters of the nanostructure were the previous optimum ones ($GH = 225$ nm, $GW = 300$ nm, producing $J_{SC} = 18.8$ mA/cm2 at normal incidence). As can be seen in figure 3.24,c, the enhancement in absorption led to higher values of the photocurrent at every incidence angle compared with the planar reference. The nanostructured configuration losses the perfect current matching condition after 20^o, as they were optimized in 1D with oscillating incident fields always parallel to the grating,

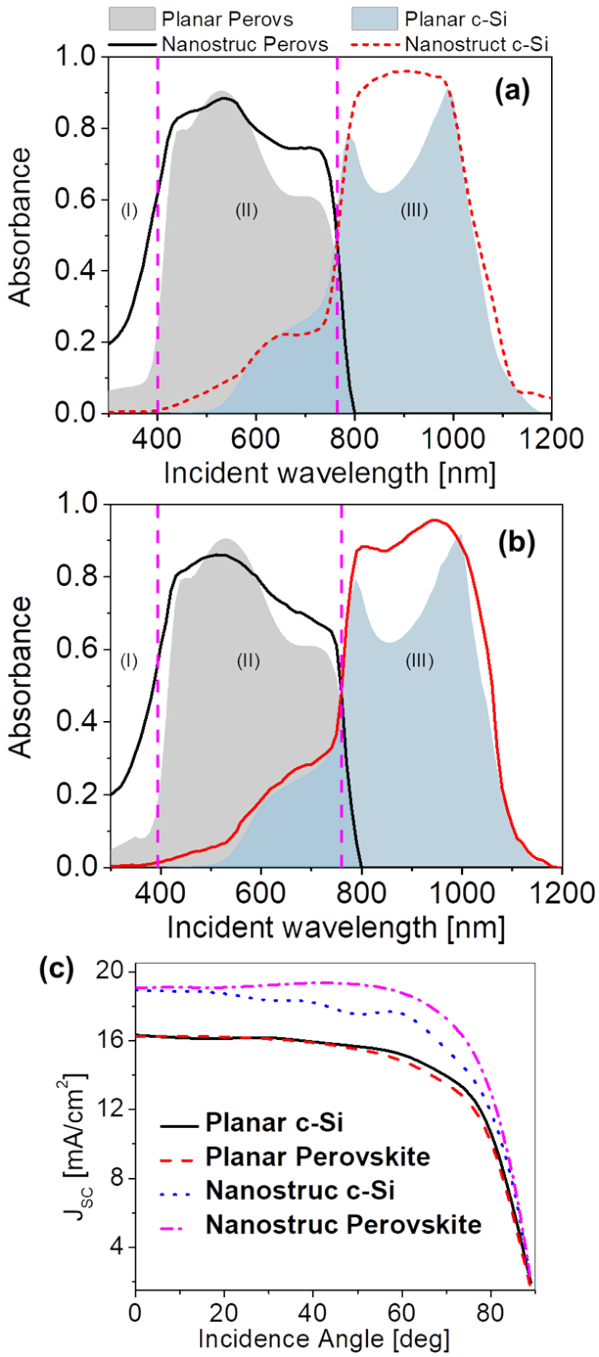

Figure 3.24: Comparison of the spectral absorbance in each subcell of a typical monolithic tandem solar cell with a planar perovskite (gray area) and c-Si (blue area) layers and that of the proposed optimum structure with a nanostructured perovskite (black solid line) and c-Si (red dashed line) layers along the solar spectrum. TE polarization is considered. Vertical dashed lines delimit three interesting spectral regions (see explanation in the text). (a) is for TE, and (b) is for TM. (c) Short-circuit current density generated in each subcell of a planar device (c-Si subcell, solid black line; perovskite subcell, dashed red line) and the proposed device (c-Si subcell, dotted blue line; perovskite subcell, dash-dotted pink line) as a function of incidence angle of the incoming light.

and thus were sensitive to polarization. Despite that fact, an average increment of 15% in the

short circuit current with respect to the planar cell was achieved up to 70°. A deeper study of the involved materials in the metasurface will be analyzed in the next sections.

3.3.3 Design of a textured back surface

Textured surfaces were used in many previous reports [217, 218] to achieve an additional enhancement of the optical absorption in the active layer by increasing the length of the optical path of the photons propagating within the device. So far, we have established the effect of the nanostructured perovskite layer in the tandem solar cell. The next step of our analysis is to check the compatibility of these textured back contacts with the nanostructured top cell, and especially to see if their geometrical misalignment is a drawback for the observed effect.

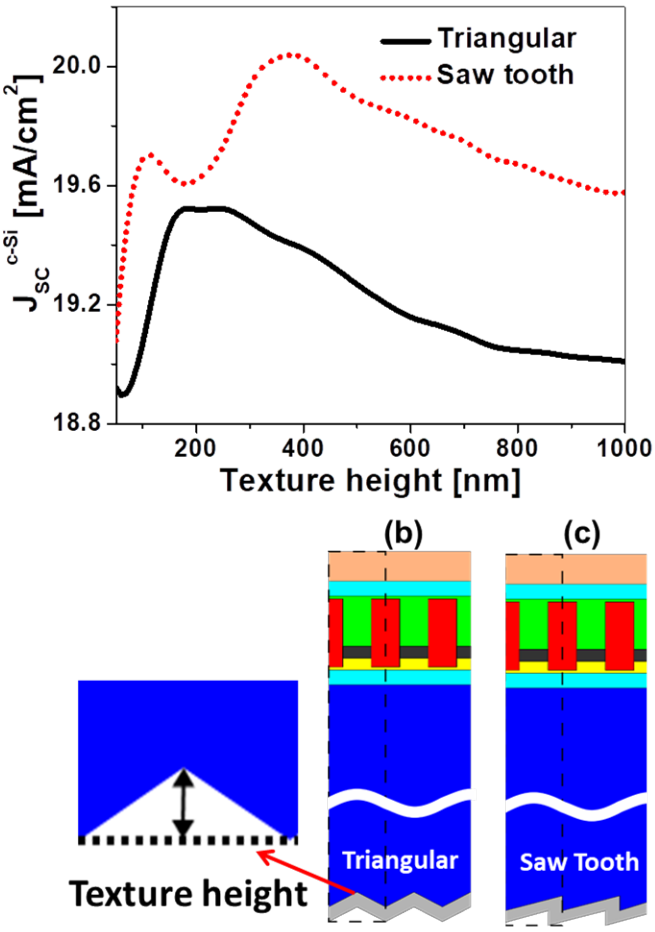

Figure 3.25: Short-circuit current density generated in the c-Si subcell of the proposed device considering a textured back contact with a triangular (black squares) or a sawtooth (red circles) profile, as a function of the height of the profile (the height of the groove etched in the silicon to form the texture surface). Schemes of the device with the considered profiles for the back contact are included in (b) and (c), respectively.

Back-textures of the bottom junction led to further improvement in the J_{SC} , by increasing the light diffusion into the c-Si layer. In our proposal, the top cell fabrication involves a spin coating process, and the metasurface assumes a planar top surface of the bottom junction. For these reasons, we focused on analyzing the influence of texturing the back contact of the bottom cell on its performance. In particular, we explored two typical profiles for the Ag

back contact: a triangular and a sawtooth grooves etched in the c-Si layer, where the Ag contact deposited on this texture profile (figure 3.25,b,c respectively). The analysis is based on maximizing the value of J_{SC} at the c-Si subcell using these textured contacts, varying the height of the profile (see the inset in figure 3.25,b) as the optimization parameter. The results of this analysis are shown in figure 3.25,a. These textured profiles provided an enhancement of the short-circuit current density only in the c-Si subcell, disturbing the current matching condition. For this reason, the geometrical parameters of the metasurface must change again to recover this condition. This confirms the ability of the proposed metasurface to optimize the solar cell performance by tuning its geometry. After the back texture optimization process, we obtain a matching current of 19.35 mA/cm^2 (GW = 300 nm and GH = 220 nm) for the triangular case, and 19.55 mA/cm^2 (GW = 300 nm and GH = 230 nm) for the sawtooth case. As it can be seen, the sawtooth profile involves an increment in J_{SC} of 20.5% respect to the planar one (the enhancement factor of the triangular one is 19.3%).

Another detail to take into account is the vertical alignment between the textured contact and the proposed metasurface. We have also studied the geometrical misalignment between the back-contact profile and the metasurface. We did this by fixing the nanostructured perovskite design position in the unit cell as in figure 3.25,b,c, and shift the position of the back texture gradually every 25 nm, and calculate the J_{SC} value. This study reveals that, there is not a significant difference (the greatest J_{SC} difference being 0.2 mA/cm2) when both nanostructures are completely misaligned. Therefore, the alignment of both structures is uncorrelated. This reinforces the idea that this back-contact texturing only provides a better diffuse reflection and light redirection towards the c-Si active layer, without any remarkable influence on the top subcell.

Figure 3.26,a shows the reflectance of the device for all configurations: planar reference, nanostructured, and nanostructured with textured back contacts (triangular and sawtooth). In the efficient absorption range of the device (from 400 nm to 1100 nm as seen in figures 3.24 and 3.21), the nanostructured configuration offered a remarkable reduction of the reflectance, especially between 600 and 1000 nm. Additionally, the texturization of the back contact reduces the reflectance even more. Particularly, the sawtooth profile produced negligible values of the reflectance between 440 nm and 570 nm, while in the rest of the range, triangular and sawtooth offered similar values. Besides this, the response of the device under oblique incidence improved when the back contact was textured. Figure 3.26,b depicts the EF (see equation 3.7) of J_{SC} for each one of our proposals with respect to the planar one as a function of the incident angle. From a general point of view, a remarkable enhancement (over 13%) was obtained for all the angles with our proposals.

The triangular profile shows a higher enhancement for a wider angular range, but the sawtooth profile provides the best solution for the usual operation of a solar cell, with values of EF over 20%. In figure 3.27, we show the detailed absorbance of every configuration. We calculate the device currents, *i. e.*, the effective photocurrent generated in both active layers (perovskite and c-Si). The absorption in the rest of the layers is considered as current losses, by integrating the photon flux of the incident light in a wavelength range from 300 to 1200 nm, considering an AM1.5g (1000 W/m) spectrum [219]. We use this definition because the optical losses are evaluated in terms of current losses [204, 220, 221, 222]. We used the following equation to calculate these current losses [204]:

$$J_{SC} = \int \frac{q}{hc} \left(R(\lambda) + A_{\mathrm{HTL}}(\lambda) + A_{\mathrm{ETL}}(\lambda) + A_{\mathrm{TCOs}}(\lambda) + A_{\mathrm{Ag}}(\lambda)\right) \lambda \Phi_{\mathrm{AM1.5g}}(\lambda) d\lambda, \qquad (3.8)$$

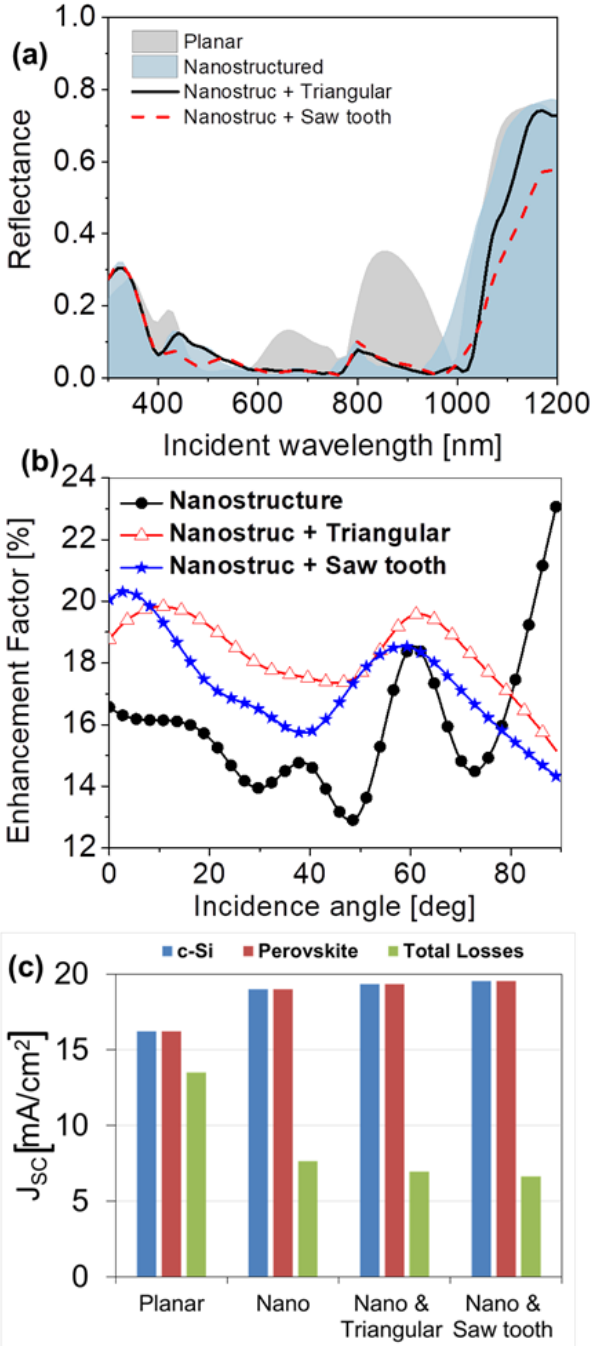

Figure 3.26: (a) Total reflectance of the device, within the solar spectrum, for four different configurations: planar (gray area), nanostructured (blue area), nanostructured with a textured back contact with a triangular (black solid line) or a sawtooth (red dashed line) profile. (b) Enhancement factor of the short-circuit current density of the three proposed configurations (nanostructured, black solid circles; nanostructured + triangular back contact, red empty triangles; nanostructured + sawtooth back contact, blue stars) with respect to the typical planar one as a function of the angle of incidence. (c) Comparison of the effective current produced from the active layers (c-Si, blue; perovskite, red) and the total losses expressed as current losses (green).

where $\Phi_{\mathrm{AM1.5g}}(\lambda)$ is the solar spectral irradiance [114], q is the electron charge, c is the speed of light in vacuum, and h is the Planck's constant. Finally, figure 3.26,c plots short circuit

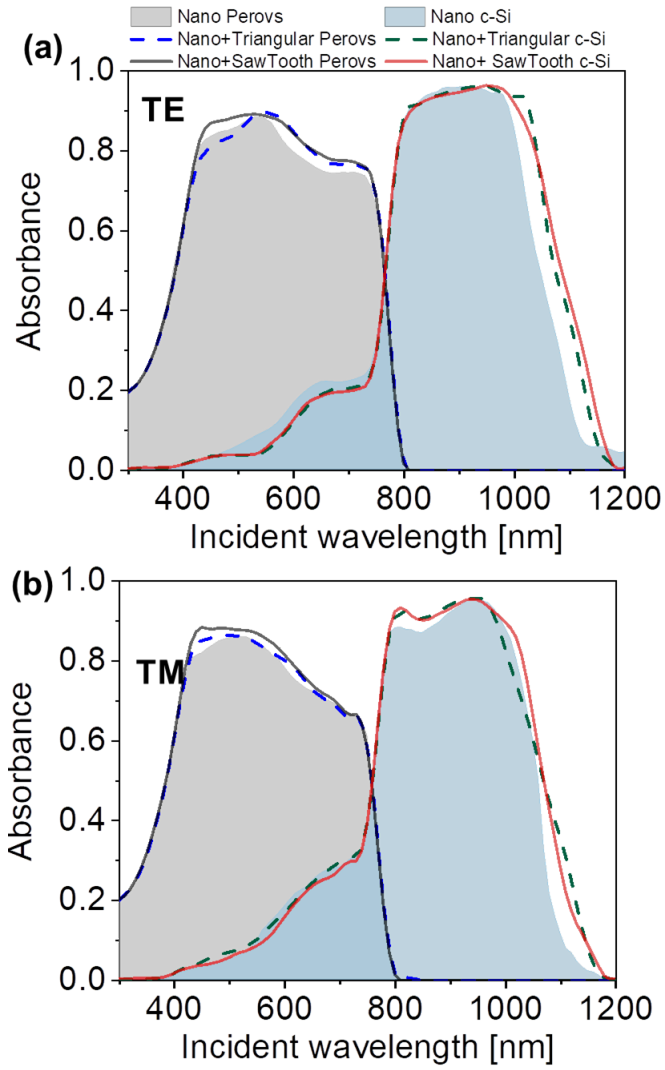

Figure 3.27: Comparison of the spectral absorbance in each subcell of a monolithic tandem solar cell considering the proposed nanostructured perovskite region and three different back-contact configurations: a planar one (filled areas), a triangular profile (dashed lines) and a sawtooth one (solid lines). Both linear polarizations, TE (a) and TM (b), are considered.

current J_{SC} due to absorption in both active layers (perovskite and c-Si), and the current losses due to the absorption in other layers, and reflection. As we can see, the inclusion of the nanostructure improves not only the perovskite subcell current generation, but also the c-Si one with respect to the planar one, at the same time, the parasitic losses decreases, which translates to a decrease in the current losses. The optical responses for all the devices are presented in figure 3.27. For both TE (figure3.27,a) and TM (figure3.27,b) polarizations, the nanostructured devices with texture surfaces provide a broadband absorption enhancement, compared with the planar device. This enhancement is due to the reduction in the device reflection (see figure 3.26,a), which is mainly produced by two mechanisms. The first one is the strong light confinement in the perovskite volume (see figure 3.23). For instance, the metasurface produces 62% lower parasitic losses in the HTL with respect to the planar cell. The second one is the reduction of the total reflectivity (as seen in figure 3.26,a), that decreases 48% with respect to the planar cell for the nanostructured proposal, reaching down to 66%

when texturing the back contact as well. Also here, the sawtooth profile is better than the triangular one.

3.3.4 Materials selection for the metasurface

The metasurface applied to the perovskite/c-Si tandem cell in the previous example is optimized by changing its geometrical parameters. The multi-layer grating structure forming the metasurface consists of three layers: HTL, the dielectric spacer (DS), and ETL. Several materials could be used to fabricate each layer based on the variety of available transport layer materials applied to perovskite solar cells [223, 224], and the variety of dielectric transparent layers applied to the spacer layer. Here in this subsection, we determine the set of materials (by varying the refractive index of these layers) and thicknesses that could achieve the best performance when applied to each layer in the metasurface individually. This optimization process allows more fabrication flexibility in the material's selection and thicknesses, and give a minimum loss equal or better than the one obtained from the geometrical optimization. In general, the losses of the device using the metasurface are lower than the losses of the planar device for any material and any thickness.

The starting point considers the following materials of the nanostructure: Spiro-OMeTAD for HTL, TiO2 for the ETL, and silicon nitride (Si3N4) for the dielectric layer. To explore the best ranges in thicknesses and materials for each one of the layers forming the nanostructure, in which the perovskite is inserted, we calculate the optical absorption at the active layer, and the parasitic absorption, that is considered as current losses. Thus, the methodology is based on looking for the minima of the optical absorption in the HTL, ETL, and DS layers, as they are not producing effective currents, and the minimum reflection of the whole structure. All of these losses (parasitic absorption, and reflection) are collected in one parameter, which is the current losses given by equation (3.8). This parameter will be our merit function for the optimization. In this way, we hold a GW value, like the optimized one in figure 3.20,c,d, and seek for the value of GH and the thicknesses and refractive indices of the ETL, HTL, and DS to achieve our goal. We should remark that the process is done considering each layer independently, due to computational restrictions to perform multidimensional calculations for this large volume model. Additionally, we also compute the short-circuit current density (J_{SC}) in both active layers to measure the device performance, as well as to preserve the current matching between the subcells.

It is worth noting that our sweeping method of the refractive index firstly assumes the ideal case of a lossless material. Once it provides a value of n providing reduced losses, we choose the realistic material closest to this value and consider its actual complex refractive index. This means that the final absorption and reflection simulations have been done with realistic and complex values of the refractive indices.

3.3.5 Optimized selection of materials

Our study implies that both the thickness of each element in our nanostructure (see figure 3.20,c,d) and their materials can vary. This may open new possibilities for the perovskite solar cell manufacturers about the material and size restrictions in the fabrication process [204]. In this section, we present a survey on the possible HTL, ETL, and DS materials, as well as their thicknesses, to reduce the optical losses in the solar cell [225].

- Hole Transport Layer analysis

Figure 3.28,a shows the results of the simulated total current losses (*i. e.*, the sum of the losses due to reflection and parasitic absorption in the non-active layers) as a function of both the thickness t_{HTL2} and refractive index of the HTL nanostructured layer, while the rest of the parameters are fixed to the values of the optimized nanostructured geometry above. We exclude the back texture from this optimization as it has no impact on the metasurface functionality. As can be seen, the calculated losses have values within an interval from 6.8 to 9.2 mA/cm^2. By comparing these values with the total losses of the planar case, which are 13.5 mA/cm^2, an evident reduction of the losses using the nanostructure appears, achieving almost 50% reduction in the best case. At this point, we want to highlight that there is a wide region (blue area with a dashed line limit) in which the losses are under 7.2 mA/cm^2. This region comprises a refractive index from 1 to 2.3, and a height of the HTL layer from 100 nm to 300 nm. The first result allows the use of several materials to play the role of hole transport, such as poly(3,4-ethylenedioxythiophene) polystyrene sulfonate (PEDOT:PSS) (refractive index of around $n = 1.46$ at λ= 600 nm, where the perovskite absorbs), or the Spiro-OMeTAD (around $n = 1.6$ at λ= 600 nm). The second result allows a wide tolerance for the thickness. This tolerance widens the possibilities for the manufacturers to obtain good results regardless of the accuracy in the layer growth. There is a region of high losses (upper left red area), which comprises the refractive index interval from 2.5 to 3, and thicknesses values under 50 nm. Currently, there are no HTL materials in this interval of indices. But even at these values, the produced optical losses would be still 32% lower than the ones of the planar cell. According to a recent review, most of the HTL materials incorporated in high efficiency perovskite cells have low refractive indices, under 2, in the VIS region [223]. This means that the vast majority of materials can offer losses lower than 8 mA/cm^2 in our design. As an example, we show on the

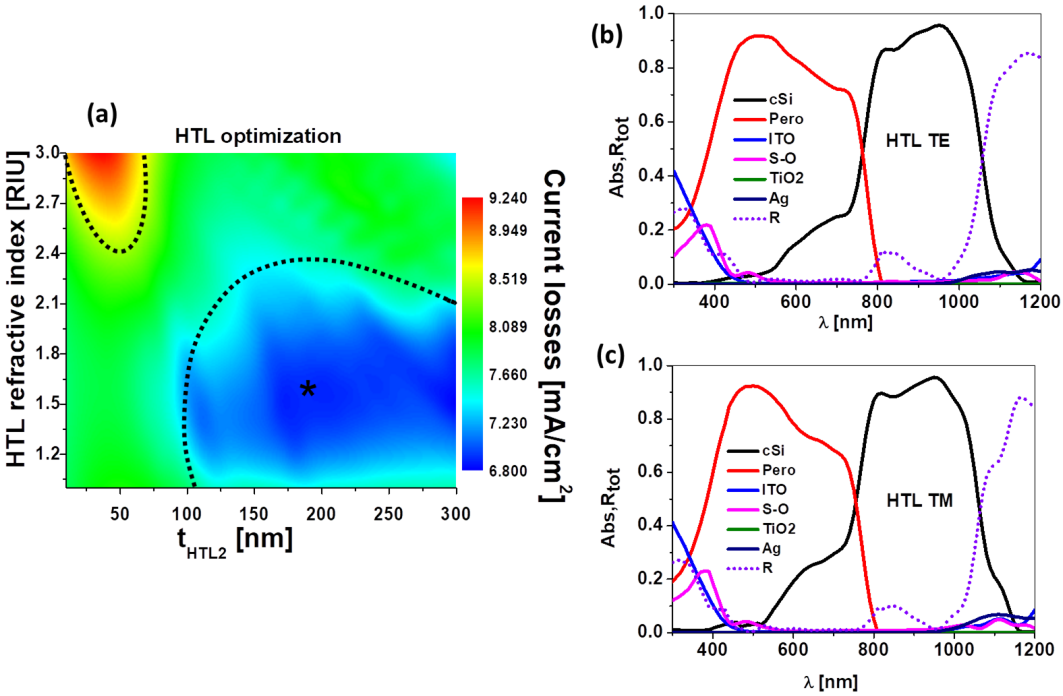

Figure 3.28: HTL analysis. (a) Current loss map depending on the refractive index of the HTL material used, and the thickness of the HTL layer. (b,c) Absorbance of every layer and total reflectance for the selected case (* in a) under (b) TE, and (c) TM illumination

right side of figure 3.28,b,c) the spectral response of the structure considering Spiro-OMeTAD

(S-O, n = 1.6) as HTL, with a 190 nm height (the point marked with a star in figure 3.28,a). Both the absorbance of each layer and the total reflectance (dashed line) are shown for an incident TE (figure 3.28,b) or a TM (figure 3.28,c) polarizations. This simulation considers the real complex refractive index of the materials in the analyzed spectral range. The most remarkable result is related to the reflectance (see figure 3.28,b,c), which undergoes a noticeable reduction in the whole spectral range and presents a wide band with a value close to zero. We want to remark that this HTL height selection affects the current matching condition, which could be retrieved by tuning the GW value without any remarkable change in the total losses. The matched J_{SC} for this case is 18.85 mA/cm^2.

- Electron Transport Layer analysis

Following the same strategy as above, figure 3.29 shows the simulated results for the electron transport layer (ETL) analysis. As before, figure 3.29,a shows a 2D map of the total losses as a function of both the thickness t_{ETL2} and the refractive index of this layer. The rest of the parameters remain as the starting point. In this case, the variation of current losses is significantly lower, ranging from 7.4 to 8.2 mA/cm^2. The region with the minimum loss (top blue area) comprises values of the refractive index from 1.2 to 2.1, and thicknesses from 160 to 300 nm. This range allows the selection of different materials to play the role of ETL, such as SnO_2 (around 1.85) or ZnO (around 1.6). This low-losses region applies to the majority of the ETL current materials, like those appearing in a recent review [224]. Although TiO_2 ($n \approx 2.38$ at λ 600 nm) is not inside this region, low losses interval (around 7.6 mA/cm^2) is available for this refractive index between 25 and 50 nm in height. As an example, we show in figure 3.29,b,c

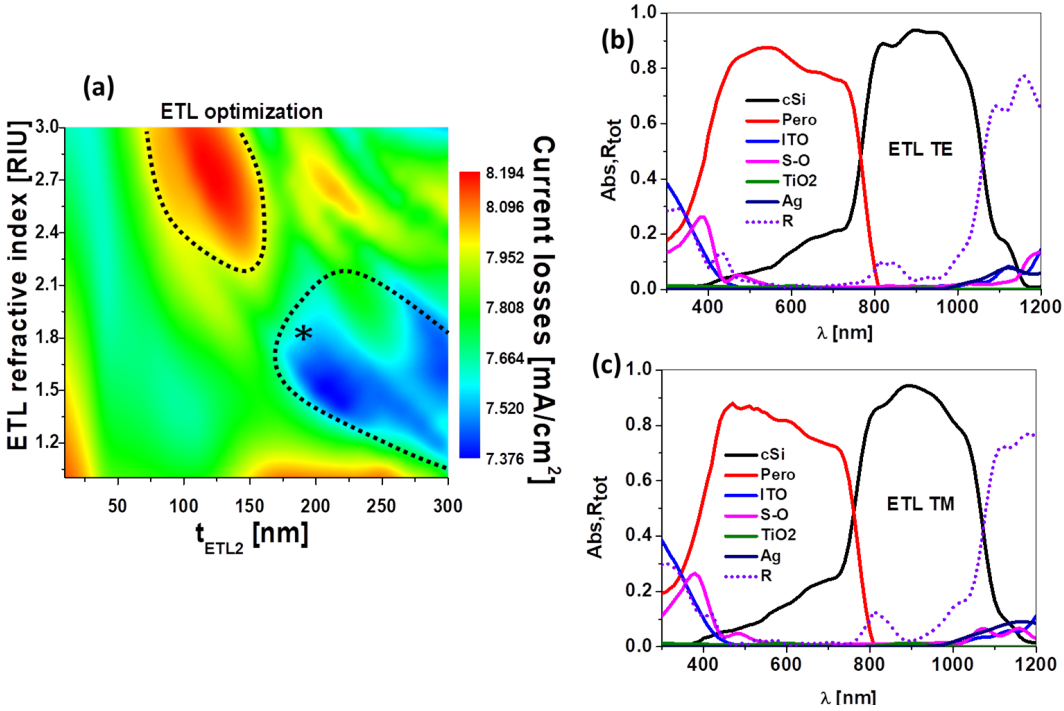

Figure 3.29: ETL analysis. (a) Current loss map depending of the refractive index of the ETL material and the thickness of the layer. (b,c) Absorbance of every layer and total reflectance for the selected case (* in a) under TE (b) and TM (c) illumination.

the spectral response of the device considering ZnO playing the role of ETL, with a height of 190 nm (star in figure 3.29,a). The complex refractive indices are considered, including the one of ZnO [226]. Both the reflection and parasitic absorption are reduced compared to those of the planar device. Actually, the matched J_{SC} for this response is 18.9 mA/cm^2, larger than the 16.2 mA/cm^2 of the planar case. A GW equal to 390 nm is required to achieve the current matching.

- Dielectric Spacer Layer analysis

The third part of the nanostructure that we study is the dielectric spacer (DS). The thickness of the DS is the GH in figure 3.20. As before, the 2D map of its current losses as a function of its refractive index and GH is depicted in figure 3.30,a. In this case, the minimum-losses region corresponds to refractive indices from 1 to 2.1, and GH values from 150 nm to 300 nm, with minimum losses current of 7.4 mA/cm^2. This refractive index range allows the use of several dielectric materials to play this role: MgF_2 ($n \approx$1.37 at λ =600 nm), SiO_2 ($n \approx$1.45 at λ =600 nm), PMMA ($n \approx$1.6 at λ =600 nm), SiN_x (can be tuned around 1.8 at λ =600 nm using the x percent of nitride in the thin-film), or Si_3N_4 ($n \approx$2 at λ =600 nm). The current losses variation into this range is noticeable, because it could reach 7.9 mA/cm^2 for some cases. In this sense, MgF_2 could be the best selection, as it lies in the middle of the low-loss zone and within a wide range of GH values, from 125 to 300 nm. Considering the selection of MgF_2 as a dielectric spacer, with an optimized geometry of GH = 240 nm, and GW = 330 nm, the absorbance and reflectance results are shown on the right side of figure 3.30, for both incident polarizations: TE (figure 3.30,b) and TM (figure 3.30,c). This case provides a matched J_{SC} of 19 mA/cm^2, which is 17.2%better than the planar case (16.2 mA/cm^2).

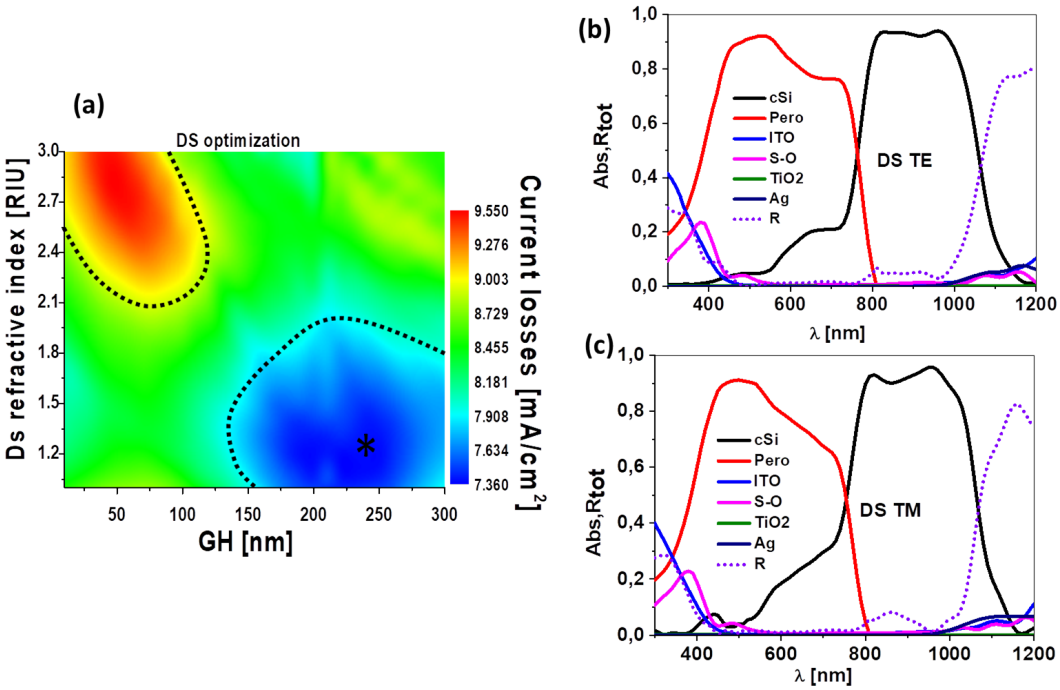

Figure 3.30: Spacer analysis. (a) Current loss map depending of the refractive index of the spacer material and the thickness of the layer. (b,c) Absorbance of every layer and total reflectance for the selected case (* in a) under TE (b) and TM (c) illumination.

As it can be observed, there is a similar behavior in all the maps (see figures 3.28,a, 3.29,a, and 3.30,a) : minimum losses tend to appear at low refractive indices and high thicknesses. The low effective index of the metasurface should have a better optical matching with surrounding layers. We also guess that high thicknesses imply both the increase of the perovskite volume and a better optical guiding effect through the grating, reducing reflections [203]. Figure 3.31

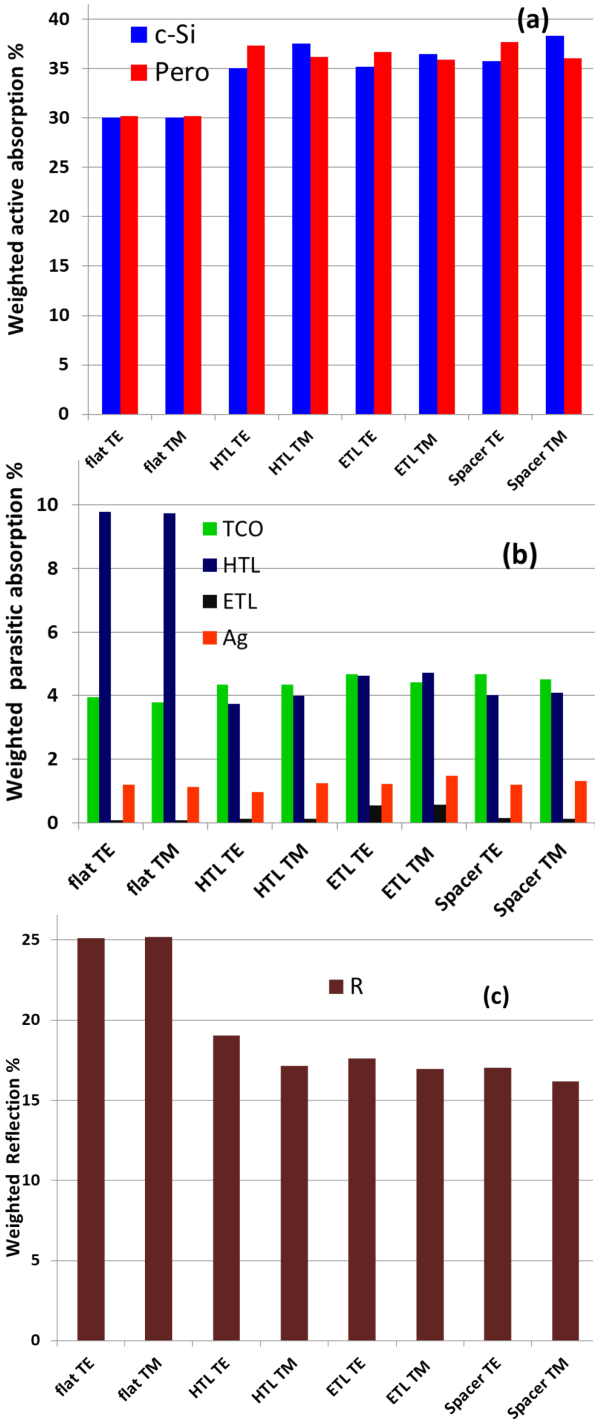

Figure 3.31: Power distribution for (a) the absorption at active layers, (b) the absorption in non-active layers (losses), and (c) power losses due to the reflectance of the structure.

shows the absorption weighted to the incident solar flux, and reflections in the layers of the planar reference and the nanostructured cases that we selected above. As before, the HTL, ETL and DS cases refer to the above selected HTL (figure 3.28,b,c), ETL (figure 3.29,b,c) and DS (figure 3.30,b,c) cases. In particular, figure 3.31,a shows the weighted absorption in both the c-Si and the perovskite volumes. TE and TM polarizations are considered. While the reference case is completely polarization insensitive, the addition of the nanostructure produces certain polarization sensitivity, as expected. This means that TE/TM polarization cannot guarantee a perfect current matching in the nanostructured case if used to illuminate the device individually. However, a non-polarized case, as expected for solar illumination, resembles the current matching condition. Figure 3.31,b shows the weighted absorption losses at each non-active layer for the same considered cases, while figure 3.31,c shows the losses due to the device reflectance. Figure 3.31,c shows a reduction of the total reflectance of the device from 25% to less than 20% for all nanostructured cases, being the lowest reflection losses for the optimized spacer layer case as 16%, which is a 36% reduction of the weighted reflection of the nanostructured device compared to the planar device. In the planar device, the HTL layer accounts for high absorption losses, which decreases by more than 50% when the HTL layer is nanostructured. The rest of the layers, TCO, Ag, and ETL have low losses. For example, TCO has around 4% of absorption losses with a little increase for the nanostructured cases. The back contact has about 1% with a little increase for the nanostructured cases. Finally, the ETL layer has negligible absorption losses except when TiO_2 is replaced by ZnO, which accounts for 0.5% absorption losses. Although the selected ETL material (ZnO) accounts for higher absorption losses with the ETL layer itself compared with TiO_2, The device with ZnO has a lower total reflectance, and better performance in terms of the J_{SC} value.

4

Optical sensors based on surface plasmons

The capability of photonic nanostructures to efficiently control light propagation and intensity at the nanoscale is widely employed in various optical devices. They can be configured as perfect absorbers [106, 227], broadband scatterers [228, 229], optical filters [230, 231, 232], etc. Optical sensors incorporating nanostructures provide devices with improved performance for various applications. As an example, they're applied to quantitative chemical analysis [233], and refractometers for gases, bio-samples, and chemical materials [234, 235, 236].

In chapter 1, and 2, we introduce the Kretschmann configuration method, and the governing equations (2.17, and 2.19). We simulate the Kretschmann design and compare the simulated results with the analytical ones at the end of chapter 2, in section 2.3.2. Kretschmann's design can be used to measure the variations of the index of refraction of various materials [237]. The basic setup of this configuration consists of a transparent prism coated with a metal layer, which will be in contact with the analyte under analysis (see figure 4.1). The key parameters to optimize the performance of this set-up are: the metal layer (or layers) thickness and material type, the index of refraction of the prim, and also, the operating wavelength.

A Kretschmann configuration based sensor can achieve maximum theoretical sensitivity of 600 deg/RIU using a low index prism ($n = 1.32$) and an angle of incidence of $\sim 81^\circ$ [237]. The requirement of a low refractive index material for the prism is limited by material availability. A few polymers, such as Cytop ™($n_{\text{Cytop}} = 1.34$) [238], exceptionally reach low values of the index of refraction. Magnesium fluoride, MgF_2 ($n_{MgF_2} = 1.37$), is another alternative with a slightly higher refractive index, but it has an advantage as a commercially available material, transparent in the VIS and NIR spectrum ($\lambda \in [300, 2000]$ nm). Besides, MgF_2 can be spin coated to produce flat interfaces when coating nanostructured reliefs [239]. Furthermore, both a large angle of incidence and a low index material, needed for an optimum Kretschmann design, reduce the device's dynamic detection range [237]. Intensive research was conducted over the last decade to overcome these limits. Different designs of SPR sensors based on spectral interrogation, and more sophisticated geometries were reported [240, 241, 242, 243, 244].

The general performance parameters of an SPR sensor are: sensitivity, Figure of Merit (FOM), resolution, linearity, dynamic range, and reproducibility [77]. However, their importance depends on the application. For example, the sensitivity and FOM are more important than the dynamic range if the sensor is applied to check small changes in the index of refraction, for example, to sense gas contamination in a closed chamber. Sensitivity is the shift of a measurable parameter of the device (a reflectance, transmission, absorption dip or peak, intensity,

temperature change, etc.) with respect to a controlled variable (angle incidence, wavelength, power, etc.) due to a change in the sensed property (refractive index, color, etc.) [77].

In spectral and angular interrogations, the FOM combines the sensitivity and the spectral line-shape characteristics in a single parameter, that compares different sensors technologies. The resolution determines the quality of the measurement, when the device is used to detect the minimum change of the sensed property. Linearity means a constant value of sensitivity through the entire dynamic range of the sensor. Although high linearity responses have been reported [241, 245, 246], most plasmonic sensors have not perfect linear response [241]. The dynamic range is the maximum change of the sensed property that can be detected with the sensor. In refractometric sensors, recent contributions show devices with wide dynamic range up to 0.5 RIU [240, 241, 242, 243, 244], and devices with a tunable dynamic range [247]. In summary, to design an efficient sensor, we need to maximize the sensitivity, FOM, resolution, linearity, and dynamic range, with reliability and reproducibility of the proposed geometry. However, if the sensor has a specific application, for example, monitoring water quality, the wide dynamic range is not as important as sensitivity and FOM. So, for some cases, we will be interested in maximizing a specific characteristic of the sensor rather than others.

The performance of a spectrally-interrogated plasmonic sensor relies on the precise measurement of the spectral location of the minimum (or maximum) of its response. So, a narrow spectral response improves the accuracy of the sensor. Fano resonances can be generated when a narrow SPR resonance mode, coherently interferes with a continuous or broad spectral response, like a diffraction order [248]. However, this superposition often generates asymmetric spectral line-shapes that can contain both minimum and maximum peaks around a single resonance. Also, these duplicated peaks are typically narrower than those obtained for symmetric profiles. These spectral features strongly depend on the characteristics of the coherent superposition responsible for a Fano resonance. Therefore, the generation of Fano resonances can improve the performance of nanophotonic structures [249, 250, 251, 252, 253] and plasmonic sensors [254, 255, 256, 257, 258, 259, 260, 261].

Some other SPR sensor designs maximize the electromagnetic energy at the metal/dielectric interface (where SPs are generated)[262]. For example, it is possible to include a subwavelength metallic grating to scatter radiation towards the region of interest, using a normal incidence illumination conditions. The scattering efficiency of this structure improves the resolution and detection range of the device. The performance of the device is high for low n, but decays as n increases. So, improving the scattering efficiency of the structure, enhances the sensor performance parameters. Wide band high scattering responses can be achieved through a high contrast in the index of refraction around the scattering object [263].

The organization of this chapter is made as follows. Sections 4.1 and 4.2 present our results in the analysis of SPR sensors that use metallic gratings to excite the SPRs. Section 4.1 shows the basics of the analysis of a simple structure made of a metallic subwavelength grating that scatters radiation towards a metallic/dielectric interface where the SPRs take place. This mechanism, along with a funneling effect caused by a multilayered structure of metallic gratings, is exploited in section 4.2 to improve the performance and analyze the differences between resonances caused by selective transmission and SPR. After this analysis with metallic gratings, we move to dielectric gratings with a nanoprism profile. This geometry has been also proved as an advisable solution for solar cells (see section 3.2). In this chapter we focus on its use to excite SPRs for sensing. First, in section 4.3 we analyze the funneling mechanism caused by this geometry and how this helps to improve the parameters of sensors based on SPRs. Then,

sections 4.4 and 4.5 consider how the analysis of the electromagnetic behavior of the sensor requires the description of the hybrid interactions between SPR, low-order grating modes, and funneling and guiding mechanisms. In this sense, section 4.4 fully exploits these interactions, modeling the hybrid resonances and taking advantage of them to push the performance of the proposed sensors. The chapter finishes with a section (section 4.5) devoted to the explanation of the sensor response as a Fano resonance between the grating behavior and the SPRs.

4.1 Basic metallic gratings

The improvement of optical sensors can be achieved through two different approaches: firstly, by increasing the performance of the existing technologies and sensing schemes; and secondly, by proposing novel designs with better performance, and different sensing mechanisms that can ease the operation and the integration of the system in different environments. In this section, we proposed a device that can be considered as an efficient alternative to the conventional Kretschmann configuration in figure 4.1,a [262]. The device is capable to operate under normal incidence conditions allowing its integration with the illumination system. For example, the device can be attached to the end of an optical fiber, setting a collimation optics that is finished by the proposed sensor arrangement fabricated on a glass substrate. The main components in the Kretschmann based sensing system are the goniometer, spectrometer, and the sensing device, which involves mechanical moving parts. Using normal incidence conditions to illuminate the device, we only need a spectrometer to operate the device.

4.1.1 Geometry and materials of the sensor

The proposed geometry of the sensor is an extruded profile with a 2D cross section that is presented in figure 4.1,b. It consists (from top to bottom in figure 4.1,b) of a dielectric transparent flat substrate, a nanostructure organized as an array of nano-slits printed on a thin metal film, and a dielectric stand-off layer that is terminated by a very thin metal/dielectric double layer. The analyte, or medium under test, is in contact with this last double layer where the SPR propagates and interacts with the media under test. The thin dielectric film is inserted between the last metal layer and the analyte to prevent the interaction between them and to serve as a protecting layer for the metal. To evaluate of the interaction mechanisms involved in this proposal, we have arbitrarily selected some feasible parameters and materials for the design in figure 4.1,b.

The material arrangement is deposited on a flat glass substrate made of SiO_2 (optical constants from [186]). The first metal nanostructure slits are made of Au (with complex refractive index data obtained from [128]) having a thickness GH, width GW, and arranged with a spatial period P. The role of the nanostructure is to generate a scattering pattern that illuminates a second metal-dielectric interface. After this nanostructure, a dielectric buffer, or stand-off layer, made of MgF_2 (refractive index was taken from [185]) is deposited with a thickness, t_{BL}. MgF_2 can be spin coated [239, 264] and the resulting surface is planarized for further deposition.

After this stand-off layer, a second metal layer, M2, is made of Ag (with complex refractive index data obtained from [128]), in the form of a thin-film having a thickness of t_{M2} is deposited. Finally, an MgF_2 dielectric film, with a thickness of 10 nm serves as a protecting layer for the Ag thin-film. The analyte is in contact with this last metal/dielectric double layer. For simplicity, we considered a water based solution as the analyte medium. Therefore, we have four material

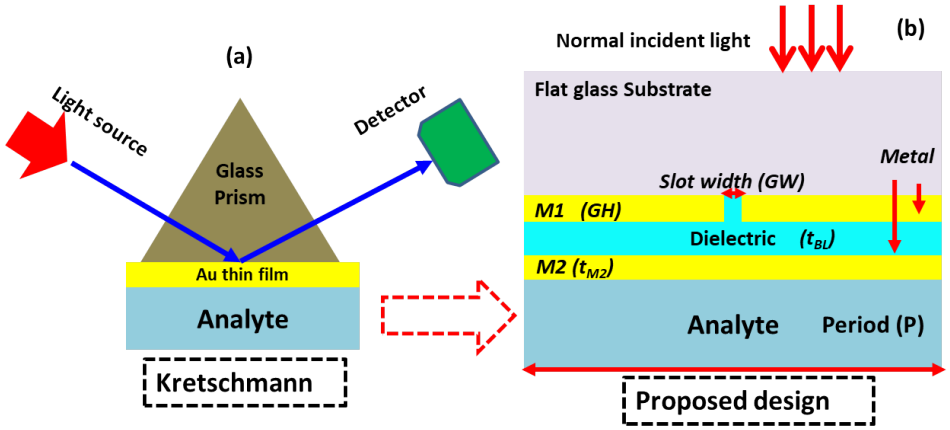

Figure 4.1: (a) Classic Kretschmann configuration with a glass prims coated with a Au thin-film in contact with the analyte. The SPR is generated at the metal/analyte interface. (b) 2D cross section of the unit cell of an array of long-wire slot antennas (nanoslits) that diffract light towards the thin metal/analyte interface where the SPR can be generated. The system is deposited on a glass substrate as a nanostructure metal layer with a geometrical parameters of GH, GW and P, a dielectric buffer layer, BL, and a final second metallic layer, M2. The SPR happens at the M2/analyte interface.

choices (for the two metals, the dielectric buffer layer, and the dielectric substrate), three thicknesses (GH, t_{BL}, and t_{M2}), and two more geometrical parameters that define the nanoslit array (GW and P).

4.1.2 Parameterization and optimization

A plasmonic sensor using the Kretschmann configuration must satisfy equation (2.19). In the proposed design, light scatters at the metallic nanostructure and generates a wide range of directions for the propagating vector. This phenomenon can be seen as subwavelength diffraction. The scattered radiation propagates through the dielectric buffer layer toward the second flat metal thin-film. Then, an SPR is generated at the metal/analyte interface when light fulfills the grating coupling matching condition equation (2.21).

The sensitivity of a plasmonic sensor, S_B, is linked to the shift of the minimum of the reflectance, in terms of the angle, $\Delta\theta$, for angular interrogation, or wavelength, $\Delta\lambda$, for spectral interrogation, when the refractive index of the analyte changes by Δn. For example, in Kretschmann configurations based on angular interrogation, it is common to express it as [237]:

$$S_{B,\theta} = \frac{\Delta\theta}{\Delta n}. \tag{4.1}$$

Alternatively, for plasmonic sensors based on spectral interrogation, the sensitivity is written as:

$$S_{B,\lambda} = \frac{\Delta\lambda}{\Delta n}, \tag{4.2}$$

where the subindex θ, or λ, defines the parameter used in the interrogation of the system. Although sensitivity, S_B, relates those parameters involved in the operation of the system, it still does not fully characterize the performance of the device. This is better expressed as the FOM of the sensor. This parameter is defined as the sensitivity, S_B, divided by the angular, or spectral, full width at half maximum (FWHM) of the spectral reflectance plot. Using this

approach, FOM is expressed as [265]:

$$\text{FOM} = \frac{S_B}{\text{FWHM}}. \tag{4.3}$$

The goal of the design is to obtain high values of S_B and FOM. When the incoming light is efficiently coupled to plasmonic absorption, the total reflectance is minimum. So we can optimize the design by searching the geometrical parameters and materials that lead to a minimum reflectance. However, we have two metallic layers in the design, and we are interested in enhancing the plasmonic absorption at the planar metal /analyte interface, which leads to a maximum field intensity inside the analyte, and hence it will be more sensitive to variations in the analyte refractive index. To limit our search to only those parameters that leads to strong SPR at the metal/analyte interface, we should combine the efficient light coupling (minimum reflectance), with the high field concentration at the desired location (maximum field inside the analyte) in a single merit function (MF). A simple definition for this function is:

$$MF = H_{max} \times (1 - R), \tag{4.4}$$

where H_{max} is the maximum field at the analyte, and R is the total reflectance of the device. Our goal is to maximize the value of MF which will make H_{max} large and R minimum.

A Comsol model is built for the unit cell of the geometry presented in figure 4.1,b. The structure is illuminated with a plane wave (TM mode) and having a magnetic field amplitude of 1 A/m oriented perpendicular to the plane presented in figure 4.1,b. We arbitrary set the geometrical parameters and materials for the design in figure 4.1,b as listed in table 4.1.

Table 4.1: Materials and layer structure of the metalslit sensor

Layer	Material	Dimensions
Substrate	SiO_2	∞
Grating	Au	height GH, width GW, and period P= 1000 nm
Buffer layer	MgF_2	$t_{BL} = 300$
Thin-film	Au	$t_{M2} = 35$ nm
Analyte	water based solution	∞

The optical response for this structure reveals three minima of the spectral reflectance (see figure 4.2,a) corresponding to three different interactions with the device layers. The magnetic field spatial distributions for the three modes are presented in figure 4.2,b,c,d. These maps reinforce the previous explanation of the involved physical mechanisms. The shortest wavelength minimum (SPRM2 in figure 4.2,a) corresponds with the SPR that happens at the metal/analyte interface. This interface is flat, allowing easier maintenance and operation. Furthermore, a strong field concentration happens at the analyte produced for this resonance as in figure 4.2,b. The second minimum (SPRM1 in figure 4.2,a) appears as an SPR at the metal grating/substrate interface. SPRM1 resonance is isolated from the analyte, and there is no direct interaction between them. The field concentration is higher at the grating substrate interface (see figure 4.2,c). There exist a third minimum related with a guided mode within the stand-off buffer dielectric layer as in figure 4.2,d. This guiding mode is produced by the funneling mechanism that exists for metal/dielectric structures with narrow aperture [201, 266, 267, 268]. Therefore, we focus our attention on the SPRM2 resonance, that is directly

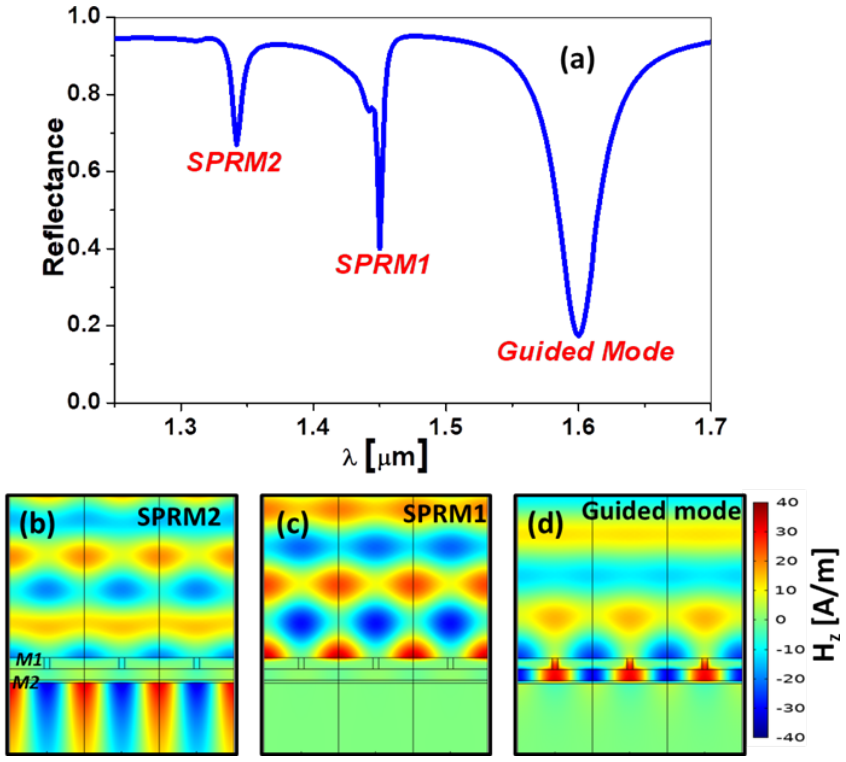

Figure 4.2: (a) Spectral response of the device showing three reflectance dips: SPRM2 appears at the M2/analyte interface, SPRM1 appears at the substrate/M1 interface and it is not accesible in this design, and a guided mode that correspond to ligth trapped within the buffer layer. (b),(c),(d) Magnetic field maps at the wavelengths where the three minima of the reflectance occur.

happening at the metal /analyte interface so, it will be more sensitive to variations in the analyte.

The optimization of the device requires the modification of the geometrical dimensions and an appropriate choice of the materials used for the deposition of the layers. To do that, we may apply a multidimensional optimization of the device where all the available parameters are considered simultaneously. This strategy would need the definition of an optimization MF (see equation 4.4),(this function cannot be mistaken with the FOM parameter in equation (4.3), FOM). To provide a clear insight into the effect of a given geometrical parameter on the response of the device we perform the optimization for each layer separately. Five geometrical parameters are at play in this device. The grating geometry (height GH, width GW, and period P). The buffer layer thickness t_{BL}, and refractive index n_{BL}. The thin metal layer thickness t_{M2}), and substrate type. Both, the metallic grating and thin-film metal layer can be from the same material or a combination of different materials. We will study the device performance for two metals that are widely used in plasmonic sensors: Ag, and Au.

The starting point for the optimization process shown in figure 4.1,b, and listed in table 4.1. First, we fix the resonance wavelength at 1500 nm arbitrarily to scan for the grating geometry (GH and GW), that maximizes the merit function for each selected metal: Ag and Au. We will show in the next step how the period parameter can be used to tune this operating wavelength. The optimization map for the device having the grating and the thin metal layer made of Ag is shown in figure 4.3,a. In this map, several combinations of the grating parameters GH and

GW lead to large MF, for example, the GH values range from 50 nm to 200 nm, and GW ranges from 50 nm to 600 nm. The highest MF is obtained for GH=100 nm, and, GW= 470 nm.

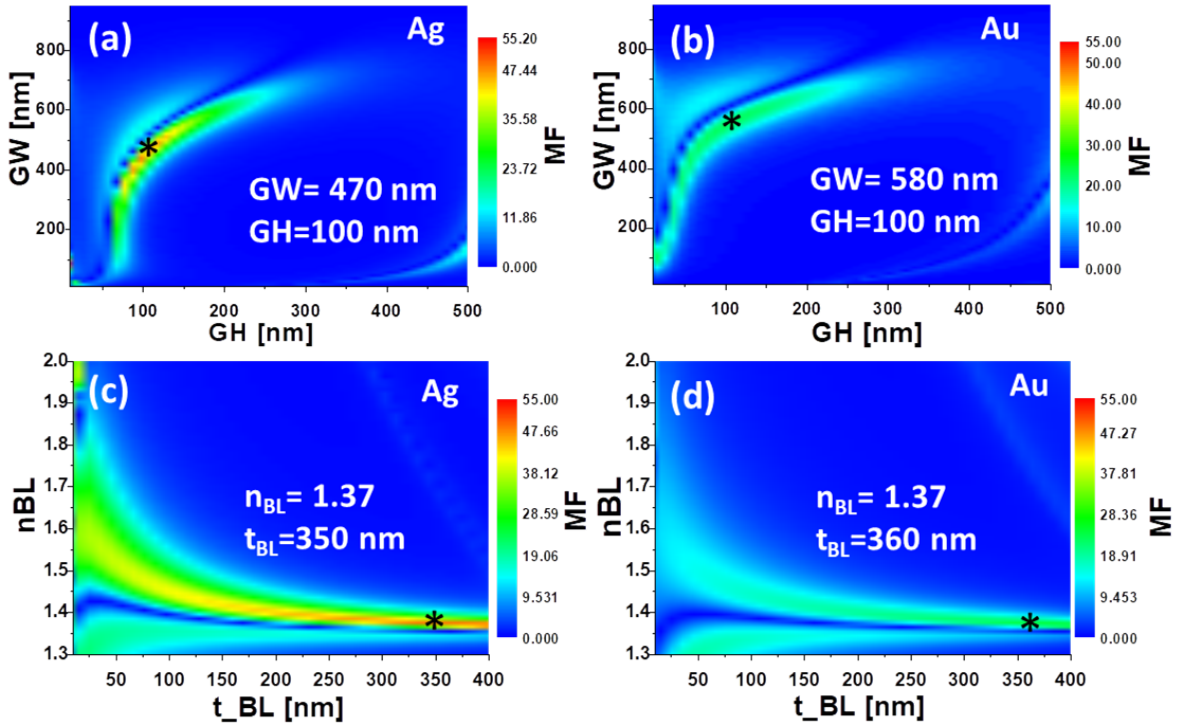

Figure 4.3: (a), (b) Optimization maps for the grating width (GW), and height (GH) of the design with Ag, and Au metals, respectively. (c), (d) Optimization maps for the buffer layer thickness t_{BL}, and material n_{BL} for Ag, and Au metals, respectively.

The optimization map for the design with both the grating and the thin metal layer made of Au is shown in figure 4.3,b. The selected optimum parameters for this case are GH = 100nm and GW = 580nm. The optimized parameters at each step are used as a starting point for the next optimization. For the buffer layer, we should search for materials that could be spin-coated or casted to fill the nanoslit and generate a flat surface to deposit the last metal layer, M2 on top of it. Some examples are MgF_2, $SiO2_2$, poly-methyl methacrylate (PMMA) (optical constants from [187]), and AZO (optical constants from [167]). This layer is of importance because it transfers the scattered radiation from the nanoslits towards the metal/dielectric interface where the SPR is generated. Both, the thickness and material type of the buffer layer, can affect the propagation of the scattered radiation coming from the nanostructured first metal layer, M1, and impinging on the second metal layer, M2. The optimization presented in figure 4.3,c for Ag and 4.3,d for Au is made in terms of the index of refraction and thickness of the buffer layer. We limit our study for refractive index between 1.3 and 2, which correspond to the majority of dielectric materials, and assume a lossless property for it (the refractive index real) to simplify the calculation. This assumption of a lossless material for the buffer layer is valid for many dielectrics such as glass, MgF_2, PMMA, etc. The highest MF is obtained for t_{BL} = 350 nm, and refractive index n_{BL}= 1.37 for the design with Ag, and t_{BL} = 360 nm, and refractive index n_{BL}= 1.37 for the Au case. The thickness of the second metal, t_{M2}, also modifies the spectral reflectance line-shape. The reflectivity is low, almost zero for a thin metal layer thickness of t_{M2} = 35 nm, which is chosen as optimum. Increasing or decreasing the thin metal layer from

this value leads to a shallower reflectance (see figure 4.4,a for Ag, and figure 4.4,b for Au), meaning a less efficient coupling of the incoming radiation into the SPR resonance. The design has almost the same behavior for Ag and Au metals when a parameter changes, however, the Ag response is always much narrower.

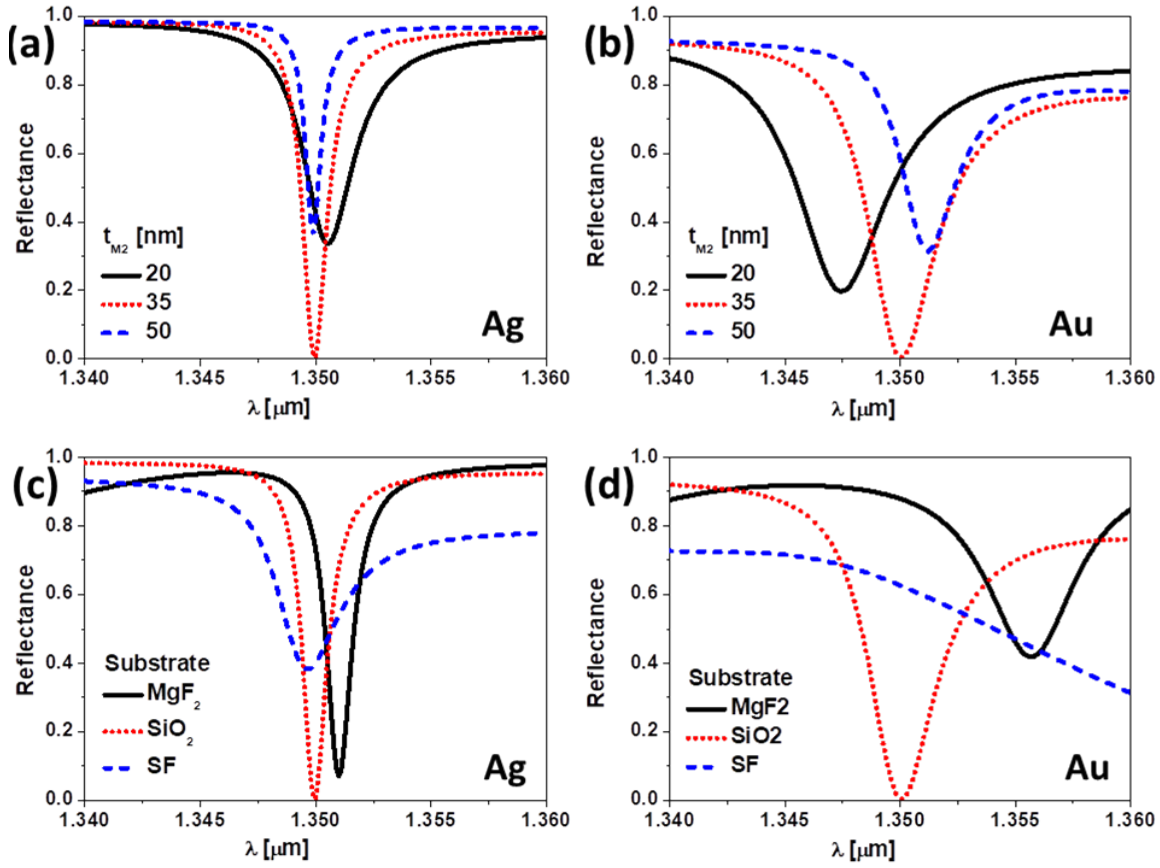

Figure 4.4: (a),(b) Spectral reflectances that show the effect of the Ag and Au thin-films respectively on their designs response. (c),(d) Spectral reflectances that show the effect of the substrate type on the reflectance line shape for Ag and Au designs, respectively.

For the substrate, some feasible options arranged from lower to higher index of refraction, n_s, are MgF_2, SiO_2, and SF glass (optical constants from [269]). As far as the optimization process has been done for a SiO_2 substrate, changing the substrate type strongly affects the optical response of the design (see figures 4.4,c, and 4.4,d for Ag, and Au, respectively). This behavior is not the same as that obtained for Kretschmann configurations, where a low index substrate is preferable to enhance sensitivity. This difference can be explained by the material arrangement of the proposed device, where the buffer layer (BL) works as an effective substrate, requiring a low index material to optimize the device. The Ag layer may oxidize and interact with the solutions, so, we need to add a passivization layer on the top of the Ag layer to protect it and prevent its interaction with the analyte. As we see from the response of the design with Ag and Au metals in figure 4.4, the design with Ag has a narrower response than Au. So, in both cases we can replace the Ag and Au thin-films by Ag-Au bi-layer, having Au adjacent to the analyte for both cases. We keep the total thickness of both layers at the optimized one (35 nm), a schematic for this change is depicted as insets of figure 4.5. The results show that a bilayer made of Ag (30 nm thick) and Au (5 nm thick) behaves better for both cases.

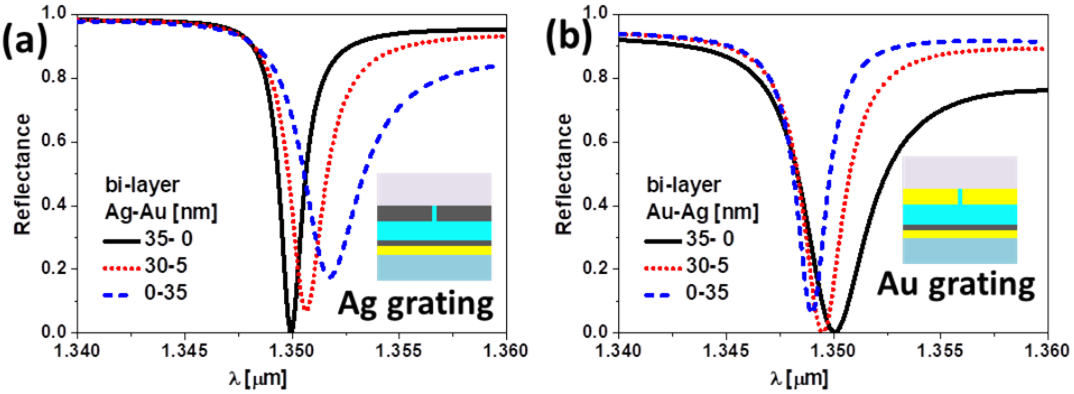

Figure 4.5: (a)(b) The effect of the bi-layer Ag-Au thin-films combinations on the reflectance line shape of the Ag and Au designs respectively. The xx-xx numbers in the legends mean the Ag-Au thicknesses.

From the previous sequential optimization, we find the optimum arrangement for each design, which is listed in table 4.2.

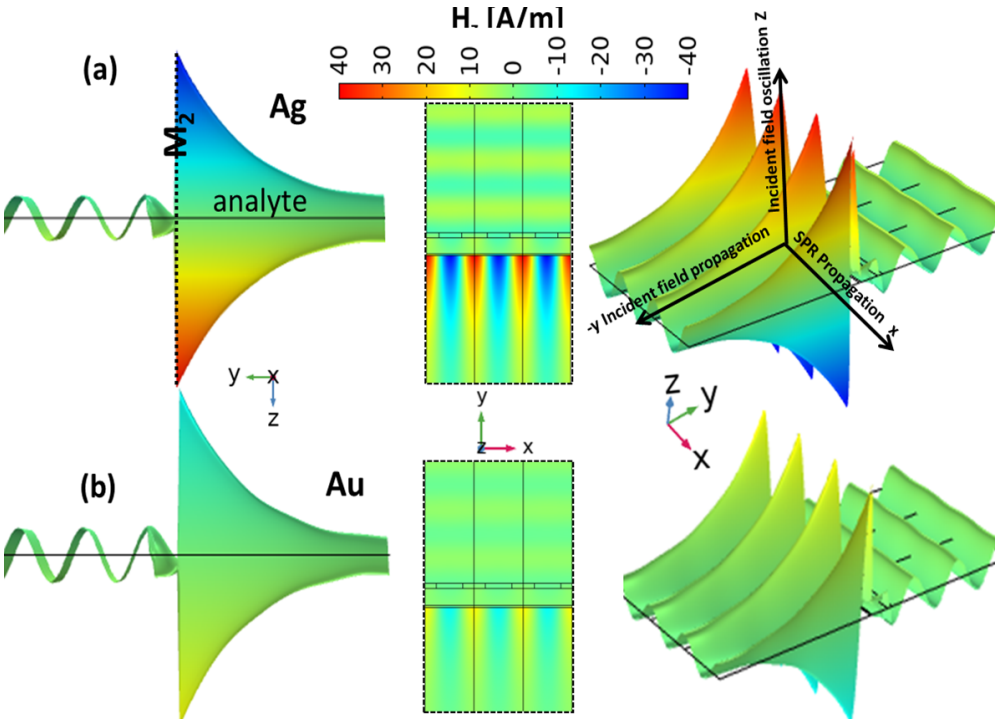

Figure 4.6: (a) ,(b) Magnetic field z- component distribution at resonance for the Ag and Au designs, respectively.

This structure produces a profile of the amplitude of the magnetic field that has a maximum at the second metal/analyte interface, where the SPR is generated. Figure 4.6 left map shows how the SPR amplitude is fitted to an exponential decay function of the form:

$$H = Ae^{-y/\delta_y} + B, \tag{4.5}$$

where A, and B are constants with magnetic field dimensions, y is the coordinate along the

direction of propagation, and δ_y is the decay length of the SPW. The fitting of the model provides a value of $\delta_y = 960$ nm, which is directly related to the interaction volume.

The field distributions at resonance in different orientations of the unit cell are shown in figure 4.6, where the propagation direction and plane of the incoming radiation and the propagation direction of the SPW are illustrated. Although it is possible to fabricate a uniform ultra-thin-film Au films as a passivization layer [270], it is easier and more practical to use dielectric materials, which can be evaporated or spin coated.

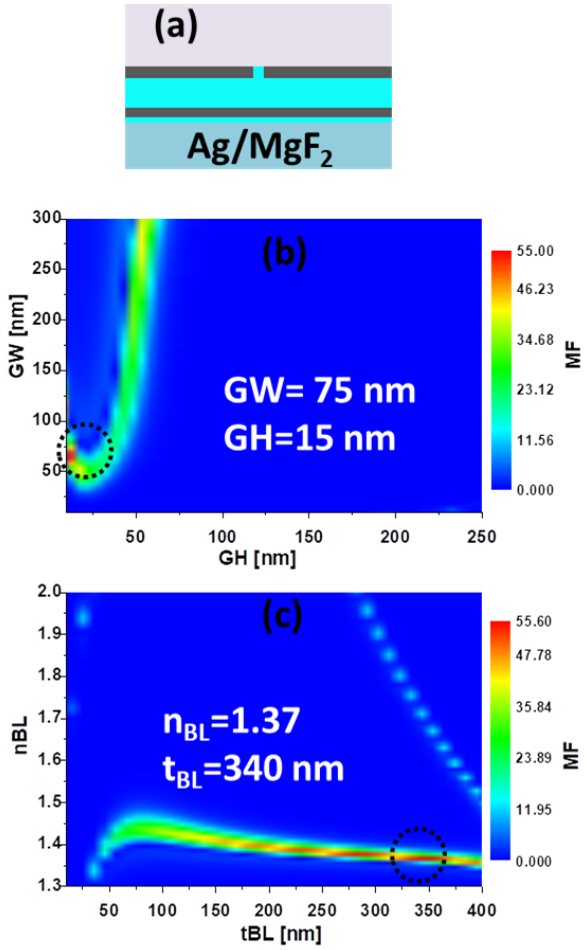

Figure 4.7: (a) A schematic for the device using a dielectric passivization layer between the Ag thin-film and the analyte. Optimization of (b) the geometrical parameters, and (c) the buffer layer for the dielectric passivization case.

In figure 4.7,a, we show the schematic of the device using 10 nm MgF_2 as a passivization layer for the design with Ag thin-film. The optimized designs with Ag, show a narrower optical response compared with those with Au (see figure 4.4). However, Ag is highly oxidized metal, and highly interactive with the environment. For these reasons, we passivate the Ag designs with a very thin layer of Au to overcome these issues, and to take advantage of the narrow response of Ag. Although the optimized Au passivation layer is very thin, it alters the response of the devices (see figure 4.4). As an alternative, we passivate the device with a thin layer made of dielectric material. Following the same optimization procedure and using the same MF, we calculate the optimum geometrical parameters of the grating GH, GW as 15 nm, and 75 nm,

respectively. The buffer layer optimization reveals a similar finding for the device without dielectric passivization as we obtain an optimum of 1.37, and 340 nm for the n_{BL}, and t_{BL} respectively. The optimized thickness of the thin metal layer t_{M2} is 35 nm, and SiO_2 is the optimum substrate.

4.1.3 Device performance

We have optimized the design with three configurations depending on the materials used for the metallic grating, thin metal film, and the passivization layer. The final device can have one of the three structures listed in table 4.2. Now, it is possible to evaluate sensitivity and FOM defined in equations (4.2, and 4.3), for these three optimized designs.

Table 4.2: Optimized geometrical parameters for metallic silts structures

Design	Material	Dimension and shape
Au/Ag-Au		
	SiO_2	∞ substrate
	Au	(GH =100 nm, GW =580 nm) grating
	MgF_2	(t_{BL}=360 nm) thin-film
	Ag-Au	(t_{M2}=30+5 nm) bi-layer thin-film
	H_2O	∞ superstrate analyte
Ag/Ag-Au		
	SiO_2	∞ substrate
	Ag	(GH =100 nm, GW =470 nm) grating
	MgF_2	(t_{BL}=350 nm) thin-film
	Ag-Au	(t_{M2}=30+5 nm) bi-layer thin-film
	H_2O	∞ superstrate analyte
Ag/Ag-MgF_2		
	SiO_2	∞ substrate
	Ag	(GH =15 nm, GW =75 nm) grating
	MgF_2	(t_{BL}=340 nm) thin-film
	Ag-MgF_2	(t_{M2}=35+5 nm) bi-layer thin-film
	H_2O	∞ superstrate analyte

We fix the refractive index dynamic range as $n_a \in (1.33, 1.35)$ to compare the three designs. The Ag/Ag-Au, and Ag/Ag-MgF_2 designs, show better performance compared with the Au/Ag-Au design. Ag/Ag-Au has a maximum sensitivity, and FOM of 1000 nm/RIU and 705 RIU^{-1} respectively. Although sensitivity slowly degrades for this design within the selected dynamic range, the FOM greatly decreased by more than 47% of its initial value and becomes 370 RIU^{-1} (see figure 4.8,a). The Au/Ag-Au design shows moderate values for the FOM but degrades fast too, having a maximum sensitivity and FOM of 940 nm/RIU and 453 RIU^{-1}, respectively (see figure 4.8,b). The Ag/Ag-MgF_2 design has maximum sensitivity and FOM of 955 nm/RIU and 734 RIU^{-1}, respectively (see figure 4.8,c). Both sensitivity and FOM for Ag/Ag-MgF_2 design, slowly degrade compared to the two other designs, where the values of

sensitivity and FOM reaches 931 nm/RIU and 534 RIU^{-1}, respectively, at $n_a = 1.35$. As a final step, we make a comparison of our results with recently reported values in this field [271].

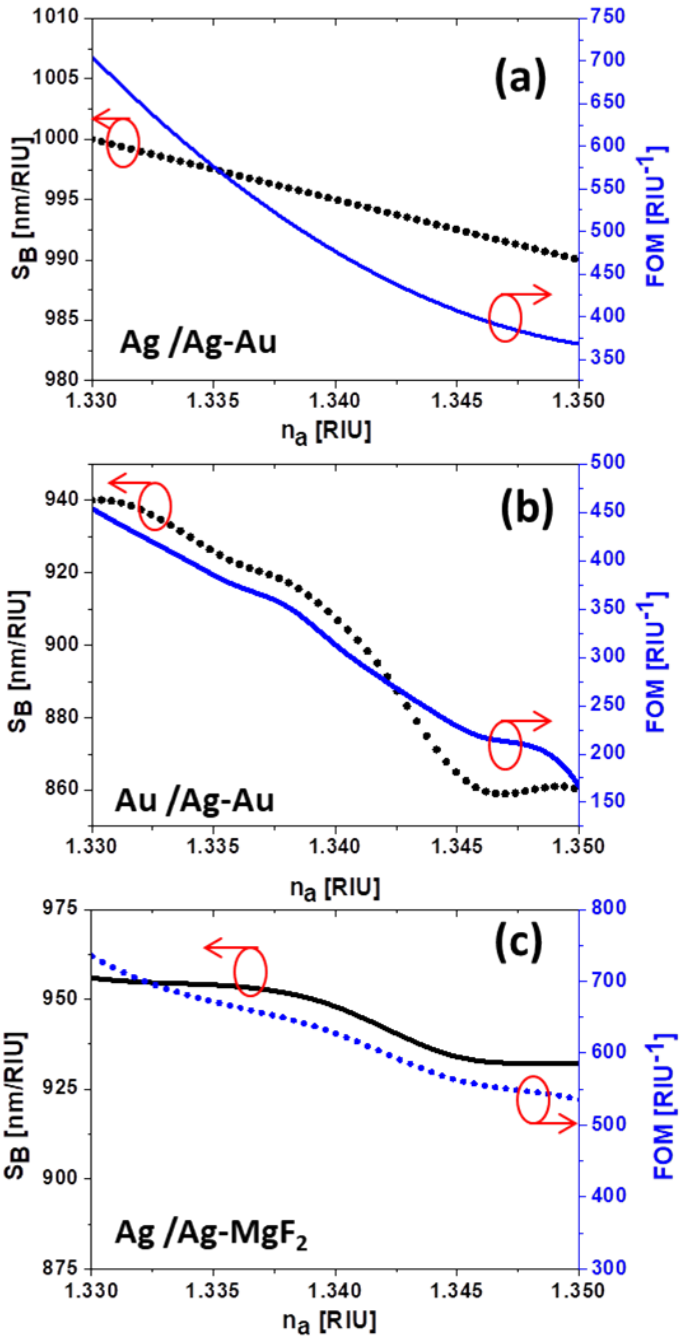

Figure 4.8: Sensitivity and FOM for different values of index of refraction of the analyte n_a for (a) the Ag/Ag-Au design, (b) the Au/Ag-Au design, and (c) the Ag/Ag-MgF_2 design.

At this point, we should emphasize that sensitivity values can be misleading because they don't fully represent the performance of the device. As a result, we can obtain a high value of sensitivity, above 1000 nm/RIU, with a low value of FOM, below 100 RIU^{-1}, that may limit its practical application. The goal is to obtain in the same device a large value of sensitivity and FOM, within a wide range of values for the index of refraction. A comparative for the

values of S_B and FOM of different previously reported designs and our work here is listed in table 4.3. When comparing the device with the previous proposal we can see that the $S_{B,\lambda}$ provided for our design is higher than those reported in [272] (graphene/graphene oxide-based SPR) [273] (silicon nanostructures) [237] (maximum theoretical limit for Kretschmann configuration), [81](nanogrooves at the analyte interface), [274] (excitation by dielectric grating) [275] (single Au nanorods), [276] (aluminum (Al) gratings coated with Au), [277] (Au coated over Ag nanoprisms), and [278] (metallic metasurfaces). The calculated value of $S_{B,\lambda} = 1000$ [nm/RIU] is comparable to those obtained for an Au flat interface [275]. This value of sensitivity is also higher when compared against $S_{B,\theta}$ reported in [279] (MoS_2-graphene structures), [280] (ZnO films), and [281] (MoS_2/graphene hybrid structure). A final comparison in terms of the FOM parameter also shows a better performance of the proposal presented in this contribution than previously reported values for this parameter [275, 277, 280, 281].

Table 4.3: Maximum values of sensitivity and FOM for the optimized silts structures, and some similar reports

Design	Interrogation	S_B [nm/RIU] or [deg/RIU]	FOM (1/RIU)
Ag/Ag-Au	Spectral	1000	705
Au/Ag-Au	Spectral	940	453
Ag/Ag-MgF_2	Spectral	955	734
[278]	Spectral	700	-
[277]	Spectral	425	3
[81]	Spectral	500	-
[254]	Spectral	717	162
[282]	Angular	1010	108
[272]	Angular	120	-
[273]	Angular	155.68	-
[237]	Angular	600	-
[276]	Angular	247	-
[280]	Angular	203	20.1
[281]	Angular	140	19

4.2 Funneling in multilayered metallic gratings

A stack of metallic gratings with subwavelength features, embedded within a low-index dielectric medium can produce selective transmission or reflection of the incoming light [267, 268, 283]. Light is strongly confined through funneling mechanisms and excites resonances that senses the variations of the refractive index of an analyte medium. In this section, we propose two terminations of a multi-layer grating structure that works as a plasmonic sensor [284]. These proposals take advantage of the narrow spectral features produced by the light funneling effect to provide a plasmonic sensor with high FOM. The termination layers of the proposed designs will take into account the compatibility with aqueous solutions for their use in sensing biomedical samples.

4.2.1 Light funneling designs for sensing applications

The proposed structure is shown in figure 4.9. The geometry is described in 2D because the material profile is extruded along the third coordinate. It is made as a multilayer metallic grating having a narrow deep aperture that reaches the substrate. The material stack is made of metallic (Ag) and dielectric (Cytop) alternating materials. To allow substrate illumination, we choose SiO_2 as the substrate. Each metallic layer has a thickness of $t_{m,1} = t_{m,2} = 70$ nm, and the dielectric layer has a thickness of $t_{d,1} = t_{d,2} = 150$ nm, that results in a total height of $h = 440$ nm. Our selection for this geometry is based on previous studies on light funneling mechanisms using a hybrid multilayer grating structure [201]. The period of the grating is fixed as $P = 1150$ nm to spectrally locate the response around $\lambda_0 = 1500$ nm, where the availability of light sources and detectors is assured. As it has been previously proved, the grating period can be changed to tune the resonance wavelengths at the desired spectral location: an increase in P produces a red-shift of the spectral response of the structure. The width of the aperture, or slot, is $GW = 50$ nm and has been optimized to give the narrowest spectral response and the highest field confinement at the analyte interface (we consider water based solution as the target analyte, $n_{\text{water}} = 1.33$).

This structure can be fabricated by successive depositions of metal and dielectric layers that can be selectively etched after exposing the stack with the desired grating pattern through, for example, e-beam lithography. Then, the etched trenches are filled with the same low-index dielectric using spin-coating techniques.

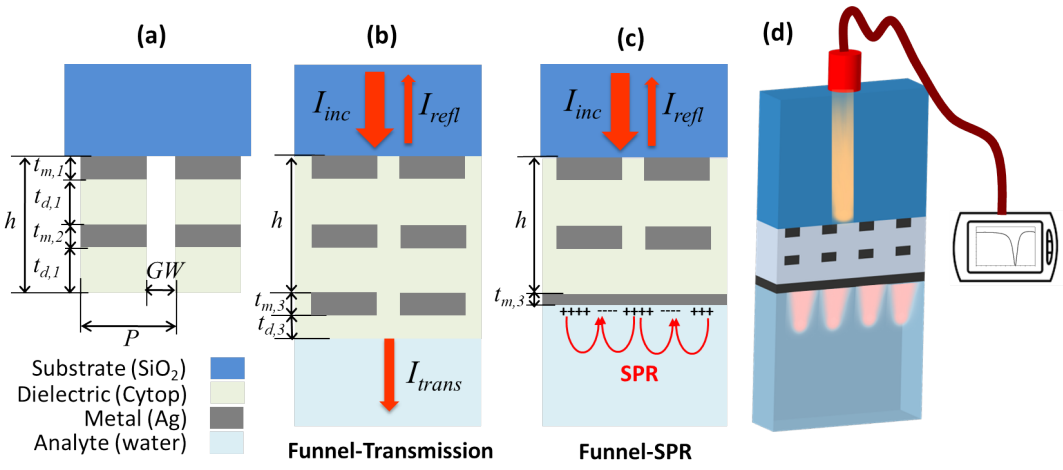

Figure 4.9: (a) Multi-layer metallic grating structure with periodic narrow slits (period, P) of width GW and height $h = t_{m,1} + t_{d_1} + t_{m,2} + t_{d,2}$. (b) The funnel-tranmission design adds another metal ($t_{m,3}$ in thickness) before etching the aperture. Then, the dielectric layer overfills the structure that has a full height of $h + t_{m,3} + t_{d,3}$. The dielectric is in contact with the analyte. The input irradiance, I_{inc}, is coming from top, and after interacting with the device is partially absorbed, transmitted (I_{trans}), and reflected (I_{refl}). These irradiances are represented as red arrows. (c) The funnel-SPR design is terminated with a continuous (no apertures) metallic layer having a thickness of $t_{m,3}$ (this thickness can be different than the one used in (b)). SPRs are generated at the interface between the metal and the analyte. Transmission towards the analyte is negligible, and the output of the system is read through the reflected irradiance, I_{refl}. (d) 3D graphical layout of the measurement system for the design in (c). Light is coming from the substrate and the reflectance is also retrieved in the same port, and the nanostructures have been enlarged to show the arrangement.

Using this basic arrangement, we analyze two possible variations of the termination of the

device. They differ in the material interfacing with the analyte. In the first design, which we name as funnel-transmission design (F-T), we stack a third metallic layer ($t_{m,3} = 70$ nm) over the two-layer basic structure (see figure 4.9,a) before etching the slits. Then, after engraving the slits, the device is finished with a flat dielectric layer (having a thickness $t_{d,3} = 70$ nm) producing a dielectric/analyte interface (figure 4.9,b). This is possible by overfilling the slots with Cytop^{TM} using a spin-coating fabrication method. The second design, named as funnel-SPR design (F-SPR), also fills the slots of the two-metallic stack with the same dielectric material (Cytop^{TM}). Then, the structure is terminated with a thin metallic layer (Ag) of $t_{m,3} = 45$ nm covering the whole device (this thickness for the third metallic layer is different than the one used in the funnel-transmission design). The analyte (water based solution) is in contact with the Ag surface (see figure 4.9,c). To improve biocompatibility and durability, we may add a very thin passivation layer (MgF_2) without compromising the good performance of the device [285].

There is a main difference between the physical mechanisms at play in both designs. The funnel-transmission device, having a dielectric/analyte interface, is based on the selective transmission of light through the subwavelength apertures towards the analyte. The funnel-SPR design generates SPRs at the metallic/analyte interface. In the following, we use both mechanisms to sense the change in the refractive index of the analyte.

A plane wave with its magnetic field oriented along the direction of the grating grooves (a TM mode) is launched from the port located at the substrate side with an amplitude of $H_0 = 1$ A/m. As a result, the modulus of the calculated magnetic field will be directly considered as field enhancement:

$$\mathrm{FE}(x, y, z) = \frac{H(x, y, z)}{H_0}, \tag{4.6}$$

where $H(x, y, z)$ is the calculated magnetic field amplitude and H_0 is the incident magnetic field amplitude. The performance of the refractometric sensor is evaluated using the two common parameters of optical sensors: sensitivity, S_B, and FOM.

4.2.2 Analysis and results

The narrow, high aspect-ratio, aperture of the geometry depicted in figure 4.9 transmits light selectively within a very narrow band. The result is the presence of absorption and transmission peaks at those wavelengths where light can generate resonances in the structure. Both the spectral response and field enhancement maps for the funnel-transmission design are shown in figures 4.10,a and 4.10,b. In these figures, the incoming light funnels through the structure and is fully coupled to resonant modes at two wavelengths located at $\lambda_{\text{F-T},1} = 1500$ nm and $\lambda_{\text{F-T},2} = 1512$ nm, respectively. In the first resonance at $\lambda_{\text{F-T},1}$, light is strongly confined within the first dielectric grating layer (having a thickness of $t_{d,1}$ in figure 4.9,a), and coupled to a plasmonic resonance at the metallic grating close to it. The transmission and absorption are almost equal. For the second resonance, located at $\lambda_{\text{F-T},2} = 1512$ nm, a weak absorption occurs within the structure, and most of the incoming light is selectively transmitted within a very narrow band. As a result, more fields will be available to interact with a large volume of the analyte. The effect of these characteristics on the performance of the structure as a sensor will be presented in the next subsection 4.2.3.

Figure 4.10,c,d shows the optical response of the funnel-SPR design presented in figure 4.9,c. This arrangement has a negligible transmission (the transmitted power does not take into account the evanescent waves generated by the plasmonic resonances). Here, the tiny slots

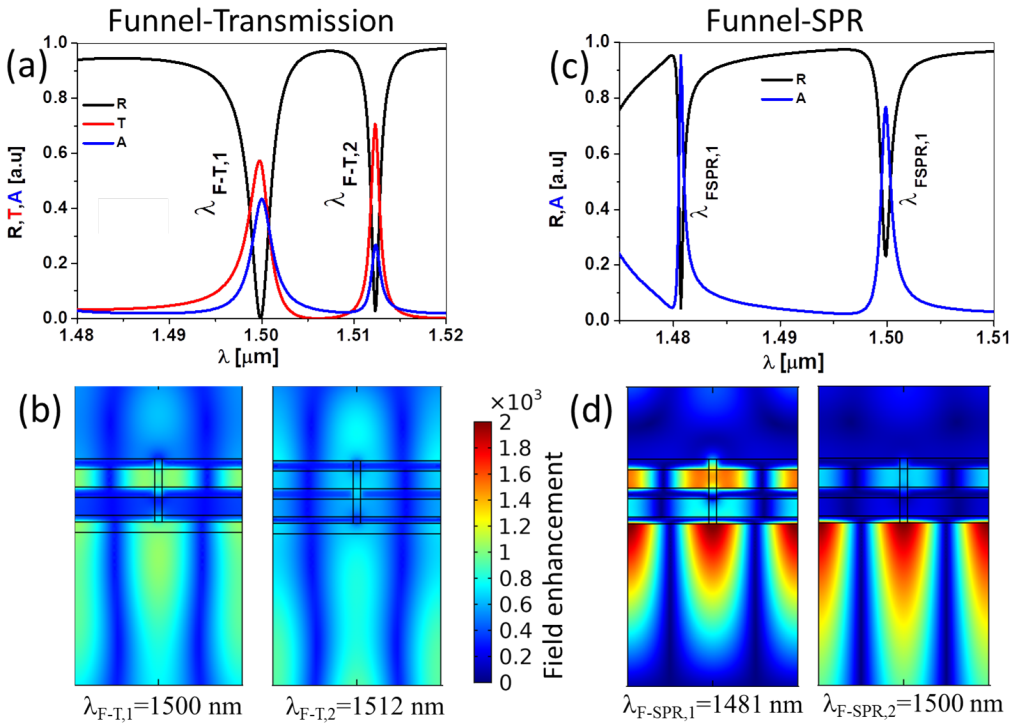

Figure 4.10: Field enhancement maps (FE, see equation (4.6)) and spectral reflectance (R), transmittance (T), and absorption (A) for the designs treated here. (a) Spectral behavior for the funnel-transmission design spectral features showing two resonant wavelengths: $\lambda_{\text{F-T},1} = 1500$ nm, and $\lambda_{\text{F-T},2} = 1512$ nm. (b) Field enhancement maps for these two wavelengths. (c) Spectral behavior for the funnel-SPR design. (d) Field enhancement maps for the two spectral features of this design at $\lambda_{\text{F-SPR},1} = 1481$ nm, and $\lambda_{\text{F-SPR},2} = 1500$ nm. In (b) and (d) light comes from top, and the analyte is located at the bottom.

funnel and guide the light towards the metal/dielectric layer where SPRs are generated. The first resonance at $\lambda_{\text{F-SPR},1} = 1481$ nm (see figure 4.10,c) shows a reflectance close to zero caused by the excitation of SPRs. The distribution of light at each dielectric layer is different, and the first dielectric layer ($t_{m,1}$ in thickness) hosts a field distribution with a larger amplitude. The interaction between the SPR resonances and the periodic funneling of light generates an asymmetric lineshape. For the second spectral peak in figure 4.10,c ($\lambda_{\text{F-SPR},2} = 1500$ nm), light scatters from the grating layers and is partially absorbed by SPR, and partially reflected. Due to this balance between reflection and absorption, the spectral peak (or dip in reflectance) is shallower. The FE map for this wavelength (see figure 4.10,d) shows a maximum at the analyte location where the SPW will interact with the analyte. This is a very interesting feature when considering the device as a refractometric sensor. The field enhancement maps (see figures 4.10,b and 4.10,d) show how the dielectric of the structure hosts a larger field enhancement for modes $\lambda_{\text{F-T},2}$ and $\lambda_{\text{F-SPR},2}$ than for modes at $\lambda_{\text{F-T},1}$ and $\lambda_{\text{F-SPR},1}$. Therefore, their behaviors when changing the index of refraction of the analyte are different.

From the spectral features shown in figure 4.10, we can make some predictions about the performance of the structures when used as refractometric sensors. As far as FOM increases as the resonance is narrower, $\lambda_{\text{F-T},2}$, and $\lambda_{\text{F-SPR},1}$ should behave better than the other resonances for the same design. Sensitivity should also follows a similar trend. On the other hand, although this is not fully analyzed here, a larger interaction volume, as it happens with $\lambda_{\text{F-SPR},2}$, should

mean a lower limit of detection of the given substance in the analyte.

4.2.3 Refractometric sensor performance

The performance of the proposed structures as refractometric sensors is analyzed by calculating the sensitivity, S_B, and FOM for different values of the index of refraction of the analyte for both designs and different modes. The range in n_a is selected near the index of refraction of water to customize the design for water soluble samples.

We first evaluate the performance of the funnel-transmission design (see figure 4.9,b). As we saw in the previous section, for the given spectral range, this design has two spectral features of the reflectance, transmittance, and absorption spectrally located at $\lambda_{\text{F-T},1}$ and $\lambda_{\text{F-T},2}$ (see figure 4.10,a).

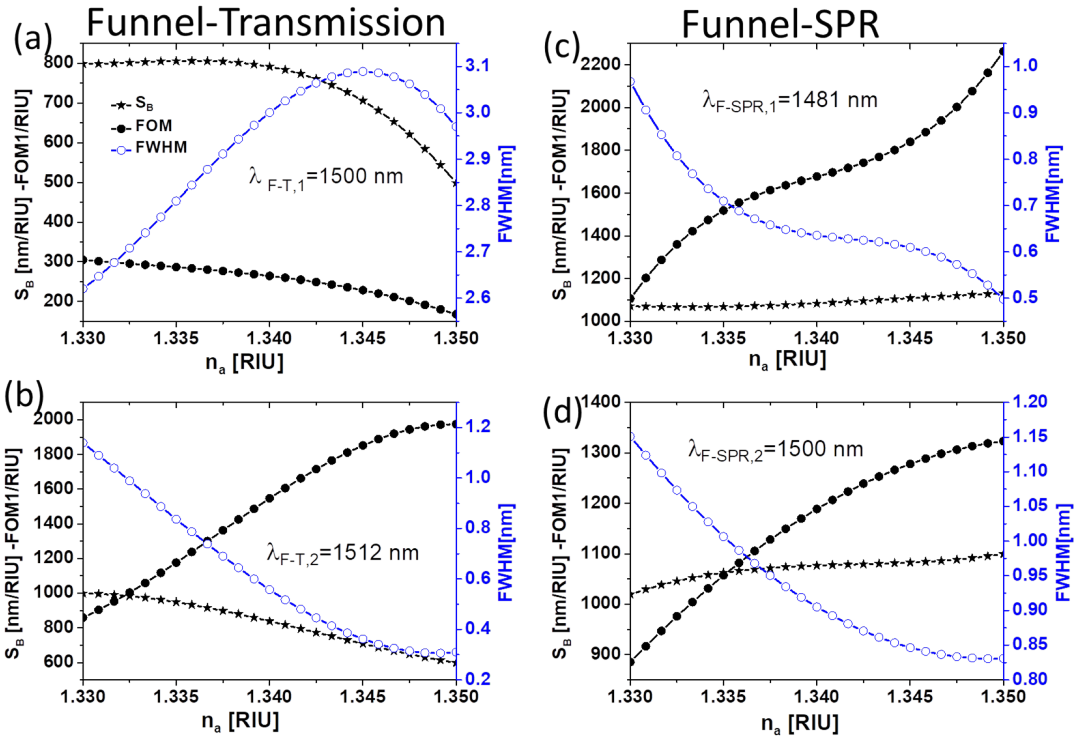

Figure 4.11: Sensitivity , FOM and FWHM *vs.* the index of refraction of the analyte for the range $n_a \in [1.33, 1.35]$. The plots for the funnel-transmission design are given in (a) and (b) for wavelengths $\lambda_{\text{F-T},1}$ and $\lambda_{\text{F-T},2}$ respectively. The responses of the funnel-SPR design are shown in (c) and (d) for $\lambda_{\text{F-SPR},1}$ and $\lambda_{\text{F-SPR},2}$ respectively.

The first dip at $\lambda = 1500$ nm has a strong plasmonic resonance in the embedded metallic grating layers. The results for this dip are shown in figure 4.11,a. The spectral response becomes wider with increasing the analyte refractive index, *i. e.* FWHM is larger, and as a result, both sensitivity and FOM decrease when increasing n_a. However, we find a range in the index of refraction where S_B remains almost constant. From the definition of the sensitivity, this constancy means a linear behavior of the spectral location of the resonant wavelength, λ_{res}, with respect to the index of refraction of the analyte, n_a. After performing this fitting we conclude that the device could operate linearly at this mode, $\lambda_{\text{F-T},1}$, in the range $n_a \in [1.33, 134]$, following the dependence: $\lambda_{\text{res}} = 805 n_a + 429$ nm, that results in a linear correlation coefficient $r = 0.99998$. The slope of the linear fitting corresponds with the

sensitivity value $S_{B,\lambda} = 805$ nm/RIU. These results confirm that the device performs better when the analyte is mainly water, as it happens with blood plasma [286]. As a consequence of the narrower spectral feature of the second resonance located at $\lambda_{\text{F-T},2} = 1512$ nm, the sensor performs better in terms of its sensitivity and FOM. In this mode, both sensitivity and FOM are larger because of the larger transmitted optical energy to the analyte side, and the narrow width, respectively (see the field enhancement maps in figure 4.10). The FWHM decreases from 2.65 nm for $n_a = 1.33$, to a 0.3 nm minimum for $n_a = 1.35$. That makes the device better suited for higher values of the refractive index. For the funnel-SPR design (see figure

Table 4.4: Maximum values of sensitivity and FOM.

Design	λ (nm)	$S_{B,\lambda}$ (@n_a) (nm/RIU)	FOM (@n_a) (1/RIU)
Funnel-Transmission	$\lambda_{\text{F-T},1} = 1500$	800 (@ 1.33)	300 (@ 1.33)
	$\lambda_{\text{F-T},1} = 1512$	1000 (@ 1.33)	1970 (@ 1.35)
Funnel-SPR	$\lambda_{\text{F-SPR},1} = 1481$	1130 (@ 1.35)	2100 (@ 1.35)
	$\lambda_{\text{F-SPR},2} = 1500$	1100 (@ 1.35)	1330 (@ 1.35)

4.9,c figure 4.10,c and 4.10,d), we have observed the generation of SPRs at the metal/analyte interface. Their lineshapes are now dependent on the coupling of the periodic funneling caused by the grating, and the SPR. This design shows high sensitivity and ultra-high FOM values reaching 1130 nm/RIU and 2100 RIU^{-1}, respectively for the mode located at $\lambda_{\text{F-SPR},1} = 1481$ nm. This behavior is presented in figure 4.11,c in terms of the index of refraction of the analyte. For the second resonance at $\lambda_{\text{F-SPR},2} = 1500$ nm, only one layer of the grating scatters the funneled light toward the metal film, so the coupling is weaker compared to $\lambda_{\text{F-SPR},1}$. The complete results of the resonance at $\lambda_{\text{F-SPR},2}$ are shown in figure 4.11,d. A summary of the maximum values of sensitivity and FOM for both designs and modes are listed in table 4.4.

4.3 Funneling in dielectric nanoprism gratings

A high aspect ratio dielectric grating can produce a funneling-like effect and focus light over a broadband wavelength range [193]. This mechanism can be used to direct light towards a thin metal /dielectric interface where an SPR is generated. We propose the use of nanoprisms embedded on a flat dielectric substrate and adjacent to the metal-dielectric layer used for sensing through the excitation of SPR [287]. This structure funnels the incoming radiation more efficiently, and therefore, plasmon resonances benefit from the increased energy reaching the plane of interest. The proposed devices perform better than similar structures and have geometrical and material arrangements that are feasible and fabricable with standard nanofabrication techniques.

4.3.1 Nanoprism design

The geometry of the proposed structure can be seen in figure 4.12,a. Light is normally incident towards the tip of an isosceles nanoprism array. We consider an MgF_2 substrate that can be etched, or patterned, with periodic longitudinal grooves having the desired triangular shape [201, 288]. These grooves are filled with AZO. This material can be spin-coated over the nanopatterned substrate to produce a planar interface for the deposition of a metal thin-film, for example, Au to assure good biocompatibility. Finally, we have considered water based solution as the medium under test to mimic biosample conditions. The optical constants for

the materials have been obtained from [185] for MgF_2, [167] for AZO, and [128] for Au. This selection of materials has been guided by a first analysis of the feasibility of the device in terms of fabrication constraints. The index distribution is appropriate when considering the matching between a low index substrate (MgF_2) and a high index buffer layer (AZO).

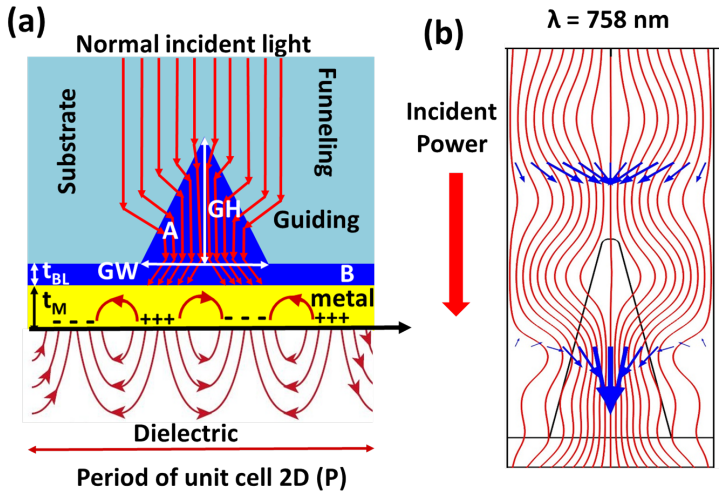

Figure 4.12: (a) Schematic diagram of the proposed structure. The red lines with arrows show how the incoming light flows through the grating towards the thin metal film. the Signs (—-, ++++) represent the surface electrons of the metal and the associated plasmonic field, their propagation along the metal surface represented by the red curves with arrows. (b) Time-averaged power flow at $\lambda = 758$ nm for the proposed structure without the metal layer where the funneling mechanism is shown.

A preliminary analysis considers a TM plane wave normally incident from the substrate side on the structure, without incorporating the metal layer. The amplitude of the incident magnetic field is 1 A/m. The results for this structure show how light is funneled and guided through the prism, reaching the region where the metal-dielectric interface generates SPR (see figure 4.12,b). The field available in this region is stronger than that of the classical Kretschmann setup. This configuration shows a very strong plasmonic resonance at some specific wavelengths determined by the geometrical parameters of the structure. Additionally, the geometry of the device and the choice of materials are of great importance to properly operate the device. The geometry of the system is determined by the thicknesses of the buffer and metal layers, t_{BL} and t_{M}, and by the parameters defining the nanoprism (width and height, GW, and GH), and its spatial periodicity, P. The three-dimensional shape of the nanoprism is extruded from a two-dimensional design (see figure 4.12,a). The prism region is divided into two portions, A and B, defining the groove array and the plane-parallel buffer layer. These two regions can be fabricated with the same material or using two materials, giving two designs with different spectral behaviors. The results obtained from the computation have been used to optimize the design with two main goals: to increase the field amplitude at the location where SPR are generated (metal-water interface) and to decrease the width of the reflectance dip associated with the resonance. This resonance is parameterized by the FWHM of the spectral reflectance. We perform the optimization by taking one geometrical or material parameter at the time. This strategy is well suited to understand how each geometrical parameter changes the overall performance of the device. Additionally, by monitoring and optimizing the field enhancement and the FWHM of the spectral reflectance, we also obtain higher values for the sensitivity and FOM. After optimization, we found that the geometrical parameters producing a better response are:$t_{\mathrm{BL}} = 100$ nm, $t_{\mathrm{M}} = 30$ nm, $GW = 325$ nm, $GH = 700$ nm, and a periodicity of

$P = 550$ nm. These values have been obtained taking into account the fabrication constraints. This is why we have considered a step of 25 nm between successive values included in the optimization. We have also avoided the use of ultra-thin or ultra-thick layers that could compromise the feasibility of the device. Figures 4.13,a,b show the maps of the Z component of the magnetic field at the resonant wavelength $\lambda = 758$ nm for the proposed structure and Kretschmann device, respectively. The incoming radiation is a plane wave having an amplitude of 1 A/m. The polarization corresponds to a TM mode. The wavelength used for optimization is chosen arbitrarily and, if necessary, can be shifted by changing the period parameter, P. To compare our results with those obtained from the classical Kretschmann configuration we evaluate its performance using the same wavelength, $\lambda = 758$ nm, to illuminate the prism. Then, we calculate the angular dependence of the reflectivity to obtain the incidence angle at which the resonance takes place for the Kretschmann prism, which is 66.28° for BK7 glass / Au [50 nm] / water based solution.

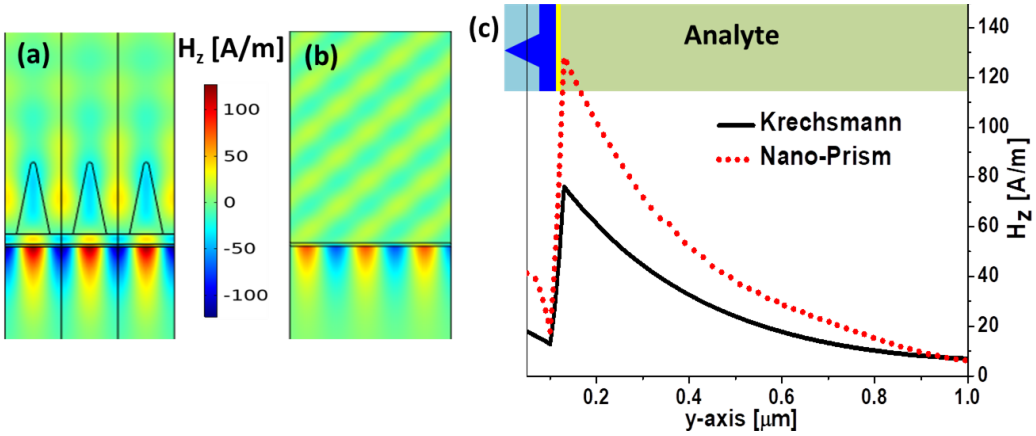

Figure 4.13: (a),(b) Map of the magnetic field at $\lambda = 758$ nm for an input magnetic field amplitude of 1 A/m and polarized as a TM mode for the proposed design and Kretchmann configurations respectively. (c) Profile of the electric field magnitude along the direction of propagation for the Krestchmann configuration (black solid line) and for the nanoprism device (red dotted line).

The map in figure 4.13,a shows a significant enhancement of the evanescent field in the analyte medium due to the focusing effects (funneling and guiding) produced by the nanoprism. This enhancement is larger in the proposed device that works under normal incidence conditions when compared with the conventional Kretschmann results in figure 4.13,b. Besides the field enhancement obtained with the nanoprism device with respect to the Kretschmann configuration, we can see (figure 4.13,c) that the plasmon resonance propagates within the medium under test along with an estimated depth of 180 nm and 300 nm for the Kretschmann setup and our proposal, respectively. Therefore, the interaction volume of the proposed nanoprism structure is larger than in the Kretschmann setup. The values of sensitivity and FOM are evaluated from the spectral behavior of the reflectance when changing the index of refraction of the medium under test. In figure 4.14,a we have plotted several reflectance curves for different values of the index of refraction of the analyte. Figure 4.14,a shows a degradation in the sharpness of the minimum when the index of refraction of the analyte becomes closer to the buffer layer index. In this situation, that involves a very thin metal film, reflectance becomes smaller because of the difference in the index of refraction diminishes. The maximum values for $S_{B,\lambda}$ and FOM obtained from figure 4.14,b are 250 [nm/RIU] and 100 [1/RIU] respectively. These values are higher than previously reported results for classical Kretschmann configurations [272, 273, 274, 276, 281]. However, these values for both $S_{B,\lambda}$ and FOM are not constant

when changing the refractive index of the analyte [281, 289, 290, 291].

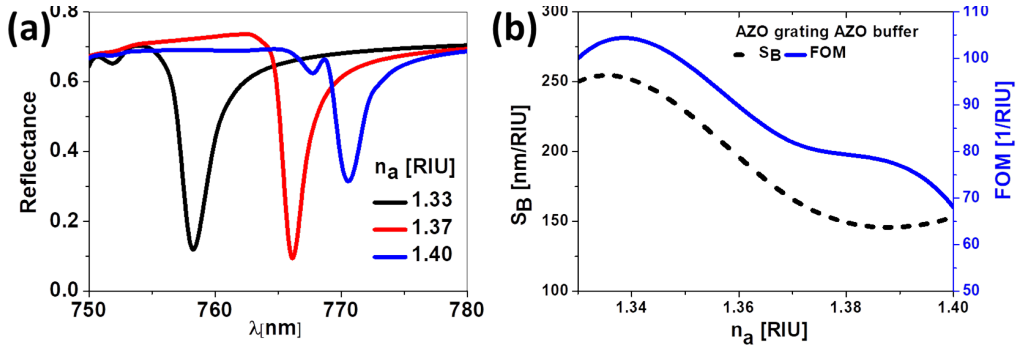

Figure 4.14: (a) Spectral reflectance for an optimum design that uses AZO as the buffer layer as a function of the index of refraction of the medium under test. The sharpness of the resonance peak degrades as the index of refraction increases. (b) Sensitivity (left axis and black dashed line) and FOM (right axis and blue solid line) as a function of the index of refraction of the medium under test.

In the previous optimization process, we paid attention to the geometry of the device. Now, we analyze how a different choice of materials can improve the performance of the device. To do that, we distinguish between the nanoprism region and the plane-parallel layer separating the nanoprism from the metallic deposition (portions A and B in figure 4.12,a). Then, the nanoprism material is still made of AZO to preserve the funneling characteristics and easiness of fabrication using spin-coating techniques. In region B we replace AZO by gallium phosphide (GaP, optical constants obtained from [292]). This change solves the degradation of the sharpness of the reflectance peak when moving to a higher index (see figure 4.14,a). This behavior is well appreciated to improve the stability and reliability of the sensor. When analyzing the final optimized design, we will resume this comparison.

The next material to analyze is the metal used for the generation of SPR. The choice of Au is based on its good biocompatibility. However, Ag (optical constants obtained from [128]) is better suited to generate a stronger SPRs. To take advantage of both characteristics, we propose a bi-metal layer made of Ag and Au as in section 4.1.2. In figure 4.15,a we have plotted four possible options for the metallic layer. The reflectance of Ag (red line in figure 4.15,a) shows a sharper, narrower and deeper, reflectance peak than Au (black line in figure 4.15,a). The peak for the Ag is located at a shorter wavelength than the resonance for an Au metallic layer. The spectral reflectance for the combination of these metals in the bilayer structure lies in between the two single-metal options, showing a better resonance as the Au layer becomes thinner. An optimum solution is a bilayer made of 25 nm-thick Ag coated with 5 nm-thick Au. This solution combines both metals with thicknesses in the range of fabrication technology. For the optimum case of a bi-metal layer considered previously, we have plotted in figure 4.15,b the spectral response for several values of the index of refraction. When comparing the spectral reflectances in figure 4.14,a and figure 4.15,b, we can also check how the sharpness of the spectral peak is maintained for a larger range in the index of refraction of the analyte. The reason for this improvement is the use of GaP in the fabrication of the buffer layer of the device. Figure 4.15,c contains the values of sensitivity and FOM for the optimized device that contains a bimetallic layer (25 nm Ag / 5 nm Au) and a GaP buffer layer.

These values are higher than those presented in figure 4.14,b where we had a single-metal Au layer and an AZO buffer layer. Figure 4.15,c includes a vertical red line that signals the upper limit in the index of refraction where the design analyzed in figure 4.14 begins to degrade the

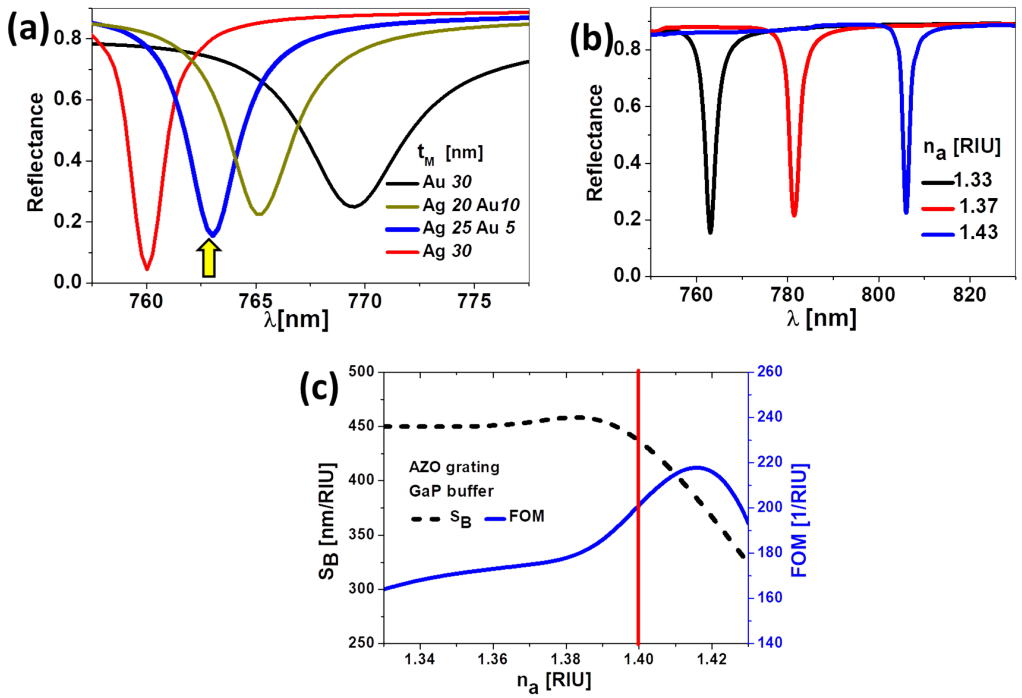

Figure 4.15: (a) Spectral reflectance for single metal 30 nm thick layer made of Au (black) or Ag (red), and for bi-metallic layer for two thicknesses combinations (blue and green). The yellow arrow selects the response for the optimum arrangement (25 nm Ag / 5 nm Au). (b) Spectral reflectivities of the optimum device that use a GaP buffer layer. The peaks show a similar sharpness for three different values of the index of refraction. (c) Sensitivity (left axis and black dashed line) and FOM (right axis and blue solid line) of the optimized sensor for an extended range of refractive index. The vertical line denotes the limit analyzed in the previous design where the buffer layer was made of AZO and the metallic layer was made of Au.

sharpness of the spectral reflectance peak. The optimum structure has a maximum $S_{B,\lambda} = 450$ nm/RIU, which is stable over a wide range of refractive index changes and corresponds to a FOM ranging from 160 to 220 1/RIU.

These values are better than some recent proposals that use graphene [272, 279, 281], silicon nanostructures [273], dielectric or metallic gratings [274, 276], oxide films [280], and metallic nanoprisms (Au coated over Ag nanoprisms) [277]. When not working at a normal incident, some other plasmonic structures, as the Au mushrooms, show a higher sensitivity but a lower FOM [282].

4.4 Hybrid mechanisms in dielectric nanoprism gratings

In this section, we configure and analyze a nanostructured device that hybridizes grating modes and SPRs. The model uses an effective index of refraction that considers the volume fraction of the involved materials, and the propagation depth of the plasmon through the structure. Our geometry is an extruded low-order diffraction grating made of dielectric nano-triangles. Surface plasmon resonances are excited at a metal/dielectric interface, which is separated from the analyte by a high-index dielectric layer. This proposal concentrates on the combination of a low-order diffraction grating and a metal/dielectric interface where the SPR is generated. Therefore, the period of the grating, P, is similar to the wavelength λ. SPRs

are excited in reflection at the interface between a thick metal layer and a dielectric buffer. On top of this dielectric layer, a periodic grating made of dielectric nano-triangles routes the light towards the metal/dielectric interface. This triangular relief also triggers funneling and guiding mechanisms that improve the performance of the devices [193, 287]. Light impinges the structure from the analyte side that is located above the dielectric grating. In this case, the excitation of an SPR depends on the index of refraction of the dielectric in contact with the metal, on the grating parameters, and the effective index obtained by the combination of the dielectric slab, the material of the nano-triangles, and the index of refraction of the analyte. This combination produces a multi-resonance behavior related to the low-order diffraction orders [293].

This hybridization has been already presented in recent contributions [294, 295], but the ultra-narrow hybridized resonances reported here, generate higher sensitivity and FOM, that expands over a wide dynamic range with reasonable performance. The device operates under normal incidence conditions, easing its integration for both illumination and signal retrieval systems, and allowing to place it on the tip of an optical fiber. A challenging application for the device presented here would be the measurement of refractive index changes of the analyte when the volume of the analyte is small (nano- or picoliters). This could be advantageously used in sensing changes of the tear film, with potential application in the diagnostics of the dry-eye syndrome [296, 297, 298].

4.4.1 Model and variations

We analyze here the performance of nanophotonic structures that combine low-order diffraction grating modes and SPRs. Figure 4.16 shows two cases with hybrid behavior. A diffraction grating of period P along $X-$direction, and made of dielectric nano-triangles with an index of refraction n_g, is placed on top of a material structure that may take several configurations described as a cross section on the XY plane. We will extrude this geometry along the $Z-$axis.

Surface plasmons are generated at a metal/dielectric interface where the real part of the dielectric permittivity of the metal (ε_m) is negative, meanwhile, the index of refraction of the dielectric remains real and positive. Our device is illuminated from top through a medium of an index of refraction n_1. Depending on the configuration, the analyte (having an index of refraction n_a) can be placed on top of the nano-triangles ($n_1 = n_a$), or at the bottom of the structure, interfacing with an index of refraction $n_2 = n_a$ (see figure 4.16,a). If the metal is thick enough (greater than some few penetration depths within the metal), the plasmon resonance is suppressed at the bottom of the structure, and a dielectric buffer layer (having a high index of the refraction, n_{BL}) between the metal and the nano-triangles is used to promote and enhance resonances on top of the metal layer (see figure 4.16,b). The substrate is placed on top for design in figure 4.16,a and at the bottom in figure 4.16,b. In the second case, it is an effective medium that combines the grating material, the analyte, and the buffer layer that effectively controls the SPR generation. The excitation of an SPR at a metal/dielectric interface coupled to a diffraction grating is driven by the wavevector matching condition [299]. The use of an effective medium is needed because of the presence of several materials in the surroundings of the metal interface: the dielectric thin layer, the dielectric triangular grating, and the analyte. Usually, the effective index of refraction is calculated with the so-called homogenization method [180]. In this method, each material contributes to the effective refractive index proportionally to its volume fraction within the interaction volume of the plasmon (*i. e.*, close to the metal/dielectric surface). We parameterize the extent of the SP with its decay length.

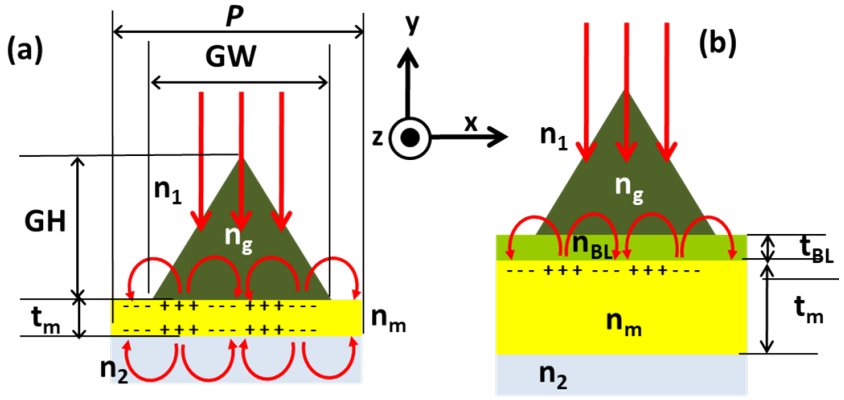

Figure 4.16: Geometrical and material cross sections of two configurations for the generation of SPRs combined with a low-order dielectric grating. This grating has a period P, and is carried out with dielectric nanotriangles. Theses nanotriangles have a width GW, and a height GH, and they are made with a dielectric material having an index of refraction n_g. The metal layer, having an index n_m, has a thickness t_m. The configuration in (b) has an additional buffer layer with an index of refraction n_{BL}, and a thickness t_{BL}. Light is coming from top in both configurations, and the plasmonic resonance can be generated on both sides of the metal layer if this is thin enough (case (a)) or only at the top metal/dielectric interface (case (b)). The substrate supporting these structures, having an index of refraction n_s, is placed on top, $n_1 = n_s$ (case (a)), or at the bottom, $n_2 = n_s$ (case (b)). Meanwhile, the analyte, with an index of refraction n_a, is located at the bottom, $n_2 = n_a$ (case(a)), or on top, $n_1 = n_a$ (case (b)). The geometrical parameters of the structure are depicted in the XY plane, being $Z-$axis the extrusion axis of the 3D nanostructure.

The structure depicted in figure 4.16,a couples radiation towards a metallic thin layer. The thickness of this layer, t_m, is thin enough ($t_m \simeq 45$ nm) to generate SPR on both sides of the metallic slab. Therefore, the analyte can be placed on top and/or at the bottom of the structure.

When the metal layer is thick enough to prevent the excitation of the SPR at the bottom interface, we find the configuration shown in figure 4.16,b. This configuration has an additional thin dielectric buffer layer (being n_{BL} its index of refraction), with a thickness t_{BL} small compared to the decay length of the SP. This material appears at the wavevector matching condition for those SPR at the top of the metal layer included in the calculation of the effective index of refraction as a combination of the indices of refraction of three materials: buffer layer (n_{BL}), nano-triangles (n_g), and analyte (n_a).

This dielectric buffer layer also controls the coupling between the diffracted wave and the SPR mode, and improves the final response of the device [287]. In this case, SPRs are only excited on top of the metal layer. The calculation of the effective index of refraction requires the estimation of the spatial extension of the plasmon measured from the top surface of the metal. This length is wavelength dependent and will be extracted from the simulations. Moreover, the presence of the diffraction grating generates low-order diffraction modes that interact with the structures. Furthermore, the combination of the grating lobes and the SPR leads, after optimization, to an enhancement in the device's sensitivity, a narrower spectral response, and therefore a larger FOM.

4.4.2 Design

In this section, we focus on the design shown in figure 4.16,b where the metal layer thickness prevents the excitation of SPR at the bottom interface of the metal layer. The analyte medium is on top of the grating ($n_1 = n_a$), and plasmons are generated at the upper metal/dielectric interface. The combination of the high-index buffer layer and the presence of the dielectric grating produces a hybrid resonance with an ultra-narrow spectral response. The geometrical and material arrangement is described in table4.5, organized from bottom to top, having SiO_2 as substrate and water as the superstrate. The values of the index of refraction for the given materials are extracted from references [128], [300], and [188] for Ag, GaP, and Si_3N_4, respectively. The index of refraction of dielectrics is purely real, and their imaginary parts are neglected within the studied spectral range. The SiO_2 substrate could be replaced

Table 4.5: Geometrical parameters and materials for the proposed device.

Material	Dimension and shape [nm]	$n(\lambda = 1.4\mu\text{m})$
SiO_2	$[\infty]$ (substrate)	$n_s = 1.45$
Ag	t_m [200] (thin-film)	$n_m = 0.13065 - i10.156$
GaP	t_{BL} [100] (thin-film)	$n_{\text{BL}} = 3.1369$
Si_3N_4	*GW* [610], *GH* [1070], *P* [1000]	$n_g = 2.0005$
H_2O	∞ superstrate (analyte)	$n_a = 1.33$

by other materials, even plastic, because it does not influence the optical behavior. For the grating and buffer layer, the selection of the dielectric materials is key to obtain a high-contrast of the index of refraction. Our grating is made of Si_3N_4 with an index of refraction $n_g \simeq 2$ at the operating wavelength ($\lambda \in [1.35, 1.55]\mu$m). This value is large compared with the index of refraction of the analyte. In this design, we take a water based solution as the analyte. We vary the index of refraction between 1.30 and 1.56 to consider for any additions, variations, or even if the water based solution is replaced by other bio-chemical media [301, 302]. As we will show, both the triangular shape of the grating relief, and the contrast in the index of refraction between the analyte and the grating enhance the funneling of light towards the dielectric/metal interface where the SPR is generated. This effect is also favored by the high-aspect ratio of the grating relief, and also narrows the spectral response of the structure. The buffer must be a transparent and high-index material: we use GaP as a starting point. Later, in the next section, we will analyze the importance of the thickness and material selection of this buffer layer to optimize the performance of the system.

This sensor can be easily implemented in an optical setup. We start with collimated light exiting from an optical fiber and directed towards a measurement cell where the analyte fills the volume between the collimation optics and the sensing surface. The spectrum of the reflected light carries information about the analyte and is collected by the same optical system towards detection. We consider that the device is illuminated from the top with a TM polarized plane wave, under normal incidence conditions. In our simulation, we have set an amplitude of 1 A/m for the magnitude of the magnetic field of the incoming wave. Then, the magnetic field map can be interpreted as a field enhancement map. Under these conditions, we have calculated the spectral reflectance, $R(\lambda)$, that is presented in figure 4.17. $R(\lambda)$ contains the mirror reflectance (0^{th} order) plus the low-order diffraction lobes ($\pm 1^{\text{st}}$ orders). The lower it is, the higher the power of the generated SPR, and thus the higher the sensitivity. In this figure, when $n_a = 1.33$, we see two minima located at λ=1.337 μm and 1.4 μm. They result from

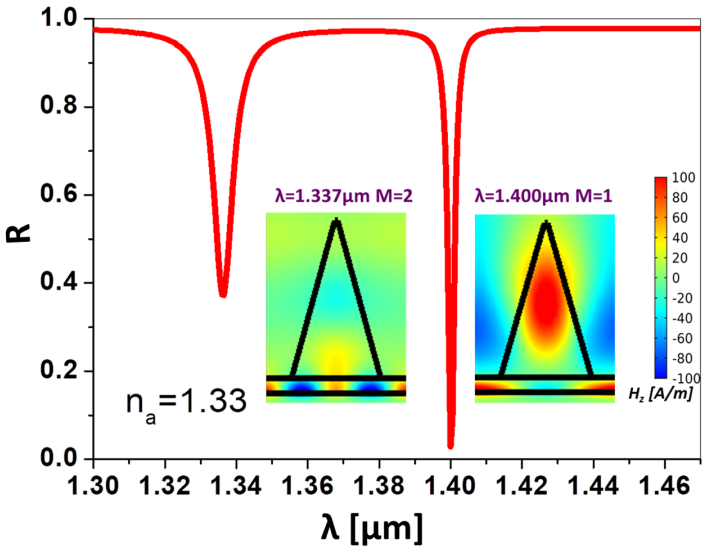

Figure 4.17: Spectral response of the proposed structure. The insets represent the magnetic field Z component for $M = 1$, and $M = 2$ (the colorbar is the same for both insets).

the coupling of diffractive orders to the SPR. The first one ($\lambda = 1.337\mu$m) corresponds with a mode that is mostly confined in the buffer layer and has very little exposure to the analyte (see inset in figure 4.17). However, the second minimum ($\lambda = 1.4\mu$m) shows a large amplitude both within the grating material and the analyte interspace, also beyond the triangular tips. At this point in the simulation, we use equation (2.21) to find the effective index of refraction (or effective permittivity), which reads as:

$$n_1 k_0 \sin\theta \pm \frac{2\pi m}{P} = k_0 \sqrt{\frac{\varepsilon_{\mathrm{m}} \varepsilon_{\mathrm{eff}}}{\varepsilon_{\mathrm{m}} + \varepsilon_{\mathrm{eff}}}},$$

where k_0 is the wavevector in vacuum, θ is the angle of incidence of the incoming wave, ε_m is the real part of the complex electric permittivity of the metal, and $\varepsilon_{\mathrm{eff}} = n_{\mathrm{eff}}^2$ is the dielectric permittivity of an effective medium in contact with the metal. We use the effective index to account for the medium near the metal surface that combines the grating and surrounding materials. First, we determine the diffraction order, M, of the resonance. This order can be obtained after analyzing the field distribution within a period of the grating. The insets in figure 4.17 show periodic field amplitude distributions that repeat once within the period for $\lambda = 1.400\mu$m, meaning $M = 1$, and twice for $\lambda = 1.337\mu$m, meaning $M = 2$. After substituting in equation (2.21), the optical constant of the metal, Ag, and the value of the period, $P = 1\mu$m, we find an effective index of refraction $n_{\mathrm{eff}}(\lambda = 1.4\mu\mathrm{m}) = 1.3869$, and $n_{\mathrm{eff}}(\lambda = 1.337\mu\mathrm{m}) = 2.5778$ (where $n_{\mathrm{eff}}^2 = \epsilon_{\mathrm{eff}}$). These values of the effective index are given by a mixing model that includes the volume fractions of the materials of the arrangement. This volume fraction is obtained by considering the amount of the volume of each material present in the unit cell (with period P) up to an arbitrary height referenced to the metal/dielectric interface, h_{eff}. When doing this calculation we find the height that fits the effective index values at each wavelength previously evaluated from equation (2.21): $h_{\mathrm{eff}}(\lambda = 1.400\mu\mathrm{m}) = 7.039\mu$m, and $h_{\mathrm{eff}}(\lambda = 1.337\mu\mathrm{m}) = 0.164\mu$m. These height values can be related to the extent of the region where the field interacts, as we will see when evaluating the field enhancement maps in the next subsection 4.4.3. The feasibility of these values supports the previously presented mode of the hybridization mechanism between SPR and low-order diffraction orders.

4.4.3 Optimization

As customary, we compare the performance of optical sensors by the sensitivity and the FOM [61, 271, 303]. Usually, when light efficiently couples to SPR, the field enhancement is larger and the reflectance reaches a minimum value. This is why we will pay attention to this enhancement (see equation (4.6)) and also to the spectral reflectivity $R(\lambda)$. These two parameters can be combined in a merit function, MF, that is defined using equation (4.4). The field enhancement parameter, FE, is defined here as the maximum value of $\mathrm{FE}(x, y, z)$ within the analyte volume. Reflectivity characterizes the behavior of the structure globally at the wavelength of resonance, $R = R(\lambda_{\mathrm{res}})$. This merit function highlights hot spots in the field map, and distinguishes the optimum coupling of the incoming radiation to the SPR (in this case, as far as transmittance is negligible, a minimum reflectance means a maximum absorption).

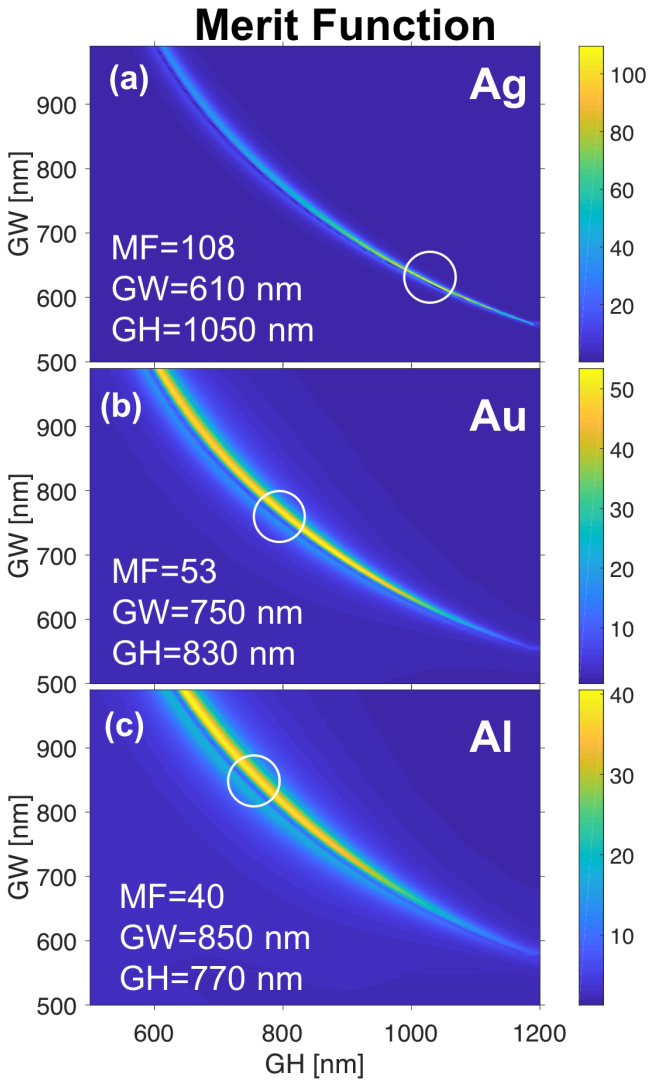

Figure 4.18: Maps of the merit function (equation (4.4)) for three metals as a function of the geometrical parameters of the grating, GW and GH. (a) is for Ag, (b) is for Au, and (c) is for Al. The grating period is $P = 1\mu$m, $\lambda = 1.4\mu$m and $n_a = 1.33$. The white circles are centered around the maximum value of the MF. The colormap expands along different ranges for each metal.

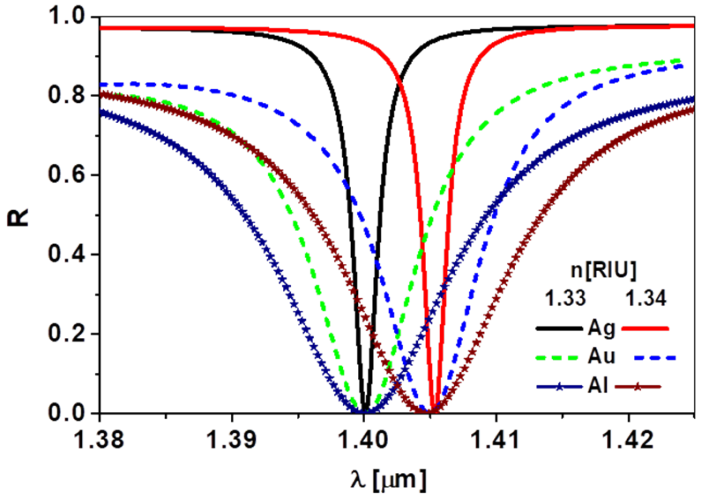

Figure 4.19: Spectral reflectance, $R(\lambda)$, of the optimized geometry for the three metals. They are analyzed for two values of the index of refraction of the analyte: $n_a = 1.33$, and $n_a = 1.34$. The spectral locations of the minima are redshifted as n_a increases.

The goal of the optimization is to set the geometrical and material parameters that maximize this merit function (see equation (4.4)). We first analyze the effect of the geometry of the dielectric grating and the metal selection, and then we will move to optimize the thickness and material choice of the buffer layer. Figure 4.18 shows how the grating geometry (grating width, GW, and grating height, GH) affects MF for fixed values of the wavelength ($\lambda = 1.4\mu$m) and the period of the grating ($P = 1\mu$m). Changing P moves the wavelength of resonance linearly (as larger P, larger is λ_{res}), and allows to tune the design for a given wavelength of interest. The three optimization maps in figure 4.18, consider three possible choices for the metal: Ag, Au, and Al. We select these materials because they are widely used in plasmonic sensors [304]. The dependence of MF with respect to GW and GH for the three metals is similar. Ag gives the largest value of MF, and Al the smallest (see the different range in the color bar on the right of the maps in figure 4.18 for each metal).

The maximum values of the MF For for the three metals under analysis and the corresponding geometrical parameters of the grating for each case are listed in table 4.6.

Table 4.6: Geometrical parameters of the grating and the MF of the optimized device for Ag, Au and Al.

Metal	GW - GH [nm]	MF	Q
Ag	610 - 1050	108	700
Au	750 - 830	53	155
Al	850 - 770	40	88

The white circles in figure 4.18 determine the location in the map where the merit function reaches the maximum value. Also, a combination of parameters close to those circles shows a large merit function that does not compromise the performance of the system. Figure 4.19 shows the spectral reflectance of the structure made with the geometrical parameters maximizing the merit function. We observe here how the response is narrower and slightly deeper for Ag (as expected from the values of the MF). The reflectances have a similar lineshape but

they differ in their linewidth. The resonances can be characterized by their quality factor parameter, $Q = \lambda_{\text{res}}/\Delta\lambda$, where $\Delta\lambda$ can be given as the FWHM. Actually, the linewidth depends on the material parameters as it corresponds with their plasmonic resonance origin. Using the definition for Q, we obtain the values listed in table 4.6.

When changing the index of refraction, reflectivity remains almost invariant in shape, but is red-shifted when the index of refraction increases from 1.33 to 1.34. A closer look at the spectral location of the minimum in reflectance (see figure 4.19) shows how Ag reflectance moves a little farther to longer wavelengths than Au and Al responses. From our results, we conclude that an Ag film optimizes the device in terms of Q and spectral shift. Furthermore, as long as the metal is not in direct contact with the analyte, biocompatibility issues of Ag are overcome.

So far, we have optimized the proposed device by changing the geometric parameters of the grating and the material of the metal layer. Now, we consider the buffer layer and how its thickness (see t_{BL} in figure 4.16), and index of refraction, n_{BL}, allow the second round of optimization. The buffer layer is responsible for guiding the diffracted light towards the metal/dielectric interface (where SPRs are generated). Its index of refraction will affect the effective index (effective dielectric permittivity, ϵ_{eff}) appearing in the wavevector matching condition (equation (2.21)). The results of this optimization step are presented in figure 4.20 where we again find an optimum configuration within a range of feasible values. Although the starting point of the optimization was a GaP layer of thickness 100 nm (MF=108), we can see that the merit function is higher (MF=135) when the index of refraction is close to 2, and the thickness is around $t_{\text{BL}} = 215$ nm. The inset in figure 4.20,a shows how the merit function varies along the line where the maximum values are located. A material well positioned to play as a buffer layer is SiN_x [199]. Figure 4.20,b shows the spectral reflectivity of the resonance for GaP and SiN_x. Also, the material almost complying with the desired value in the index of refraction is Si_3N_4 (which is the same one used to build the grating nano-triangles). This is a favorable situation from the fabrication point of view because it saves an additional material process, and also eliminates the index step between the nano-triangles and the buffer layer. The actual shape of the resonant minimum using Si_4N_3 is quite close to the one for SiN_x represented in figure 4.20,b.

The excited SP extends from the metal/dielectric surface towards the analyte and its amplitude decays inside the dielectric medium in contact with the metal. The buffer layer is made of GaP and it is 100 nm thick, which is thin enough since the SP amplitude usually extends several hundreds of nanometers before completely decaying within the dielectric medium. Therefore, the electromagnetic field associated with the plasmon resonance interacts both with the grating material and the analyte. Figure 4.21 presents the evolution of the FE parameter for both resonances at $\lambda = 1.337\mu$m (in black) and $\lambda = 1.4\mu$m. In the case of $\lambda = 1.4\mu$m we have plotted the non-optimized case (in red) when the grating is made of GaP, and the optimized one (in blue) corresponding with a grating and buffer layer made of SiN_x. If we check how the field evolves from the metal/dielectric interface (see insets in figure 4.21) along the dashed lines in the map, for the case of $\lambda = 1.4\mu$m, we identify two maxima (see red and blue lines in figure 4.21). One of the maxima is located at the metal/dielectric surface, and the other is placed at the grating region. Again, the resonance at $\lambda = 1.4\mu$m is better suited for its use in a sensor, because it interacts more intensely with the analyte medium at the grating gap.

The field enhancement is as high as FE=108 for $\lambda = 1.4\mu$m, 4.7 times larger than for

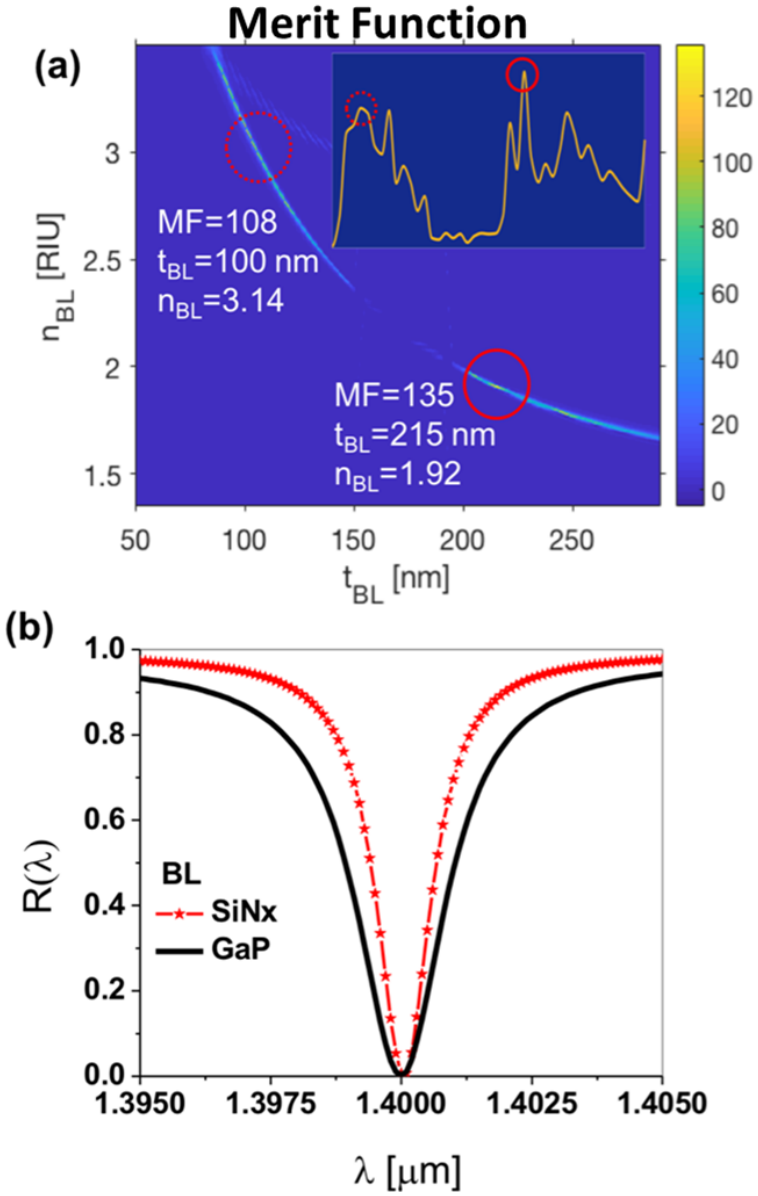

Figure 4.20: (a) Dependence of the merit function in terms of the characteristics of the buffer layer $(n_{\mathrm{BL}}, t_{\mathrm{BL}})$. Although the index of refraction cannot be varied continuously, we may check that a higher index of refraction means a lower thickness of the buffer layer. The red circles locate the non-optimum (dashed) and optimum cases (solid). The inset shows the variation of the merit function (MF) along the line of the maximum values. (b) Spectral response of the device for a non-optimum buffer layer made of GaP (black) and the optimum case corresponding to buffer layer made of SiNx, having an index of refraction close to 1.92 (red).

$\lambda = 1.337\mu$m at the analyte volume. Besides the field enhancement, the resonance extends deeper in the analyte at $\lambda = 1.4\mu$m, as predicted by the value of h_{eff} calculated through an effective index mixing model in subsection 4.5.2.

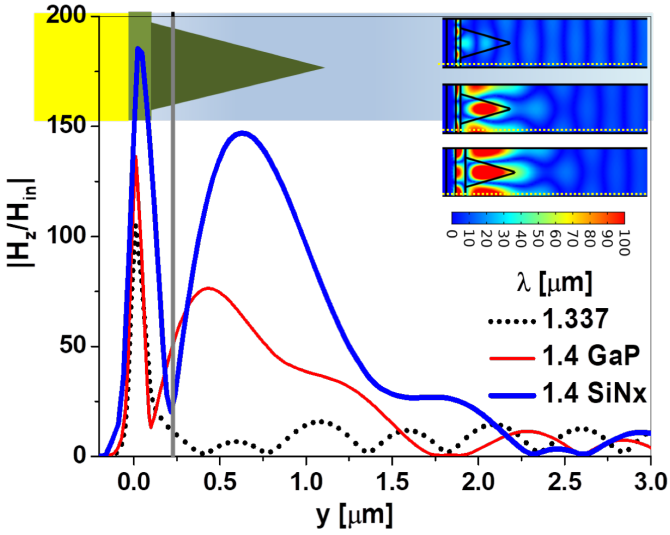

Figure 4.21: Evolution of the $z-$component of the magnetic field, given as the ratio $|H(y)/H_{\text{in}}|$, as a function of the distance from the metal/dielectric interface ($y = 0\mu$m). Light is coming from the right. The dashed black line corresponds to $\lambda = 1.337\mu$m, and the solid red line is for $\lambda = 1.4\mu$m, both for a non optimized GaP grating material. The blue solid line is also for $\lambda = 1.4\mu$m, when the material of the grating and the buffer layer is the optimun one (SiN_x). The optimization also requires a thicker buffer layer of 200 nm, that is represented as a vertical gray solid line. This plot shows how resonances extend differently within the analyte medium. The insets represent the maps of the modulus of the magnetic field for the three cases. The dashed white lines in these maps locate the lines where the profiles are plotted.

4.4.4 Analysis and characterization

All the previous changes and parameterizations are used to evaluate sensitivity and FOM when these devices work as refractometric sensors. Therefore, to complete the evaluation of the device we calculate the sensitivity and FOM for different analyte refractive index values, where the device operates efficiently, which determines the device dynamic range. The geometric and material parameters of this optimum design are presented in table 4.7. Figure 4.22 represents how sensitivity and FOM change with the index of refraction of the analyte, n_a, within the studied index range. Sensitivity, $S_{B,\lambda}$, is steadily increasing with n_a from 480 nm/RIU (at $n_a = 1.3$) till 975 nm/RIU at $n_a = 1.568$. Also, FOM increases with n_a, and shows a large variation from 413 RIU^{-1} (at $n_a = 1.30$) until reaching a value of 12829 RIU^{-1} (at $n_a = 1.568$).

This change is caused by the abrupt narrowing of the spectral reflectance, which FWHM is as small as 0.08 nm for the resonance observed at $n_a = 1.568$. The calculation has stopped at $n_a = 1.568$ because we consider the associated FWHM narrow enough to require a high-resolution spectrometer to operate the system. These values are very competitive with current reported values of sensitivity and FOM for similar refractometric sensors, and show how the proposed nanostructure helps to improve the performance. The insets in this figure represent the lineshape of the resonance for $n_a = 1.33$ at the left, and $n_a = 1.56$ to the right. These insets expand along the same wavelength interval of 6.5 nm, but the central wavelength of the resonance changes ($\lambda_{\text{res}}(n_a = 1.33) = 1.4001\mu$m, and $\lambda_{\text{res}}(n_a = 1.56) = 1.5603\mu$m). At this point, we guess that the thin dielectric buffer layer, isolating the metal from the analyte, reduces the extent of the plasmonic resonance within the analyte volume. However, we have

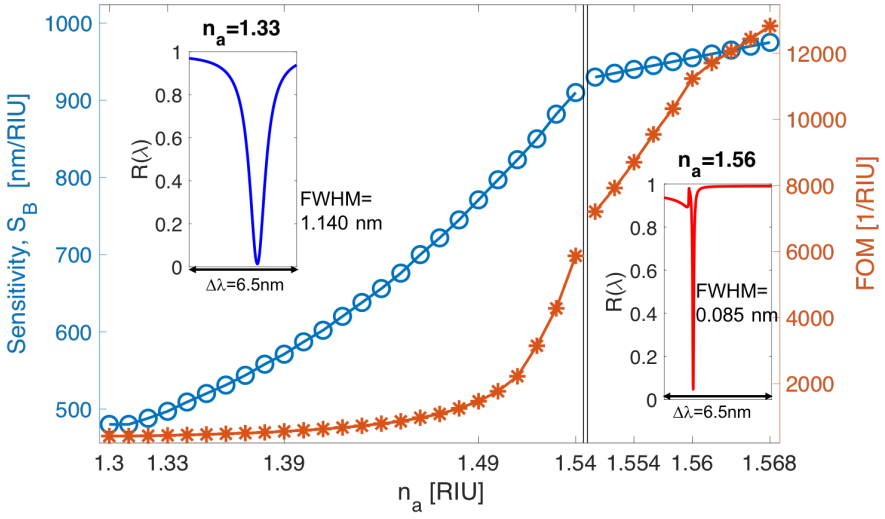

Figure 4.22: Sensitivity, and FOM for the optimized device at different values of analyte refractive index, n_a. The plot is divided into two portions. The left part describes the evolution from $n_a = 1.3$ up to $n_a = 1.54$, and the right portion is for a narrower range: $n_a \in [1.55, 1.568]$. The insets show the lineshape of the resonance for $n_a = 1.33$ (left), and $n_a = 1.56$ (right) and the values of their FWHM. For better comparison, the plotted wavelength interval is the same (6.5 nm) for both insets.

Table 4.7: Geometrical parameters and materials for the optimum design at $\lambda = 1.4\mu$m.

Material	Dimensions [nm]
SiO_2 (substrate)	∞
Ag (metal)	t_m [200]
SiN_x (buffer layer)	t_{BL} [215]
Si_3N_4 (nanotriangle)	GW [610], GH [1050], P [1000]
H_2O (analyte)	∞

checked that by removing this isolation layer, the performance of the system is not compromised by this buffer layer because it increases the contrast of the index of refraction. Although a configuration without a buffer layer behaves slightly better for a low index of refraction analytes, the maximum sensitivity and FOM for the studied range of the index of refraction of the analyte, n_a, are worse ($S_{B,\lambda} = 867$ nm/RIU, and FOM $= 5385$ RIU^{-1}) than when including an optimized buffer layer. Moreover, this layer preserves the analyte from its contamination with the metallic layer, as Ag is highly keen on oxidation processes and hardly biocompatible.

4.5 Fano resonances in dielectric nanorectangular gratings

The excitation of SPR by a metallic grating provides high-performance devices with a narrow spectral response. However, metallic gratings generate reflection and absorption losses, besides the scattering. So, even if we could totally couple the incoming radiation to the device, some of the optical energy will be absorbed in the grating structure. As a result, the field concentration at the analyte volume is limited by the field that reaches the metal/analyte interface. A proposal to overcome this limit and produce a high field concentration at the

analyte volume is to excite the SPR using a high index lossless dielectric grating. This grating can be embedded in a low index host to achieve the highest refractive index contrast possible. The high refractive index contrast of the grating improves the amplitude of the SPR, and can extend the dynamic range of the device (see sections 4.2, 4.3, 4.4). A systematic study for the parameters of this design will give a close insight on these assumptions.

4.5.1 Model and physical mechanism

Fano resonances manifest when a discrete state interferes with a continuum of states [248]. In our case, the discrete state is given by the excitation of SPs, and the continuous contribution comes from the dispersive character of the subwavelength grating; which has a smoother variation than the sharp spectral response of plasmon resonances. When different SPR modes coexist for a given frequency ω, the coupling between a narrow SPR mode with frequency ω_0 and the broad background spectra creates the simplest scenario for interference and Fano resonances [305, 306]. For a narrow spectral range around the SPR, the slow-varying spectral response of the continuous background, $r_{\mathrm{bk}}(\omega)$, can be expanded as a Taylor series without a significant loss in the accuracy. We can write r_{bk} as a polynomial expansion in frequency, ω, centered around the SPR, ω_0:

$$r_{\mathrm{bk}}(\omega) = \sum_{j=0}^{\infty} r_{\mathrm{bk},j}(\omega - \omega_0)^j, \tag{4.7}$$

where $r_{\mathrm{bk},j}$ represents the coefficients of the polynomial expansion. Our model considers a Lorentzian shape for the plasmon response, and a linear variation for the continuous spectrum. The linear response is valid as long as the spectral range is narrow enough compared with the width of the SPR. Therefore, under the linear approach of the continuous spectral contribution, the spectral reflectivity can be described as:

$$R(\omega) = \left| [r_{\mathrm{bk},0} + r_{\mathrm{bk},1}(\omega - \omega_0)] + f\frac{\gamma}{(\omega - \omega_0)i + \gamma} \right|^2. \tag{4.8}$$

The term in square brackets is the first order polynomial approximation to the broad spectral response of the system. This linearization works because the analyzed spectral range, $\Delta\omega$, is quite narrow around the central frequency of the resonance ($\Delta\omega \simeq 0.03\omega_0$). The second term is a Lorentzian shape centered at ω_0, with a width γ. Both responses are considered in amplitude and are coupled through the complex coefficient f, which describes their interference. We can interpret the coefficients of our model as: $r_{\mathrm{bk},0}$ describes the mean reflectivity for frequencies out of the resonance, and $r_{\mathrm{bk},1}$ is associated with the slope of this spectral reflectivity. The modulus of f describes the interaction of the plasmon resonance with the broad spectral response. If the plasmon resonance produces a dip in reflectance, the phase of f takes values around π denoting a minus sign, *i. e.*, a decrease in reflectivity. More generally speaking, f is related to the asymmetry of a Fano resonance profile. The plasmon resonance is then defined by its central frequency, ω_0, and its width, γ. Finally, a combination of the two defines the quality factor of the resonance:

$$Q = \omega_0/\gamma, \tag{4.9}$$

that we use to optimize the analyzed structures.

4.5.2 Design

We analyze the Fano resonance in a structure with a 2D periodic dielectric grating embedded in a dielectric layer [285]. In a practical realization, radiation can be delivered and extracted

through a fiber probe (see figure 4.23,a). Figure 4.23,b shows the material and geometric arrangement of the device, with the substrate located on top to preserve a typical configuration where the liquid analyte is at the bottom. The 2D arrangement is extruded along the third dimension (Z axis). Light arrives under normal incidence conditions from the semi-infinite substrate towards the nanostructure. Then, the reflected light is collected by the measurement system, and we monitor the spectral reflectivity. A key point of this proposal is the high contrast in the index of refraction achieved by the combination of two dielectric materials: GaP ($n_{\mathrm{GaP}} > 3$), and MgF_2 ($n_{\mathrm{MgF_2}} < 1.38$). This arrangement surpasses the limitations of having metallic scatterers within a dielectric matrix [262].

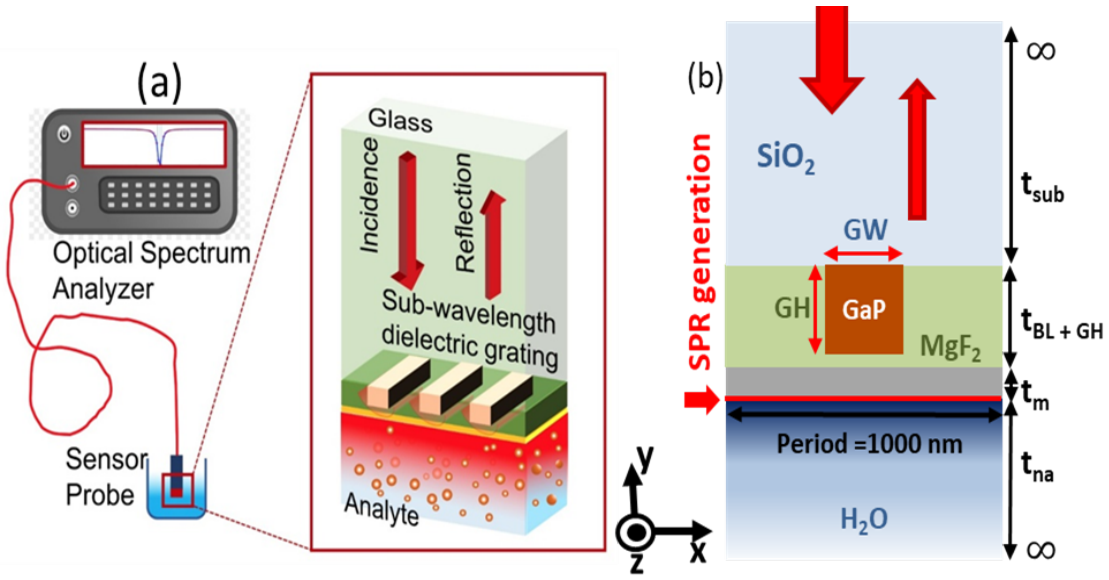

Figure 4.23: (a) Proposed sketch of our Fano-resonance sensor. The device can be attached to a fiber optics probe in contact with the analyte. This portion is represented in more detail as a 3D view. (b) Material arrangement, and geometry of the nanostructure of the sensor. Light comes from top to bottom through the substrate (made of SiO_2), and reaches the dielectric grating (composed of MgF_2 and GaP), and the metallic thin layer (Ag). The SPR takes place at the metal/analyte interface. The analyte is assumed to be liquid (H_2O) and it is located at the bottom of this sketch. Ag is selected as the metallic material and it has been represented as a yellow layer. A 10 nm thick passivization layer of MgF_2 is added and represented as a thin line located between the metal and the analyte. The reflected power is routed towards an optical spectrum analyzer.

The device can be built on a glass substrate (SiO_2). The first structure is a 2D grating of GaP rectangles with period P, width GW, and a thickness (height) GH. The grating relief is overfilled with MgF_2 by spin coating[239], with a thickness of $GH+t_{\mathrm{BL}}$. This MgF_2 layer generates a plane surface where we deposit an Ag thin layer of thickness t_m. Finally, the structure is coated with an additional MgF_2 thin layer that passivizes the properties of Ag, maintaining its good optical response and complying with bio-protection standards [307]. The sample under analysis, the analyte, is in direct contact with this last surface. For biological samples, we select water based solution as the medium in contact with the sensor itself. The optical constants of the materials involved in this design are taken from recognized source [128, 185, 300]. The actual structure is formed as shown in table 4.8.

At this point, our results show a negligible dependence on the substrate characteristics; allowing for flexible and plastic substrates without substantial performance degradation. We

Table 4.8: Materials and layer structure of the modeled device

Layer	Material	Dimensions
Substrate	SiO_2	∞
Grating	GaP	height GH, width GW, and period P= 1000 nm
Buffer layer	MgF_2	height GH+t_{BL}
Thin-film	Ag	$t_m = 40$ nm
Passivization layer	MgF_2	$t_{\mathrm{PL}} = 10$ nm
Analyte	water based solution	∞

can shift the spectral response of the system by varying P (here we take $P = 1000$ nm). We analyze the structures with Comsol to extract information about the spectral reflectivity. Also, we map the electromagnetic field generated by the structure to identify the locations where the electric field is enhanced and where the system sustains plasmon resonances at the desired interface for a large interaction volume (device/analyte). From a physical point of view, two components combine to generate a Fano line-shape:

- the wide spectral response generated by the subwavelength dielectric grating
- the narrow SPR produced at the metal/dielectric interface.

This combination is responsible for the observed Fano resonances that disturb the SPR and generates symmetric or asymmetric line-shapes depending on their mutual interaction (parameterized with f in equation (4.8)). The subwavelength grating is made of two dielectric materials (GaP and MgF_2) showing a high contrast in the index of refraction. Figures 4.24,a and 4.24,b show how the numerically evaluated reflectivity fits with the model (equation (4.8)) for two cases: (a) symmetric line-shape with an almost pure Lorentzian shape, and (b) asymmetric. The fit provides the parameters of the model that quantifies the design. Among these parameters, we chose ω_0 and γ to characterize the performance of the resonance for sensing applications through the definition of the quality factor of the resonance, Q (see equation (4.9)).

As the geometrical parameters vary, the coupling between these two modes changes too, resulting in symmetric (figure 4.24,a) or asymmetric (figure 4.24,b) line-shapes. The symmetric case (a) corresponds with an almost real value of $f^a = 0.795e^{i0.99\pi}$. The asymmetric case (b) shows an almost imaginary value of $f^b = 0.156e^{i0.48\pi}$. Both cases are well described through the hybrid plasmonic-Fano resonance model in equation (4.8). Figure 4.24 includes insets of the maps of the magnetic field amplitude, H_z, that shows the field enhancement located at the region of interest, where the SPR is excited and propagates through the analyte within a given interaction volume at the metal/analyte interface (actually, the analyte is in contact with the MgF_2 buffer layer). From these figures, we define the field enhancement parameter, FE, that describes the maximum field within the interaction volume for a given geometry of the device. This volume comprises the region in the analyte where the plasmon resonance propagates. Later on, in Section 4.5.4 we present a quantitative parameter, δ_y, that can be used to evaluate this volume. FE is the ratio between the maximum value of the field and the amplitude of the incoming wavefront.

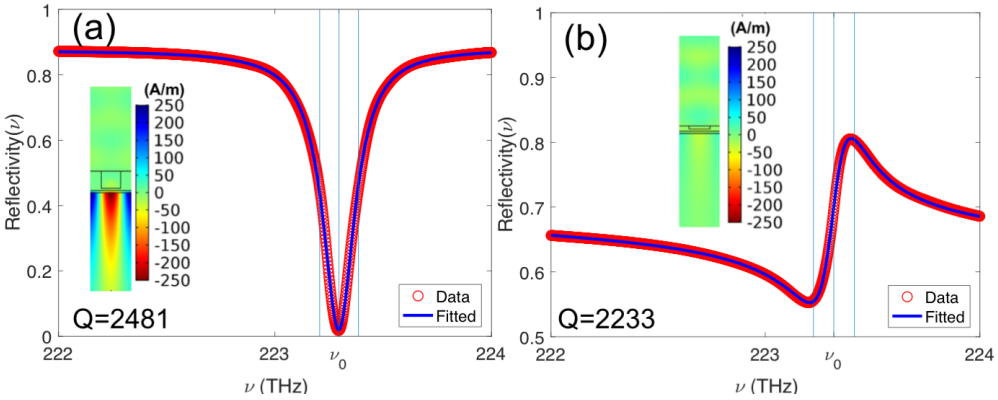

Figure 4.24: Fitting of computed spectral response (red circles) to the Fano model (blue solid lines) for two different cases showing a symmetric (a) and asymmetric (b) line-shapes. The vertical lines correspond to the central frequency, $\nu_0 = \omega_0/2\pi$, and the width given by $\gamma/2\pi$ (expressed in THz) obtained from the model (see equation (4.8)). The insets represent the near field distributions of the magnetic field, H_z, where we can extract the field enhancement parameter. The value of the quality factor of the resonance, $Q = \omega_0/\gamma$, is given for each plot. The fitting coefficients (see equation (4.8)) for each spectra are: $\nu_0^a = 223.30$ THz , $\gamma^a = 0.09$ THz , $r_{\mathrm{bk},0}^a = 0.94, r_{\mathrm{bk},1} = 0.7 \times 10^{-5}$, $f^a = 0.795e^{i0.99\pi}$, and $\nu_0^b = 223.32$ THz, $\gamma^b = 0.10$ THz, $r_{\mathrm{bk},0}^b = 0.81$, $r_{\mathrm{bk},1} = 1.2 \times 10^{-3}$, $f^b = 0.156e^{i0.48\pi}$, where the superscript denotes the plotted spectra (a or b).

4.5.3 Optimization

We optimize the performance of the device as a plasmonic sensor by combining two parameters that describe both the sharpness of the resonance, and the amount of light that interacts with the analyte. These two parameters are the quality factor of the resonance, Q (see equation (4.9)), calculated from the fitting of the spectral results with the model (see equation (4.8)), and the field enhancement values, FE, obtained at the region of interaction.

The two parameters Q, and FE, are both included in a Merit Function of the form:

$$\text{Merit Function} = \sqrt{Q \times \text{FE}}. \tag{4.10}$$

We choose the merit function in equation (4.10) after evaluating other combinations of these two parameters, including the arithmetic-mean, and the root-mean-squared. All of them produced the same output for the geometric parameters (GW and GH) of the structure where the Merit Function is maximized. We present the results of the optimization process for different parameters in figure 4.25.

The maps in figures 4.25,a,b represent the values of the quality factor, Q, and the field enhancement parameter, FE, in terms of two geometric parameters of the dielectric grating: GW, and GH. We choose first these parameters as optimization variables because they are the main players in the process, as shown in previous results [262, 287]. This is why the rest of the parameters, including the grating period p, are kept constant. Figure 4.25,c contains the Merit Function map that identifies a region of values that combines a high value of Q and FE. Our evaluation provides a value of GW= 500 nm, and GH= 475 nm (presented in figure 4.25,c as a red circle). This optimization ignores the symmetry of the resonance, as far as both (symmetric and asymmetric) line-shapes are well described through the plasmonic-Fano resonance (equation (4.8)). However, as shown in the following optimization step, the optimum spectral reflectivity is a symmetric mode.

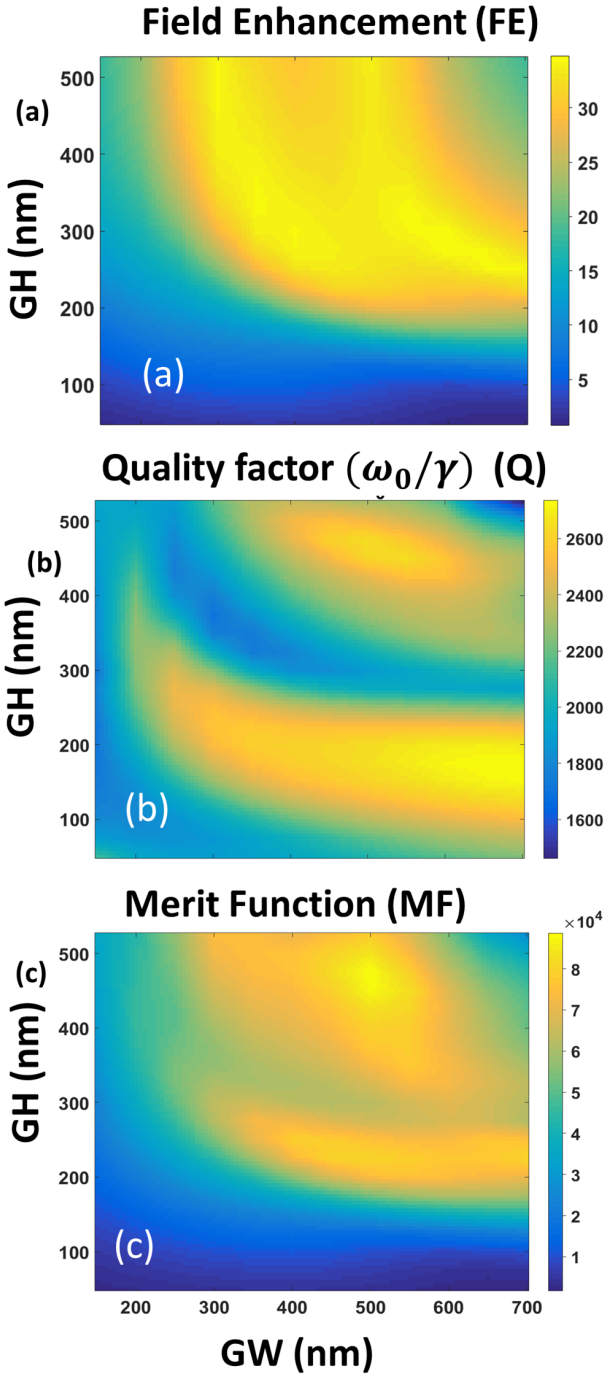

Figure 4.25: Maps of the quality factor (a), Q, the field enhancement parameter (b), FE, and the Merit Function (c) defined in equation (4.10), as a function of the geometrical parameters GW and GH. These maps are used to select the values for an optimum performance of the system. The red circle in the Merit Function map corresponds with its maximum value obtained at GH= 475 nm, and GW= 500 nm.

4.5.4 Device analysis

Once the shape of the grating is fixed, we analyze other geometrical parameters. The thickness of the metallic layer, t_m, affects the SP generated at the metal/dielectric interface

and its longitudinal range. Through further optimization, we find a value of $t_m = 50$ nm. This evaluation is represented in figure 4.26,a where the spectral shape allows choosing $t_m = 50$ nm as the one showing the smallest line-width in reflectance, and larger field enhancement. The map of the magnetic field is plotted in figure 4.26,b,c for two cases ($t_m = 20$ nm, and $t_m = 50$ nm). We see that the field is stronger for $t_m = 50$ nm, that is the thickness chosen for the metallic layer. As far as the input wavefront has an amplitude of 1 A/m, the plotted amplitude of the magnetic field is also FE. We also analyzed the period of the grating, P, and its effect is shown in figure 4.26,d. The spectral reflectivity shifts towards longer wavelengths when the period increases. Also, through another analysis to optimize the thickness of the MgF_2, t_{BL}, we found a small performance change for values between 10 and 100 nm. We found that $t_{BL} = 50$ nm produces a minimum width (minimum FWHM), and a maximum FE (see figure 4.26,e). Also, we set the passivization layer at $t_{PL} = 10$ nm (minimum fabricable thickness) to allow the best plasmon propagation possible.

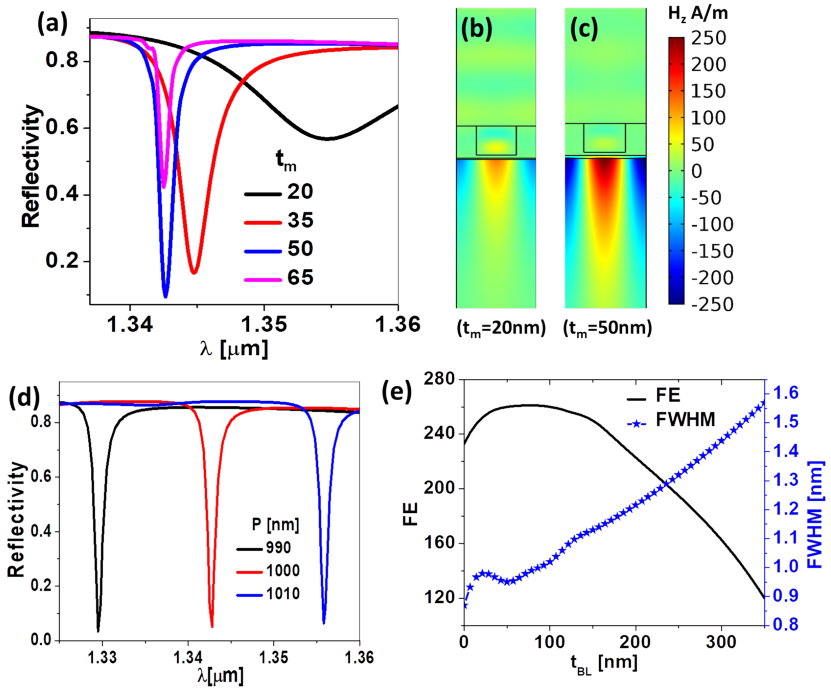

Figure 4.26: (a) Spectral reflectivity for several values of the metal layer thickness, t_m. (b) and (c) Near field amplitude maps showing the field enhancement for two values of $t_m = 20$ nm, and $t_m = 50$ nm, where the last value clearly provides a larger amplitude within the interaction volume. (d) Spectral reflectivity for three values of the period of the grating, P. (e) Variation of the field enhancement parameter (FE), and the FWHM of the resonance as a function of the thickness of the buffer layer, t_{BL}

A previous proposal (the metallic slits in section 4.1) optimized the material setup of a subwavelength metallic grating to maximize the amount of energy transferred to the metal surface for SPR generation [262]. In the design presented here, a subwavelength dielectric grating, involving a nanostructure with a high-contrast of the index of refraction, scatters radiation and reveals very narrow widths of Fano-type resonances, and optimum coupling to the metallic/analyte interface. This provides a higher scattering efficiency (see figure 4.27). Both metallic and dielectric gratings create a continuum diffraction pattern (described in the first term of equation (4.8)). Unfortunately, metallic gratings support modes where the incoming wave is absorbed (through SPR on the grating surface itself), scattered, or reflected. The

dielectric GaP grating is transparent at the operating wavelengths. Moreover, it only generates guiding modes at its surface, and avoids the excitation of additional SPRs. To understand the advantages of our GaP structure with respect to a metallic subwavelength element, we compare the enhancement of the spectral characteristics of both gratings.

Figure 4.27 represents the scattering cross-section of these subwavelength gratings, and shows that for dielectric materials the scattering cross-section at the resonant wavelength is 3 times larger. Therefore, more radiation is scattered towards the metal/dielectric interface where the SPR is generated. In contrast, the metal grating absorbs radiation and redirects part of it towards modes appearing at the unavailable inner metal/dielectric interface [262]. In both cases, the geometries were optimized for optimum performance. The interaction volume describes the portion in the analyte that is exposed to a large value of the electromagnetic field due to the generation and propagation of the plasmon resonance. The size of the interaction volume determines the part of the analyte which can be sensed using the device, and hence the efficiency of the device to sense different amounts of the analyte. This interaction volume increases with an optimized geometry that gives a large value of FE.

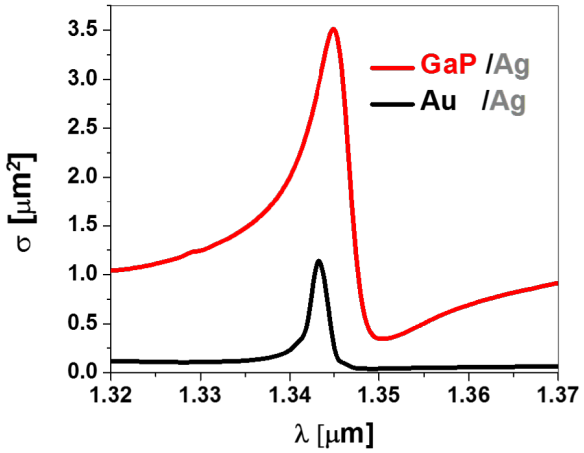

Figure 4.27: Scattering cross section, σ, for the proposed geometry with GaP grating (red solid line) and Au grating (black solid line) [262]. Ag is used at the metal/analyte interface.

In figure 4.28,a we compare the amplitude of the magnetic field, H_z, within the analyte for three cases: our design, Kretschmann configuration, and metallic subwavelength grating structure. All these three designs were optimized for later comparison. The parameters of our design have been obtained through the method presented in section 4.5.3, the Kretschmann configuration corresponds with an optimum choice of materials and angle of incidence (as described in the introduction section), and the metallic subwavelength grating was derived from section 4.1. We fit the amplitude dependence with distance to an exponential decay function in equation (4.5). The enhancement factor amplitude of the maximum field is calculated using equation (4.6) as $\times$277, $\times$183, and $\times$116 for our structure , the Kretschmann setup, and metallic grating case, respectively. These numbers are derived after fitting of the amplitude evolution presented in figure 4.28,a with the model in equation (4.5). As far as the input amplitude is normalized at 1 A/m, $H_{z,0}$ represents the field enhancement. Figure 4.28,b represents the magnetic field for the three cases. This translates in a $\times$1.5 larger field with our system compared with the Kretschmann configuration, and more than double respect to he metallic grating case. Furthermore, the decay lengths, δ_y, are 1162 nm, 1013 nm, and 1085 nm for our structure, the Kretschmann setup, and the metallic grating case, respectively. Therefore, our

design generates a larger volume of interaction, and has a potentially lower limit of detection. These results surpass those obtained for metallic grating structures, and also significatively better than classical Kretschmann configuration.

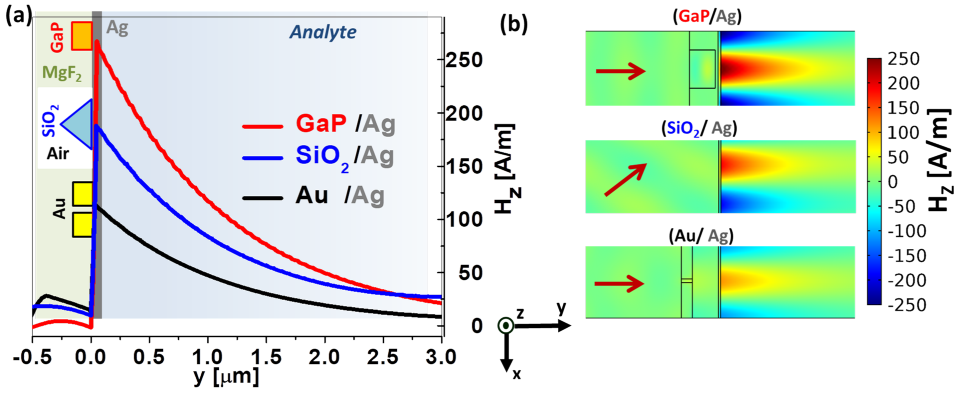

Figure 4.28: (a) Evolution of the near field in the region of interest for three different geometries. GaP/Ag denotes the design presented in this section. SiO_2/Ag corresponds to the classical Kretschmann configuration. Au/Ag shows the response for a subwavelength metallic grating for the design in section 4.1. (b) Magnetic field amplitude distributions for the three cases.

4.5.5 Characterization of the hybrid plasmonic-Fano resonance sensor

Until now, high-sensitivity plasmonic sensors operating under normal incidence and based on spectral measurements show important limitations in detection range and linearity [81, 82, 262, 274, 287]. These limitations are related to the presence of unprofitable modes where the field enhancement delocalized from the metal/analyte interface [262]. Our device is linear in a wide range of index of refraction of the analyte, $n \in [1.3, 2]$, thanks to the high coupling efficiency of the dielectric subwavelength grating, which forwards the radiation into the interaction interface. Figure 4.29,a shows the linear dependence of the SPR wavelength with the index of refraction of the analyte, n_a. This linear behavior is linked with the smooth dependence of n, which does not present absorption peaks along with the analyzed wavelength range. This broadband feature permits multifunctional operation in biological applications in water, glucose, urea, etc, [308]. To validate our proposal, we evaluate sensitivity, $S_{B,\lambda}$, and FOM. For a system that performs with a maximized Merit Function (see equation (4.10) in subsection 4.5.3), we evaluate the shape and characteristics of the spectral resonance line-shapes through the width of the Lorentzian term, γ, of the Fano resonance (see equation (4.8)), and identify it with the FWMH appearing in equation (4.3). To do so, we fit the numerically evaluated spectral response with the analytical model presented in section 4.5.1 (see equation (4.8)). This eliminates any ambiguity due to asymmetric profiles, and makes the procedure more robust. From the FWHM, we obtain the values of sensitivity and FOM for the optimized device (see figure 4.29,b). The maximum sensitivity is $S_{B,\lambda} \approx 1000$ nm/RIU, and the maximum FOM is ≈ 775 RIU^{-1}. These values are higher than recently reported values for similar sensors [281, 309, 310, 311, 312, 313, 314, 315]. Fiber optics based sensors exhibit higher sensitivity than our proposal, but present a lower FOM [316, 317]. In figure 4.29,b the $S_{B,\lambda}$ drops from 1000 at $n_a = 1.33$, to 980.5 nm/RIU at $n_a = 2$, which indicates a stability in the $S_{B,\lambda}$ in the whole range. The FOM has a minimum value of 667 RIU^{-1} at $n_a = 1.725$. These figures are competitive for our design because it extends the range of operation to a higher index of refraction if compared to recent advances in the field (see Table 4.9).

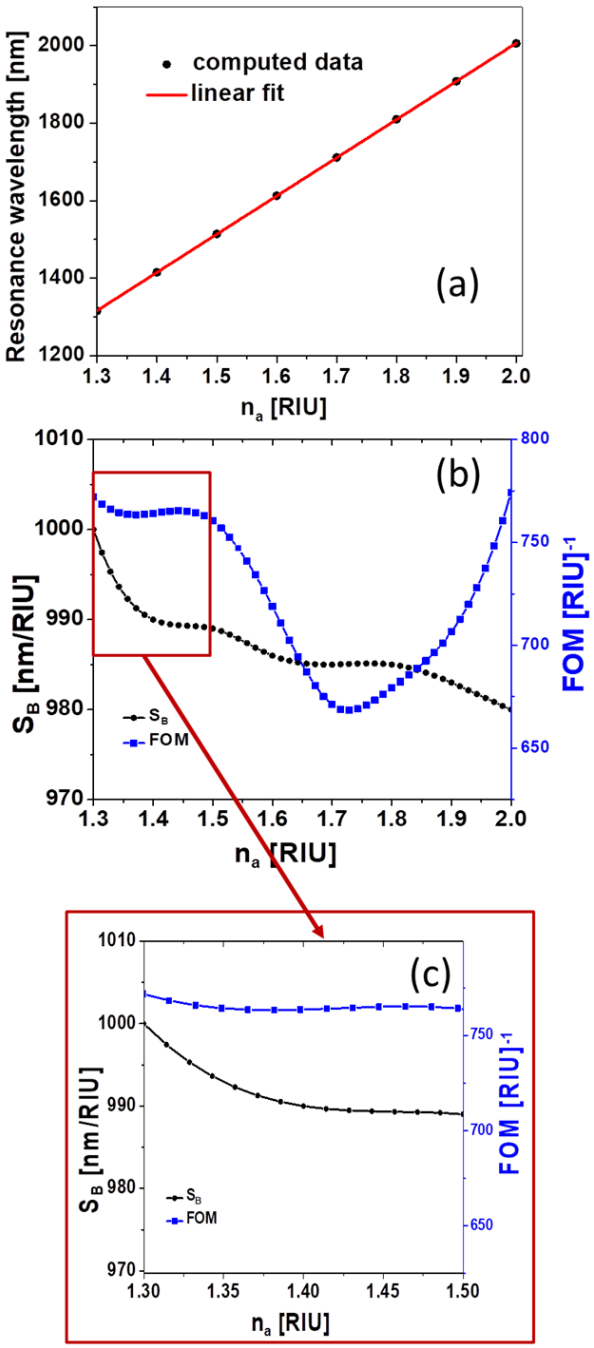

Figure 4.29: (a) Dependence of the central frequency of the resonance as a function of the index of refraction of the analyte. The red line corresponds with the linear fitting of the numerical results. (b) Sensitivity, $S_{B,\lambda}$, and FOM as a function of the index of refraction of the analyte, n_a. (c) Detailed portion of (b) showing a range in the refractive index that maintains an almost constant behavior of the device.

Sensitivity and FOM are almost constant in the range $n_a \in [1.3, 1.5]$, as shown in figure 4.29,c. A constant trend indicates high stability and reliability in the measurements, resulting in a more robust device. Experimentally [318], scientists achieve a FOM of 730 RIU^{-1} that leads

Table 4.9: Comparison of sensor performance *versus* the results obtained in this work. All the sensors are spectrally interrogated.

Ref	$S_{B,\lambda}$	FOM [1/RIU]	Dynamic Range
[255]	370 [nm/RIU]	2846	1.333-1.334
[256]	1.1×10^8 [1/m]	2.33×10^4	1.00-1.04
[257]	425 [nm/RIU]	4.7-7.1	1.33-1.50
[258]	452 [nm/RIU]	56.5	1.0-1.2
[259]	67 [nm/RIU]	—	1.332-1.344
[260]	586 [nm/RIU]	62	1.00-1.05
[261]	900 [nm/RIU]	—-	1.33-1.36
this work	1000 [nm/RIU]	775	1.33-2.00

to the detection of ultra-low concentrations of 10^{-10}M. Table 4.9 summarizes the performance of several sensors with different methods involving Fano resonances. As we mention in section 4, high sensitivity and FOM over a wide range of refractive index are key for multifunctional and efficient sensors. However, in most cases, enhancing one of these parameters diminishes the others. Sometimes, the good performance of a given sensor is strongly degraded when moving away from the optimum point of operation of the value of the analyte refractive index [256]. Our device performs better in sensitivity, FOM, and dynamic range (in terms of variation of the index of refraction of the analyte).

5

Hybrid technology devices

Chapter 3 analyzed several options to improve the performance of solar cells of various technologies. These options included the use of nanophotonic structures. In chapter 4 we proposed several designs to improve the performance of optical sensors based on spectral interrogation. The operation of these devices depends on the optical signal handling (illumination and detection). As an improvement, the excitation of SPRs in normal incidence conditions is key to simplify this optical scheme, ease the illumination and acquisition signal system, allowing a lower cost solution [80, 81, 82, 274]. In this chapter we will merge together some concepts of chapters 3 and 4 to generate hybrid devices with novel capabilities.

What if the front surface of a solar cell were functionalized to work as an optical sensor? This question was asked and answered a long time ago in previously published results. The answer includes materials and sensitized coatings to selectively detect some specimens and substances using solar cells. The published results report applications for optical sensing[319], gas sensing [320, 321], refractive index sensing [322, 323, 324], chemical sensing [325], and multi-functional sensors [326]. The advantage is clear: the signal is directly generated by the solar cell and, ideally, there is no need for sophisticated and voluminous read-out elements (goniometers and spectrometer for angular and spectral interrogation techniques)[287, 327, 328].

So, the next simplification derives from the replacement of the spectral interrogation procedures, which requires high resolution spectrometers. The idea is to use the electric response of solar cells or the bolometric effect, as the base to generate an optoelectronic interrogation of the device. The available low-cost technology used in electrical measurement can greatly simplify the sensing system [322]. This method ensures high measurement reliability and reduces the cost of the whole system. As an additional desirable characteristic is to have low-cost flexible devices that can be obtained with plastic substrates and thin-film technology. Such a sensor generates electrical currents upon light exposure, being the extracted signal sensitive to environmental changes.

Although a solar cell exemplifies this situation, its planar front interface is not selective enough in wavelength, and its sensitivity to small changes in the index of refraction of the exposed medium is not relevant. Therefore, to sensitize a solar cell, it is customary to modify its design and provide the required capabilities. Also, plasmonic absorption in metal surfaces, that is transferred to heat through the bolometric effect needs to be high enough for generating a reliable electrical signal from the device.

A perovskite solar cell has a high absorption coefficient, and the photo-generated charge

carriers present a large diffusion length compared to most of the thin-film solar cell materials [329]. Moreover, we are witnessing progress in efficiency [330, 331] and stability [332] of perovskite solar cells that is boosting the scientific interest. Perovskite solar cells are not as stable and robust as those based on silicon since this is not a mature solution yet, but a developing technology. However, due to the extraordinary properties of this material, and considering the fast increase of the solar cell's efficiency and stability, they are considered by the photovoltaic community as one of the possible substitutes of silicon. Therefore, we think it is worth exploring other applications of this promising technology, such as communication and sensing.

The implementation of metallic or dielectric nanostructures in the top of perovskite solar cell, can make the device spectrally selective and more sensible to environmental changes. Also, the excitation of SPR in a thin metal layer using diffraction from a dielectric grating embedded in a low index matrix can improve the light coupling to the plasmonic resonance mode and hence the absorption in the metal layer. In both cases, the response of each device should benefit from this combination to provide better performance for sensing applications.

5.1 Bolometric refractometric sensor

The bolometric effect allows us to electrically monitor spectral characteristics of plasmonic sensors; it provides a lower cost and simpler sample characterization compared with angular and spectral signal retrieval techniques. In our proposal here, a monochromatic light source illuminates a spectrally selective plasmonic nanostructure. This arrangement is formed by a dielectric low-order diffraction grating that combines two materials with a high-contrast in the index of refraction. Light interacts with this structure and reaches a thin metallic layer, that is also exposed to the analyte. The narrow absorption generated by SPRs hybridized with low-order grating modes heats the metal layer where plasmons are excited. The temperature change caused by this absorption modifies the resistance of a metallic layer through the bolometric effect. Therefore, a refractometric change in the analyte varies the electric resistivity under resonant excitation. We monitor the change in resistance by an external electric circuit. This optoelectronic feature must be included in the definition of the sensitivity and FOM parameters.

5.1.1 Design and optimization

We model and simulate an alternative measurement technique that exploits the bolometric effect [333], which is triggered by the absorption of electromagnetic radiation [334, 335]. This way, we avoid costly spectral measurement systems because the output signal is electrical by definition [336]. This effect is also responsible for the variation in resistivity caused by a change in temperature. This mechanism has been widely used in antenna-coupled detectors in the IR [334, 335, 337, 338]. In a nutshell, our device works under normal incidence conditions and a spectrometer is unnecessary because we measure an electrical signal directly related to the sensed property. A monochromatic laser source eases integration with off-the-shelf driving and signal acquisition electronics, both for illumination and signal retrieval. Our sensor is based on a dielectric grating that couples radiations into a dielectric/metal interface where the SPR is excited. The shape of the resonance is described best as a hybrid-Fano resonance between the pure SPR and a wider response generated by the grating [285]. The resonance strongly depends on the index of refraction of the analyte, which is in contact with the metal layer. At the resonant wavelength, the metal absorbs most of the incident radiation and works

almost like a perfect absorber. This absorption increases the temperature in the metal layer, that consequently changes its electric resistance through the bolometric effect. This mechanism is parameterized by the Temperature Coefficient of Resistance (TCR) of the material. This optically induced variation in resistance can be measured as a voltage change by an external circuit biased with a voltage or current source (see figure 5.1,a).

To simulate the device we have used a multiphysics package, Comsol Multiphysics, that evaluates the interaction between electromagnetic and thermal domains.

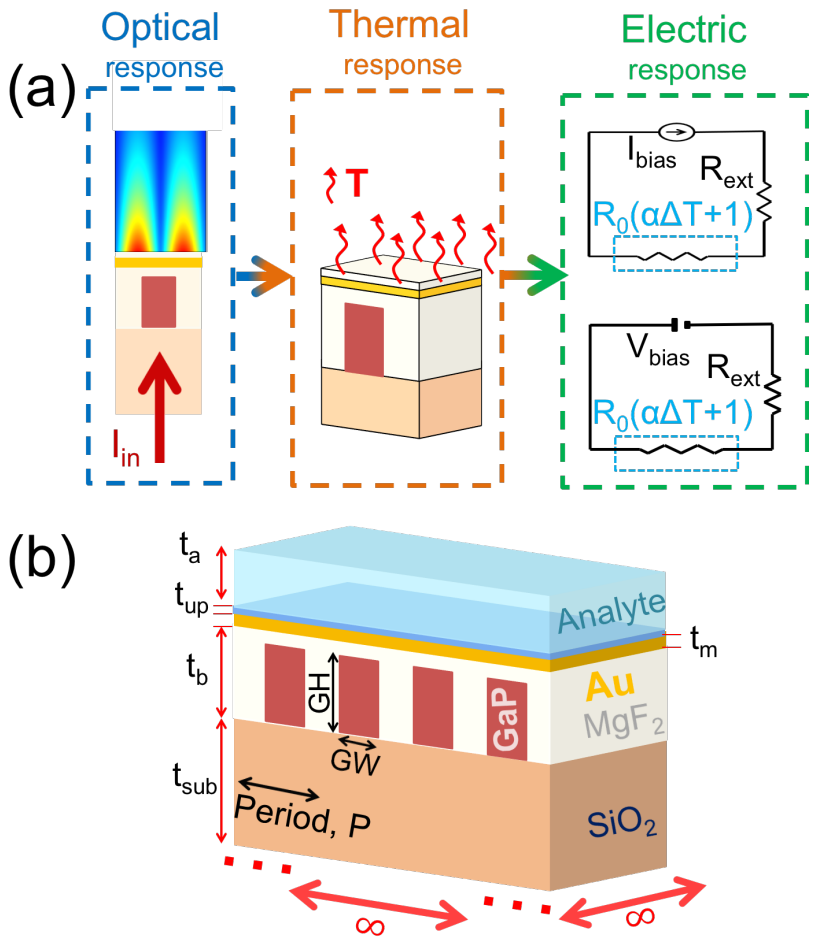

Figure 5.1: (a) Schematic representation of the physical phenomena (optical, thermal, and electronic responses) present in the proposed device. At the resonant wavelength, the excited plasmons (optical response) enhance absorption within the metal which increases its temperature (thermal response). This temperature increase also changes the electric resistivity of the metal layer, through the bolometric effect, which is read by an external circuit (electric response). (b) Geometric and material arrangement of our structure. The dimensions and the optical and thermal constants are provided in Table 5.1.

The proposed device is built on a SiO_2 substrate as a rectangular extruded GaP grating of period P, and with a rectangular profile (GW is the width and GH is the height). This nanostructure is overfilled with MgF_2 for a total thickness of t_b (being $t_b > GH$). From a fabrication point of view, the MgF_2 layer can be spin coated to generate a flat surface. On top of this layer, we find an Au coating of thickness t_m to generate the SPRs. As long

as the metal is connected to an external circuit, a thin isolation layer of SiO_2 (t_{up} in thickness) must be placed between the metal and the analyte to maintain reliable electric connections. The arrangement of these layers and structures is shown in figure 5.1,b. The dimensions of the layers and the structure, along with the optical and thermal constants of the material used in the design are presented in Table 5.1. The analyte is considered as an aqueous medium having a purely real index of refraction, $n_a = 1.333$.

Physically, Fano resonances appear when a discrete and narrow spectral resonance interferes coherently with a broadband background. In our case, the narrow peak is caused by an SPR appearing at the metal/dielectric interface; and the broadband spectral background (compared with the very narrow SPR), is produced by the radiation scattered from the grating structure, that is illuminated by the same source [285]. The total absorption spectrum of the structure is linked with the SPR, which complies with the wave vector matching condition defined in equation (2.21) [299, 339]. Our goal is to increase as much as possible the temperature of the Au layer. To do so, we must enhance absorption at the metal layer which, in combination with the nanostructure, we consider as an almost-perfect absorber figure 5.2,a shows the spectral absorption of an optimized structure (see parameters in Table 5.1) with an absorption maximum of 0.999 at $\lambda_{res} = 1.351$ μm. The resonant wavelength can be tuned by adjusting the periodicity P in equation (2.21). The magnetic field maps of the device for several wavelengths are shown in figure 5.2,b. As far as the amplitude of the incoming wavefront is $H_0 = 1$ A/m, these maps can be interpreted as field enhancement, FE maps ($FE(x, y, z) = |H(x, y, z)|/H_0$). We have also represented the magnetic field enhancement when the system is detuned from the resonance at both sides of the resonance ($\lambda = 1.3$ μm and $\lambda = 1.4$ μm) [285].

Table 5.1: Dimensional and material constants of the device. The optical constants are given at $\lambda_0 = 1.35$ μm.

Material	Dimensions [nm]	n	k [W/mK]
SiO_2 (substrate)	t_{sub} [∞]	1.447	1.3
GaP (grating)	GW [350], GH [550], P [1000]	3.14	110
MgF_2	$t_b = GH + 50$ [600]	1.372	27
Au	t_m [35]	0.411+i9.185	310
SiO_2	t_{up} [10]	1.447	1.3
Aqueous solution (analyte)	t_a [∞]	1.33	

The results show how the magnetic field enhancement is significant in a large volume of the analyte near the nanostructure for the resonant wavelength. This also improves the sensitivity of the device for variations in the index of refraction of the analyte.

The physical linked mechanisms can be described as follows. The relative change in electric resistivity of materials is linearly proportional to the change in temperature through the bolometric constant (temperature coefficient of resistance (TCR) α), as:

$$\frac{\Delta R}{R} = \alpha \Delta T. \tag{5.1}$$

The value of the TCR for Au is $\alpha = 0.0036$ K^{-1} . The temperature variation, ΔT, is also proportional to the absorbed power, and this absorbed power can be calculated as:

$$\nabla \cdot (k_t \nabla T) = Q_h, \tag{5.2}$$

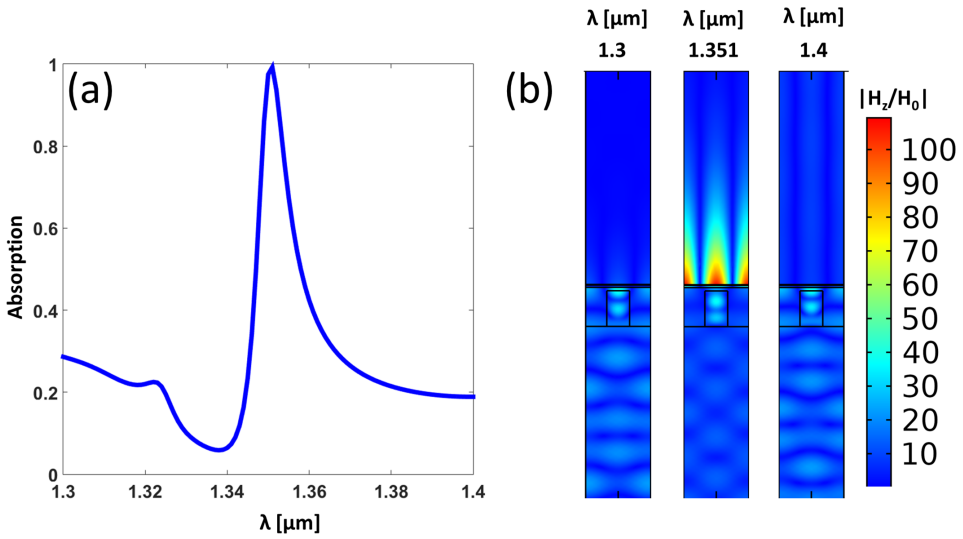

Figure 5.2: (a) Spectral absorption of the structure showing the resonance peak at $\lambda = 1.351\mu$m. (b) Magnetic field enhancement maps for several wavelengths ($\lambda = [1.3, 1.351, 1.4]$ μm).

where k_t is thermal conductivity, and Q_h is the heat power density which is related to the spatial distribution of the electromagnetic power absorbed by the metal layer. Therefore, equation (5.2) links the electromagnetic and thermal domains, and equation (5.1) translates the thermal results into electric properties.

5.1.2 Sensing by electrical interrogation using bolometric effect

We consider an optical irradiance of 100 W/cm^2 and an initial temperature of 293.15 K. Although this value of irradiance is high, it is achievable using regular laser diodes. Moreover, the footprint of the device is very small, so a narrower beam can be adapted to shine on the active area of the sensor, increasing the irradiance.

In this case figure 5.3,a shows the maximum temperature in terms of the wavelength of the illumination source. As expected from our design, the maximum response appears at $\lambda_{\text{res}} = 1.351$ μm. For this case, the temperature reaches a maximum of 294.9 K. Figure 5.3,b represents the temperature maps at 1.351 μm and 1.4 μm wavelengths, resonant, and non-resonant, respectively. To isolate the environmental changes in temperature from those caused by a change in the refractive index, we can use a Wheatstone bridge where our sensor is combined with a dummy element that responds to the environmental temperature but it is not exposed to the analyte. This solution has been previously used with bolometric antenna-coupled detectors [340].

To read out the device's response, the metal layer is connected to an external electric circuit (e.g., a voltage divider). The output from the bolometric element—the Au layer—also depends on the value of the resistance of the thin metal layer, R_0. This value depends on the geometry as $R_0 = \rho_0 L/(t_m \times w)$, where ρ_0 is the resistivity of the metal at room temperature, L is the length, and the denominator contains the transversal section as the product of the thickness, t_m, and the transversal width, w. For generality, we may approximate this value as $R_0 = 10\ \Omega$. The proposed device uses a 35 nm thick layer of Au with resistivity $\rho_{\text{Au}} = 2.2 \times 10^{-8}$ Ω.m [341]. As an example, an element with width $w = 10$ μm, and length

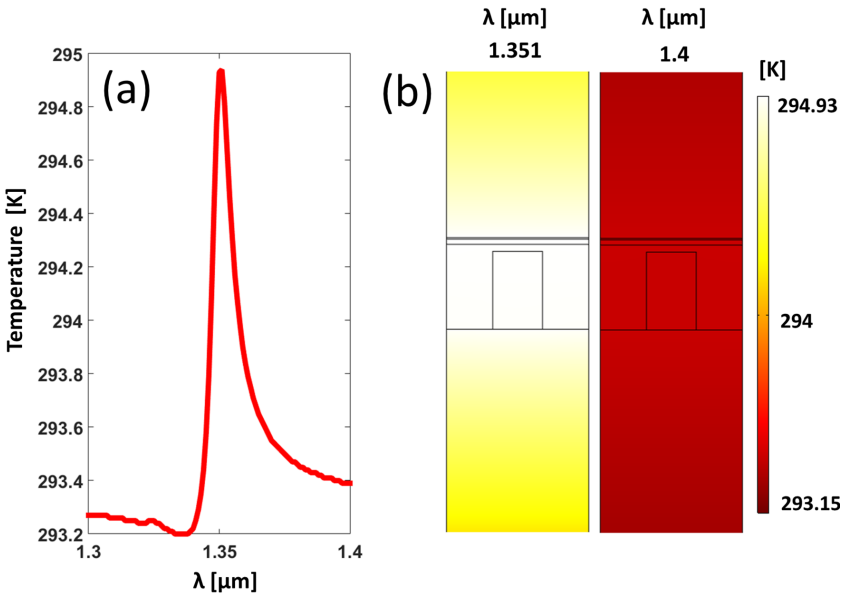

Figure 5.3: (a) Maximum temperature reached at the structure in terms of the wavelength. (b) Temperature distribution within the structure for the resonant ($\lambda = 1.351$ μm) and non-resonant ($\lambda = 1.400$ μm) wavelengths.

$L = 160$ μm, generates a resistance of $R_0 = 10.05$ Ω. Therefore, we can see that the proposed element is small enough to allow a very compact design of the sensor, which is desirable to measure tiny volumes of analyte, like human tear samples. In these conditions, the spectral variation of resistance also shows the peak at the resonant frequency (see figure 5.4,a). Therefore, by considering the physical mechanisms involved in the sensor, we obtain an electric signal related to the variation in the index of refraction of the analyte. As an example, we have calculated the spectral variation in resistance, $\Delta R(\lambda)$, for two values of the index of refraction of the analyte, $n_{a,1} = 1.33$, and $n_{a,2} = 1.34$. We show how the resonant peaks move from $\lambda_1 = 1.351$ μm to $\lambda_2 = 1.361$ μm, respectively. Figure 5.4,b shows the change in resistance for a fixed value of the optical excitation at $\lambda = 1.351$ μm; while the index of refraction of the analyte varies from 1.33 to 1.34. The response is symmetric when moving towards a lower index of refraction. For a practical operation of the device, as a bolometric system, it requires a connection to an external biasing source. Depending on the biasing strategy (voltage bias or current bias), the voltage change, ΔV_{out}, due to a change in resistance, ΔR, is given as:

$$\Delta V_{\text{out},V_{\text{bias}}} = V_{\text{bias}} \frac{R_{\text{ext}}}{(R_0 + R_{\text{ext}})^2} \Delta R, \tag{5.3}$$

for a voltage bias, V_{bias}, that sources a voltage divider with an external resistance R_{ext}, and

$$\Delta V_{\text{out},I_{\text{bias}}} = I_{\text{bias}} \Delta R, \tag{5.4}$$

for a current bias I_{bias}. In both cases, the signal ΔV_{out} is proportional to ΔR. The plots in figure 5.4 represent the dependence of ΔV_{out} with respect to the wavelength (see figure 5.4,a), and with respect to the index of refraction (figure 5.4,b). This dependence allows to define the sensitivity, S_B, and FOM of this sensor [342, 343]:

$$S_B = \frac{\partial}{\partial n_a}(\Delta R), \tag{5.5}$$

$$\text{FOM} = \frac{S_B}{\Delta R}. \tag{5.6}$$

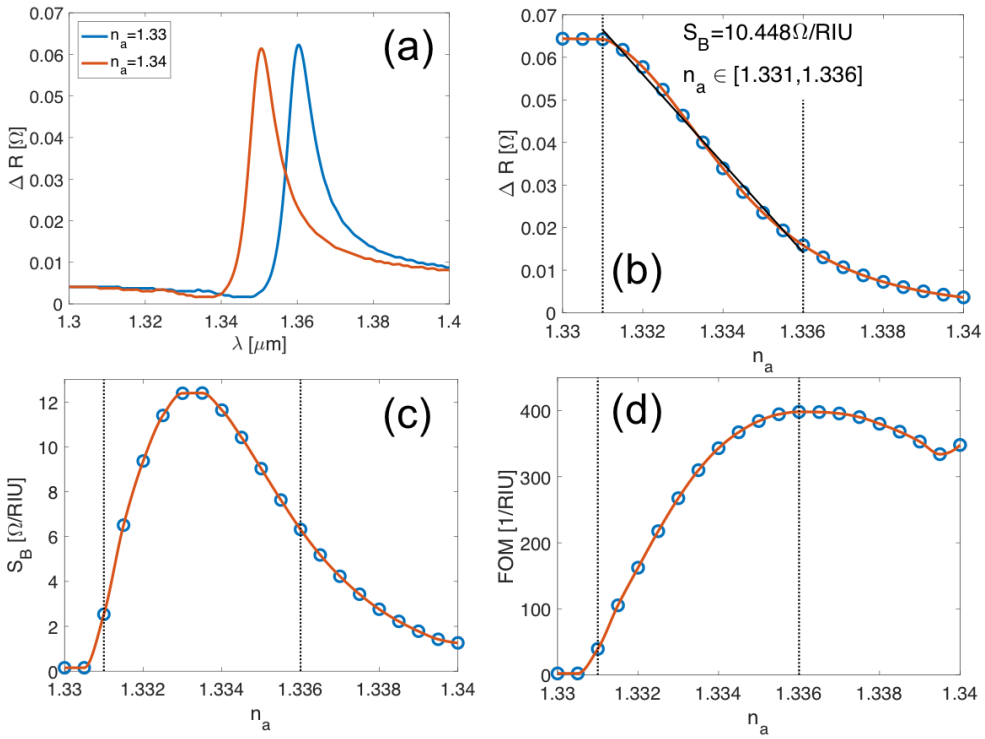

Figure 5.4: (a) Variation of the resistance of the structure as a function of wavelength. (b) Variation of the resistance with the index of refraction of the analyte when the structure is illuminated on resonance ($\lambda = 1.351$ μm). The linear fitting in the interval $n_a \in [1.331, 1.336]$ defines a value of sensitivity, $S_B = 10.45$ Ω/RIU. (c) Variation of the sensitivity, S_B, as a function of the index of refraction of the analyte, n_a. (d) Dependence of the FOM in terms of n_a. The open circles in (b-d) denote the evaluated values, and the solid lines represent an interpolation of these dependences. The vertical dotted lines in (b-d) show the range in the index of refraction, n_a, where the system is linear.

These expressions have been adapted from previously reported contributions where the change in the refractive index is measured by other parameters than the wavelength (spectral interrogation) or angle (angular interrogation) [75, 344, 345, 346]. For comparison, we model a Kretschmann's design that uses a glass prism of refractive index 1.447 working at $\lambda = 1.351$ nm with a metallic Au layer 35 nm thick. This system provides an angular shift of 0.6°: when the refractive index of the analyte changes from 1.331 to 1.336. In reflectance, the FWHM of the spectral lineshape is 0.68 nm. This results in a sensitivity of $S_B = 120$ deg/RIU and a FOM=176 RIU^{-1}. When necessary, full optimized results of angular interrogated devices are reported by Huang et al. [237] figures 5.4,c,d show the sensitivity and FOM defined in equations (5.9) and (5.6). We can see how S_B reaches a maximum value of $S_{B,\text{max}} = 12.4$ Ω/RIU at $n_a = 1.3335$, and $\text{FOM}_{\text{max}} = 398.2$ at $n_a = 1.336$. So, this would be best for aqueous samples. All these values are competitive with recently reported devices [336], plus, it is based in a simpler physical mechanism [347]. Also, from figure 5.4,b we can make a linear fit of ΔR within a given range in the index of refraction. This fit reveals an almost linear dependence when $n_a \in [1.331, 1.336]$ and sensitivity $S_B = 10.45$ Ω/RIU. This range in the index of refraction of the analyte (marked between vertical dotted lines in figures 5.4,a,c) corresponds with a

variation around $n_a = 1.333$, which is the index of refraction of water in the VIS. This index slightly decreases when moving towards longer wavelengths. Therefore, this system seems appropriate to monitor the parameters of substances in aqueous media. If necessary, the design can be tuned to perform at other ranges in the index of refraction by slightly modifying the geometry of the arrangement, for example, by changing the periodicity of the subwavelength grating, P [262]. A potential application of this design is the sensing of a human tear with a refractive index $n_{\text{tear}} = 1.336 \pm 0.001$ at $\lambda = 589$ nm [348, 349], or the salinity of water with an index of refraction ranging from 1.33 till 1.35 [350, 351].

5.2 Nanostructured electrode for solar cell based sensors

A typical perovskite solar cell arrangement has a structure as listed in table 5.2 from bottom to top [352, 353](the squared brackets embrace the dimensions of the layers). This device is illuminated from the substrate side with normal incident orientation. The layout of this structure is presented in figure 5.5,a. We modify this structure for sensing application

Table 5.2: Materials and typical layer structure of a perovskite solar cell.

Layer	Material	thicknesses [nm]
Back contact	Au	200
Hole transport layer	Spiro-OMeTAD	160
Active layer	perovskite	300
Electron transport layer	TiO_2	30
Transparent top contact	ITO	70
Substrate	SiO_2	∞

as follows [354]: (i) the SiO_2 substrate moves to the other side, adjacent to the Au layer; (ii) the ITO layer is replaced with a 50 nm-thick Ag (Ag) layer (this thickness is optimized for better performance); and (iii) we add an extruded dielectric grating with a triangular profile on top of the Ag layer. This nanostructured relief is responsible for the spectral selectivity of the device. The parameters of this nanostructure are its period, P, and the width and height of the triangular shape, GW, and GH, respectively. They will be optimized to maximize the absorption at the active layer maintaining a narrow spectral response for better sensing performance.

The triangular nanostructure is made of Si_3N_4 to have a favorable contrast in the index of refraction of the medium under test (in this case, the sensed material is air). Therefore, the modified structure is (from bottom to top): SiO_2 substrate/Au [200 nm]/Spiro-OMeTAD [160 nm]/$MAPbI_3$ perovskite [300 nm]/TiO_2 [30 nm]/Ag [50 nm]/Si_3N_4 [P, GW, GH]/air (see figure 5.5,b). The insets in figure 5.5 represent the mechanism at play in both designs. In the standard arrangement, ITO works as an antireflection coating and as an electrode to extract the photo-generated current from the device. The Ag layer in the modified design works as a reflector and rejects most of the incoming radiation except those wavelengths where the nanostructure generates an SPR [355, 356]. These resonances result in strong absorption peaks at the active layer of the cell. Moreover, this absorption is very sensitive to refractive index changes of the medium on top of the grating, *i. e.*, air.

A transverse magnetic polarized light (TM) was set for the incident field with an amplitude

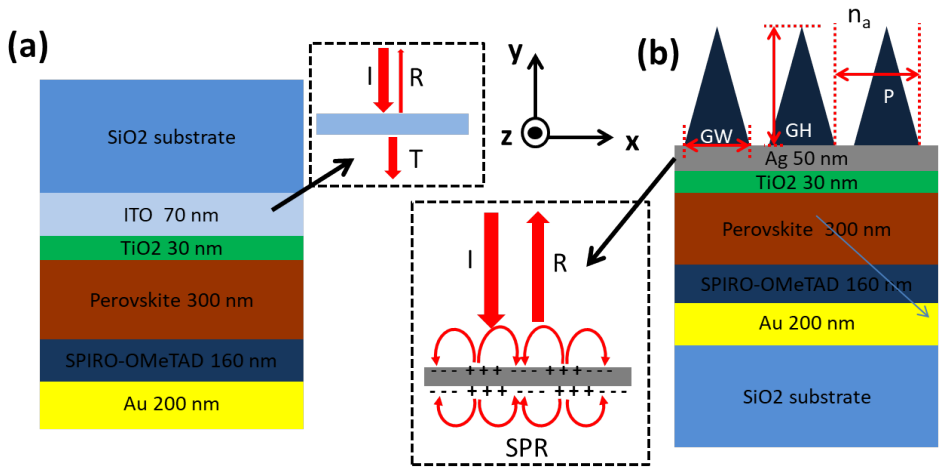

Figure 5.5: (a) Standard perovskite material arrangement. (b) Modified design for sensing applications, where the top ITO contact is replaced with an Ag layer and a dielectric grating with triangular shape with the top medium above the cell with refractive index n_a. In both cases, light is coming from top oscillating in Z direction and propagating in $-Y$ direction, the 2D cross section of the structure is contained in the XY plane, as seen the the coordinate inset in the top middle. The insets in dashed rectangles show the mechanisms at play in this structures.

of 1 A/m, oriented along the Z axis. Then, we evaluate the field distribution, and the reflection and absorption losses within different layers at the cell.

5.2.1 Optical response

To begin with, we compare the spectral responses of the standard and modified designs. This evaluation shows how the standard perovskite solar cell is well suited for energy harvesting, meanwhile, the modified design shows spectral features applicable to sensing. The modified design needs further optimization to maximize the coupling of the incident radiation to the SPR, and the availability of this resonance to generate photo-currents at the active layer. As far as the SPR is affected by a change in the refractive index, the absorption at the active layer will also reflect those changes.

From figure 5.6,a, we can see how a perovskite solar cell with ITO contacts shows high optical absorption at the active layer (red dashed line) within most of the VIS spectrum. The losses are mainly due to reflection and parasitic absorption in different layers. As an example, the absorption of the ITO electrode is represented as a green solid line. This figure also compares the behavior of the standard structure when the transparent electrode is replaced by a Ag one (50 nm-thick) that reflects most of the incoming light, and accounts for some absorption mainly at lower wavelengths in the range 300–400 nm (see blue solid line in figure 5.6,a).

Accordingly, the absorption at the perovskite layer drops, precluding the use of the cell as an energy harvesting device (see black solid line in figure 5.6,a). The reflectance of the structure for the standard design is represented in figure 5.6,b as a red dashed curve. We have also plotted the reflectance of the cell when the ITO electrode is replaced with an Ag layer (50 nm-thick) on top of the TiO_2 layer, Again, we can see how this metallic layer strongly disturbs the performance of the structure as an energy harvesting device. The previous spectral behavior changes when including the effect of the dielectric grating. We have selected a spectral region

where the perovskite cell absorbs the most ($\lambda = 610$ nm). Now, we add a Si_3N_4 pyramidal grating with geometrical parameters: $P = 600$ nm, $GW = 350$ nm, and $GH = 1050$ nm. The results for the absorption and reflectance are plotted in figure 5.6,c for $\lambda = 610$ nm. The reflectance reaches an almost null value within this range (black solid line), which means a high absorption at the Ag and active layers (see red and blue solid lines). These results are confirmed when evaluating the magnetic field distribution (see figure 5.6,d).

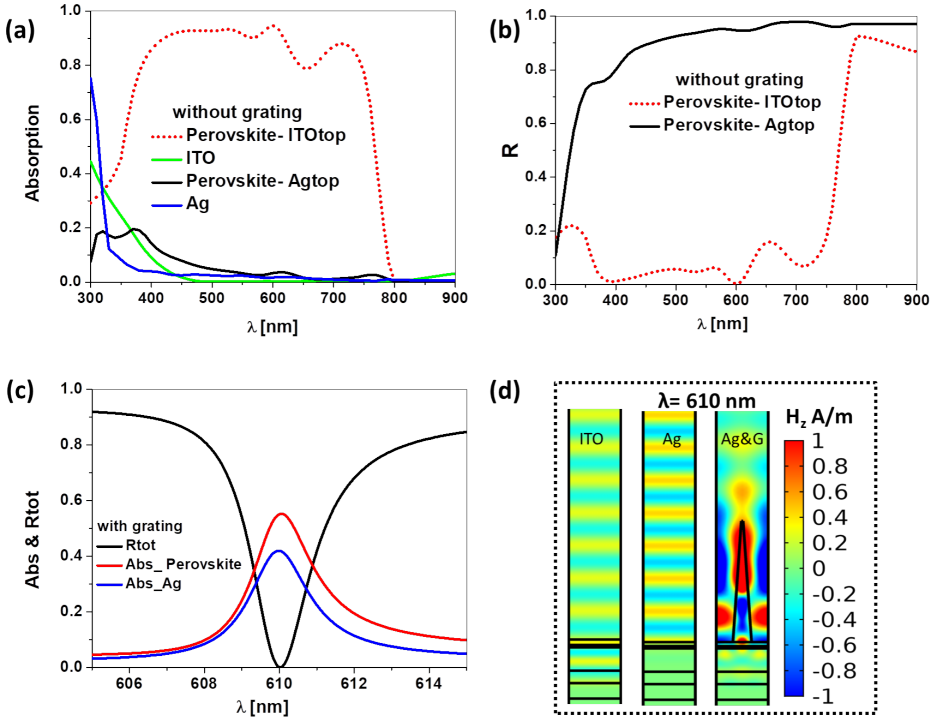

Figure 5.6: (a) Optical absorption in the active layer and top contact for the planer perovskite solar cells. (b) Spectral reflection for this two planer cases without grating. (c) The absorption in perovskite layer (red line), absorption in Ag top contact (blue line) and the total reflectance of the whole device (black line) for the proposed design with Ag/grating layer. (d) Magnetic field maps for the device with ITO (left), Ag only (middle), and Ag+grating (right) at the resonance wavelength $\lambda = 610$ nm, showing how light reaches the active layer only in the case of ITO and Ag+grating. The case with Ag only does not transmit light to the active layer significantly.

These three maps (see figure 5.6,d) produced using a TM normal incident of a plane wave. The input wave is magnetic field oscillates parallel to the grating, with an amplitude of 1 A/m, and wavelength of $\lambda = 610$ nm. In figure 5.6,d, the map at the left is for the standard perovskite cell, the map at the middle is for the same cell where ITO is replaced with Ag, and the one to the right corresponds with the case of the Ag layer plus the dielectric grating. It is worth noting how the field reaches the perovskite layer as hot spots (for the Ag plus grating case) instead of a plane wave distribution (when using plane-parallel thin layers).

To improve the capabilities of this device as a refractometric sensor for gases, we perform an optimization of the geometry of the device. This optimization relies on the maximization

of the absorption at the active layers of the modified structure and combines a good coupling to the SPR with the device output. Therefore, the merit function is defined as:

$$\mathrm{MF} = A_{\text{active layer}}. \tag{5.7}$$

At the same time, when maximizing the absorption at the perovskite layer, the lineshape becomes narrower, which is good to increase both sensitivity and the FOM of the device taken as a sensor. This optimization is made by changing the profile of the triangular dielectric grating using parameters GW and GH for a fixed period $P = 600$ nm. We will also fix the wavelength of interest at $\lambda = 610$ nm. The parameter P is left for additional tuneability of the device. After obtaining the optimum profile parameters of the grating, we will make refinement of the design in terms of the thickness of the Ag layer.

5.2.2 Optimization

The merit function map in terms of the geometrical parameters of the grating (GW and GH) is presented in figure 5.7,a. It shows regions where the absorption is high in the perovskite layer. If we plot reflectance, we obtain a similar map with the same regions showing minimum reflectivity. The black circle in figure 5.7,a locates the highest absorption for the selected wavelength. The value of the absorption at this maximum point is 57% at the active layer. This high value is due to SPR excited by the dielectric nanostructure in the top metallic thin-film. Actually, this result contrast with the 4% in absorption when only an Ag layer replaces the ITO electrode (without dielectric grating). The geometrical parameters for this maximum in the merit function are: $GW = 215$ nm and $GH = 1560$ nm. The tolerance that maintains almost the same values is $\pm$ 25 nm which could be achieved easily using the available lithographic techniques.

The absorption in the Ag and perovskite layers, and the total reflectance are shown in figure 5.7,b for the optimized geometry. To better understand the effect of the optimization, we have also plotted the absorption at the perovskite layer for the non-optimized values (see dotted line) used in figure 5.6,c. Although the intensity has not increased significantly, we can see how the lineshape is much narrower in the optimized case. This will be of importance when evaluating the system as a refractometric sensor.

It is important to check the capability to tune the response at different wavelengths to adjust the device using available commercial light sources or to detect at a specific detection band. We fix all the parameters except the period of the grating P, and we only change the grating period. As expected, figure 5.8,a shows a blue shifting when reducing P, and a red-shifting when increasing it. As far as perovskite solar cells have a wide absorption band that covers the VIS-NIR (typically from 300 nm to 800 nm), we can use the period P to tune the response to any desired wavelength in this band.

The metal thickness, t_{Ag}, is an important parameter of the device. Figure 5.8,b shows the absorption within the perovskite layer. We can see how the top contact becomes almost transparent when the Ag layer is 10 or 20 nm thick. In these conditions, the SPR does not reveal itself in the lineshape. This happens with thicker Ag layers.

The peak in absorption becomes spectrally narrower as the thickness of the metal increases. However, a thick Ag layer is not practical because it blocks the light reaching the perovskite layer. In this sense, we choose a thickness for Ag as t_{Ag}= 50 nm because at this value we have

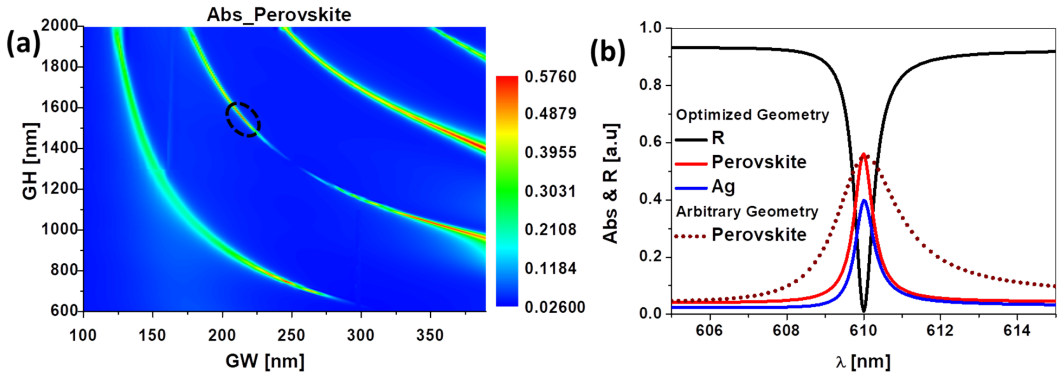

Figure 5.7: (a) Optical absorption in the perovskite layer with the grating parameters GW, and GH for a fixed Period P 600 nm at a single wavelength at, $\lambda = 610$ nm, using TM polarized light of 1 A/m amplitude the highlighted black dashed circle defines the location of the point where the absorption in perovskite is maximized. (b) The absorption in perovskite layer (red line), absorption in Ag top contact (blue line), the total reflectance of the whole device (black line) for the optimized geometry, and the absorption in perovskite layer (brown dashed line) for the arbitrarily selected geometry before optimization.

both high absorption and narrow response. A thickness of 40 nm could achieve a little better absorption but the line width is wider than in the case of 50 nm thickness.

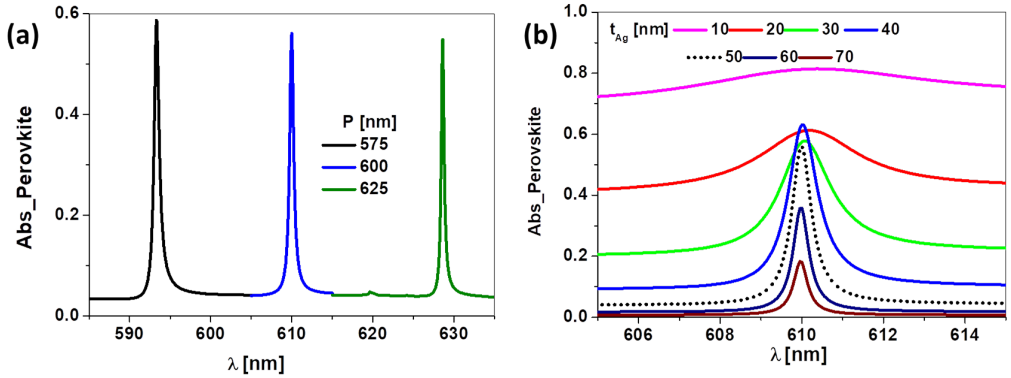

Figure 5.8: (a) Effect of the period of the grating P, on the wavelength, of resonance. The resonant wavelength is proportional to the period of the dielectric grating P. (b) Effect of the thickness of the metal layer on the spectral relevance of the SPR. The optimum thickness, $t_{\mathrm{Ag}} = 50$ nm, is plotted as a dashed line.

5.2.3 Device Performance

We used the common sensor parameters, sensitivity and FOM to quantify the optical sensor's performance. Here, we aim to sense the change in refractive index of the medium in contact with the nanostructured grating and the metallic layer, for example due to exposure of a gas. If we use optical interrogation, the sensitivity is defined as the shift in the wavelength of the reflection dip caused by refractive index change [61, 357] (see equation 4.2). The associated FOM takes into account the optical signal FWHM to normalize the sensors performance for compare (see equation 4.3). Our goal is to optoelectronically interrogate the device. Therefore,

we need another opto-electrical term that is the responsivity, $\mathcal{R}$, which is defined as [358]:

$$\mathcal{R}_S(\lambda) = \frac{I_{\text{photo}}}{P_{\text{input}}(\lambda)}, \tag{5.8}$$

whereI_{photo} is the ideal photo-generated current, and $P_{\text{input}}(\lambda)$ is the incident light power that is delivered by a tunable source. The sensitivity and FOM will be calculated using equations (4.2), and (4.3), but the wavelength shift will be for the reponsivity dip instead of the reflectivity dip to replace the optical interrogation with an optoelectronic one.

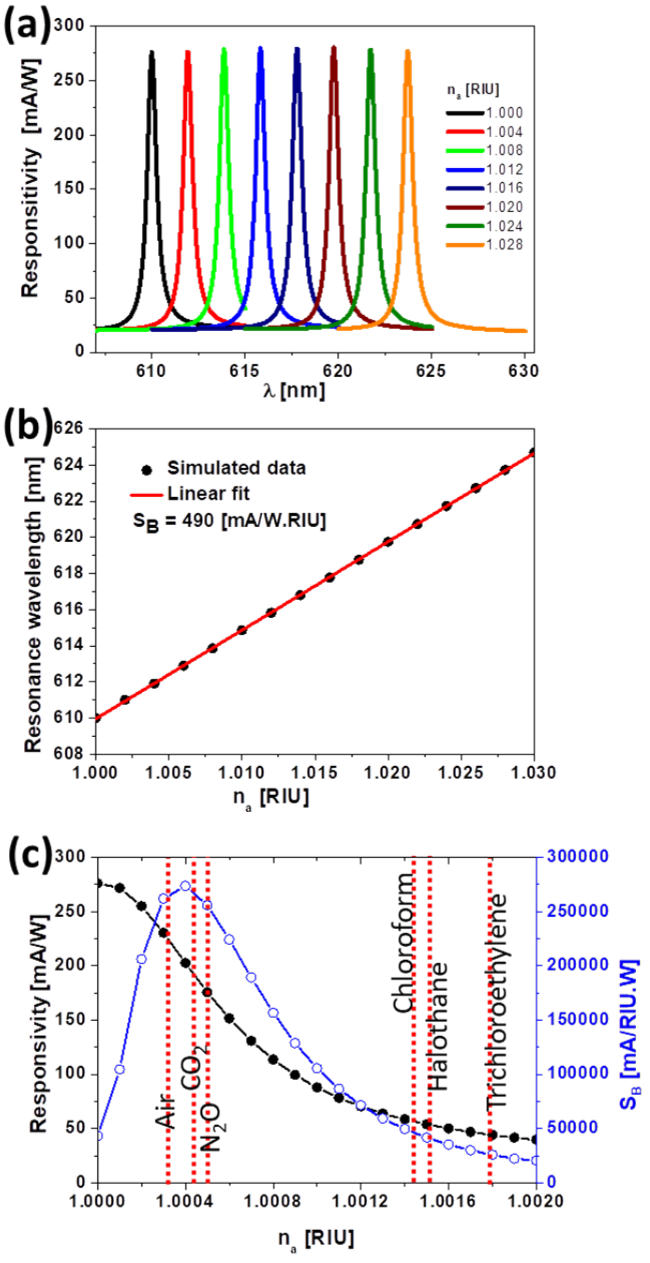

Figure 5.9: (a) Spectral responsivity of the optimized device for different values of the refractive index of the analyte medium, n_a. (b) Resonance wavelength in terms of the refractive index change. It shows a linear behavior through the whole scanned refractive index range.

The responsivity of the optimized device is very narrow in wavelength due to the SPR resonance coupled to the absorption in the active layer, we plot the responsivity for different values of refractive index in figure 5.9,a ranging from 1 to 1.03, which represents an air medium that is perturbed by some controlled external mechanisms (change in concentration, temperature, composition, etc.) [359]. Due to their origin as plasmonic resonances, the spectral responsivity can be fitted to Lorentzian lineshapes. An important result of this fitting is the FWHM of the resonance. We have found that FWHM is almost constant through the examined refractive index range and has a value of 0.6 nm. After evaluating these parameters, we can obtain the Sensitivity, $S_{B,\lambda}$, and the FOM using equations (4.2), and (4.3). These calculations provide a maximum spectral sensitivity of $S_{B,\lambda,\max} = 490$ nm/RIU, and a $\mathrm{FOM}_{\max} = 816.6$ RIU^{-1}.

The resonance wavelength, which shifts when the refractive index changes, is nearly linear as seen from figure 5.9,b and the linear fitting provides a value of $S_{B,\lambda,\mathrm{linear}} = 490$ nm/RIU. Along with the simple and low-cost optoelectronic interrogation at normal incident conditions, the device has high sensitivity and high FOM values are comparable with many recent reported optical sensors with high sensitivity [360, 361, 362, 363, 364].

Another application for this sensor is to detect the existence of gas contaminants of pollution from inorganic gases like carbon dioxide (CO_2), nitrous oxide (N_2O), or organic vapors such as chloroform vapor, halothane, and trichloroethylene [365]. In this case, the electric response of the device illuminated by a monochromatic source can be used to detect such ultra-small variations in the air refractive index through the change in the output responsivity of the device (see figure 5.9,c). The change in responsivity for such small changes in the air refractive index is high, so, it reveals very high values of the sensor sensitivity (see figure 5.9,c). This sensor characteristic is very useful to monitor the changes in the gas quality of closed atmospheres of laboratories, clean rooms, and industrial locations [366, 367]. And assures perfect specified conditions for the atmosphere in these locations.

5.3 Self-powered plasmonic sensor for gases

A plasmonic nanostructure on the top of solar cell and interact with the incoming light and produce several resonance mechanisms along with the wide absorption band of the cell. We will show here, how nanophotonic structures boost the capabilities of perovskite-based solar cells for their use as refractometric sensors through the excitation of multiple resonances at the cell front surface exposed to air. This transformation from a solar cell to a sensor also implies a discussion to properly describe the performance of the system as a dedicated refractometric sensors, or as a solar cell.

We numerically analyze and propose a modified perovskite solar cell to work as a refractometric sensor for gases [368]. An interesting use for this device is in environmental research applications, as well as in industrial inert atmospheres or laboratory clean rooms [366, 367]. As a simple sensor for gases, it may help to detect volatile compounds with potential environmental hazards, and to monitor air quality parameters and gas composition [369, 370, 371, 372]. The measurement of the index of refraction of air, as a ubiquitous gas, is of interest since long ago [373, 374]. Several proposals have been presented to monitor air quality and composition [367, 371, 372, 375, 376]. It is also known that the index of refraction of air, or any other gas or gas mixture, depends on physical parameters (temperature and pressure) and chemical composition (humidity, presence of natural or artificial specimens). Then, a refractometric sensor can check if some preset conditions are fulfilled, or a known specimen varies its concentration.

To do that, several optical technologies have been applied to sense refractometric changes in gases. For example, we can find interferometric systems [359, 377, 378, 379, 380], plasmonic devices [375, 381, 382, 383], or sensor based on specialized fibers and photonic crystals [367, 369, 376, 384, 385].

Our system, based on the selective resonances generated by subwavelength metallic gratings on a modified perovskite cell can provide an alternative. The capabilities of optical gas sensors rely on the accuracy and resolution of the involved optical instruments. A high-performance sensor requires high quality optical subsystems, making the device more complex and expensive. The sensor proposed in this section delivers an electric signal to voltage, or current, meters, that are, by far, more available at lower cost.

The calculation is made in two steps. First, a linearly polarized monochromatic wave illuminates the structure from the air. The structure is excited with a plane wavefront under normal incidence conditions, and having a total irradiance of 50 mW/cm^2. The magnetic vector is oriented along the direction of the slits (TM polarization), *i. e.*, perpendicular to the plane represented in figure 5.10,a. Then, the energy absorbed at the active layer is calculated using the material parameters of every layer in the structure. This is a 2D simulation because we consider an extruded geometry along the direction of the slits. The period of the subwavelength grating is repeated using periodic boundary conditions. Each portion of the structure is defined geometrically and optically using its complex refractive index. The result is the identification of several peaks in the spectral absorption, which correspond to selective resonances of the nanostructured subwavelength grating. The second step transforms this absorbed power assuming that each photon generates a hole-electron pair that is collected by the top and bottom electrodes (assuming a collection efficiency equal to 1). This combined mechanism (selective absorption + current generation), and a monochromatic illumination allow refractometric sensing.

Figure 5.10,a shows a typical layer structure used for perovskite solar cells illuminated from the substrate [172, 173]. In the same figure, we have also evaluated the spectral absorption for two values of the index of refraction of the media in contact with the front surface (see figure 5.10,b). Our first approach is to consider air as the analyte ($n_a = 1$), and slightly change its index of refraction while we monitor the response of the system. In energy harvesting applications, the performance of the cell is parameterized with its efficiency, which is related to the short-circuit current, or the short-circuit density current, delivered by the cell, I_{SC} or J_{SC}, respectively.

This current is proportional to the optical absorbed power at the active layer of the cell, which also depends on the spectral composition of the radiation. In our analysis, we can numerically evaluate the absorbed power within the perovskite layer, A_{perov}, and therefore obtain the optoelectronic response of the cell [193]. This signal is also dependent on the index of refraction of the medium in front of the cell that becomes the analyte. Therefore, we evaluate the sensitivity of the cell as a sensor, which is defined as the change of a physical property of the device with respect to an environmental change. In this case, we use the responsivity of the cell, $\mathcal{R}$ (in mA/W), as the parameter that changes with the refractive index of the analyte, n_a. [343, 386]. In figure 5.10,c we represent the change in responsivity, $\mathcal{R}$, as a function of the index of refraction of the analyte when the system is illuminated at $\lambda = 600$ nm and 50 mW/cm^2 in irradiance. When I_{SC} is used to define the sensitivity, $S_B = \partial I_{SC}/\partial n_a$, we find a value of $S_B = 190$ mA/RIU (where RIU means refractive index units). However, when using responsivity, we obtain $S_B = \partial \mathcal{R}/\partial n_a = 70$ mA/(W.RIU). We use responsivity because

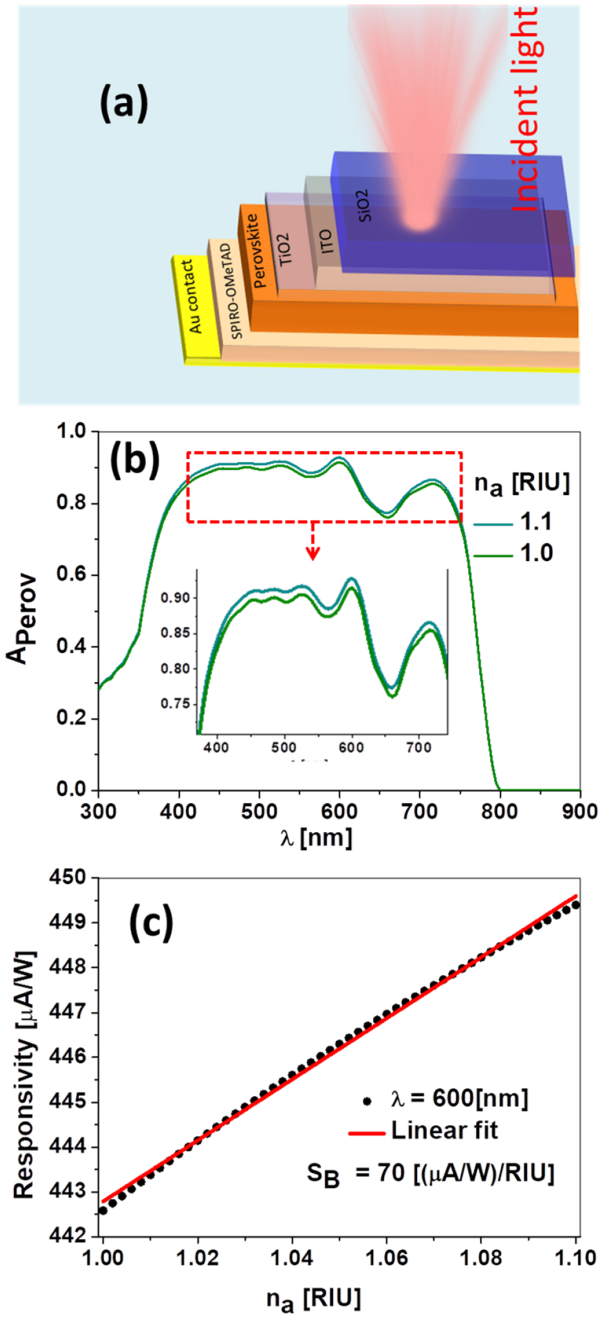

Figure 5.10: (a) Layer structure of a perovskite solar cell. The cell is illuminated through the SiO_2 (glass) substrate. From top to bottom: air, glass (SiO_2, $t_{SiO_2} = 3$ mm), top electrode (ITO, $t_{ITO} = 70$ nm), buffer layer (TiO_2, $t_{TiO_2} = 30$ nm), active layer (perovskite ($MAPbI_3$), $t_{perovs} = 300$ nm), buffer layer ($t_{spiro} = 160$ nm), and bottom electrode ($t_{Au} = 200$ nm). (b) Spectral absorption of active layer for two indices of refraction of the outer medium, $n_a = 1.0$ and n_a=1.1. (c) Responsivity, $\mathcal{R}$ as a function of n_a. The sensitivity of this device is given by the slope of the linear fit: $S_B = 70$ mA/(W.RIU).

of its robustness and flexibility to define the sensitivity independently from the power of the source illuminating the cell. As it is being demonstrated, this idea shows the potential that it is worth exploring. Therefore, the next step is to change the design of the cell and improve its optical sensor's performance, while maintaining the structure of a working perovskite solar

cell. This approach would allow easy implementation, so customized solar cells could work as refractometric sensors. A similar approach has been successfully proved when adapting a CMOS device for sensing [387], and when perovskite photodetectors are used in VIS light communication systems [388]. The solar cell becomes closer to a photodetector when the delivered electric signal varies for changes in n_a, acting as a sensor. Then, the performance parameters commonly used in sensing (sensitivity, FOM) may not be directly applicable here, so the capabilities of the system should be related with detection figures of merit as responsivity, noise equivalent power, detectivity, etc.[388, 389]

5.3.1 Proposed structure and materials

The performance of a planar perovskite solar cell with an ITO top contact as a refractometric sensor is not competitive. However, we can improve the device by replacing the ITO top electrode by a nanostructured metallic layer. Also, we move the SiO_2 substrate (or any other substrate, including flexible materials) behind the non transparent Au electrode to expose the front surface to the analyte. In this way, we mostly preserve the structure of the solar cell and act only on the surface of a flipped, almost-finished, functional device.

The geometry and material choice for the top contact, presented in figure 5.11,a is a metallic thin layer (in our case, an Ag layer with a thickness of t_m=150 nm), where periodic slits are etched to trigger funneling light mechanisms at selected wavelengths [267]. The sub-wavelength period of the grating, $p = 375$ nm, precludes the existence of high-order diffraction modes. Consequently, the aperture is also subwavelength, having a width $GW = 50$ nm, and showing a high aspect ratio with a height equal to the thickness of the metallic layer ($GH = t_m = 150$ nm), meaning that the slit reaches the TiO_2 buffer layer. Figure 5.11,b shows the spectral absorption at the active layer for the proposed structure and geometry. This spectral shape is clearly different from the one belonging to a conventional perovskite solar cell (see figure 5.10,b), and shows three maxima in the spectral absorption, located at $\lambda_{\mathrm{I}} = 385$ nm, $\lambda_{\mathrm{II}} = 715$ nm, and $\lambda_{\mathrm{III}} = 783$ nm. It shows more peaks at different wavelengths, but these three are the most relevant in the analyzed spectral range. If we compare figure 5.10,b, and figure 5.11,b we see relative low value in absorption for the modified cell. The main reason for this decreased absorption is the high reflection caused by the Ag non-transparent top

electrode that replaces the ITO layer. Since our goal is not energy harvesting, instead of enhancing the total photo-generated current generated by a broadband spectrum, we aim to increase the variation of the photo-current delivered by the device with respect to a change in the index of refraction. The device is illuminated with a monochromatic laser source centered at one of the maximum absorption wavelengths. This increases the variation of the current when changing the index of refraction. The next optimization step is to find the geometry of the apertures that maximizes the short-circuit current of the solar cell at each peak. When done, this optimization will provide higher values in absorption for each wavelength, as we will show in the following section (see also figure 5.12).

To understand the origin of each peak, we plot the Poynting vector and the electric field vector maps (see inset in figure 5.11,a and figure 5.11,c). The observed maxima have different field distributions within the structure, where resonances II and III generate stronger fields within the active layer. The peak at λ_{I} is related to plasmonic resonances caused by the periodic narrow slit. This origin is supported by the presence of hot spots in the electric field distribution at the metal/air interface (see figure 5.11,c). The radiation at λ_{II} funnels through the gap until reaching the active layer [284]. The peak at λ_{III} corresponds to the strongest

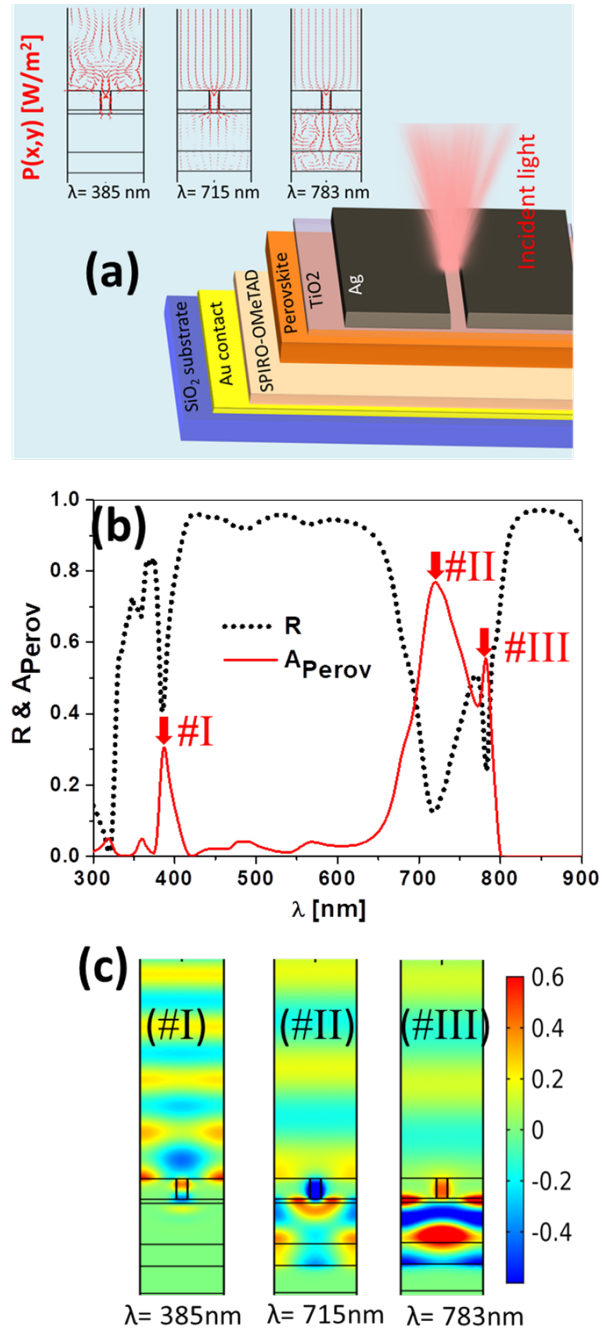

Figure 5.11: (a) Layer structure of a perovskite solar cell where the top electrode has been replaced by a nanostructured metallic layer having a thickness of $t_{\mathrm{Ag}} = 150nm$. A periodic grating with subwavelength period, $p = 375$ nm, and apertures, $GW = 50$ nm, allows light funneling towards the active layer of the cell. The inset at the left show three maps of the Poynting vector where we see how the power is directed towards different portions of the solar cell for λ_{I}, λ_{II}, and λ_{III}. (b) Spectral reflectance of the structure (black dotted line), and spectral absorption of the active layer (red solid line). Both the spectral absorption and reflectance show three peaks (I, II, and III) at $\lambda_{\mathrm{I}} = 385$ nm, $\lambda_{\mathrm{II}} = 715$ nm, and $\lambda_{\mathrm{III}} = 783$ nm. (c) Electric field distribution for the same wavelengths considered in (a) and (b). The three resonances show their maximum amplitude at different layers within the solar cell.

field distribution at the active layer. However, as we will see when analyzing its behavior with respect to the index of refraction of the analyte, this peak does not shift significantly in wavelength when changing the index of refraction, and should not be caused by a plasmonic resonance but by selective transmission through the apertures [284].

5.3.2 Optimization of the device

We focus on engineering opto-electronically interrogated device able to sense changes in the index of refraction of the analyte. We will show the geometry of the design and the operation wavelengths where the proposed system provides the largest variation of the electric signal with respect to the index of refraction of the environment. In some cases, the spectral shift of the optical response of the optimized geometry allows operating the device using spectral interrogation techniques.

The common geometry and material arrangement of a perovskite solar cell can be seen in figure 5.10,a. This basic design is modified at the top surface: the ITO transparent electrode is replaced by a nanostructured metallic layer (see figure 5.11,a). When including it on top of the active perovskite layer, the absorption drops. It decreases because the metallic coating is highly reflective and also dissipates energy causing losses. However, at some selected wavelengths, the absorption at the active layer, and consequently the output signal delivered by the cell, increases due to this subwavelength grating. The slits grooved on the metallic coating generate funneling and plasmonic resonances that selectively increase the amount of energy reaching the perovskite layer.

The analysis of the system requires the definition of a function of merit for optimization purposes. In this case, we select the amount of energy absorbed by the perovskite active layer as the function of merit. The reason for this choice is the direct relation between the signal delivered from the cell and the absorption at the perovskite layer. Due to the geometry selected in this analysis, that is an extruded 2D arrangement, the calculation can be made in 2D, allowing a faster and more reliable optimization. The optimization is made by a parametric sweeping of the geometry of the nanostructure (GW and GH). In practice, we maximize the optical absorption at the solar cell active layer, A_{perov}. We maximize it for those wavelengths generating a large absorption at the active layer because they will generate a large electric signal, which is better suited to sense environmental changes. After optimizing this variable, we have obtained the spectral absorption for the three wavelengths of interest. The actual parameters that maximize absorption are given in table 5.3 for each wavelength. So, we have maximized the amount of energy absorbed at the perovskite active layer through the combination of plasmonic resonances, funneling effects, and selective transmission, by varying the geometrical parameters of the slits. In figure 5.12, we represent the maps of the absorption at the perovskite active layer, A_{perov}, in terms of the width (GW) and height (GH) of the slits, for each wavelength of the resonances, identified previously (see labels in table 5.3)

We can see that the maximum absorption, $A_{\text{perov}} = 94\%$ (see figure 5.12,b), is obtained for a wide slit at $\lambda_{\text{II}} = 715$ nm. The colormap of these plots has been normalized independently for each wavelength. To compare the results among them, it is necessary to consider the maximum value for each one.

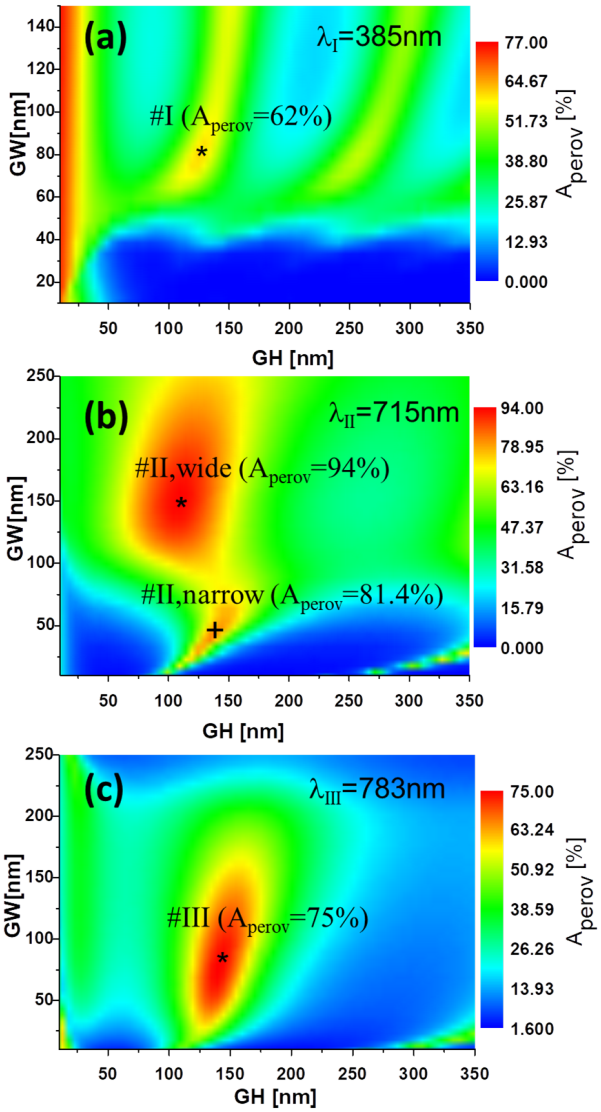

Figure 5.12: Maps of the absorption at the perovskite active layer, A_{perov}, in terms of the height (GH) and width (GW) of the slits, maintaining the thickness of the metal layer, and the grating period. Each map corresponds to one of the three spectral resonances centered at $\lambda_{\text{I}}, \lambda_{\text{II}}$, and λ_{III}. There are two maxima for λ_{II}, labeled as # II-wide and # II-narrow according to the width of the slit. The value of A_{perov} is given for every optimum design. We have represented these plots using color maps with different ranges to emphasize the variations for each case. Therefore, the comparison between maps should consider the applicable ranges. The optimum designs are marked and labeled as in table 5.3.

Table 5.3: Optimized geometrical parameters of the low-order diffraction grating.

λ [nm]	label	p [nm]	GW [nm]	$GH = t_m$ [nm]
385	# I	375	80	125
715	# II-narrow	375	40	140
	# II-wide	375	150	110
783	# III	375	75	140

5.3.3 Results and Discussion

Figure 5.13 shows the spectral absorption of the optimized devices for each wavelength previously selected (see figure 5.12 and table 5.3). We see how the absorbed power is significantly larger after optimization.

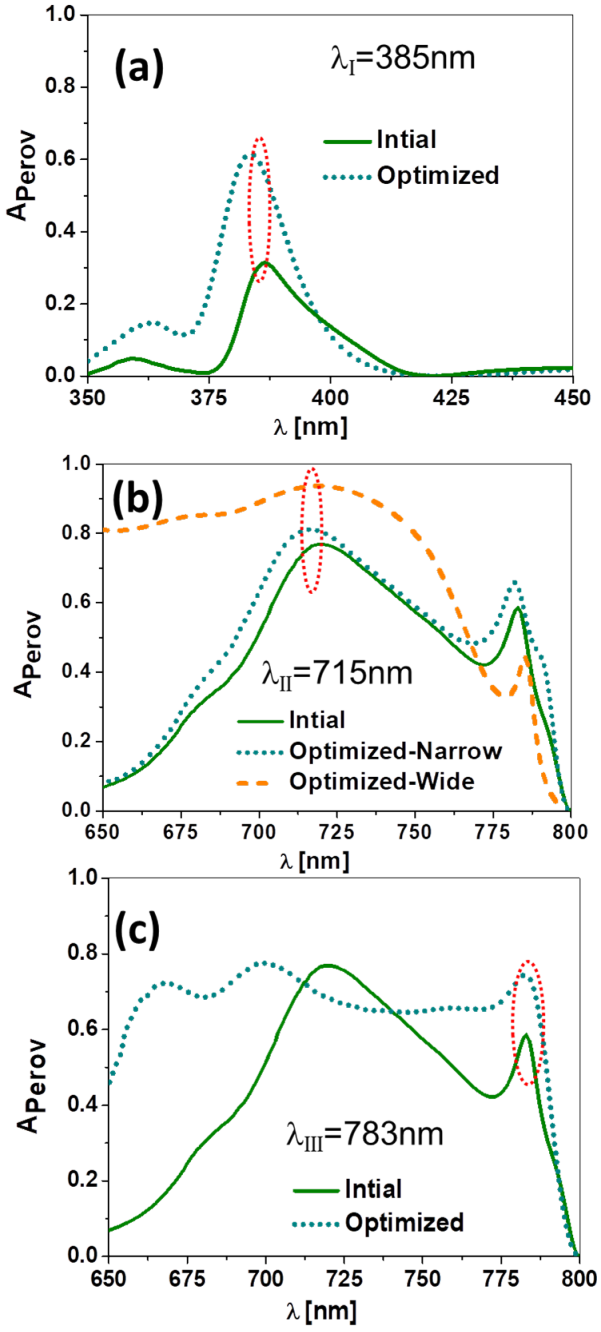

Figure 5.13: Spectral absorption in the active layer for the optimum geometrical parameters at the three resonant wavelengths. the absorption in the active layer for the design with the arbitrary selected geometry is included for each case to show the effect of the optimization process .

To explore the capabilities of the proposed device for spectral and optoelectronic interrogation methods, we have evaluated the spectral absorption for each optimized case, and for two

different values of the index of refraction, $n_a = 1.0$ and 1.1. This range is much larger than the expected variations in the index of refraction, and explores how this device behaves when adding nebulized liquids in the atmosphere, or when the analyte is under extreme values of pressure and temperature [359]. Besides, this extended range reveals better how the spectral absorption changes with respect to the index of refraction (as shown in figure 5.14). In our calculation, we have considered the gases as non-absorptive (meaning a negligible value of the imaginary part of the index of refraction). We have also neglected the contribution of scattering, but this simplification should be raised if nano- and micrometer size particles were taken into account [390].

In figure 5.14, we show how each design undergoes a spectral shift, $\Delta\lambda$, and absorption intensity changes, ΔI, as the refractive index changes. In this last case, a variation in the absorption at the active layer translates in a change in the photo-generated current, and hence in responsivity. A larger $\Delta\lambda$, or ΔI, means a higher sensitivity because it generates a larger measurable change when the index of refraction varies. However, the measurement method is different: $\Delta\lambda$ is obtained through a spectral interrogation scheme, and ΔI is measured using an optoelectronic set-up where the electric signal delivered by the cell is processed by an external circuit. In this case, the electronic output signal of the device senses the variation of the refractive index, which means an optoelectronic interrogation.

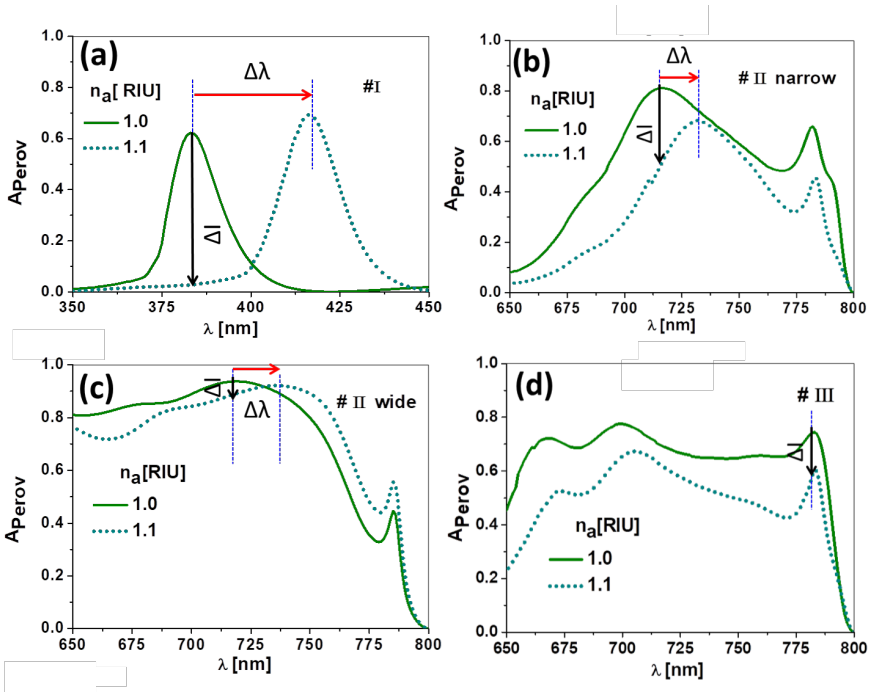

Figure 5.14: Spectral absorption for the four optimized designs at the three resonant wavelengths. These absorptions are calculated for two values of the index of refraction of the analyte, $n_a = 1.0$ and 1.1. The vertical blue dotted line represents the wavelength of resonance for $n_a = 1.0$, and 1.1. $\Delta\lambda$ is the spectral shift of the resonance when varying the index of refraction, and ΔI shows the variation in absorption at the perovskite active layer.

We simulate our device's performance to measure the index of refraction of gases (with index of refraction very close to 1.0). The system works with a monochromatic light source tuned to the selected resonant wavelength of each one of the designs ($\lambda_{\mathrm{I}}, \lambda_{\mathrm{II}-narrow} = \lambda_{\mathrm{II}-wide}$, or λ_{III}). To properly compare the four designs, the light source illuminates the device with

the same irradiance of 50 mW/cm^2. This value is achievable using regular diode lasers. At the same time, the spectral width of the resonance is large enough compared with the typical linewidth of commercial laser diodes (well below 0.1 nm), to consider the light source as purely monochromatic (as a delta function in λ that samples the absorbed spectral). This irradiance generates a photo-current, I_{SC}, that is retrieved from the cell and delivered to an electronic read-out circuit. When changing the index of refraction of the analyte, the current varies, and so does the delivered signal. The photo-current is used to calculate the responsivity, $\mathcal{R}$, [358] (see equation (5.8)).

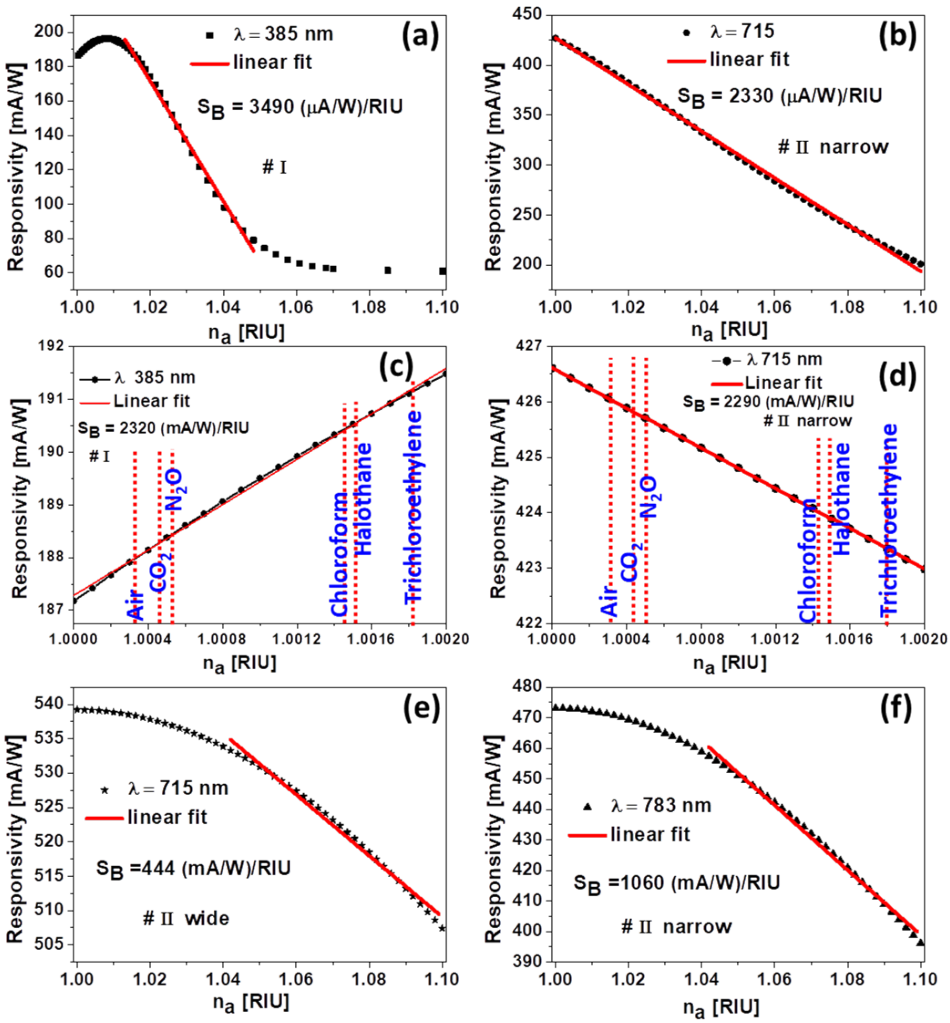

Figure 5.15: (a,b,e,f) Variation of the responsivity, $\mathcal{R}$, as a function of the index of refraction of the analyte, n_a, for the four optimum design selected in this paper. A linear fitting for the range in the index of refraction where the variation in the current is almost linear line, The slope of the fitting give the average value of the sensitivity of the device, S_B within this range. (c,d) is a zoom for the data in (a,b) for a small variation in the index of refraction of air (*i. e.* n_a=1). This change represent the case when small amounts of gas inserted in air. Some possible gases that could be detected are placed on the vertical dashed red lines in (c,d).

The change in the responsivity with respect to n_a is presented in figure 5.15. As pointed out in the introduction section, the sensitivity of this sensor can be defined as the variation of

$\mathcal{R}$ with respect to the index of refraction of the analyte, n_a[343, 386, 391]:

$$S_B = \frac{\partial \mathcal{R}}{\partial n_a}, \tag{5.9}$$

and the FOM is also redefined in terms of the responsivity, $\mathcal{R}$ [343, 386]:

$$\text{FOM} = \frac{S_B}{\mathcal{R}}. \tag{5.10}$$

These definitions are adaptations of those applicable to plasmonic sensors interrogated in wavelength or angle of incidence, as it happens with Kretschmann and Otto configurations.

The evaluation of the sensitivity for the four designs presented in this section, can be made using equation (5.9). Table 5.4 summarizes the performance of the four designs in terms of sensitivity and FOM (equations (5.9), and (5.10)). This table also includes the variations $\Delta\lambda$ and ΔA_{perovs}, that are applicable for a spectral interrogation method, or an optoelectronic technique, respectively. The idea is to express the sensor characteristics using electric parameters, where I_{SC} is proportional to A_{perov}, and therefore, the sensitivity is given using its definition in terms of $\mathcal{R}$. figure 5.15 plots the responsivity for the four designs treated in this contribution.

For the first peak at λ_{I}, the change in photo-current when varying the index of refraction is large, in accordance with a 60% change in the absorption at the active layer (see figure 5.14,a, and table 5.4). This means a high sensitivity to refractive index changes, but results in a limited dynamic range since the current decays sharply (see figure 5.15,a). The spectral absorption of the second peak at λ_{II} (see figure5.14, b # II-narrow case), generates a smaller spectral shift while maintaining a significant variation in intensity. Its responsivity is high and linear within the studied range in the index of refraction (see figure 5.15,b). This expanded range in linearity is desirable, and compared to the previous design at λ_{I}, makes this design operationally more robust and stable.

Figure 5.14,c,d contains a detailed zoom of the responsivity in the range na $\in$ [1.000, 1.001] that comprises the expected variations in the index of refraction of air or controlled atmospheres. We have selected designs # I and # II-narrow because they show better behavior (higher S_B). We can see, that these designs, even in this narrow range, provide competitive values of sensitivity. The corresponding performance values are also shown in table 5.4. Some possible gases that could be detected are placed on the vertical dashed red lines in figure 5.14,c,d.

The spectral absorption for designs # II-wide, and # III presents a lower value of ΔI (see figure 5.14,c,d) that corresponds with a lower value of sensitivity (see figure 5.15,c,d and table 5.4). Even more, in the design # III at $\lambda_{\text{III}} = 783$ nm, the spectral shift, $\Delta\lambda$, is negligible and precludes its operation using spectral interrogation methods. This fact is in agreement with the physical interpretation of this peak as a selective transmittance through the slits [284]. The FOM results summarized in table 5.4 are moderate compared with previously reported values [319, 320, 321, 322, 324, 325, 326].

FOM for angular and spectral interrogation systems is defined as the ratio between sensitivity, S_B, and the capability of the system to distinguish a variation in the signal. This resolution capability is given as the FWHM of the measured lineshape (in terms of angle or wavelength). The case treated in this paper generates an electric signal, the current delivered by the perovskite cell, that senses the variation in the index of refraction. This current will

be affected by noise and fluctuations due to the intrinsic variations of the sensor, and related with the stability and noise level of the light source, the detector, and the signal acquisition electronics. Most of these variations can be accounted for and controlled. In the end, all these uncertainties are summarized in a variation of the responsivity, $\Delta\mathcal{R}$. which plays the same role as the FWHM used to define FOM for spectral or angular interrogation. A modification of the FOM adapted to this measurement procedure would be defined as:

$$\mathrm{FOM}^* = \frac{S_B}{\Delta\mathcal{R}}, \tag{5.11}$$

where the * superscript is given here to distinguish this definition from the one given in equation (5.10). In the practical case that we treat here, when comparing the denominator in equation (5.10) with $\Delta\mathcal{R}$, we can conclude that the definition is given in equation (5.10) clearly underestimates the FOM for our system.

From the definition of responsivity (see equation (5.8)), we can derive its uncertainty, $\sigma_{\mathcal{R}}$, that can be used in equation (5.11), considering $\Delta\mathcal{R} = \sigma_{\mathcal{R}}$, as:

$$\Delta\mathcal{R} = \sigma_{\mathcal{R}} = \sqrt{\left(\frac{\partial\mathcal{R}}{\partial I_{SC}}\right)^2 \sigma_{I_{SC}}^2 + \left(\frac{\partial\mathcal{R}}{\partial P_{\mathrm{input}}}\right)^2 \sigma_{P_{\mathrm{input}}}^2} = \sqrt{\frac{I_n^2}{P_{\mathrm{input}}^2} + \mathcal{R}^2\left(\frac{\Delta P_{\mathrm{input}}}{P_{\mathrm{input}}}\right)^2}, \tag{5.12}$$

where $\Delta P_{\mathrm{input}}/P_{\mathrm{input}}$ describes the stability in the power of the illuminating light source. Assuming an accurate measurement of the current, we have taken its uncertainty as the noise in the intensity of the photodetector $\sigma_{I_{SC}} = I_n$. The uncertainty of the illuminating power has been written in terms of the relative power stability of the source, $\sigma_{P_{\mathrm{input}}} = \Delta P_{\mathrm{input}}$. The device described in this contribution is quite close to a photodetector. Therefore, as it has been already proposed for perovskite based detectors [389], we should consider photodetection quality parameters to assess the performance of the device. Among these parameters, the noise equivalent power, NEP, is defined as $\mathrm{NEP} = I_n/\mathcal{R}$, and evaluated for perovskite detectors as $\mathrm{NEP} = 4.6 \times 10^{-12}$ W at a wavelength $\lambda = 700$ nm [389].

When taking the worst-case scenario with the largest value in responsivity evaluated in this paper ($\mathcal{R} = 539$ mA/W at $\lambda = 715$ nm), we obtain an estimation of the maximum noise in intensity: $I_n = \mathrm{NEP} \times \mathcal{R} = 2.5 \times 10^{-3}$ pA. Taking into account this very small value of I_n, we find that the largest contribution to the variation in responsivity is coming from the second term in equation (5.12). This means that, after neglecting the first term within the square root in equation (5.12), we obtain :

$$\Delta\mathcal{R} = \sigma_{\mathcal{R}} \simeq \mathcal{R}\frac{\Delta P_{\mathrm{input}}}{P_{\mathrm{input}}}, \tag{5.13}$$

meaning that the relative variation in responsivity is equal to the relative variation in input power: $\Delta\mathcal{R}/\mathcal{R} = \Delta P_{\mathrm{input}}/P_{\mathrm{input}}$. Using this approximation and combining equations (5.10) and (5.11), it is possible to obtain a relation between FOM and FOM* as:

$$\mathrm{FOM}^* = \left(\frac{\Delta P_{\mathrm{input}}}{P_{\mathrm{input}}}\right)^{-1} \times \mathrm{FOM}, \tag{5.14}$$

showing that both performance parameters are proportional, and the proportionality constant depends on the stability in the power of the light source, *i. e.*, a more stable light source means a larger multiplicative term in equation (5.14). A value of $\Delta P_{\mathrm{input}}/P_{\mathrm{input}} = 10^{-3}$ is attainable

with the current laser diode technology. This means that FOM* = 1000 × FOM. This previous discussion makes possible a conservative evaluation of $\Delta\mathcal{R}$ that we have included in the last column of table 5.4, where we have found that FOM* reaches a significant maximum value of FOM* = 17700 RIU^{-1}, which is competitive with existing technologies. Within the range na = [1.000,1.001], this value is FOM* = 12200. This value would mean a capability of measuring the change in the index of refraction as low as 8×10^{-5} RIU, which may account for variations in the index of refraction of air [323, 373, 374, 377, 379, 385].

Table 5.4: Performance parameters for the four designs.

Design type	$\Delta\lambda_{\text{res}}$ [nm]	ΔA_{perov} [%]	S_B [mA(W.RIU)$^{-1}$]	FOM [RIU^{-1}]	FOM* [RIU^{-1}]
Planar cell	NA	1.4	70	0.15	NA
# I	33.2	60.0	3490	17.7	17700
# I (zoom)	-	-	2320	12.2	12200
# II-narrow	17.5	31.8	2330	5.5	5450
# II-narrow (zoom)	-	-	2290	5.4	5380
# II-wide	16.5	5.4	444	0.82	824
# III	0	15.0	1060	2.24	2240

6

Conclusions

In this thesis, we have explored different ways to improve the performance of photonic devices using nanostructures to control light. Specifically, we have developed designs that use interference and diffractive effects, and plasmonic resonances, showing the role of each mechanism in promoting the absorption capability at the desired location in the devices. Also, we have analyzed new strategies for the device setup and working methodology that ease its integrability in different systems, and reduce its final cost. We have selected the characteristic parameters for each device to evaluate the enhancement provided by our designs, for example, J_{SC} for solar cells, and the sensitivity, S_B, and figure of merit, FOM, for optical sensors. The original contributions of this work are compared with similar recent reports under each corresponding section, and revised below as a summary.

Now, we itemize the main conclusions of our work

- *Optical model validation.*
  - The use of Finite Element Methods, through a well accepted computational tool, as Comsol Multiphysics, has been fully validated and applied in this dissertation. We have integrated this method successfully in a design process that we have applied extensively in this work.
- *Nanostructures for solar cell devices.*

  In this topic, we have proposed several nanophotonic structures to improve the performance of solar cells, ranging from low-cost amorphous silicon hydrogenated cells, to high performance cells based on novel materials, as in tandem perovskite/c-Si cells. All the analysis has been made taking into account the feasibility of the design and the fabrication constraints both for geometry, and material selection.
  - We have analyzed quantitatively the importance of every layer in an amorphous silicon hydrogenated solar cell, focusing on their role in the optical behavior of the cell.
  - We have designed a double layer antireflection coating having a planar geometry, optimized its performance, and evaluated its limitations
  - We have proposed a one dimensional, and extruded, nanostructured dielectric grating on top of the layer to increase the transmittance towards the active layer of the

cell and reduce the reflectivity. Several geometries have been analyzed and we have found that the triangular profile behaves the best, reaching an increase in the short circuit current of 9%.

- We have arranged a high-aspect-ratio nanostructured grating as a scaffold to grow an ultra-thin amorphous silicon hydrogenated solar cell on it. We have identified that optical funneling and guiding increase the optical path within the structure, and the exposed area. Our analysis has taken into account the fabrication issues related to a conformal deposition of the layers of the cell. After optimizing the parameters of this nanophotonic structure we found an improvement of the short circuit current by 50%.
- We have analyzed the power budget of these previous designs to understand better the role of the parasitic losses in the thermal mitigation of the Staebler-Wronsky effect that degrades the performance of amorphous silicon cells.
- We have optically evaluated the performance of a planar tandem perovskite/c-Si solar cell. We calculated the thickness of the active layer for the top perovskite solar cell to achieve the current matching condition required for the good operation of the whole device. We have included a metasurface in the form of multilayer gratings in the perovskite top cell that decreases the reflectance of the tandem device. We have included a nanotexture in the back contact of the tandem cell to improve its characteristics. These additions along with the metasurface increase the short circuit current of the cell by 20%.

- *Plasmonic sensors.*

  We have proposed several designs that use plasmonic resonances as optical probes to sense the variation of the index of refraction of the analyte. We have defined a merit function that combines those magnitudes of interest for the given application. This merit function has been optimized by changing both the geometry and the material selection of the structure under analysis.

  When necessary, we have considered the biocompatibility issues of the sensor and the analyte. To avoid the contact of silver with water-based analytes, we have proposed bimetallic layers that exploit the biocompatibility of gold and the excellent plasmonic response of silver. Also, some dielectric passivization layers have been proposed, finding that the overall performance of the device is not affected significantly.

  We studied several designs incorporating metal, or dielectric nanostructures to improve the performance of plasmonic sensors. This performance is parameterized by the dynamic range in the sensed refractive index, the sensitivity of the device, and the figure of merit of the sensor.

  - We have designed a plasmonic sensor that uses a periodic grating made of nanoslits on a silver or gold layers, and embedded in a low index buffer layer made of magnesium florid (MgF_2) . The buffer layer can be spin coated to form a planar surface for the deposition of a second thin film metal layer made of silver. This thin film silver layer can be passivated with a 10 nm gold or MgF_2 for biocompatibility issue. This structure works under normal incidence conditions and can be attached to the end of an optical fiber. This design is devoted to sense aqueous solutions having a refractive index in the range n $\in$ (1.3-1.35). The sensitivity, and figure of merit for this design reaches values of the 955 nm/RIU, and 734 RIU^{-1}, respectively.

- We have proposed a stack of metallic gratings etched with deep grooves of dielectric materials. The multilayer grating stuck can be terminated with a thin metal layer at where surface plasmon resonance can be generated and we call it Funnel-SPR. Also, it can be terminated with a thin dielectric layer to permit selective spectral transmission, which we call Funnel-T. Both designs funnel light towards the analyte in a spectral selective manner, showing high field enhancement values. The system can work with liquid analytes and water-based substances. The value of the sensitivity and figure of merit for the Funnel-SPR ($\lambda_{F-SPR,1}$) is as high as 1130 nm/RIU, and 2100 RIU^{-1}, at $n_a = 1.35$, respectively. We have found that the dynamic range is limited to the range $n_a \in (1.30, 1.35)$.
- We have analyzed an extruded design with a triangular profile that increases the available optical field at the sensing surface by the generation of surface plasmon resonances. We have selected materials showing a high-contrast in their index of refraction to extend the surface plasmon resonance deeper in the analyte and to increase the dynamic range of the device, reaching a total dynamic range of 1.43 RIU, a sensitivity of 450 nm/RIU, and a figure of merit of 220 RIU^{-1}.
- We have modified the extruded design with a triangular profile from Si_3N_4 embedded in the analyte, and on top of a thick metal layer. This design has a higher refractive index contrast with the surrounding medium than the ZnO triangular profile embedded in MgF_2. This higher refractive index contrast further extends the dynamic range of the device, reaching a total dynamic range of 1.56 RIU. The value of sensitivity reaches 940 nm/RIU, besides, the figure of merit sharply increases when moving to a higher index of refraction.
- We have analyzed a nanostructure that presents Fano resonances that combine the narrow spectral surface plasmon resonances with the wide diffractive response of almost sub-wavelength gratings. The physical analytical model has been fitted with the responses calculated from computational electromagnetism, to select those designs with better performance. This design behaves with a 1000 nm/RIU, and 775 RIU^{-1} for the sensitivity and figure of merit, respectively, and has an ultra wide dynamic range of $n_a \in (1.33, 2.00)$.

- *Hybrid sensing devices.*

  As a natural output of the analysis of the solar cells and plasmonic sensors, we have proposed three designs of optical sensors based on hybrid mechanisms. In this analysis, we have included a multiphysics analysis of the involved physical mechanisms.

  - We have used the bolometric effect to extract the signal from a refractometric sensor based on the excitation of surface plasmon resonances. We have optimized the nanophotonic structure to increase the temperature selectively with respect to the index of refraction of the analyte. Actually, the metal structure used to generate the plasmonic resonances is part of the read-out electronic circuit. We have to adapt the definition of the sensitivity and figure of merit to the proposed optoelectronic interrogation. The values of these parameters are: the sensitivity reaches a value of 12.4 Ω/RIU at $n_a = 1.3335$, and the maximum figure of merit is 382 RIU^{-1} at $n_a = 1.3360$.
  - We have modified the design of a perovskite ITO-free solar cells by adding a metallic/dielectric grating nanostructured electrode. We have optimized this electrode for

sensing applications. This approach has been evaluated as a refractometric sensor for gases.

– We have modified a perovskite solar cell by replacing the top transparent electrode with a nanostructured top metallic electrode. The nanostructured metallic electrode is responsible for the spectral selectivity of the system. The modified perovskite solar cell is operated using a monochromatic light source. We have optimized the system for gas detection. The signal extraction of the device is fully electronic. Therefore, we have defined a modified figure of merit that explicitly takes into account this electric operational mode. The value of the modified figure of merit for the proposed sensor is 17700 RIU^{-1}. Within the range $n_a \in (1.000, 1.001)$, the modified figure of merit is 12200 RIU^{-1}. This value would mean a capability of measuring change in the index of refraction as low as 8×10^{-5} RIU, that may account for variations in the index of refraction of air.

Outlook and future work

Flexible optoelectronic devices appear in many applications like smart-phones, laptops, displays, and other machines. In most of the efficient optoelectronic devices, transparent oxides (for example, indium tin oxide) plays a principal role in the device operation to provide an illumination window and electrical contact for the device. ITO's are fabricated from expensive materials, and are rigid, so we need to replace them with other efficient electrodes to achieve flexible optoelectronic devices. As a future step, we will study a design of nanostructured metallic electrodes that incorporates nanophotonic structures to work as an efficient electrode for flexible optoelectronics devices.

6.1 Conclusiones

In this section we have included the translation of the conclusions into Spanish.

En esta tesis hemos explorado diversas manera de mejorar el comportamiento de dispositivos fotónicos utilizando nano-estructuras. En particular, hemos desarrollado diseños que utilizan efectos interferenciales, difractivos, y resonancias plasmónicas, indicando el papel de cada mecanismos en el aumento de la absorbancia en las regiones de interés del dispositivo. También hemos analizado nuevas estrategias para la construcción del dispositivo y nuevas metodologías de operación que facilitan la integración en diversos dispositivos, reduciendo su coste final. Hemos seleccionado los parámetros característicos de cada dispositivo para evaluar los avances ligados a nuestros diseños. Por ejemplo, la densidad de corriente en circuito abierto, J_{sc}, para células solares, y la sensibilidad, S_B, y la figura de mérito, FOM, para sensores ópticos. Las contribuciones originales de esta tesis han sido comparadas con publicaciones recientes en cada una de las secciones, y están descritas a continuación:

- *Validación del modelo óptico*

  – El uso de un Método de Elementos Finitos, mediante Comsol Multiphysics, que es una herramienta computacional bien aceptada, ha sido completamente validado. Hemos integrado este método con éxito en un proceso de diseño que hemos aplicado extensivamente en este trabajo.

- *Nanoestructuras para células solares*

  En este apartado hemos propuestos varias estructuras nanofotónicas para la mejora del rendimiento de células solares, desde los dispositivos de bajo coste de células de silicio amorfo hidrogenado, hasta céluas de alto rendimiento con nuevos materiales, tales como células de perovskitas y de silicio cristalino. Todo el análisis ha sido hecho considerando la realización práctica del diseño y las limitaciones de fabricación, tanto para la geometría como la selección del material.

  En particular:

  - Hemos analizado cuantitativamente la importancia de cada capa en una célula solar de silicio amorfo hidrogenado, fijándonos en su papel en el comportamiento óptico de la célula.
  - Hemos diseñado un recubrimiento antirreflejante de doble capa con geometría plana, con su rendimiento optimizado, habiendo evaluado sus limitaciones.
  - Hemos propuesto una red periódica nanoestructurada, extruida, y dieléctrica que se coloca sobre la célula para incrementar la transmitancia hacia la capa activa de la célula, disminuyendo la reflectividad. Hemos analizado varias geometrías y hemos encontrado que el perfil triangular es el que más incrementa la densidad de corriente de circuito cerrado, hasta un 9%.
  - Hemos propuesto el uso de una red nanoestructurada de alta razón de aspecto que actúa como una plantilla para construir una célula de solar ultrafina de silicio amorfo hidrogenado. Hemos identificado que el confinamiento y guiado óptico incrementan el camino óptico dentro de la estructura y también el área expuesta. Nuestro análisis ha tenido en cuenta los problemas de fabricación ligados a la deposición conformal de todas las capas de la célula. Después de optimizar los parámetros de esta estructura nanofotónica hemos encontrado un aumento del 50% en la corriente de circuito cerrado.
  - Hemos analizado el balance energético de estos diseños para entender mejor el papel que juegan las pérdidas parásitas en la recuperación térmica de células de silicio amorfo degradadas mediante el efecto Staebler-Wronsky.
  - Hemos evaluado ópticamente el rendimiento de una célula solar plana tándem perovskita / silicio cristalino. Hemos calculado el espesor de la capa activa de la célula de perovskita que permite conseguir el ajuste entre las corrientes que es necesario para el buen funcionamiento del dispositivo. Hemos incluido una metasuperficie con forma de una red multicapa en la célula de perovskita, que disminuye la reflectancia del tándem. Hemos texturizado el contacto inferior de la célula tándem para mejorar sus características. Todo ello permite aumentar un 20% la corriente de circuito cerrado.

- *Sensores plasmónicos.*

  Hemos propuesto varios diseños que utilizan resonancias plasmónicas como elementos que sensibles a las variaciones del índice de refracción del analito. Hemos definido una función de mérito que combina las magnitudes de interés en cada una de las aplicaciones estudiadas. Esta función de merito has sido optimizada cambiando la geometría y los materiales elegidos para cada estructura.

  Cuando ha sido necesario, hemos considerado los problemas de biocompatibilidad entre el sensor y el analito. Para evitar el contacto de la plata con analitos con base acuosa,

hemos propuesto capas bimetálicas que explotan la biocompatibilidad del oro con la excelente respuesta plasmónica de la plata. También hemos propuesto el uso de capas dieléctricas de pasivación, encontrando que el comportamiento global del dispositivo no se ver afectado significativamente.

Hemos estudiado varios diseños que incorporan nanoestructuras metálicas o dieléctricas para mejorar el comportamiento de los sensores plasmónicos. Este rendimiento ha sido parametrizado mediante el rango dinámico en el índice de refracción medida, la sensibilidad del dispositivo, y la figura de mérito del sensor.

En particular:

- Hemos diseñado un sensor plasmónico que utiliza una red periódica heca de nanoaperturas hechas sobre una capa metálica incluida dentro de un capa dieléctrica de bajo índice. Esta estructura trabaja en incidencia normal y puede ser acoplada al final de una fibra óptica. Este elemento está preparado para medir soluciones acuosas con índices de refración en el rango $n_a \in (1.33, 1.35)$. La sensibilidad, y la figura de mérito para una configuración Ag/Ag-MGF_2 alcanza los valores de 955 nm/RIU y 734 RIR^{-1} respectivamente.
- Hemos propuesto un apilamiento de redes metálicas con aperturas profundas y rellenadas con material dieléctrico. Esta estructura confina la luz y la dirige hacia el analito de forma selectiva espectralmente, mostrando altos valores de aumento del campo eléctrico. El sistema puede trabajar con analitos líquidos y sustancias con base acuosa. El valor de la sensibilidad y de la figura de mérito para un diseño basado en confinamiento y resonancias de plasmones superficiales toman los valores 1130 nm/RIU y 2100 RIU^{-1} para $n_a = 1.35$, respectivamente. Hemos evaluado que el rango dinámico está limitado por los valores $n_a \in (1.30, 1.35)$.
- Hemos analizado un diseño extruido con perfil triangular que incrementa el campo óptico disponible en la zona de sensado debido a la generación de resonancias de plasmones superficiales. Hemos elegido materiales que presentan un alto contraste en su índice de refracción para ampliar la región de la resonancia plasmónica en el analito, e incrementar el rango dinámico total hasta 1.43 RIU, con una sensibilidad de 450 nm/RIU, y una figura de mérito de 220 RIU^{-1}
- Hemos modificado el diseño extruido mediante un perfil triangular de Si_3N_4 in contacto con el analito y colocado sobre una capa metálica gruesa. Este diseño presenta un alto contraste del índice de refracción con respecto al medio que le rodea, mayor que el que se produce mediante un perfil triangular de ZnO embebido en MgF_2. Este mayor índice de refracción extiende el rango dinámico hasta 1.56 RIU. El valor de la sensitividad alcanza 940 nm/RIU y el valor de la figura de mérito se incrementa fuertemente cuando nos vamos hacia valores más altos del índice de refracción.
- Hemos analizado una nanoestructura que presenta resonancias de Fano que combinan la estrecha respuesta espectral de las resonancias plasmóncias con la mayor anchura espectral de la respuesta difractiva de redes con periodos del orden de la longitud de onda. El modelo físico ajusta las respuestas espectrales obtenidas mediante electromagnetismo computacional, y permite seleccionar los dispositivos con mejor rendimiento. Este diseño consigue valores de 1000 nm/RIU y 775 RIU^{-1}, para la sensibiliddad y figura de mérito respectivamente. Además, corresponde a un rango dinámico ultra ancho, $n_a \in (1.33, 2.00)$.

- *Sensores híbridos.*

  Como una evolución natural del análisis de células solares y de sensores plasmónicos, hemos propuesto tres diseños de sensores ópticos basados en mecanismos híbridos. En este análisis hemos incluido una cálculo multifísico considerando los mecanismos físicos incluidos.

  En particular:

  - Hemos utilizado el efecto bolométrico para extrare la señal de un sensor refractométrico basado en la excitación de resonancias de plasmones superficiales. Hemos optimizado la estructura nanofotónica para incrementar la temperatura selectivamente con respecto al índice de refracción del analito. Realmente, la estructura metálica utilizada para generar la resonancia plasmónica es parte del circuito electrónico de lectura. Hemos adaptado la definición de la sensibilidad y de la figura de mérito a la interrogación optoelectrónica propuesta. La sensibilidad alcanza el valor de 12.4 Ω/RIU para $n_a = 1.3335$ y el valor máximo de la figura de mérito es 382 RIU^{-1} para $n_a = 1.3360$.
  - Hemos modificado el diseño de una célula solar de perovskita sin ITO, añadiendole un electrodo nano-estructurado con una red metalica y dieléctrica. Hemos optimizado este electrodo para aplicaciones de sensado. Este diseño se ha evaluado para un sensor refractométrico de gases.
  - Hemos modificado una célula solar de perovskita reemplazando el electrodo transparente superior por un electrodo metálico nano-estructurado. Este electrodo es el responsable de la respuesta espectral selectiva del sistema. Esta célula solar modificada es iluminada por una fuente monocromática. Hemos optmizado el sistema para la detección de gases. La adquisición de la señal es completamente electrónica. Por ello, hemos definido una figura de mérito modificada que explícitamente tiene en cuenta este modo de funcionamiento. El valor de esta función de mérito modificada es 17700 RIU^{-1}. Para el rango $n_a \in (1.000, 1.001)$ se alcanza un valor de esta figura de mérito modificada de 12200 RIU^{-1}. Este valor implica una capacidad de medida de cambios del índice de refracción tan bajos como 8×10^{-5} RIU, lo que permite medidas de variación del índice de refracción del aire.

Glossary

β	The complex electromagnetic wave propagation constant.
$\beta\prime$	Real part of the electromagnetic wave propagation constant.
$A(\lambda)$	Spectral absorbance.
I_n	Noise in intensity of the photodetector.
J_{SC}	Short-circuit current density.
K_0	The wave vector of electromagnetic wave in vacuum.
K_t	Thermal conductivity.
NEP	Noise equivalent power.
Q	Quality factor parameter.
Q_h	The heat power density.
R	Reflectance .
R_i	Electrical resistance, i is 0 or 1 for initial and final resistances, respectively .
T	Transmittance .
Ω	Unit of electrical resistance.
$\Phi_{\mathrm{AM1.5}}(\lambda)$	The solar spectral irradiance.
α	temperature coefficient of resistance.
$\beta\prime\prime$	Imaginary part of the electromagnetic wave propagation constant.
δ_y	Plasmon propagation depth in the dielectric medium.
ϵ	The Complex electric permittivity of materials.
$\epsilon\prime$	Real part of the electric permittivity of materials.
$\epsilon\prime\prime$	Imaginary part of the electric permittivity of materials.
ϵ_0	Electric permittivity in vacuum.
γ	Fano resonance width coefficient.
λ	Wavelength of electromagnetic wave.
μ_0	Magnetic permeability in vacuum.

∇	mathematical vector differential operator.
ω	Angular frequency variable.
ω_0	Natural angular frequency.
ρ	Electrical resistivity.
σ	Electrical conductivity.
$\sigma_{I_{\mathrm{SC}}}$	Uncertainty in short circuit current measurement.
$\sigma_{P_{\mathrm{input}}}$	Uncertainty in input optical power measurement.
$\sigma_{\mathcal{R}}$	Uncertainty in responsivity measurement.
$\mathbf{B}(\cdot)$ or $B(\cdot)$	Magnetic field.
$\mathbf{E}(\cdot)$ or $E(\cdot)$	Electric field.
f	Fano resonance complex coefficient.
θ	Angle of incidence, reflection, or refraction.
$\tilde{n}$	Complex refractive index.
$\triangle$	Delta, a mathematical notation means the variation.
ε_{eff}	The dielectric permittivity of an effective medium.
c	Speed of light in vacuum.
h	Planck's constant.
k	Imaginary of refractive index.
n	Real part of refractive index.
$p(\lambda)$	Optical power spectral density.
q	Electron charge.
r	Arbitrary spatial vector.
r_i	Reflection coefficient for i can be s-polarization or p-polarization .
t	time.
t_i	Transmission coefficient for i can be s-polarization or p-polarization .
$\mathcal{R}_S$	Ratio of output current to input optical power of a diode.

Acronyms

Ag	Silver.
Al	Aluminum.
ARC	Anti-reflection coatings.
aSiH	Amorphous Silicon hydrogenated.
ATR	attenuated total reflection.
Au	Gold.
AZO	Zinc oxide doped aluminum.
c-Si	Crystalline-silicon.
Deg	Degree , angle unit.
DS	Dielectric spacer.
EF	Enhancement factor.
EM	Electromagnetic.
ETL	Electron transport layers.
FDTD	Finite-difference time-domain.
FE	Field enhancement.
FEM	Finite element method.
FOM	Figure of merit.
FOM*	Modified figure of merit.
FWHM	Full width at half maximum.
HTL	Hole transport layers.
iaSiH	Intrinsic amorphous Silicon hydrogenated.
ITO	Indium tin oxide.
IZO	Zinc oxide doped indium.
LRSPR	Long-range surface plasmon resonance.
LSPR	localized surface plasmon resonance.

$MAPbI_3$	Methylammonium lead halides.
MF	Merit function.
naSiH	n-type amorphous Silicon hydrogenated.
NIR	Near infrared.
NREL	National Renewable Energy Laboratory.
paSiH	p-type amorphous Silicon hydrogenated.
RIU	Refractive index unit.
S_B	Bulk sensitivity.
Si_3N_4	Silicon nitride.
SiO_2	Silicon dioxide.
SPP	Surface plasmon polariton.
SPR	surface plasmon resonance.
SPW	surface plasmon wave.
SWE	Staebler–Wronski effect.
TC	Transparent contacts.
TCO	Transparent conducting oxide.
TCR	Temperature coefficient of resistance.
TE	Transverse electric.
TiO_2	Titanium dioxide.
TM	Transverse magnetic.
VIS	Visible.
ZnO	Zinc oxide.

List of Figures

List of Tables

Bibliography

[1] X. Cheng, "Nanostructures: fabrication and applications," in *Nanolithography* (M. Feldman, ed.), ch. 10, pp. 348 – 375, Woodhead Publishing, 2014.

[2] A. N. Boto, P. Kok, D. S. Abrams, S. L. Braunstein, C. P. Williams, and J. P. Dowling, "Quantum interferometric optical lithography exploiting entanglement to beat the diffraction limit," *Physical Review Letters*, vol. 85, pp. 2733–2736, 2000.

[3] S. Lal, S. Link, and N. J. Halas, "Nano optics from sensing to waveguiding," *Nature Photonics*, vol. 1, p. 641, 2007.

[4] C. E. J. Png and Y. Akimov, *Nanophotonics and Plasmonics An Integrated View*. No. 104, CRC Press, 2017.

[5] A. F. Koenderink, A. Alu, and A. Polman, "Nanophotonics shrinking light based technology," *Science*, vol. 348, no. 6234, pp. 516–521, 2015.

[6] T. V. Shahbazyan and M. I. Stockman, *Plasmonics: theory and applications*. Springer, 2013.

[7] T. Gric, "Introductory chapter: Plasmonics," in *Plasmonics*, IntechOpen, 2018.

[8] A. R. Parker and H. E. Townley, "Biomimetics of photonic nanostructures," *Nature Nanotechnology*, vol. 2, p. 347, 2007.

[9] V. R. Almeida, Q. Xu, C. A. Barrios, and M. Lipson, "Guiding and confining light in void nanostructure," *Optics Letters*, vol. 29, no. 11, pp. 1209–1211, 2004.

[10] H. Lund, "Renewable energy strategies for sustainable development," *Energy*, vol. 32, no. 6, pp. 912–919, 2007.

[11] M. A. Green, "Silicon photovoltaic modules a brief history of the first 50 years," *Progress in Photovoltaics Research and applications*, vol. 13, no. 5, pp. 447–455, 2005.

[12] M. A. Woodhouse, B. Smith, A. Ramdas, and R. M. Margolis, "Crystalline silicon photovoltaic module manufacturing costs and sustainable pricing: 1H 2018 benchmark and cost reduction road map," tech. rep., National Renewable Energy Lab.(NREL), Golden, CO (United States), 2019.

[13] M. A. Woodhouse, D. J. Feldman, R. Fu, B. Smith, K. A. Horowitz, A. Ramdas, and R. M. Margolis, "The international supply chain and manufacturing costs for photovoltaic modules, and project economics of systems including storage," tech. rep., National Renewable Energy Lab.(NREL), Golden, CO (United States), 2019.

[14] J.-H. Lambert, *Photometria, sive de Mensura et gradibus luminis, colorum et umbrae.* Sumptibus viduae E. Klett, 1760.

[15] A. Goetzberger, "Optical confinement in thin Si solar cells by diffuse back reflectors," in *15th Photovoltaic Specialists Conference*, pp. 867–870, 1981.

[16] E. Yablonovitch and G. D. Cody, "Intensity enhancement in textured optical sheets for solar cells," *IEEE Transactions on Electron Devices*, vol. 29, no. 2, pp. 300–305, 1982.

[17] S. Mokkapati and K. Catchpole, "Nanophotonic light trapping in solar cells," *Journal of Applied Physics*, vol. 112, no. 10, p. 101101, 2012.

[18] Y. Hishikawa, T. Kinoshita, M. Shima, M. Tanaka, S. Kiyama, S. Tsuda, and S. Nakano, "Optical confinement and optical loss in high efficiency a Si solar cells," in *Conference Record of the Twenty Sixth IEEE Photovoltaic Specialists Conference 1997*, pp. 615–618, 1997.

[19] S. Faÿ, S. Dubail, U. Kroll, J. Meier, Y. Ziegler, and A. Shah, "Light trapping enhancement for thin film silicon solar cells by roughness improvement of the ZnO front TCO," in *16th EC Photovoltaic Solar Energy Conference*, pp. 361–364, 2000.

[20] J. Krvc, M. Zeman, F. Smole, and M. Topivc, "Optical modeling of aSiH solar cells deposited on textured glass SnO_2 substrates," *Journal of Applied Physics*, vol. 92, no. 2, pp. 749–755, 2002.

[21] L. Tsakalakos, J. Balch, J. Fronheiser, B. A. Korevaar, O. Sulima, and J. Rand, "Silicon nanowire solar cells," *Applied Physics Letters*, vol. 91, no. 23, p. 233117, 2007.

[22] S. Pillai, K. R. Catchpole, T. Trupke, and M. A. Green, "Surface plasmon enhanced silicon solar cells," *Journal of Applied Physics*, vol. 101, no. 9, p. 093105, 2007.

[23] C. H. Sun, P. Jiang, and B. Jiang, "Broadband moth eye antireflection coatings on silicon," *Applied Physics Letters*, vol. 92, no. 6, p. 061112, 2008.

[24] K. Nakayama, K. Tanabe, and H. A. Atwater, "Plasmonic nanoparticle enhanced light absorption in GaAs solar cells," *Applied Physics Letters*, vol. 93, no. 12, p. 121904, 2008.

[25] V. E. Ferry, M. A. Verschuuren, H. B. Li, R. E. Schropp, H. A. Atwater, and A. Polman, "Improved red response in thin film aSiH solar cells with soft imprinted plasmonic back reflectors," *Applied Physics Letters*, vol. 95, no. 18, p. 183503, 2009.

[26] J. Zhu, C. M. Hsu, Z. Yu, S. Fan, and Y. Cui, "Nanodome solar cells with efficient light management and self cleaning," *Nano Letters*, vol. 10, no. 6, pp. 1979–1984, 2009.

[27] S. Mokkapati, F. Beck, A. Polman, and K. Catchpole, "Designing periodic arrays of metal nanoparticles for light trapping applications in solar cells," *Applied Physics Letters*, vol. 95, no. 5, p. 053115, 2009.

[28] Z. Yu, A. Raman, and S. Fan, "Fundamental limit of nanophotonic light trapping in solar cells," *Proceedings of the National Academy of Sciences*, vol. 107, no. 41, pp. 17491–17496, 2010.

[29] Y. Lu and A. Lal, "High efficiency ordered silicon nano conical frustum array solar cells by self powered parallel electron lithography," *Nano Letters*, vol. 10, no. 11, pp. 4651–4656, 2010.

[30] E. Garnett and P. Yang, "Light trapping in silicon nanowire solar cells," *Nano Letters*, vol. 10, no. 3, pp. 1082–1087, 2010.

[31] C. Battaglia, J. Escarre, K. Soderstrom, M. Charriere, M. Despeisse, F. J. Haug, and C. Ballif, "Nanomoulding of transparent zinc oxide electrodes for efficient light trapping in solar cells," *Nature Photonics*, vol. 5, no. 9, p. 535, 2011.

[32] J. Grandidier, D. M. Callahan, J. N. Munday, and H. A. Atwater, "Light absorption enhancement in thin film solar cells using whispering gallery modes in dielectric nanospheres," *Advanced Materials*, vol. 23, no. 10, pp. 1272–1276, 2011.

[33] C. Battaglia, C. M. Hsu, K. Soderstrom, J. Escarre, F. J. Haug, M. Charriere, M. Boccard, M. Despeisse, D. T. Alexander, M. Cantoni, *et al.*, "Light trapping in solar cells can periodic beat random," *ACS Nano*, vol. 6, no. 3, pp. 2790–2797, 2012.

[34] H. Tan, R. Santbergen, A. H. Smets, and M. Zeman, "Plasmonic light trapping in thin film silicon solar cells with improved self assembled silver nanoparticles," *Nano Letters*, vol. 12, no. 8, pp. 4070–4076, 2012.

[35] K. X. Wang, Z. Yu, V. Liu, Y. Cui, and S. Fan, "Absorption enhancement in ultrathin crystalline silicon solar cells with antireflection and light trapping nanocone gratings," *Nano Letters*, vol. 12, no. 3, pp. 1616–1619, 2012.

[36] U. W. Paetzold, M. Smeets, M. Meier, K. Bittkau, T. Merdzhanova, V. Smirnov, D. Michaelis, C. Waechter, R. Carius, and U. Rau, "Disorder improves nanophotonic light trapping in thin film solar cells," *Applied Physics Letters*, vol. 104, no. 13, p. 131102, 2014.

[37] S. Sandhu, Z. Yu, and S. Fan, "Detailed balance analysis of nanophotonic solar cells," *Optics Express*, vol. 21, no. 1, pp. 1209–1217, 2013.

[38] A. Deinega, S. Eyderman, and S. John, "Coupled optical and electrical modeling of solar cell based on conical pore silicon photonic crystals," *Journal of Applied Physics*, vol. 113, no. 22, p. 224501, 2013.

[39] R. Guo, H. Huang, P. Chang, L. Lu, X. Chen, X. Yang, Z. Fan, B. Zhu, and D. Li, "Coupled optical and electrical modeling of thin film amorphous silicon solar cells based on nanodent plasmonic substrates," *Nano Energy*, vol. 8, pp. 141–149, 2014.

[40] A. Lenert, D. M. Bierman, Y. Nam, W. R. Chan, I. Celanovic, M. Soljacic, and E. N. Wang, "A nanophotonic solar thermophotovoltaic device," *Nature Nanotechnology*, vol. 9, p. 126, 2014.

[41] U. W. Paetzold, W. Qiu, F. Finger, J. Poortmans, and D. Cheyns, "Nanophotonic front electrodes for perovskite solar cells," *Applied Physics Letters*, vol. 106, no. 17, p. 173101, 2015.

[42] W. Shockley and H. J. Queisser, "Detailed balance limit of efficiency of p-n junction solar cells," *Journal of Applied Physics*, vol. 32, no. 3, pp. 510–519, 1961.

[43] S. A. Mann and E. C. Garnett, "Resonant nanophotonic spectrum splitting for ultrathin multijunction solar cells," *ACS Photonics*, vol. 2, no. 7, pp. 816–821, 2015.

[44] S. A. Mann, S. Z. Oener, A. Cavalli, J. E. M. Haverkort, E. P. A. M. Bakkers, and E. C. Garnett, "Quantifying losses and thermodynamic limits in nanophotonic solar cells," *Nature Nanotechnology*, vol. 11, p. 1071, 2016.

[45] W. I. Nam, Y. J. Yoo, and Y. M. Song, "Geometrical shape design of nanophotonic surfaces for thin film solar cells," *Optics Express*, vol. 24, no. 14, pp. A1033–A1044, 2016.

[46] P. Wang, R. Li, B. Chen, F. Hou, J. Zhang, Y. Zhao, and X. Zhang, "Gradient energy alignment engineering for planar perovskite solar cells with efficiency over 23%," *Advanced Materials*, p. 1905766, 2020.

[47] W. S. Yang, B. W. Park, E. H. Jung, N. J. Jeon, Y. C. Kim, D. U. Lee, S. S. Shin, J. Seo, E. K. Kim, J. H. Noh, and S. I. Seok, "Iodide management in formamidinium lead-halide based perovskite layers for efficient solar cells," *Science*, vol. 356, no. 6345, pp. 1376–1379, 2017.

[48] K. A. Bush, A. F. Palmstrom, Z. J. Yu, M. Boccard, R. Cheacharoen, J. P. Mailoa, D. P. McMeekin, R. L. Z. Hoye, C. D. Bailie, T. Leijtens, I. M. Peters, M. C. Minichetti, N. Rolston, R. Prasanna, S. Sofia, D. Harwood, W. Ma, F. Moghadam, H. J. Snaith, T. Buonassisi, Z. C. Holman, S. F. Bent, and M. D. McGehee, "23.6% efficient monolithic perovskite silicon tandem solar cells with improved stability," *Nature Energy*, vol. 2, p. 17009, 2017.

[49] W. Ahmad, J. Khan, G. Niu, and J. Tang, "Inorganic $CsPbI_3$ perovskite based solar cells a choice for a tandem device," *Solar Rapid Research Letters*, vol. 1, no. 7, p. 1700048, 2017.

[50] D. Chen, P. Manley, P. Tockhorn, D. Eisenhauer, G. Koppel, M. Hammerschmidt, S. Burger, S. Albrecht, C. Becker, and K. Jager, "Nanophotonic light management for perovskite silicon tandem solar cells," *Journal of Photonics for Energy*, vol. 8, no. 2, pp. 1–13, 2018.

[51] M. J. Mendes, S. Haque, O. S. Sobrado, A. Araujo, H. Aguas, E. Fortunato, and R. Martins, "Optimal enhanced solar cell ultra thinning with broadband nanophotonic light capture," *iScience*, vol. 3, pp. 238–254, 2018.

[52] R. Schmager, G. Gomard, B. S. Richards, and U. W. Paetzold, "Nanophotonic perovskite layers for enhanced current generation and mitigation of lead in perovskite solar cells," *Solar Energy Materials and Solar Cells*, vol. 192, pp. 65–71, 2019.

[53] E. Kretschmann and H. Raether, "Notizen: Radiative decay of non radiative surface plasmons excited by light," *Zeitschrift für Naturforschung A*, vol. 23, no. 12, pp. 2135–2136, 1968.

[54] A. Otto, "Excitation of nonradiative surface plasma waves in silver by the method of frustrated total reflection," *Zeitschrift fur Physik A Hadrons and Nuclei*, vol. 216, no. 4, pp. 398–410, 1968.

[55] I. Pockrand, J. Swalen, J. Gordon, and M. Philpott, "Surface plasmon spectroscopy of organic monolayer assemblies," *Surface Science*, vol. 74, no. 1, pp. 237–244, 1978.

[56] J. Gordon and S. Ernst, "Surface plasmons as a probe of the electrochemical interface," *Surface Science*, vol. 101, no. 1, pp. 499–506, 1980.

[57] C. Nylander, B. Liedberg, and T. Lind, "Gas detection by means of surface plasmon resonance," *Sensors and Actuators*, vol. 3, pp. 79–88, 1982.

[58] B. Liedberg, C. Nylander, and I. Lunstrom, "Surface plasmon resonance for gas detection and biosensing," *Sensors and Actuators*, vol. 4, pp. 299–304, 1983.

[59] B. Liedberg, C. Nylander, and I. Lundstrom, "Biosensing with surface plasmon resonance how it all started," *Biosensors and Bioelectronics*, vol. 10, no. 8, pp. i–ix, 1995.

[60] F. F. Bier, F. Kleinjung, and F. W. Scheller, "Real time measurement of nucleic acid hybridization using evanescent wave sensors steps towards the genosensor," *3rd European Conference on Optical Chemical Sensors and Biosensors, Sensors and Actuators B Chemical*, vol. 38, no. 1, pp. 78–82, 1997.

[61] J. Homola, I. Koudela, and S. S. Yee, "Surface plasmon resonance sensors based on diffraction gratings and prism couplers sensitivity comparison," *Sensors and Actuators B Chemical*, vol. 54, no. 1-2, pp. 16–24, 1999.

[62] T. R. Jensen, M. D. Malinsky, C. L. Haynes, and R. P. Van Duyne, "Nanosphere lithography tunable localized surface plasmon resonance spectra of silver nanoparticles," *The Journal of Physical Chemistry B*, vol. 104, no. 45, pp. 10549–10556, 2000.

[63] Y. Kim, R. C. Johnson, and J. T. Hupp, "Gold nanoparticle based sensing of spectroscopically silent heavy metal ions," *Nano Letters*, vol. 1, no. 4, pp. 165–167, 2001.

[64] M. D. Malinsky, K. L. Kelly, G. C. Schatz, and R. P. Van Duyne, "Chain length dependence and sensing capabilities of the localized surface plasmon resonance of silver nanoparticles chemically modified with alkanethiol self assembled monolayers," *Journal of the American Chemical Society*, vol. 123, no. 7, pp. 1471–1482, 2001.

[65] N. Nath and A. Chilkoti, "A colorimetric gold nanoparticle sensor to interrogate biomolecular interactions in real time on a surface," *Analytical Chemistry*, vol. 74, no. 3, pp. 504–509, 2002.

[66] A. J. Haes and R. P. Van Duyne, "A nanoscale optical biosensor sensitivity and selectivity of an approach based on the localized surface plasmon resonance spectroscopy of triangular silver nanoparticles," *Journal of the American Chemical Society*, vol. 124, no. 35, pp. 10596–10604, 2002.

[67] K. L. Kelly, E. Coronado, L. L. Zhao, and G. C. Schatz, "The optical properties of metal nanoparticles the influence of size shape and dielectric environment," *The Journal of Physical Chemistry B*, vol. 107, no. 3, pp. 668–677, 2003.

[68] A. G. Brolo, R. Gordon, B. Leathem, and K. L. Kavanagh, "Surface plasmon sensor based on the enhanced light transmission through arrays of nanoholes in gold films," *Langmuir*, vol. 20, no. 12, pp. 4813–4815, 2004.

[69] C. Sonnichsen and A. P. Alivisatos, "Gold nanorods as novel nonbleaching plasmon based orientation sensors for polarized single particle microscopy," *Nano Letters*, vol. 5, no. 2, pp. 301–304, 2005.

[70] J. Homola and M. Piliarik, "Surface plasmon resonance (spr) sensors," in *Surface plasmon resonance based sensors*, pp. 45–67, Springer, 2006.

[71] A. Hassani and M. Skorobogatiy, "Design of the microstructured optical fiber based surface plasmon resonance sensors with enhanced microfluidics," *Optics Express*, vol. 14, no. 24, pp. 11616–11621, 2006.

[72] B. Sepulveda, A. Calle, L. M. Lechuga, and G. Armelles, "Highly sensitive detection of biomolecules with the magneto optic surface plasmon resonance sensor," *Optics Letters*, vol. 31, no. 8, pp. 1085–1087, 2006.

[73] E. M. Larsson, J. Alegret, M. Kall, and D. S. Sutherland, "Sensing characteristics of NIR localized surface plasmon resonances in gold nanorings for application as ultrasensitive biosensors," *Nano Letters*, vol. 7, no. 5, pp. 1256–1263, 2007.

[74] J. Homola, "Surface plasmon resonance sensors for detection of chemical and biological species," *Chemical Reviews*, vol. 108, no. 2, pp. 462–493, 2008.

[75] J. Guo, P. D. Keathley, and J. Hastings, "Dual-mode surface-plasmon-resonance sensors using angular interrogation," *Optics Letters*, vol. 33, no. 5, pp. 512–514, 2008.

[76] K. Lin, Y. Lu, J. Chen, R. Zheng, P. Wang, and H. Ming, "Surface plasmon resonance hydrogen sensor based on metallic grating with high sensitivity," *Optics Express*, vol. 16, no. 23, pp. 18599–18604, 2008.

[77] M. Piliarik and J. Homola, "Surface plasmon resonance SPR sensors approaching their limits," *Optics Express*, vol. 17, no. 19, pp. 16505–16517, 2009.

[78] D. W. Huang, Y. F. Ma, M. J. Sung, and C. P. Huang, "Approach the angular sensitivity limit in surface plasmon resonance sensors with low index prism and large resonant angle," *Optical Engineering*, vol. 49, no. 5, pp. 1–6, 2010.

[79] S. J. Zalyubovskiy, M. Bogdanova, A. Deinega, Y. Lozovik, A. D. Pris, K. H. An, W. P. Hall, and R. A. Potyrailo, "Theoretical limit of localized surface plasmon resonance sensitivity to local refractive index change and its comparison to conventional surface plasmon resonance sensor," *Journal of the Optical Society of America A*, vol. 29, no. 6, pp. 994–1002, 2012.

[80] T.-W. Lee and S. K. Gray, "Remote grating-assisted excitation of narrow-band surface plasmons," *Optics Express*, vol. 18, no. 23, pp. 23857–23864, 2010.

[81] A. Dhawan, M. Canva, and T. Vo-Dinh, "Narrow groove plasmonic nano-gratings for surface plasmon resonance sensing," *Optics Express*, vol. 19, no. 2, pp. 787–813, 2011.

[82] A. Polyakov, K. Thompson, S. Dhuey, D. Olynick, S. Cabrini, P. Schuck, and H. Padmore, "Plasmon resonance tuning in metallic nanocavities," *Scientific Reports*, vol. 2, p. 933, 2012.

[83] M. R. R. Khan and S. W. Kang, "A high sensitivity and wide dynamic range fiber optic sensor for low concentration VOC gas detection," *Sensors*, vol. 14, no. 12, pp. 23321–23336, 2014.

[84] S. Unser, I. Bruzas, J. He, and L. Sagle, "Localized surface plasmon resonance biosensing current challenges and approaches," *Sensors*, vol. 15, no. 7, pp. 15684–15716, 2015.

[85] W. Wei, J. Nong, G. Zhang, L. Tang, X. Jiang, N. Chen, S. Luo, G. Lan, and Y. Zhu, "Graphene-based long-period fiber grating surface plasmon resonance sensor for high-sensitivity gas sensing," *Sensors*, vol. 17, no. 1, p. 2, 2017.

[86] R. Li, H. An, W. Huang, and Y. He, "Molybdenum oxide nanosheets meet ascorbic acid tunable surface plasmon resonance and visual colorimetric detection at room temperature," *Sensors and Actuators B: Chemical*, vol. 259, pp. 59–63, 2018.

[87] H. Wang, H. Zhang, J. Dong, S. Hu, W. Zhu, W. Qiu, H. Lu, J. Yu, H. Guan, S. Gao, Z. Li, W. Liu, M. He, J. Zhang, Z. Chen, and Y. Luo, "Sensitivity enhanced surface plasmon resonance sensor utilizing a tungsten disulfide WS_2 nanosheets overlayer," *Photonics Research*, vol. 6, no. 6, pp. 485–491, 2018.

[88] C. Cen, H. Lin, J. Huang, C. Liang, X. Chen, Y. Tang, Z. Yi, X. Ye, J. Liu, Y. Yi, and S. Xiao, "A tunable plasmonic refractive index sensor with nanoring strip graphene arrays," *Sensors*, vol. 18, no. 12, 2018.

[89] X. Chen, L. Xia, and C. Li, "Surface plasmon resonance sensor based on a novel D shaped photonic crystal fiber for low refractive index detection," *IEEE Photonics Journal*, vol. 10, no. 1, pp. 1–9, 2018.

[90] S. Chakma, M. A. Khalek, B. K. Paul, K. Ahmed, M. R. Hasan, and A. N. Bahar, "Gold coated photonic crystal fiber biosensor based on surface plasmon resonance design and analysis," *Sensing and Bio Sensing Research*, vol. 18, pp. 7–12, 2018.

[91] C. Liu, W. Su, Q. Liu, X. Lu, F. Wang, T. Sun, and P. K. Chu, "Symmetrical dual D shape photonic crystal fibers for surface plasmon resonance sensing," *Optics Express*, vol. 26, no. 7, pp. 9039–9049, 2018.

[92] I. R. Matias, S. Ikezawa, and J. Corres, *Fiber Optic Sensors: current status and future possibilities*, vol. 21. Springer, 2016.

[93] L. Yue, B. Yan, M. Attridge, and Z. Wang, "Light absorption in perovskite solar cell fundamentals and plasmonic enhancement of infrared band absorption," *Solar Energy*, vol. 124, pp. 143–152, 2016.

[94] B. Wu, X. Wu, C. Guan, K. Fai Tai, E. K. L. Yeow, H. Jin Fan, N. Mathews, and T. C. Sum, "Uncovering loss mechanisms in silver nanoparticle blended plasmonic organic solar cells," *Nature Communications*, vol. 4, p. 2004, 2013.

[95] A. I. Kuznetsov, A. E. Miroshnichenko, M. L. Brongersma, Y. S. Kivshar, and B. Luk'yanchuk, "Optically resonant dielectric nanostructures," *Science*, vol. 354, no. 6314, p. aag2472, 2016.

[96] M. Kaltenbrunner, M. S. White, E. D. Głowacki, T. Sekitani, T. Someya, N. S. Sariciftci, and S. Bauer, "Ultrathin and lightweight organic solar cells with high flexibility," *Nature Communications*, vol. 3, p. 770, 2012.

[97] M. A. Green, "Thin film solar cells review of materials technologies and commercial status," *Journal of Materials Science Materials in Electronics*, vol. 18, no. 1, pp. 15–19, 2007.

[98] K. W. Boer, *Handbook of the physics of thin film solar cells*. Springer Science Business, 2014.

[99] A. Kowsar, S. F. U. Farhad, M. Rahaman, M. S. Islam, A. Y. Imam, S. C. Debnath, M. Sultana, M. A. Hoque, A. Sharmin, and Z. H. Mahmood, "Progress in major thin-film solar cells growth technologies, layer materials and efficiencies," *International Journal of Renewable Energy Research IJRER*, vol. 9, no. 2, pp. 579–597, 2019.

[100] D. Staebler and C. Wronski, "Reversible conductivity changes in discharge-produced amorphous Si," *Applied Physics Letters*, vol. 31, no. 4, pp. 292–294, 1977.

[101] A. Vora, J. Gwamuri, J. M. Pearce, P. L. Bergstrom, and D. O. Guney, "Multi-resonant silver nano-disk patterned thin film hydrogenated amorphous silicon solar cells for Staebler-Wronski effect compensation," *Journal of Applied Physics*, vol. 116, no. 9, p. 093103, 2014.

[102] W. C. Choy, *Organic solar cells materials and device physics*. No. 5, Springer, 2012.

[103] N. Lu, J. Wang, D. Geng, L. Li, and M. Liu, "Understanding the transport mechanism of organic-inorganic perovskite solar cells the effect of exciton or free charge on diffusion length," *Organic Electronics*, vol. 66, pp. 163–168, 2019.

[104] R. S. Crandall, "Transport in hydrogenated amorphous silicon p-i-n solar cells," *Journal of Applied Physics*, vol. 53, no. 4, pp. 3350–3352, 1982.

[105] N. I. Landy, S. Sajuyigbe, J. J. Mock, D. R. Smith, and W. J. Padilla, "Perfect metamaterial absorber," *Physical Review Letters*, vol. 100, p. 207402, 2008.

[106] N. Liu, M. Mesch, T. Weiss, M. Hentschel, and H. Giessen, "Infrared perfect absorber and its application as plasmonic sensor," *Nano Letters*, vol. 10, no. 7, pp. 2342–2348, 2010.

[107] S. Fahr, C. Ulbrich, T. Kirchartz, U. Rau, C. Rockstuhl, and F. Lederer, "Rugate filter for light trapping in solar cells," *Optics Express*, vol. 16, no. 13, pp. 9332–9343, 2008.

[108] M. Born and E. Wolf, *Principles of optics: Electromagnetic theory of propagation, interference and diffraction of light*, vol. VII,VIII. Elsevier, 2013.

[109] D. Wagner and P. Irsigler, "On the annealing behaviour of the Staebler-Wronski effect in aSiH," *Applied Physics A*, vol. 35, no. 1, pp. 9–12, 1984.

[110] J. D. Jackson, *Classical electrodynamics*. John Wiley & Sons, 2007.

[111] J. Boroumand, S. Das, A. Vazquez-Guardado, D. Franklin, and D. Chanda, "Unified electromagnetic-electronic design of light trapping silicon solar cells," *Scientific Reports*, vol. 6, p. 31013, 2016.

[112] R. A. Pala, J. White, E. Barnard, J. Liu, and M. L. Brongersma, "Design of plasmonic thin-film solar cells with broadband absorption enhancements," *Advanced Materials*, vol. 21, no. 34, pp. 3504–3509, 2009.

[113] W. Wang, S. Wu, K. Reinhardt, Y. Lu, and S. Chen, "Broadband light absorption enhancement in thin-film silicon solar cells," *Nano Letters*, vol. 10, no. 6, pp. 2012–2018, 2010.

[114] NREL, "National renewable energy laboratory (nrel) ms excel spreadsheet file available online." https://rredc.nrel.gov/solar/spectra/am1.5, 2019.

[115] A. Naqavi, K. Soderstrom, F.-J. Haug, V. Paeder, T. Scharf, H. P. Herzig, and C. Ballif, "Understanding of photocurrent enhancement in real thin film solar cells: towards optimal one-dimensional gratings," *Optics Express*, vol. 19, no. 1, pp. 128–140, 2011.

[116] T. Lanz, B. Ruhstaller, C. Battaglia, and C. Ballif, "Extended light scattering model incorporating coherence for thin-film silicon solar cells," *Journal of Applied Physics*, vol. 110, no. 3, p. 033111, 2011.

[117] K. Jager, M. Fischer, R. Van Swaaij, and M. Zeman, "A scattering model for nano-textured interfaces and its application in opto-electrical simulations of thin-film silicon solar cells," *Journal of Applied Physics*, vol. 111, no. 8, p. 083108, 2012.

[118] S. Altazin, L. Stepanova, K. Lapagna, P. Losio, J. Werner, B. Niesen, A. Dabirian, M. Morales Masis, S. De Wolf, C. Ballif, *et al.*, "Design of perovskite/crystalline-silicon tandem solar cells," in *32nd European Photovoltaic Solar Energy Conference and Exhibition*, pp. 1276–1279, 2016.

[119] S. A. Maier, *Plasmonics: fundamentals and applications*. Springer Science & Business Media, 2007.

[120] A. Taflove and S. C. Hagness, *Computational electrodynamics: the finite-difference time-domain method*. Artech House, 2005.

[121] K. Yee, "Numerical solution of initial boundary value problems involving Maxwell's equations in isotropic media," *IEEE Transactions on antennas and propagation*, vol. 14, no. 3, pp. 302–307, 1966.

[122] C.-F. Yang, B.-C. Wu, and C.-J. Ko, "A ray-tracing method for modeling indoor wave propagation and penetration," *IEEE transactions on Antennas and Propagation*, vol. 46, no. 6, pp. 907–919, 1998.

[123] M. Fagan, *Finite element analysis*. Longman group UK limited, 1996.

[124] S. C. Brenner and L. R. Scott, *The mathematical theory of finite element methods*. Springer, 1994.

[125] M. G. Larson and F. Bengzon, *The finite element method: theory, implementation, and applications*, vol. 10. Springer Science & Business Media, 2013.

[126] S. Littmarck and F. Saeidi, "https://www.comsol.com/company," 1986.

[127] O. Schenk, K. Gärtner, W. Fichtner, and A. Stricker, "Pardiso: a high-performance serial and parallel sparse linear solver in semiconductor device simulation," *Future Generation Computer Systems*, vol. 18, no. 1, pp. 69–78, 2001.

[128] P. B. Johnson and R.-W. Christy, "Optical constants of the noble metals," *Physical Review B*, vol. 6, no. 12, p. 4370, 1972.

[129] F. Galvez, D. P. de Lara, J. Spottorno, M. García, and J. Vicent, "Heating effects of low power surface plasmon resonance sensors," *Sensors and Actuators B: Chemical*, vol. 243, pp. 806–811, 2017.

[130] X. Luo, Z.-Q. Cheng, X. Zhai, Z.-M. Liu, S.-Q. Li, J.-P. Liu, L.-L. Wang, Q. Lin, and Y.-H. Zhou, "A tunable dual-band and polarization-insensitive coherent perfect absorber based on double-layers graphene hybrid waveguide," *Nanoscale Research Letters*, vol. 14, no. 1, p. 337, 2019.

[131] X. Shen, T. J. Cui, J. Zhao, H. F. Ma, W. X. Jiang, and H. Li, "Polarization-independent wide-angle triple-band metamaterial absorber," *Optics Express*, vol. 19, no. 10, pp. 9401–9407, 2011.

[132] Q. Zhang, M. M. Tavakoli, L. Gu, D. Zhang, L. Tang, Y. Gao, J. Guo, Y. Lin, S.-F. Leung, S. Poddar, *et al.*, "Efficient metal halide perovskite light-emitting diodes with significantly improved light extraction on nanophotonic substrates," *Nature Communications*, vol. 10, no. 1, p. 727, 2019.

[133] M. A. Green, E. D. Dunlop, D. H. Levi, J. Hohl-Ebinger, M. Yoshita, and A. W. Ho-Baillie, "Solar cell efficiency tables (version 54)," *Progress in Photovoltaics: Research and Applications*, vol. 27, no. 7, pp. 565–575, 2019.

[134] C. Battaglia, A. Cuevas, and S. De Wolf, "High efficiency crystalline silicon solar cells status and perspectives," *Energy and Environmental Science*, vol. 9, no. 5, pp. 1552–1576, 2016.

[135] H. Dai, L. Yang, and S. He, "$< 50 - \mu$m thin crystalline silicon heterojunction solar cells with dopant-free carrier-selective contacts," *Nano Energy*, vol. 64, p. 103930, 2019.

[136] O. Ellabban, H. Abu-Rub, and F. Blaabjerg, "Renewable energy resources: Current status, future prospects and their enabling technology," *Renewable and Sustainable Energy Reviews*, vol. 39, pp. 748–764, 2014.

[137] K. Chopra, P. Paulson, and V. Dutta, "Thin-film solar cells an overview," *Progress in Photovoltaics Research and Applications*, vol. 12, no. 2-3, pp. 69–92, 2004.

[138] S. Ananthakumar, J. R. Kumar, and S. M. Babu, "Third-generation solar cells concept, materials and performance an overview," in *Emerging Nanostructured Materials for Energy and Environmental Science*, pp. 305–339, Springer, 2019.

[139] A. Ojo, W. Cranton, and I. Dharmadasa, "Photovoltaic solar cells: Materials, concepts and devices," in *Next Generation Multilayer Graded Bandgap Solar Cells*, pp. 17–40, Springer, 2019.

[140] W. Kern and K. K. Schuegraf, "Deposition technologies and applications: Introduction and overview," in *Handbook of Thin Film Deposition Processes and Techniques*, pp. 11–43, Elsevier, 2001.

[141] M. Moon, M. Alam, M. Rahman, J. Hossain, A. B. M. Ismail, *et al.*, "Comparative study of the second generation aSiH, CdTe, and CIGS thin-film solar cells," in *Advanced Materials Research*, vol. 1154, pp. 102–111, Trans Tech Publications, 2019.

[142] Z. Ma and D. Liu, *Inorganic Flexible Optoelectronics: Materials and Applications*. John Wiley & Sons, 2019.

[143] W. Xiang and W. Tress, "Review on recent progress of all-inorganic metal halide perovskites and solar cells," *Advanced Materials*, vol. 31, no. 44, p. 1902851, 2019.

[144] Y. Shirota and H. Kageyama, "Organic materials for optoelectronic applications: Overview," in *Handbook of Organic Materials for Electronic and Photonic Devices*, pp. 3–42, Elsevier, 2019.

[145] M. Stuckelberger, R. Biron, N. Wyrsch, F.-J. Haug, and C. Ballif, "Progress in solar cells from hydrogenated amorphous silicon," *Renewable and Sustainable Energy Reviews*, vol. 76, pp. 1497–1523, 2017.

[146] K.-H. Kim, "Thermal activation of boron-and phosphorus-doped amorphous silicon and the contribution to improved efficiency in hydrogenated amorphous silicon solar cells," *Journal of the Korean Physical Society*, vol. 75, no. 9, pp. 703–707, 2019.

[147] P. Lechner and H. Schade, "Photovoltaic thin-film technology based on hydrogenated amorphous silicon," *Progress in Photovoltaics: Research and Applications*, vol. 10, no. 2, pp. 85–97, 2002.

[148] S. C. Agarwal and S. Omar, "Forty years of the Staebler Wronski effect," *Philosophical Magazine*, vol. 98, no. 27, pp. 2512–2528, 2018.

[149] I. Pola, D. Chianese, L. Fanni, and R. Rudel, "Analysis of annealing and degradation effects on a-Si PV modules," in *Proceeding of the 23rd European Photovoltaic Solar Energy Conference*, 2008.

[150] S. Fujikake, H. Ota, M. Ohsawa, T. Hama, Y. Ichikawa, and H. Sakai, "Light induced recovery of a si solar cells," *Solar Energy Materials And Solar Cells*, vol. 34, no. 1-4, pp. 449–454, 1994.

[151] A. DHOUIB and S. FILALI, "Operating temperatures of photovoltaic panels," in *Energy and the Environment*, pp. 494–498, Elsevier, 1990.

[152] S. B. Mallick, M. Agrawal, and P. Peumans, "Optimal light trapping in ultra-thin photonic crystal crystalline silicon solar cells," *Optics Express*, vol. 18, no. 6, pp. 5691–5706, 2010.

[153] Z. C. Holman, A. Descoeudres, L. Barraud, F. Z. Fernandez, J. P. Seif, S. De Wolf, and C. Ballif, "Current losses at the front of silicon heterojunction solar cells," *IEEE Journal of Photovoltaics*, vol. 2, no. 1, pp. 7–15, 2012.

[154] J. Poortmans and V. Arkhipov, *Thin film solar cells: fabrication, characterization and applications*, vol. 5. John Wiley & Sons, 2006.

[155] N. Sahraei, S. Venkataraj, A. G. Aberle, and I. M. Peters, "Investigation of the optical absorption of aSiH solar cells on micro- and nano-textured surfaces," *Energy Procedia*, vol. 33, pp. 166–172, 2013. PV Asia Pacific Conference 2012.

[156] R. Varache, A. Valla, N. Nguyen, and D. Munoz, "Front side recombination losses analysis in rear emitter silicon heterojunction solar cells," *Proceedings of the 4th International Conference on Crystalline Silicon Photovoltaics (SiliconPV 2014): Energy Procedia*, vol. 55, pp. 302–309, 2014.

[157] S. Ruhle, "Tabulated values of the Shockley–Queisser limit for single junction solar cells," *Solar Energy*, vol. 130, pp. 139–147, 2016.

[158] F. Dimroth and S. Kurtz, "High-efficiency multijunction solar cells," *MRS Bulletin*, vol. 32, no. 3, pp. 230–235, 2007.

[159] M. W. Wanlass, "Monolithic tandem solar cell," May 28 1991. US Patent 5,019,177.

[160] M. Yamaguchi, K. H. Lee, K. Araki, and N. Kojima, "A review of recent progress in heterogeneous silicon tandem solar cells," *Journal of Physics D Applied Physics*, vol. 51, no. 13, p. 133002, 2018.

[161] R. Wang, M. Mujahid, Y. Duan, Z. K. Wang, J. Xue, and Y. Yang, "A review of perovskites solar cell stability," *Advanced Functional Materials*, p. 1808843, 2019.

[162] J. Werner, B. Niesen, and C. Ballif, "Perovskite/silicon tandem solar cells: Marriage of convenience or true love story? an overview," *Advanced Materials Interfaces*, vol. 5, no. 1, p. 1700731, 2018.

[163] T. Todorov, O. Gunawan, and S. Guha, "A road towards 25% efficiency and beyond: perovskite tandem solar cells," *Molecular Systems Design & Engineering*, vol. 1, no. 4, pp. 370–376, 2016.

[164] Y. Hu, L. Song, Y. Chen, and W. Huang, "Two-terminal perovskites tandem solar cells: Recent advances and perspectives," *Solar Rapid Research Letters*, vol. 3, no. 7, p. 1900080, 2019.

[165] SOPRA, "refractive index libirary." `http://www.sspectra.com/sopra.html/`, 2020.

[166] J. Kischkat, S. Peters, B. Gruska, M. Semtsiv, M. Chashnikova, M. Klinkmuller, O. Fedosenko, S. Machulik, A. Aleksandrova, G. Monastyrskyi, *et al.*, "Mid-infrared optical properties of thin films of aluminum oxide, titanium dioxide, silicon dioxide, aluminum nitride, and silicon nitride," *Applied Optics*, vol. 51, no. 28, pp. 6789–6798, 2012.

[167] R. Treharne, A. Seymour-Pierce, K. Durose, K. Hutchings, S. Roncallo, and D. Lane, "Optical design and fabrication of fully sputtered CdTe/CdS solar cells," in *Journal of Physics: Conference Series*, vol. 286, p. 012038, IOP Publishing, 2011.

[168] A. M. Bakry and A. H. E. Naggar, "Doping effects on the optical properties of evaporated aSiH films," *Thin Solid Films*, vol. 360, no. 1, pp. 293–297, 2000.

[169] A. Belfar, "The role of p+-layer dopant concentration, p+-layer band gap and p+-layer thickness in the performances of aSiH n–i–p–p+ solar cells with double layer window nanocrystalline silicon," *Optik-International Journal for Light and Electron Optics*, vol. 126, no. 24, pp. 5688–5693, 2015.

[170] S. Singh, S. Kumar, and N. Dwivedi, "Band gap optimization of p–i–n layers of aSiH by computer aided simulation for development of efficient solar cell," *Solar Energy*, vol. 86, no. 5, pp. 1470–1476, 2012.

[171] M. Sharma, S. Juneja, S. Sudhakar, D. Chaudhary, and S. Kumar, "Optimization of aSiH absorber layer grown under a low pressure regime by plasma-enhanced chemical vapor deposition: Revisiting the significance of the p/i interface for solar cells," *Materials Science in Semiconductor Processing*, vol. 43, pp. 41–46, 2016.

[172] A. Shiri, M. L. Villinger, S. Shabahang, A. K. Jahromi, C. H. Villinger, and A. F. Abouraddy, "Broadband omni-resonance doubles the near-infrared quantum-efficiency of a thin film solar cell," in *Frontiers in Optics*, pp. JW4A–83, Optical Society of America, 2019.

[173] A. Peter Amalathas and M. M. Alkaisi, "Nanostructures for light trapping in thin film solar cells," *Micromachines*, vol. 10, no. 9, p. 619, 2019.

[174] S. Morawiec, M. Mendes, F. Priolo, and I. Crupi, "Plasmonic nanostructures for light trapping in thin-film solar cells," *Materials Science in Semiconductor Processing*, vol. 92, pp. 10–18, 2019.

[175] L. J.-H. Lin and Y.-P. Chiou, "Optical design of GaN/$In_xGa_{1-x}N$/cSi tandem solar cells with triangular diffraction grating," *Optics Express*, vol. 23, pp. A614–A624, Jun 2015.

[176] J. Gwamuri, A. Vora, J. Mayandi, D. O. Guney, P. L. Bergstrom, and J. M. Pearce, "A new method of preparing highly conductive ultra-thin indium tin oxide for plasmonic-enhanced thin film solar photovoltaic devices," *Solar Energy Materials and Solar Cells*, vol. 149, pp. 250–257, 2016.

[177] M. Elshorbagy, K. Abdel-Hady, H. Kamal, and J. Alda, "Broadband anti-reflection coating using dielectric Si_3N_4 nanostructures. application to amorphous-si-h solar cells," *Optics Communications*, vol. 390, pp. 130–136, 2017.

[178] R. Dubey, K. Jhansirani, and S. Singh, "Investigation of solar cell performance using multilayer thin film structure (SiO_2/Si_3N_4) and grating," *Results in Physics*, vol. 7, pp. 77–81, 2017.

[179] H. Kikuta, Y. Ohira, H. Kubo, and K. Iwata, "Effective medium theory of two-dimensional subwavelength gratings in the non-quasi-static limit," *Journal of the Optical Society of America A*, vol. 15, no. 6, pp. 1577–1585, 1998.

[180] S. Rytov, "Electromagnetic properties of a finely stratified medium," *Soviet Physics Journal of Experimental and Theoretical Physics*, vol. 2, pp. 466–475, 1956.

[181] F. Fadakar Masouleh, N. Das, and S. M. Rozati, "Nano-structured gratings for improved light absorption efficiency in solar cells," *Energies*, vol. 9, no. 9, p. 756, 2016.

[182] W. Stork, N. Streibl, H. Haidner, and P. Kipfer, "Artificial distributed-index media fabricated by zero-order gratings," *Optics Letters*, vol. 16, no. 24, pp. 1921–1923, 1991.

[183] P. Lalanne and M. Hutley, *Artificial media optical properties-subwavelength scale*, vol. 1. Marcel Dekker, 2003.

[184] E.-J. Guo, H. Guo, H. Lu, K. Jin, M. He, and G. Yang, "Structure and characteristics of ultrathin indium tin oxide films," *Applied Physics Letters*, vol. 98, no. 1, p. 011905, 2011.

[185] M. J. Dodge, "Refractive properties of magnesium fluoride," *Applied Optics*, vol. 23, no. 12, pp. 1980–1985, 1984.

[186] I. H. Malitson, "Interspecimen comparison of the refractive index of fused silica," *Journal of the Optical Society of America A*, vol. 55, no. 10, pp. 1205–1209, 1965.

[187] G. Beadie, M. Brindza, R. A. Flynn, A. Rosenberg, and J. S. Shirk, "Refractive index measurements of poly (methyl methacrylate) (PMMA) from 0.4–1.6 μm," *Applied Optics*, vol. 54, no. 31, pp. F139–F143, 2015.

[188] K. Luke, Y. Okawachi, M. R. E. Lamont, A. L. Gaeta, and M. Lipson, "Broadband mid-infrared frequency comb generation in a Si_3N_4 microresonator," *Optics Letters*, vol. 40, no. 21, pp. 4823–4826, 2015.

[189] P. Chaudhuri, S. Ray, A. Batabyal, and A. Barua, "Thickness dependence of light-induced effects in aSi solar cells," *Solar cells*, vol. 31, no. 1, pp. 13–21, 1991.

[190] J. Mu llerova, L. Pruvsakova, M. Netrvalova, V. Vavruvnkova, and P. vsutta, "A study of optical absorption in amorphous hydrogenated silicon thin films of varied thickness," *Applied Surface Science*, vol. 256, no. 18, pp. 5667–5671, 2010.

[191] S. Hasegawa and Y. Imai, "Thickness dependence of electrical and optical properties and ESR in undoped aSiH," *Philosophical Magazine B*, vol. 46, no. 3, pp. 239–251, 1982.

[192] J.-W. Shin, K.-M. Park, J.-E. Kim, and S.-Y. Choi, "The properties of aSiH pin solar cell by intrinsic layer's thickness," *Molecular Crystals and Liquid Crystals*, vol. 551, no. 1, pp. 257–263, 2011.

[193] M. H. Elshorbagy and J. Alda, "Funneling and guiding effects in ultrathin aSiH solar cells using one-dimensional dielectric subwavelength gratings," *Journal of Photonics for Energy*, vol. 7, no. 1, p. 017002, 2017.

[194] Y. Jang, J. B. Kim, T. E. Hong, S. J. Yeo, S. Lee, E. A. Jung, B. K. Park, T.-M. Chung, C. G. Kim, D.-J. Lee, H.-B.-R. Lee, and S.-H. Kim, "Highly-conformal nanocrystalline molybdenum nitride thin films by atomic layer deposition as a diffusion barrier against cu," *Journal of Alloys and Compounds*, vol. 663, pp. 651–658, 2016.

[195] T. Karabacak and T.-M. Lu, "Enhanced step coverage by oblique angle physical vapor deposition," *Journal of Applied Physics*, vol. 97, no. 12, p. 124504, 2005.

[196] S. M. George, "Atomic layer deposition: An overview," *Chemical Reviews*, vol. 110, no. 1, pp. 111–131, 2010.

[197] A. Paranjpe, S. Gopinath, T. Omstead, and R. Bubber, "Atomic layer deposition of AlO_x for thin film head gap applications," *Journal of The Electrochemical Society*, vol. 148, no. 9, p. G465, 2001.

[198] H. Cho, N. Lee, H. Choi, H. Park, C. Jung, S. Song, H. Yuk, Y. Kim, J.-W. Kim, K. Kim, *et al.*, "Remote plasma atomic layer deposition of SiNx using cyclosilazane and H_2/N_2 plasma," *Applied Sciences*, vol. 9, no. 17, p. 3531, 2019.

[199] S. Duttagupta, F. Ma, B. H. andThomas Mueller, and A. G. Aberle, "Optimised antireflection coatings using silicon nitride on textured silicon surfaces based on measurements and multidimensional modelling," *Energy Procedia*, vol. 15, pp. 78–83, 2012.

[200] M. Pathak, J. M. Pearce, and S. Harrison, "Effects on amorphous silicon photovoltaic performance from high-temperature annealing pulses in photovoltaic thermal hybrid devices," *Solar Energy Materials and Solar Cells*, vol. 100, pp. 199–203, 2012.

[201] P. Zhu, P. Jin, H. Shi, and L. J. Guo, "Funneling light into subwavelength grooves in metal/dielectric multilayer films," *Optics Express*, vol. 21, no. 3, pp. 3595–3602, 2013.

[202] M. Mivelle, P. Viktorovitch, F. I. Baida, A. El Eter, Z. Xie, T.-P. Vo, E. Atie, G. W. Burr, D. Nedeljkovic, J.-Y. Rauch, *et al.*, "Light funneling from a photonic crystal laser cavity to a nano-antenna: overcoming the diffraction limit in optical energy transfer down to the nanoscale," *Optics Express*, vol. 22, no. 12, pp. 15075–15087, 2014.

[203] M. H. Elshorbagy, B. García-Cámara, E. López-Fraguas, and R. Vergaz, "Efficient light management in a monolithic tandem perovskite/silicon solar cell by using a hybrid metasurface," *Nanomaterials*, vol. 9, no. 5, p. 791, 2019.

[204] D. Grant, K. Catchpole, K. Weber, and T. White, "Design guidelines for perovskite/silicon 2-terminal tandem solar cells: an optical study," *Optics Express*, vol. 24, no. 22, pp. A1454–A1470, 2016.

[205] J. M. Siqueiros, R. Machorro, and L. E. Regalado, "Determination of the optical constants of MgF_2 and ZnS from spectrophotometric measurements and the classical oscillator method," *Applied Optics*, vol. 27, no. 12, pp. 2549–2553, 1988.

[206] M. Morales-Masis, S. M. De Nicolas, J. Holovsky, S. De Wolf, and C. Ballif, "Low-temperature high-mobility amorphous IZO for silicon heterojunction solar cells," *IEEE Journal of Photovoltaics*, vol. 5, no. 5, pp. 1340–1347, 2015.

[207] P. Loper, M. Stuckelberger, B. Niesen, J. Werner, M. Filipic, S.-J. Moon, J.-H. Yum, M. Topic, S. De Wolf, and C. Ballif, "Complex refractive index spectra of $CH_3NH_3PbI_3$ perovskite thin films determined by spectroscopic ellipsometry and spectrophotometry," *The Journal of Physical Chemistry Letters*, vol. 6, no. 1, pp. 66–71, 2015.

[208] M. Filipic, P. Loper, B. Niesen, S. D. Wolf, J. Krc, C. Ballif, and M. Topic, "$CH_3NH_3PbI_3$ perovskite/silicon tandem solar cells characterization based optical simulations," *Optics Express*, vol. 23, no. 7, pp. A263–A278, 2015.

[209] T. Siefke, S. Kroker, K. Pfeiffer, O. Puffky, K. Dietrich, D. Franta, I. Ohlidal, A. Szeghalmi, E. B. Kley, and A. Tunnermann, "Materials pushing the application limits of wire grid polarizers further into the deep ultraviolet spectral range," *Advanced Optical Materials*, vol. 4, no. 11, pp. 1780–1786, 2016.

[210] T. A. F. Konig, P. A. Ledin, J. Kerszulis, M. A. Mahmoud, M. A. El Sayed, J. R. Reynolds, and V. V. Tsukruk, "Electrically tunable plasmonic behavior of nanocube–polymer nanomaterials induced by a redox-active electrochromic polymer," *ACS Nano*, vol. 8, no. 6, pp. 6182–6192, 2014.

[211] H. T. Nguyen, F. E. Rougieux, B. Mitchell, and D. Macdonald, "Temperature dependence of the band-band absorption coefficient in crystalline silicon from photoluminescence," *Journal of Applied Physics*, vol. 115, no. 4, p. 043710, 2014.

[212] S. D. Stranks, G. E. Eperon, G. Grancini, C. Menelaou, M. J. Alcocer, T. Leijtens, L. M. Herz, A. Petrozza, and H. J. Snaith, "Electron-hole diffusion lengths exceeding 1 micrometer in an organometal trihalide perovskite absorber," *Science*, vol. 342, no. 6156, pp. 341–344, 2013.

[213] Q. Lin, A. Armin, R. C. R. Nagiri, P. L. Burn, and P. Meredith, "Electro-optics of perovskite solar cells," *Nature Photonics*, vol. 9, no. 2, pp. 106–112, 2015.

[214] Y. Kim, S. A. Choulis, J. Nelson, D. D. C. Bradley, S. Cook, and J. R. Durrant, "Device annealing effect in organic solar cells with blends of regioregular poly(3-hexylthiophene) and soluble fullerene," *Applied Physics Letters*, vol. 86, no. 6, p. 063502, 2005.

[215] W. Qarony, Y. A. Jui, G. M. Das, T. Mohsin, M. I. Hossain, and S. N. Islam, "Optical analysis in $CH_3NH_3PbI_3$ and $CH_3NH_3PbI_2Cl$ based thin-film perovskite solar cell," *American Journal of Energy Research*, vol. 3, pp. 19–24, 2015.

[216] A. N. Cho and N. G. Park, "Impact of interfacial layers in perovskite solar cells," *ChemSusChem: Chemistry-Sustainability-Enery-Materials*, vol. 10, no. 19, pp. 3687–3704, 2017.

[217] L. J. Lin and Y.-P. Chiou, "Improving thin-film crystalline silicon solar cell efficiency with back surface field layer and blaze diffractive grating," *Solar Energy*, vol. 86, no. 5, pp. 1485–1490, 2012.

[218] S. A. Cybart, P. Roediger, E. Ulin Avila, S. M. Wu, T. J. Wong, and R. C. Dynes, "Nanometer scale high aspect ratio trench etching at controllable angles using ballistic reactive ion etching," *Journal of Vacuum Science Technology B*, vol. 31, no. 1, p. 010604, 2013.

[219] Z. Shi and A. H. Jayatissa, "Perovskites-based solar cells: A review of recent progress, materials and processing methods," *Materials*, vol. 11, no. 5, p. 729, 2018.

[220] I. M. Peters, Y. S. Khoo, and T. M. Walsh, "Detailed current loss analysis for a PV module made with textured multicrystalline silicon wafer solar cells," *IEEE Journal of Photovoltaics*, vol. 4, no. 2, pp. 585–593, 2014.

[221] Z. C. Holman, A. Descoeudres, S. De Wolf, and C. Ballif, "Record infrared internal quantum efficiency in silicon heterojunction solar cells with dielectric/metal rear reflectors," *IEEE Journal of Photovoltaics*, vol. 3, no. 4, pp. 1243–1249, 2013.

[222] K. Bittkau, T. Kirchartz, and U. Rau, "Optical design of spectrally selective interlayers for perovskite/silicon heterojunction tandem solar cells," *Optics Express*, vol. 26, no. 18, pp. A750–A760, 2018.

[223] P.-K. Kung, M.-H. Li, P.-Y. Lin, Y.-H. Chiang, C.-R. Chan, T.-F. Guo, and P. Chen, "A review of inorganic hole transport materials for perovskite solar cells," *Advanced Materials Interfaces*, vol. 5, no. 22, p. 1800882, 2018.

[224] J. Lian, B. Lu, F. Niu, P. Zeng, and X. Zhan, "Electron-transport materials in perovskite solar cells," *Small Methods*, vol. 2, no. 10, p. 1800082, 2018.

[225] M. H. Elshorbagy, E. López-Fraguas, F. A. Chaudhry, J. M. Sánchez-Pena, R. Vergaz, and B. García-Cámara, "A monolithic nanostructured-perovskite/silicon tandem solar cell: feasibility of light management through geometry and materials selection," *Scientific Reports*, vol. 10, no. 1, pp. 1–8, 2020.

[226] C. Stelling, C. R. Singh, M. Karg, T. A. F. Konig, M. Thelakkat, and M. Retsch, "Plasmonic nanomeshes their ambivalent role as transparent electrodes in organic solar cells," *Scientific Reports*, vol. 7, no. 1, p. 42530, 2017.

[227] S. Luo, J. Zhao, D. Zuo, and X. Wang, "Perfect narrow band absorber for sensing applications," *Optics Express*, vol. 24, no. 9, pp. 9288–9294, 2016.

[228] J. Ziegler, C. Worister, C. Vidal, C. Hrelescu, and T. A. Klar, "Plasmonic nanostars as efficient broadband scatterers for random lasing," *ACS Photonics*, vol. 3, no. 6, pp. 919–923, 2016.

[229] S. Jayawardhana, A. P. Mazzolini, and P. R. Stoddart, "Collection efficiency of scattered light in single-ended optical fiber sensors," *Optics Letters*, vol. 37, no. 11, pp. 2142–2144, 2012.

[230] B. Monacelli, J. B. Pryor, B. A. Munk, D. Kotter, and G. D. Boreman, "Infrared frequency selective surface based on circuit-analog square loop design," *IEEE Transactions on Antennas and Propagation*, vol. 53, no. 2, pp. 745–752, 2005.

[231] C. Debus and P. H. Bolivar, "Frequency selective surfaces for high sensitivity terahertz sensing," *Applied Physics Letters*, vol. 91, no. 18, p. 184102, 2007.

[232] S. N. Azemi, F. H. W. Mustaffa, M. F. Jamlos, A. A. Al-Hadi, and P. J. Soh, "Frequency selective surface for structural health monitoring," in *IOP Conference Series: Materials Science and Engineering*, vol. 318, p. 012033, IOP Publishing, 2018.

[233] C. L. Wong, G. C. K. Chen, X. Li, B. K. Ng, P. Shum, P. Chen, Z. Lin, C. Lin, and M. Olivo, "Colorimetric surface plasmon resonance imaging (SPRI) biosensor array based on polarization orientation," *Biosensors and Bioelectronics*, vol. 47, pp. 545–552, 2013.

[234] M. Matuschek, D. P. Singh, H.-H. Jeong, M. Nesterov, T. Weiss, P. Fischer, F. Neubrech, and N. Liu, "Chiral plasmonic hydrogen sensors," *Small*, vol. 14, no. 7, p. 1702990, 2018.

[235] D. Madaan, A. Kapoor, and V. Sharma, "Ultrahigh sensitivity plasmonic refractive-index sensor for aqueous environment," *IEEE Photonics Technology Letters*, vol. 30, no. 2, pp. 149–152, 2018.

[236] L. Zhang, J. Zhang, F. Wang, J. Shen, Y. Zhang, L. Wu, X. Lu, L. Wang, Q. Fan, and W. Huang, "An Au@ Ag nanocube based plasmonic nano-sensor for rapid detection of sulfide ions with high sensitivity," *RSC Advances*, vol. 8, no. 11, pp. 5792–5796, 2018.

[237] D.-W. Huang, Y.-F. Ma, M.-J. Sung, and C.-P. Huang, "Approach the angular sensitivity limit in surface plasmon resonance sensors with low index prism and large resonant angle," *Optical Engineering*, vol. 49, no. 5, p. 054403, 2010.

[238] Y.-G. Zhao, W.-K. Lu, Y. Ma, S.-S. Kim, S. T. Ho, and T. J. Marks, "Polymer waveguides useful over a very wide wavelength range from the ultraviolet to infrared," *Applied Physics Letters*, vol. 77, no. 19, pp. 2961–2963, 2000.

[239] H. Kruger, E. Kemnitz, A. Hertwig, and U. Beck, "Transparent MgF_2-films by sol–gel coating: Synthesis and optical properties," *Thin Solid Films*, vol. 516, no. 12, pp. 4175–4177, 2008.

[240] K.-S. Lee and M. A. El-Sayed, "Gold and silver nanoparticles in sensing and imaging: sensitivity of plasmon response to size, shape, and metal composition," *The Journal of Physical Chemistry B*, vol. 110, no. 39, pp. 19220–19225, 2006.

[241] B. Shuai, L. Xia, Y. Zhang, and D. Liu, "A multi-core holey fiber based plasmonic sensor with large detection range and high linearity," *Optics Express*, vol. 20, no. 6, pp. 5974–5986, 2012.

[242] G. Lan, S. Liu, X. Zhang, Y. Wang, and Y. Song, "Highly sensitive and wide-dynamic-range liquid-prism surface plasmon resonance refractive index sensor based on the phase and angular interrogations," *Chinese Optics Letters*, vol. 14, no. 2, p. 022401, 2016.

[243] N. Luan and J. Yao, "A hollow-core photonic crystal fiber-basedspr sensor with large detection range," *IEEE Photonics Journal*, vol. 9, no. 3, pp. 1–7, 2017.

[244] K. Tong, J. Guo, M. Wang, P. Dang, F. Wang, Y. Zhang, and M. Wang, "An optical fiber surface plasmon resonance biosensor for wide range detection," *The European Physical Journal Applied Physics*, vol. 80, no. 1, p. 11201, 2017.

[245] R. Ahmad, N. Tripathy, and Y.-B. Hahn, "Wide linear-range detecting high sensitivity cholesterol biosensors based on aspect-ratio controlled ZnO nanorods grown on silver electrodes," *Sensors and Actuators B: Chemical*, vol. 169, pp. 382–386, 2012.

[246] R. Ahmad, M. Vaseem, N. Tripathy, and Y.-B. Hahn, "Wide linear-range detecting nonenzymatic glucose biosensor based on CuO nanoparticles inkjet-printed on electrodes," *Analytical Chemistry*, vol. 85, no. 21, pp. 10448–10454, 2013.

[247] Y. Chen, X. Li, H. Zhou, X. Hong, and Y. Geng, "Refractive index detection range adjustable liquid-core fiber optic sensor based on surface plasmon resonance and a nanoporous silica coating," *Journal of Physics D: Applied Physics*, vol. 49, no. 35, p. 355102, 2016.

[248] A. E. Miroshnichenko, S. Flach, and Y. S. Kivshar, "Fano resonances in nanoscale structures," *Reviews of Modern Physics*, vol. 82, no. 3, p. 2257, 2010.

[249] E. Prodan, C. Radloff, N. J. Halas, and P. Nordlander, "A hybridization model for the plasmon response of complex nanostructures," *Science*, vol. 302, no. 5644, pp. 419–422, 2003.

[250] Y. Sonnefraud, N. Verellen, H. Sobhani, G. A. Vandenbosch, V. V. Moshchalkov, P. Van Dorpe, P. Nordlander, and S. A. Maier, "Experimental realization of subradiant, superradiant, and fano resonances in ring/disk plasmonic nanocavities," *ACS Nano*, vol. 4, no. 3, pp. 1664–1670, 2010.

[251] B. Gerislioglu, A. Ahmadivand, and N. Pala, "Single- and multimode beam propagation through an optothermally controllable fano clusters-mediated waveguide," *Journal of Lightwave Technology*, vol. 35, no. 22, pp. 4961–4966, 2017.

[252] B. Gerislioglu, A. Ahmadivand, and N. Pala, "Functional quadrumer clusters for switching between fano and charge transfer plasmons," *IEEE Photonics Technology Letters*, vol. 29, no. 24, pp. 2226–2229, 2017.

[253] A. Ahmadivand, B. Gerislioglu, and N. Pala, "Active control over the interplay between the dark and hidden sides of plasmonics using metallodielectric Au–Ge_2Sb2Te_5 unit cells," *The Journal of Physical Chemistry C*, vol. 121, no. 36, pp. 19966–19974, 2017.

[254] A. A. Yanik, A. E. Cetin, M. Huang, A. Artar, S. H. Mousavi, A. Khanikaev, J. H. Connor, G. Shvets, and H. Altug, "Seeing protein monolayers with naked eye through plasmonic fano resonances," *Proceedings of the National Academy of Sciences*, vol. 108, no. 29, pp. 11784–11789, 2011.

[255] Y. Zhang, W. Liu, Z. Li, Z. Li, H. Cheng, S. Chen, and J. Tian, "High-quality-factor multiple fano resonances for refractive index sensing," *Optics Letters*, vol. 43, no. 8, pp. 1842–1845, 2018.

[256] Y. Deng, G. Cao, and H. Yang, "Tunable fano resonance and high-sensitivity sensor with high figure of merit in plasmonic coupled cavities," *Photonics and Nanostructures-Fundamentals and Applications*, vol. 28, pp. 45–51, 2018.

[257] B. Ai, C. Song, L. Bradley, and Y. Zhao, "Strong fano resonance excited in an array of nanoparticle-in-ring nanostructure for dual plasmonic sensor applications," *The Journal of Physical Chemistry C*, 2018.

[258] G.-D. Liu, X. Zhai, L.-L. Wang, Q. Lin, S.-X. Xia, X. Luo, and C.-J. Zhao, "A high-performance refractive index sensor based on fano resonance in Si split-ring metasurface," *Plasmonics*, vol. 13, no. 1, pp. 15–19, 2018.

[259] F. Peng, Z. Wang, G. Yuan, L. Guan, and Z. Peng, "High-sensitivity refractive index sensing based on fano resonances in a photonic crystal cavity-coupled microring resonator," *IEEE Photonics Journal*, vol. 10, no. 2, pp. 1–8, 2018.

[260] O. Mahboub, R. El Haffar, and A. Farkhsi, "Optical fano resonance in MIM waveguides with a double splits ring resonator," *Journal of New Frontiers in Spatial Concepts*, vol. 13, pp. 181–187, 2018.

[261] K.-L. Lee, C.-C. Chang, M.-L. You, M.-Y. Pan, and P.-K. Wei, "Enhancing surface sensing sensitivity of metallic nanostructures using blue-shifted surface plasmon mode and fano resonance," *Scientific Reports*, vol. 8, no. 1, p. 9762, 2018.

[262] H. Elshorbagy, Mahmoud, A. Cuadrado, and J. Alda, "High-sensitivity integrated devices based on surface plasmon resonance for sensing applications," *Photonics Research*, vol. 5, no. 6, pp. 654–661, 2017.

[263] B. Riedel, J. Hauss, U. Geyer, J. Guetlein, U. Lemmer, and M. Gerken, "Enhancing outcoupling efficiency of indium-tin-oxide-free organic light-emitting diodes via nanostructured high index layers," *Applied Physics Letters*, vol. 96, no. 24, p. 111, 2010.

[264] S. Fujihara, M. Tada, and T. Kimura, "Preparation and characterization of MgF_2 thin film by a trifluoroacetic acid method," *Thin Solid Films*, vol. 304, no. 1-2, pp. 252–255, 1997.

[265] L. J. Sherry, S.-H. Chang, G. C. Schatz, R. P. Van Duyne, B. J. Wiley, and Y. Xia, "Localized surface plasmon resonance spectroscopy of single silver nanocubes," *Nano Letters*, vol. 5, no. 10, pp. 2034–2038, 2005.

[266] F. Pardo, P. Bouchon, R. Haïdar, and J.-L. Pelouard, "Light funneling mechanism explained by magnetoelectric interference," *Physical Review Letters*, vol. 107, no. 9, p. 093902, 2011.

[267] P. Bouchon, F. Pardo, B. Portier, L. Ferlazzo, P. Ghenuche, G. Dagher, C. Dupuis, N. Bardou, R. Haïdar, and J.-L. Pelouard, "Total funneling of light in high aspect ratio plasmonic nanoresonators," *Applied Physics Letters*, vol. 98, no. 19, p. 191109, 2011.

[268] J.-W. Li, J.-S. Hong, W.-T. Chou, D.-J. Huang, and K.-R. Chen, "Light funneling profile during enhanced transmission through a subwavelength metallic slit," *Plasmonics*, vol. 13, no. 6, pp. 2249–2254, 2018.

[269] SCHOTT, "optical glass data sheets 2015-07-22 ." `https://refractiveindex.info/download/data/2015/schott-optical-glass-collection-datasheets-july-2015-us.pdf/`.

[270] K. Leosson, A. S. Ingason, B. Agnarsson, A. Kossoy, S. Olafsson, and M. C. Gather, "Ultra-thin gold films on transparent polymers," *Nanophotonics*, vol. 2, no. 1, pp. 3–11, 2013.

[271] B. Spackova, P. Wrobel, M. Bocková, and J. Homola, "Optical biosensors based on plasmonic nanostructures: A review," *Proceedings of the IEEE*, vol. 104, no. 12, pp. 2380–2408, 2016.

[272] B. Meshginqalam, M. T. Ahmadi, R. Ismail, and A. Sabatyan, "Graphene/graphene oxide-based ultrasensitive surface plasmon resonance biosensor," *Plasmonics*, pp. 1–7, 2016.

[273] Q. Ouyang, S. Zeng, L. Jiang, L. Hong, G. Xu, X.-Q. Dinh, J. Qian, S. He, J. Qu, P. Coquet, *et al.*, "Sensitivity enhancement of transition metal dichalcogenides/silicon nanostructure-based surface plasmon resonance biosensor," *Scientific Reports*, vol. 6, p. 28190, 2016.

[274] M. Sun, T. Sun, Y. Liu, L. Zhu, F. Liu, Y. Huang, and C. Chang-Hasnain, "Integrated plasmonic refractive index sensor based on grating/metal film resonant structure," in *High Contrast Metastructures V*, vol. 9757, p. 97570Q, International Society for Optics and Photonics, 2016.

[275] M. A. Otte, B. Sepulveda, W. Ni, J. P. Juste, L. M. Liz-Marzán, and L. M. Lechuga, "Identification of the optimal spectral region for plasmonic and nanoplasmonic sensing," *ACS Nano*, vol. 4, no. 1, pp. 349–357, 2009.

[276] W. Su, G. Zheng, and X. Li, "Design of a highly sensitive surface plasmon resonance sensor using aluminum-based diffraction grating," *Optics Communications*, vol. 285, no. 21, pp. 4603–4607, 2012.

[277] E. Martinsson, M. M. Shahjamali, K. Enander, F. Boey, C. Xue, D. Aili, and B. Liedberg, "Local refractive index sensing based on edge gold-coated silver nanoprisms," *The Journal of Physical Chemistry C*, vol. 117, no. 44, pp. 23148–23154, 2013.

[278] Y.-F. C. Chau, J.-Y. Syu, C.-T. C. Chao, H.-P. Chiang, and C. M. Lim, "Design of crossing metallic metasurface arrays based on high sensitivity of gap enhancement and transmittance shift for plasmonic sensing applications," *Journal of Physics D: Applied Physics*, vol. 50, no. 4, p. 045105, 2016.

[279] J. Maurya and Y. Prajapati, "A comparative study of different metal and prism in the surface plasmon resonance biosensor having MoS_2-graphene," *Optical and Quantum Electronics*, vol. 48, no. 5, pp. 1–12, 2016.

[280] A. Paliwal, M. Tomar, and V. Gupta, "Table top surface plasmon resonance measurement system for efficient urea biosensing using ZnO thin film matrix," *Journal of Biomedical Optics*, vol. 21, no. 8, pp. 087006–087006, 2016.

[281] L. Wu, J. Guo, X. Dai, Y. Xiang, and D. Fan, "Sensitivity enhanced by MoS_2-graphene hybrid structure in guided-wave surface plasmon resonance biosensor," *Plasmonics*, pp. 1–5, 2017.

[282] Y. Shen, J. Zhou, T. Liu, Y. Tao, R. Jiang, M. Liu, G. Xiao, J. Zhu, Z.-K. Zhou, X. Wang, *et al.*, "Plasmonic gold mushroom arrays with refractive index sensing figures of merit approaching the theoretical limit," *Nature Communications*, vol. 4, no. 1, pp. 1–9, 2013.

[283] T. W. Hughes and S. Fan, "Plasmonic circuit theory for multiresonant light funneling to a single spatial hot spot," *Nano Letters*, vol. 16, no. 9, pp. 5764–5769, 2016.

[284] M. H. Elshorbagy, A. Cuadrado, and J. Alda, "Plasmonic sensors based on funneling light through nanophotonic structures," *Plasmonics*, 2020.

[285] M. H. Elshorbagy, A. Cuadrado, G. Gonzalez, F. J. Gonzalez, and J. Alda, "Performance improvement of refractometric sensors through hybrid plasmonic–fano resonances," *Journal of Lightwave Technology*, vol. 37, pp. 2905–2913, July 2019.

[286] Y. L. Jin, J. Y. Chen, L. Xu, and P. N. Wang, "Refractive index measurement for biomaterial samples by total internal reflection," *Physics in Medicine and Biology*, vol. 51, no. 20, pp. N371–N379, 2006.

[287] M. H. Elshorbagy, A. Cuadrado, and J. Alda, "Plasmonic sensor based on dielectric nanoprisms," *Nanoscale Research Letters*, vol. 12, no. 1, p. 580, 2017.

[288] R. L. Hailes, A. M. Oliver, J. Gwyther, G. R. Whittell, and I. Manners, "Polyferrocenylsilanes: synthesis, properties, and applications," *Chemical Society Reviews*, vol. 45, no. 19, pp. 5358–5407, 2016.

[289] N. Luan and J. Yao, "High refractive index surface plasmon resonance sensor based on a silver wire filled hollow fiber," *IEEE Photonics Journal*, vol. 8, no. 1, pp. 1–9, 2016.

[290] A. K. Mishra, S. K. Mishra, and B. D. Gupta, "Spr based fiber optic sensor for refractive index sensing with enhanced detection accuracy and figure of merit in visible region," *Optics Communications*, vol. 344, pp. 86–91, 2015.

[291] B.-H. Liu, Y.-X. Jiang, X.-S. Zhu, X.-L. Tang, and Y.-W. Shi, "Hollow fiber surface plasmon resonance sensor for the detection of liquid with high refractive index," *Optics Express*, vol. 21, no. 26, pp. 32349–32357, 2013.

[292] D. Aspnes and A. Studna, "Dielectric functions and optical parameters of Si, Ge, GaP, GaAs, GaSb, InP, InAs, and InSb from 1.5 to 6.0 ev," *Physical Review B*, vol. 27, no. 2, p. 985, 1983.

[293] M. H. Elshorbagy, A. Cuadrado, B. García-Cámara, R. Vergaz, J. A. Gómez-Pedrero, and J. Alda, "Ultra-narrow spectral response of a hybrid plasmonic-grating sensor," *IEEE Sensors Journal*, 2019.

[294] S. Pi, X. Zeng, N. Zhang, D. Ji, B. Chen, H. Song, A. Cheney, Y. Xu, S. Jiang, D. Sun, *et al.*, "Dielectric-grating-coupled surface plasmon resonance from the back side of the metal film for ultrasensitive sensing," *IEEE Photonics Journal*, vol. 8, no. 1, pp. 1–7, 2015.

[295] Y. Li, Y. Liu, Z. Liu, Q. Tang, L. Shi, Q. Chen, G. Du, B. Wu, G. Liu, and L. Li, "Grating-assisted ultra-narrow multispectral plasmonic resonances for sensing application," *Applied Physics Express*, vol. 12, no. 7, p. 072002, 2019.

[296] O. S. Khalil, "Noninvasive photonic-crystal material for sensing glucose in tears," *Clinical Chemistry*, vol. 50, no. 12, pp. 2236–2237, 2004.

[297] A. Benito, G. M. Pérez, S. Mirabet, M. Vilaseca, J. Pujol, J. M. Marín, and P. Artal, "Objective optical assessment of tear-film quality dynamics in normal and mildly symptomatic dry eyes," *Journal of Cataract & Refractive Surgery*, vol. 37, no. 8, pp. 1481–1487, 2011.

[298] R. Kottaiyan, G. Yoon, Q. Wang, R. Yadav, J. M. Zavislan, and J. V. Aquavella, "Integrated multimodal metrology for objective and noninvasive tear evaluation," *The Ocular Surface*, vol. 10, no. 1, pp. 43–50, 2012.

[299] M. Abutoama and I. Abdulhalim, "Self-referenced biosensor based on thin dielectric grating combined with thin metal film," *Optics Express*, vol. 23, no. 22, pp. 28667–28682, 2015.

[300] S. Adachi, "Optical dispersion relations for GaP, GaAs, GaSb, InP, InAs, InSb, Al_x Ga_{1-x} As, and In_{1-x} Ga_x As_y P_{1-y}," *Journal of Applied Physics*, vol. 66, no. 12, pp. 6030–6040, 1989.

[301] Y. L. Jin, J. Y. Chen, L. Xu, and P. N. Wang, "Refractive index measurement for biomaterial samples by total internal reflection," *Physics in Medicine and Biology*, vol. 51, pp. N371–N379, oct 2006.

[302] V. Mulloni and L. Pavesi, "Porous silicon microcavities as optical chemical sensors," *Applied Physics Letters*, vol. 76, no. 18, pp. 2523–2525, 2000.

[303] N. Cennamo, M. Pesavento, L. De Maria, R. Galatus, F. Mattiello, and L. Zeni, "Comparison of different photoresist buffer layers in SPR sensors based on D-shaped POF and gold film," in *Optical Fiber Sensors Conference (OFS), 2017 25th*, pp. 1–4, IEEE, 2017.

[304] M. Mitsushio, K. Miyashita, and M. Higo, "Sensor properties and surface characterization of the metal-deposited spr optical fiber sensors with Au, Ag, Cu, and Al," *Sensors and Actuators A: Physical*, vol. 125, no. 2, pp. 296–303, 2006.

[305] F. L. Pedrotti, S. Leno, and S. Pedrotti, *Introduction to optics 2nd edition.* No. 477-481., New Jersey: Prentice Hall, 1993.

[306] S. Fan and J. D. Joannopoulos, "Analysis of guided resonances in photonic crystal slabs," *Physical Review B*, vol. 65, no. 23, p. 235112, 2002.

[307] A. K. Sharma, "Simulation and analysis of Au-MgF_2 structure in plasmonic sensor in near infrared spectral region," *Optics & Laser Technology*, vol. 101, pp. 491–498, 2018.

[308] R. Verma and B. D. Gupta, "A novel approach for simultaneous sensing of urea and glucose by SPR based optical fiber multianalyte sensor," *Analyst*, vol. 139, no. 6, pp. 1449–1455, 2014.

[309] Z.-W. Ding, T.-T. Lang, Y. Wang, and C.-L. Zhao, "Surface plasmon resonance refractive index sensor based on tapered coreless optical fiber structure," *Journal of Lightwave Technology*, vol. 35, no. 21, pp. 4734–4739, 2017.

[310] Q.-Q. Meng, X. Zhao, C.-Y. Lin, S.-J. Chen, Y.-C. Ding, and Z.-Y. Chen, "Figure of merit enhancement of a surface plasmon resonance sensor using a low-refractive-index porous silica film," *Sensors*, vol. 17, no. 8, p. 1846, 2017.

[311] A. K. Pandey and A. K. Sharma, "Simulation and analysis of plasmonic sensor in NIR with fluoride glass and graphene layer," *Photonics and Nanostructures-Fundamentals and Applications*, vol. 28, pp. 94–99, 2018.

[312] Z. Zhang, J. Yang, X. He, J. Zhang, J. Huang, D. Chen, and Y. Han, "Plasmonic refractive index sensor with high figure of merit based on concentric-rings resonator," *Sensors*, vol. 18, no. 1, p. 116, 2018.

[313] M. S. Rahman, M. R. Hasan, K. A. Rikta, and M. Anower, "A novel graphene coated surface plasmon resonance biosensor with tungsten disulfide (WS_2) for sensing DNA hybridization," *Optical Materials*, vol. 75, pp. 567–573, 2018.

[314] Y. Xiang, J. Zhu, L. Wu, Q. You, B. Ruan, and X. Dai, "Highly sensitive terahertz gas sensor based on surface plasmon resonance with graphene," *IEEE Photonics Journal*, vol. 10, no. 1, pp. 1–7, 2018.

[315] E. Luan, H. Yun, L. Laplatine, Y. Dattner, D. M. Ratner, K. C. Cheung, and L. Chrostowski, "Enhanced sensitivity of subwavelength multibox waveguide microring resonator label-free biosensors," *IEEE Journal of Selected Topics in Quantum Electronics*, vol. 25, no. 3, pp. 1–11, 2019.

[316] A. A. Rifat, R. Ahmed, G. A. Mahdiraji, F. M. Adikan, A. E. Miroshnichenko, *et al.*, "Highly sensitive selectively coated photonic crystal fiber-based plasmonic sensor," *Optics Letters*, vol. 43, no. 4, pp. 891–894, 2018.

[317] A. K. Sharma, A. K. Pandey, and B. Kaur, "A review of advancements (2007-2017) in plasmonics-based optical fiber sensors," *Optical Fiber Technology*, vol. 43, pp. 20–34, 2018.

[318] B. Liu, S. Chen, J. Zhang, X. Yao, J. Zhong, H. Lin, T. Huang, Z. Yang, J. Zhu, S. Liu, *et al.*, "A plasmonic sensor array with ultrahigh figures of merit and resonance linewidths down to 3 nm," *Advanced Materials*, vol. 30, no. 12, p. 1706031, 2018.

[319] R. Gupta and F. Yakuphanoglu, "Photoconductive Schottky diode based on Al/p-Si/SnS_2/Ag for optical sensor applications," *Solar Energy*, vol. 86, no. 5, pp. 1539–1545, 2012.

[320] S. Roy, C. Jacob, and S. Basu, "Studies on Pd/3C-SiC Schottky junction hydrogen sensors at high temperature," *Sensors and Actuators B: Chemical*, vol. 94, no. 3, pp. 298–303, 2003.

[321] K. Kang, K. Na, D. Kwon, J.-Y. Lee, and I. Park, "Self-powered gas sensor using thin-film photovoltaic cell and microstructured colorimetric film," in *2017 19th International Conference on Solid-State Sensors, Actuators and Microsystems (TRANSDUCERS)*, pp. 1536–1539, IEEE, 2017.

[322] L. Qin, C. Zhang, R. Li, and X. Li, "Silicon-gold core-shell nanowire array for an optically and electrically characterized refractive index sensor based on plasmonic resonance and schottky junction," *Optics Letters*, vol. 42, no. 7, pp. 1225–1228, 2017.

[323] K. Li, N. Zhang, N. M. Y. Zhang, G. Liu, T. Zhang, and L. Wei, "Ultrasensitive measurement of gas refractive index using an optical nanofiber coupler," *Optics Letters*, vol. 43, no. 4, pp. 679–682, 2018.

[324] L. Augel, Y. Kawaguchi, S. Bechler, R. Korner, J. Schulze, H. Uchida, and I. A. Fischer, "Integrated collinear refractive index sensor with Ge PIN photodiodes," *ACS Photonics*, vol. 5, no. 11, pp. 4586–4593, 2018.

[325] B. Liu, L. Chen, G. Liu, A. N. Abbas, M. Fathi, and C. Zhou, "High-performance chemical sensing using Schottky-contacted chemical vapor deposition grown monolayer MoS_2 transistors," *ACS Nano*, vol. 8, no. 5, pp. 5304–5314, 2014.

[326] Y. Hu, J. Zhou, P.-H. Yeh, Z. Li, T.-Y. Wei, and Z. L. Wang, "Supersensitive, fast-response nanowire sensors by using Schottky contacts," *Advanced Materials*, vol. 22, no. 30, pp. 3327–3332, 2010.

[327] K. Ma, L. Liu, P. Zhang, Y. He, and Q. Peng, "Optimization of angle-pixel resolution for angular plasmonic biosensors," *Sensors and Actuators B: Chemical*, vol. 283, pp. 188–197, 2019.

[328] Y.-S. Sohn, "A study on the sensitivity of surface plasmon resonance sensor chips with various material configurations in angle and intensity detection modes," *Journal of Sensor Science and Technology*, vol. 26, no. 6, pp. 402–407, 2017.

[329] M. A. Green, A. Ho Baillie, and H. J. Snaith, "The emergence of perovskite solar cells," *Nature Photonics*, vol. 8, p. 506, 2014.

[330] Q. Tai, K. C. Tang, and F. Yan, "Recent progress of inorganic perovskite solar cells," *Energy and Environmental Science*, vol. 12, pp. 2375–2405, 2019.

[331] Q. Zeng, X. Zhang, C. Liu, T. Feng, Z. Chen, W. Zhang, W. Zheng, H. Zhang, and B. Yang, "Inorganic $CsPbI_2Br$ perovskite solar cells: The progress and perspective," *Solar Rapid Research Letters*, vol. 3, no. 1, p. 1800239, 2019.

[332] F. A. Roghabadi, M. Alidaei, S. M. Mousavi, T. Ashjari, A. S. Tehrani, V. Ahmadi, and S. M. Sadrameli, "Stability progress of perovskite solar cells dependent on the crystalline structure: From 3D ABX_3 to 2D Ruddlesden–Popper perovskite absorbers," *Journal of Materials Chemistry A*, vol. 7, no. 11, pp. 5898–5933, 2019.

[333] M. H. Elshorbagy, A. Cuadrado, J. A. Gómez-Pedrero, and J. Alda, "Opto-electronic refractometric sensor based on surface plasmon resonances and the bolometric effect," *Applied Sciences*, vol. 10, no. 4, p. 1211, 2020.

[334] A. Cuadrado, J. Alda, and F. J. Gonzalez, "Distributed bolometric effect in optical antennas and resonant structures," *Journal of Nanophotonics*, vol. 6, no. 1, pp. 1–13, 2012.

[335] A. Cuadrado, J. Alda, and F. J. González, "Multiphysics simulation for the optimization of optical nanoantennas working as distributed bolometers in the infrared," *Journal of Nanophotonics*, vol. 7, no. 1, pp. 1–16, 2013.

[336] T. Tsukagoshi, Y. Kuroda, K. Noda, N. Binh-Khiem, T. Kan, and I. Shimoyama, "Compact surface plasmon resonance system with Au/Si Schottky barrier," *Sensors*, vol. 18, no. 2, p. 399, 2018.

[337] I. Codreanu, F. J. Gonzalez, and G. D. Boreman, "Detection mechanisms in microstrip dipole antenna-coupled infrared detectors," *Infrared Physics & Technology*, vol. 44, no. 3, pp. 155–163, 2003.

[338] J. Alda and G. D. Boreman, *Infrared antennas and resonant structures*. SPIE, 2017.

[339] P. Bharadwaj, A. Bouhelier, and L. Novotny, "Electrical excitation of surface plasmons," *Physical Review Letters*, vol. 106, no. 22, p. 226802, 2011.

[340] P. Krenz, J. Alda, and G. Boreman, "Orthogonal infrared dipole antenna," *Infrared Physics & Technology*, vol. 51, no. 4, pp. 340–343, 2008.

[341] D. R. Lide, *Handbook of Chemistry and Physics*. CRC Press, 75th. ed., 1997.

[342] G. Zheng, J. Cong, L. Xu, and J. Wang, "High-resolution surface plasmon resonance sensor with fano resonance in waveguide-coupled multilayer structures," *Applied Physics Express*, vol. 10, no. 4, p. 042202, 2017.

[343] D. V. Nesterenko and Z. Sekkat, "Resolution estimation of the Au, Ag, Cu, and Al single-and double-layer surface plasmon sensors in the ultraviolet, visible, and infrared regions," *Plasmonics*, vol. 8, no. 4, pp. 1585–1595, 2013.

[344] M. Wiki and R. Kunz, "Wavelength-interrogated optical sensor for biochemical applications," *Optics Letters*, vol. 25, no. 7, pp. 463–465, 2000.

[345] K. Cottier, M. Wiki, G. Voirin, H. Gao, and R. Kunz, "Label-free highly sensitive detection of (small) molecules by wavelength interrogation of integrated optical chips," *Sensors and Actuators B: Chemical*, vol. 91, no. 1-3, pp. 241–251, 2003.

[346] J.-N. Yih, F.-C. Chien, C.-Y. Lin, H.-F. Yau, and S.-J. Chen, "Angular-interrogation attenuated total reflection metrology system for plasmonic sensors," *Applied Optics*, vol. 44, no. 29, pp. 6155–6162, 2005.

[347] L. Wen, L. Liang, X. Yang, Z. Liu, B. Li, and Q. Chen, "Multiband and ultrahigh figure-of-merit nanoplasmonic sensing with direct electrical readout in Au-silicon nanojunction," *ACS Nano*, vol. 13, no. 6, pp. 6963–6972, 2019.

[348] J. P. Craig, P. A. Simmons, S. Patel, and A. Tomlison, "refractive index and osmolality of human tears," *Optometry and Vision Science*, vol. 72, no. 10, pp. 718–724, 1995.

[349] V. A. dos Santos, L. Schmetterer, M. Gröschl, G. Garhofer, D. Schmidl, M. Kucera, A. Unterhuber, J.-P. Hermand, and R. M. Werkmeister, "In vivo tear film thickness measurement and tear film dynamics visualization using spectral domain optical coherence tomography," *Optics Express*, vol. 23, no. 16, pp. 21043–21063, 2015.

[350] R. Austin and G. Halikas, "The index of refraction of seawater," tech. rep., UC San Diego: Scripps Institution of Oceanography, 1976.

[351] X. Quan and E. S. Fry, "Empirical equation for the index of refraction of seawater," *Applied Optics*, vol. 34, no. 18, pp. 3477–3480, 1995.

[352] P. Vivo, J. K. Salunke, and A. Priimagi, "Hole transporting materials for printable perovskite solar cells," *Materials*, vol. 10, no. 9, p. 1087, 2017.

[353] J. Kim, A. Ho Baillie, and S. Huang, "Review of novel passivation techniques for efficient and stable perovskite solar cells," *Solar Rapid Research Letters*, vol. 3, no. 4, p. 1800302, 2019.

[354] M. H Elshorbagy, A. Cuadrado, and J. Alda, "Narrow absorption in ITO-Free perovskite solar cells for sensing applications analyzed through electromagnetic simulation," *Applied Sciences*, vol. 9, no. 22, p. 4850, 2019.

[355] C. Hu and D. Liu, "High performance grating coupled surface plasmon resonance sensor based on Al/Au bimetallic layer," *Modern Applied Science*, vol. 4, no. 6, p. 8, 2010.

[356] E. Babaei, Z. Sharifi, and R. Gordon, "Improving sensitivity of existing surface plasmon resonance systems with grating coupled short range surface plasmons," *Journal of the Optical Society of America B*, vol. 36, no. 8, pp. F144–F148, 2019.

[357] J. van Gent, P. V. Lambeck, H. J. Kreuwel, G. J. Gerritsma, E. J. Sudholter, D. N. Reinhoudt, and T. J. Popma, "Optimization of a chemooptical surface plasmon resonance based sensor," *Applied Optics*, vol. 29, no. 19, pp. 2843–2849, 1990.

[358] X. Gan, R. J. Shiue, Y. Gao, I. Meric, T. F. Heinz, K. Shepard, J. Hone, S. Assefa, and D. Englund, "Chip integrated ultrafast graphene photodetector with high responsivity," *Nature Photonics*, vol. 7, no. 11, p. 883, 2013.

[359] C. Giraudet, L. Marlin, D. Begue, F. Croccolo, and H. Bataller, "Concentration dependent refractive index of CO_2/CH_4 mixture in gaseous and supercritical phase," *The Journal of Chemical Physics*, vol. 144, no. 13, p. 134304, 2016.

[360] G. Klos, M. Miola, and D. S. Sutherland, "Increased refractive index sensitivity by circular dichroism sensing through reduced substrate effect," *The Journal of Physical Chemistry C*, vol. 123, no. 12, pp. 7347–7355, 2019.

[361] N. Muhammad, Z. Ouyang, Q. Liu, X. Tang, Z. L. Deng, and A. Daud Khan, "Sensitive label-free sensor with high figure of merit based on plasmonic metasurface with unit cell of double two-split nanorings," *Journal of Materials Science*, vol. 54, no. 8, pp. 6301–6309, 2019.

[362] A. Alipour, A. Farmani, and A. Mir, "High sensitivity and tunable nanoscale sensor based on plasmon induced transparency in plasmonic metasurface," *IEEE Sensors Journal*, vol. 18, no. 17, pp. 7047–7054, 2018.

[363] S. K., Y. Lee, J. Y. Kim, J. H. Yang, H. J. Kwon, J. Y. Hwang, C. Moon, and J. E. Jang, "Color sensitive and spectrometer free plasmonic sensor for biosensing applications," *Biosensors and Bioelectronics*, vol. 126, pp. 743–750, 2019.

[364] B. Yin, S. Wu, M. Wang, W. Liu, H. Li, B. Wu, and Q. Wang, "High sensitivity refractive index and temperature sensor based on cascaded dual -wavelength fiber laser and SNHNS interferometer," *Optics Express*, vol. 27, no. 1, pp. 252–264, 2019.

[365] W. Edmondson, "Gas analysis by refractive index measurement," *British Journal of Anaesthesia*, vol. 29, no. 12, pp. 570–574, 1957.

[366] H. Ishida, Y. Kagawa, T. Nakamoto, and T. Moriizumi, "Odor-source localization in the clean room by an autonomous mobile sensing system," *Sensors and Actuators B: Chemical*, vol. 33, no. 1-3, pp. 115–121, 1996.

[367] J. Hromadka, S. Korposh, M. C. Partridge, S. W. James, F. Davis, D. Crump, and R. P. Tatam, "Multi-parameter measurements using optical fibre long period gratings for indoor air quality monitoring," *Sensors and Actuators B: Chemical*, vol. 244, pp. 217–225, 2017.

[368] M. H. Elshorbagy, A. Cuadrado, B. Romero, and J. Alda, "Enabling selective absorption in perovskite solar cells for refractometric sensing of gases," *Scientific Reports*, vol. 10, no. 1, p. 7761, 2020.

[369] S. Topliss, S. James, F. Davis, S. Higson, and R. Tatam, "Optical fibre long period grating based selective vapour sensing of volatile organic compounds," *Sensors and Actuators B: Chemical*, vol. 143, no. 2, pp. 629–634, 2010.

[370] A. Mirzaei, S. Leonardi, and G. Neri, "Detection of hazardous volatile organic compounds (VOCs) by metal oxide nanostructures-based gas sensors: A review," *Ceramics International*, vol. 42, no. 14, pp. 15119–15141, 2016.

[371] L. Spinelle, M. Gerboles, M. G. Villani, M. Aleixandre, and F. Bonavitacola, "Field calibration of a cluster of low-cost available sensors for air quality monitoring. Part A: ozone and nitrogen dioxide," *Sensors and Actuators B: Chemical*, vol. 215, pp. 249–257, 2015.

[372] L. Spinelle, M. Gerboles, M. G. Villani, M. Aleixandre, and F. Bonavitacola, "Field calibration of a cluster of low-cost commercially available sensors for air quality monitoring. part B: NO, CO and CO_2," *Sensors and Actuators B: Chemical*, vol. 238, pp. 706–715, 2017.

[373] B. Edlen, "The refractive index of air," *Metrologia*, vol. 2, no. 2, p. 71, 1966.

[374] P. E. Ciddor, "Refractive index of air: new equations for the visible and near infrared," *Applied Optics*, vol. 35, no. 9, pp. 1566–1573, 1996.

[375] C. Caucheteur, V. Malachovska, C. Ribaut, and R. Wattiez, "Cell sensing with near-infrared plasmonic optical fiber sensors," *Optics & Laser Technology*, vol. 78, pp. 116–121, 2016.

[376] A. Afsari and M. J. Sarraf, "Design of a hydrogen sulfide gas sensor based on a photonic crystal cavity using graphene," *Superlattices and Microstructures*, vol. 138, p. 106362, 2020.

[377] G. Z. Xiao, A. Adnet, Z. Zhang, F. G. Sun, and C. P. Grover, "Monitoring changes in the refractive index of gases by means of a fiber optic Fabry-Perot interferometer sensor," *Sensors and Actuators A: Physical*, vol. 118, no. 2, pp. 177–182, 2005.

[378] D. Pawar, B. B. Rao, and S. Kale, "Highly porous graphene coated optical fiber in Fabry-Perot interferometric mode for NH_3 gas sensing," in *International Conference on Fibre Optics and Photonics*, pp. Tu4A–58, Optical Society of America, 2016.

[379] S. Pevec and D. Donlagic, "Miniature fiber-optic Fabry-Perot refractive index sensor for gas sensing with a resolution of $5x10^{-9}$ RIU," *Optics Express*, vol. 26, no. 18, pp. 23868–23882, 2018.

[380] X. Wang, S. Wang, J. Jiang, K. Liu, P. Zhang, W. Wu, and T. Liu, "High-accuracy hybrid fiber-optic Fabry-Pérot sensor based on MEMS for simultaneous gas refractive-index and temperature sensing," *Optics Express*, vol. 27, no. 4, pp. 4204–4215, 2019.

[381] T. Allsop, V. Kundrat, K. Kalli, G. B. Lee, R. Neal, P. Bond, B. Shi, J. Sullivan, P. Culverhouse, and D. J. Webb, "Methane detection scheme based upon the changing optical constants of a zinc oxide/platinum matrix created by a redox reaction and their effect upon surface plasmons," *Sensors and Actuators B: Chemical*, vol. 255, pp. 843–853, 2018.

[382] M. Mansouri, A. Mir, and A. Farmani, "Numerical modeling of a nanostructure gas sensor based on plasmonic effect," *Jounal of Optoelectornical Nanostructures*, vol. 4, no. 2, pp. 29–43, 2019.

[383] R. S. El Shamy, D. Khalil, and M. A. Swillam, "Mid infrared optical gas sensor using plasmonic Mach-Zehnder interferometer," *Scientific Reports*, vol. 10, no. 1, pp. 1–9, 2020.

[384] Z. Zhang, J. He, B. Du, K. Guo, and Y. Wang, "Highly sensitive gas refractive index sensor based on hollow-core photonic bandgap fiber," *Optics Express*, vol. 27, no. 21, pp. 29649–29658, 2019.

[385] S. Sun, Y. Xu, L. Ren, J. Xu, T. Jia, L. Zhang, J. Xiao, B. Wang, W. Yang, S. Cheng, *et al.*, "Research on the gas refractive index sensing based on microfiber double-knot resonator with a parallel structure," *Optik*, p. 164207, 2020.

[386] G. Zheng, J. Cong, L. Xu, and J. Wang, "High-resolution surface plasmon resonance sensor with fano resonance in waveguide-coupled multilayer structures," *Applied Physics Express*, vol. 10, no. 4, p. 042202, 2017.

[387] A. Shakoor, B. C. Cheah, D. Hao, M. Al-Rawhani, B. Nagy, J. Grant, C. Dale, N. Keegan, C. McNeil, and D. R. S. Cumming, "Plasmonic sensor monolithically integrated with a CMOS photodiode," *ACS Photonics*, vol. 3, no. 10, pp. 1926–1933, 2016.

[388] E. López-Fraguas, B. Arredondo, C. Vega-Colado, G. del Pozo, M. Najafi, D. Martín-Martín, Y. Galagan, J. M. Sánchez-Pena, R. Vergaz, and B. Romero, "Visible light communication system using an organic emitter and a perovskite photodetector," *Organic Electronics*, vol. 73, pp. 292–298, 2019.

[389] L. Dou, Y. M. Yang, J. You, Z. Hong, W.-H. Chang, G. Li, and Y. Yang, "Solution-processed hybrid perovskite photodetectors with high detectivity," *Nature Communications*, vol. 5, no. 1, p. 5404, 2014.

[390] A. Cuadrado, L. M. Sanchez-Brea, F. J. Torcal-Milla, J. A. Quiroga, and J. A. Gomez-Pedrero, "Numerical model of the inhomogeneous scattering by the human lens," *Biomedical Optics Express*, vol. 10, no. 5, pp. 2161–2176, 2019.

[391] J. Becker, A. Trügler, A. Jakab, U. Hohenester, and C. Sönnichsen, "The optimal aspect ratio of gold nanorods for plasmonic bio-sensing," *Plasmonics*, vol. 5, no. 2, pp. 161–167, 2010.

Abbreviations in bibliography: volume(vol), number(no), chapter(ch), page(p), pages(pp).

List of publications

Publications in international journals

1. Mahmoud H. Elshorbagy, Kamal Abdel-Hady, Hala Kamal, Javier Alda, "Broadband anti-reflection coating using dielectric Si3N4 nanostructures. Application to amorphous-Si-H solar cells", *Optics Communications, 390, 130-136, 2017.*

2. Mahmoud H. Elshorbagy, J Alda, "Funneling and guiding effects in ultrathin aSi-H solar cells using one-dimensional dielectric subwavelength gratings", *Journal of Photonics for Energy 7 (1), 017002, 2017.*

3. Mahmoud H. Elshorbagy, A Cuadrado, J Alda, "High-sensitivity integrated devices based on surface plasmon resonance for sensing applications", *Photonics Research 5 (6), 654-661, 2017.*

4. Mahmoud H. Elshorbagy, A Cuadrado, J Alda, "Plasmonic sensor based on dielectric nanoprisms", *Nanoscale research letters 12 (1), 1-7, 2017.*

5. Mahmoud H. Elshorbagy, A Cuadrado, J Alda, "Narrow Absorption in ITO-Free Perovskite Solar Cells for Sensing Applications Analyzed through Electromagnetic Simulation", *Applied Sciences 9 (22), 4850, 2019.*

6. Mahmoud H. Elshorbagy, A Cuadrado, G González, FJ González, J Alda, "Performance improvement of refractometric sensors through hybrid plasmonic–fano resonances", *Journal of Lightwave Technology 37 (13), 2905-2913, 2019.*

7. Mahmoud H. Elshorbagy, B García-Cámara, E López-Fraguas, R Vergaz, "Efficient light management in a monolithic tandem perovskite/silicon solar cell by using a hybrid metasurface", *Nanomaterials 9 (5), 791, 2019.*

8. Mahmoud H. Elshorbagy, Alexander Cuadrado, Braulio García-Cámara, Ricardo Vergaz, José Antonio Gómez-Pedrero, Javier Alda, "Ultra-narrow spectral response of a hybrid plasmonic-grating sensor", *IEEE Sensors Journal, 20 (7), 3520-3528, 2019.*

9. Mahmoud H. Elshorbagy, A Cuadrado, JA Gómez-Pedrero, J Alda, "Opto-Electronic Refractometric Sensor Based on Surface Plasmon Resonances and the Bolometric Effect", *Applied Sciences 10 (4), 1211, 2020.*

10. Mahmoud H. Elshorbagy, A Cuadrado, J Alda, "Plasmonic sensors based on funneling light through nanophotonic structures", *Plasmonics, 1-7, 2020.*

11. Mahmoud H. Elshorbagy, Eduardo López-Fraguas, Fateh A Chaudhry, José Manuel Sánchez-Pena, Ricardo Vergaz, Braulio García-Cámara, "A monolithic nanostructured-perovskite/silicon tandem solar cell: feasibility of light management through geometry and materials selection", *Scientific Reports, 10 (1), 2271, 2020.*

12. Mahmoud H. Elshorbagy, Alexander Cuadrado, Beatriz Romero, Javier Alda, "Enabling selective absorption in perovskite solar cells for refractometric sensing of gases", *Scientific Reports 10, (1), 7761, 2020.*

Publications in Conferences

1. Mahmoud H. Elshorbagy, A Cuadrado, J Alda, "Performance enhancement in solar cells using nanophotonic structures", *X Reunión Española de Optoelectrónica, OPTOEL*, Santiago de Compostela, Spain, 2017.

2. Mahmoud H. Elshorbagy, A Cuadrado, J Alda. "Funneling and guiding effects in nanostructures", *10^a Reunión Española de Optoelectrónica, OPTOEL*, Santiago de Compostela, Spain, 2017.

3. A Cuadrado, Mahmoud H. Elshorbagy, FJ Torcal-Milla, LMS Brea,"Scattering producido por las vesículas del cristalino y su efecto en las cataratas", *XII Reunión Nacional de Óptica, 97*, Castellón, Spain 2018.

4. Mahmoud H. Elshorbagy, A Cuadrado, B García-Cámara, R Vergaz, J Alda, "Sensing refractive index changes by guided surface plasmon waves at dielectric – dielectric interface using a 1D grating array", *XII Reunión Nacional de Óptica, 97*, Castellón, Spain, 2018.

5. B García-Cámara, R Vergaz, F Algorri, E López-Fraguas, Mahmoud H. Elshorbag, "The Quest of Directional Light Scattering", *Conference: 40th PIERS*, Toyama, Japan, 2018.

6. Mahmoud H. Elshorbagy, A Cuadrado, JA Gómez-Pedrero, J Alda, "Enhanced performance of plasmonic sensors using multilayer gratings", *XI Reunión Española de Optoelectrónica, OPTOEL*, Zaragoza, Spain, 2019.

7. B Garcia-Camara, E Lopez-Fraguas, Mahmoud H. Elshorbagy, R Vergaz, "Dielectric nanostructures to enhance the efficiency of solar cells", *META 2019, the 10th International Conference on Metamaterials, Photonic Crystals and Plasmonics*, Lisbon, Portugal, 2019.

8. Mahmoud H. Elshorbagy, Alexander Cuadrado, Javier Alda, *Invited lecture*, "Nanostructuring photovoltaic cells: How to push some limits", *META 2019, the 10th International Conference on Metamaterials, Photonic Crystals and Plasmonics*, Lisbon, Portugal, 2019.